Technical Report Documentation Page

| 1. Report No.<br>FHWA/TX-10/9-5498-1 | 2. Government Accession No. | 3. Recipient's Catalog No. |
|---|---|---|
| 4. Title and Subtitle<br>Modeling the Response of Fracture Critical Steel Box-Girder Bridges | | 5. Report Date<br>February 2010<br>6. Performing Organization Code |
| 7. Author(s)<br>Timothy Barnard, Catherine G. Hovell, James P. Sutton, Joshua M. Mouras, Bryce J. Neuman, Vasileios A. Samaras, Janghwan Kim, Eric B. Williamson, and Karl H. Frank | | 8. Performing Organization Report No.<br>9-5498-1 |
| 9. Performing Organization Name and Address<br>Center for Transportation Research<br>The University of Texas at Austin<br>1616 Guadalupe St, Suite 4.202<br>Austin, TX 78701 | | 10. Work Unit No. (TRAIS)<br>11. Contract or Grant No.<br>9-5498 |
| 12. Sponsoring Agency Name and Address<br>Texas Department of Transportation<br>Research and Technology Implementation Office<br>P.O. Box 5080<br>Austin, TX 78763-5080 | | 13. Type of Report and Period Covered<br>Technical Report<br>September 2005–August 2009<br>14. Sponsoring Agency Code |
| 15. Supplementary Notes<br>Project performed in cooperation with the Texas Department of Transportation and the Federal Highway Administration. | | |

16. Abstract

Bridges that are classified as *fracture critical* by AASHTO require more frequent inspections than other types of bridges, resulting in greater costs for their maintenance. Several historical events have shown, however, that severe damage can occur to a bridge without necessarily resulting in its collapse. A primary objective of this research project was to characterize the redundancy that exists in twin steel box-girder bridges, which are widely used in Texas and are classified as fracture critical. The main goal of the research was to develop guidelines for modeling a bridge's behavior in the event that a fracture of a critical tension flange takes place.

The research carried out under this project included laboratory testing, experimental evaluation of a full-scale box-girder bridge, and detailed structural analyses. Data gathered from the experimental testing program were used to validate nonlinear finite element models as well as simplified engineering models. Based on the results of this research, engineers now have guidelines for modeling the response of twin steel box-girder bridges following the fracture of one of its girders.

| 17. Key Words<br>Bridges, fracture critical, design guidelines, finite element analysis. | 18. Distribution Statement<br>No restrictions. This document is available to the public through the National Technical Information Service, Springfield, Virginia 22161; www.ntis.gov. |
|---|---|

| 19. Security Classif. (of report)<br>Unclassified | 20. Security Classif. (of this page)<br>Unclassified | 21. No. of pages<br>172 | 22. Price |
|---|---|---|---|

Form DOT F 1700.7 (8-72) Reproduction of completed page authorized

# Modeling the Response of Fracture Critical Steel Box-Girder Bridges

Timothy Barnard
Catherine G. Hovell
James P. Sutton
Joshua M. Mouras
Bryce J. Neuman
Vasileios A. Samaras
Janghwan Kim
Eric B. Williamson
Karl H. Frank

| | |
|---|---|
| CTR Technical Report: | 9-5498-1 |
| Report Date: | February 9, 2010 |
| Project: | 9-5498 |
| Project Title: | Methods of Evaluating the Redundancy of Steel Bridges |
| Sponsoring Agency: | Texas Department of Transportation |
| Performing Agency: | Center for Transportation Research at The University of Texas at Austin |

Project performed in cooperation with the Texas Department of Transportation and the Federal Highway Administration.

Center for Transportation Research
The University of Texas at Austin
1616 Guadalupe St, Suite 4.202
Austin, TX 78701

www.utexas.edu/research/ctr

# Disclaimers

**Author's Disclaimer**: The contents of this report reflect the views of the authors, who are responsible for the facts and the accuracy of the data presented herein. The contents do not necessarily reflect the official view or policies of the Federal Highway Administration or the Texas Department of Transportation (TxDOT). This report does not constitute a standard, specification, or regulation.

**Patent Disclaimer**: There was no invention or discovery conceived or first actually reduced to practice in the course of or under this contract, including any art, method, process, machine manufacture, design or composition of matter, or any new useful improvement thereof, or any variety of plant, which is or may be patentable under the patent laws of the United States of America or any foreign country.

# Engineering Disclaimer

NOT INTENDED FOR CONSTRUCTION, BIDDING, OR PERMIT PURPOSES.

Project Engineer: Eric B. Williamson
Professional Engineer License State and Number: Texas No. 94410
P. E. Designation: Research Supervisor

# Acknowledgments

The authors wish to express their thanks for the guidance from the TxDOT Project Directors Alan Kowalik and Keith Ramsey, the Project Monitoring Committee, and Peter Forsling of the FHWA for his role as a Project Advisor.

# Table of Contents

# List of Tables

# List of Figures

# Chapter 1. Introduction

## 1.1 Fracture Critical Bridges: Background

In the winter of 1967, the Silver Point Bridge in Point Pleasant, West Virginia suddenly collapsed into the Ohio River (Figure 1.1). The investigation of the failure determined that the fracture of a single eye-bar connecting the bridge's suspension chain released the primary load path, which resulted in the total collapse of the structure (Scheffey, 1971). This event demonstrated that the failure of individual members could have a significant influence on the stability of an entire bridge structure, and it led to a reconsideration of code and safety requirements for bridges theoretically susceptible to this type of failure.

Fracture critical member provisions were first introduced into the American Association of State Highway Transportation Officials (AASHTO) Bridge Design Specifications in 1978. In the current draft of that document, a fracture critical member is defined as a "component in tension whose failure is expected to result in the collapse of the bridge or the inability of the bridge to perform its function" (AASHTO, 2007). All bridges designed with fracture critical members or components are designated as fracture critical bridges.

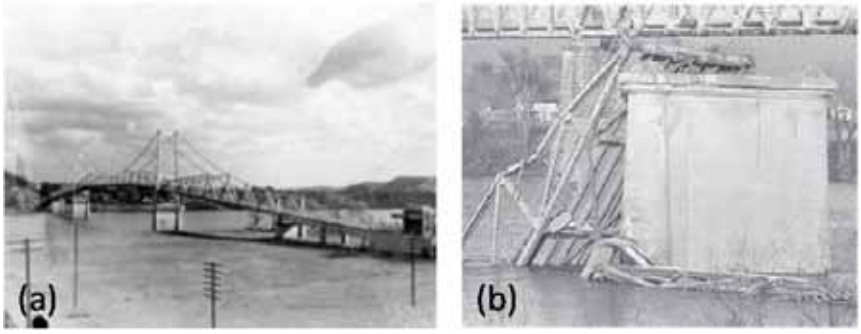


*Figure 1.1: The Point Pleasant Bridge (a) In service, (b) After failure*

The bridge design process is affected by many factors, including economics, aesthetics, function, and traffic volume, and many popular bridge structural systems are classified as fracture critical. In fact, approximately 11% of all steel bridges in the United States have this designation (Connor, et al., 2005). As long as the risk of a brittle fracture of an integral component of a bridge's main load path is minimized, a fracture critical bridge is not inherently unsafe. For this reason, the design of fracture critical bridges is permitted, but a primary requirement is that such bridges must undergo a full inspection every two years. Fracture critical bridge inspections are labor intensive—and therefore costly—requiring the examination of every welded connection to a fracture critical member. Olson estimated the cost to be approximately $400,000 per day (Olson, 2008). Similar costs have been estimated by TxDOT.

## 1.2 Fracture Critical Bridges: In Service

The fracture critical provisions in the AASHTO Bridge Design Specifications (2007) assume that if a fracture critical member were to fail, the remaining bridge structure would lack a redundant load path to support its loads. A number of incidents involving the full-depth fracture

of in-service, two-girder bridges (all designated as fracture critical) provide evidence that, in certain cases, a redundant load path does exist in these structures even though they have not been given credit for such. In 1976, the US 52 Bridge over the Mississippi River near Savanna, Illinois sustained a full-depth fracture of one of its two girders, but it remained in service until static deflections of 6.5 in. prompted an inspection that discovered the fracture (Fisher, 1977). In 1977, a full-depth fracture of one of the two girders on the Neville Island Bridge on I 79 in Pittsburg, Pennsylvania resulted in deflections so slight that motorists were unaffected, and the fracture remained unnoticed until it was spotted by a nearby boater (Schwendeman, 1978) (Figure 1.2). A similar case was documented in 2003, when a bird-watcher noticed a full-depth fracture in the Brandywine River Bridge on I 95 in Wilmington, Delaware (Quiel, 2003).

*Figure 1.2: Opposing views of the Neville Island Bridge girder fracture*

Conflicting evidence on how the loss of a fracture critical member affects overall bridge performance has prompted bridge owners to question the applicability of the fracture critical provisions. One common concern is that, if a fracture critical bridge's stability is not always decisively linked to the performance of its fracture critical members, the increased inspection requirements for this designation of structure require owners to utilize an unnecessarily large amount of labor and financial resources.

## 1.3 Research Initiative

The Texas Department of Transportation (TxDOT) owns and operates a vast inventory of more than 50,000 bridges throughout the state. Many of these bridges are two-girder bridges and are classified as fracture critical by the AASHTO guidelines. Under the current schedule, TxDOT spends over $26 million annually on bridge inspections. A significant portion of this allocation is spent on the bi-annual inspection of all the fracture critical bridges in the state. If a substantial proportion of fracture critical bridges do in fact have the redundant capacity to support their loads in the event of the loss of a fracture critical component, TxDOT may be over-utilizing their resources for the frequent inspections of these bridges.

In search of guidance in reevaluating the inspection schedule for fracture critical bridges, TxDOT and the Federal Highway Administration (FHWA) co-sponsored a large-scale research program at the Ferguson Structural Engineering Laboratory (FSEL) at The University of Texas at Austin. The overall goal of the project was to provide bridge engineers with methods for evaluating the redundancy of fracture critical steel bridges. The research focused specifically on investigating the redundant capacity of fracture critical box-girder bridges, which are common throughout the state of Texas (Figure 1.3). Using tools to estimate the load carrying capacities of

their structures in the event of a loss of a fracture critical member, bridge owners would be able to appropriately tailor their maintenance schedules to their bridge inventory.

Supported by significant experimental, computational, and financial resources, the comprehensive research program at FSEL continued for four years and consisted of a set of interrelated experimental and computational initiatives. The techniques used to work toward the ultimate goal of the project included structural analyses performed through 'hand-calculation' methods, analyses performed through detailed computer-based simulations, the testing of laboratory specimens to quantify experimentally the capacity of specific bridge components, and the full-scale testing of a twin steel box-girder bridge (i.e., a fracture critical bridge) reconstructed at FSEL for use in this project.

*Figure 1.3: A typical two-box steel girder bridge in Austin, TX*

## 1.4 Scope of Work

The scope of TxDOT Research Project 9-5498 was extensive, and it involved a unique experimental program that included both laboratory tests and the full-scale destructive testing of a twin steel box-girder bridge (Figure 1.4). The laboratory tests focused on the pull-out behavior of shear studs embedded in a concrete deck. These tests provided essential data for quantifying the response of a component that formed a part of the critical load path essential to the redundancy of twin steel box-girder bridges. These tests were performed both statically and dynamically and led to the development of design guidelines that considered the effects of stud embedment depth, stud spacing, stud positioning, and the presence of a haunch. Details of this effort can be found in the report "The Tensile Capacity of Welded Shear Studs" (Mouras, 2009).

*Figure 1.4: The FSEL test-bridge*

Findings from the full-scale bridge tests revealed the inherent redundancy of the bridge evaluated during this research program. From a perspective of redundancy, the bridge considered during this project represented one of the worst cases. It was a simply supported bridge and therefore did not possess any inherent redundancy that is attributed to structures that are statically indeterminate. Furthermore, all external braces that could have contributed to redistributing loads from the fractured girder to the intact girder were removed following construction based on standard TxDOT practice. In addition, the bridge rails were constructed with expansion joints that limited the capacity that these components could contribute to the overall strength of the bridge. Finally, the bridge was horizontally curved in plan, and the exterior girder was the one where a simulated fracture was induced. All of these effects combined to make the bridge less redundant than it might have otherwise been. Yet, despite these limitations, the bridge tested in this study performed remarkably well. In the first test, a linear-shape-charge explosive was used to rapidly cut through the bottom flange of the exterior girder, simulating what would occur during a fracture. Figure 1.5 shows a sequence of photos that were taken from the high-speed video that was used to record the event, and Figure 1.6 shows the condition of the bottom flange of the fractured girder following the test. Despite the equivalent of an HS-20 truck positioned directly above the fracture at the most severe location, the bridge deflected less than an inch.


*Figure 1.5: First bridge fracture test (bottom flange simulated fracture by explosion)*

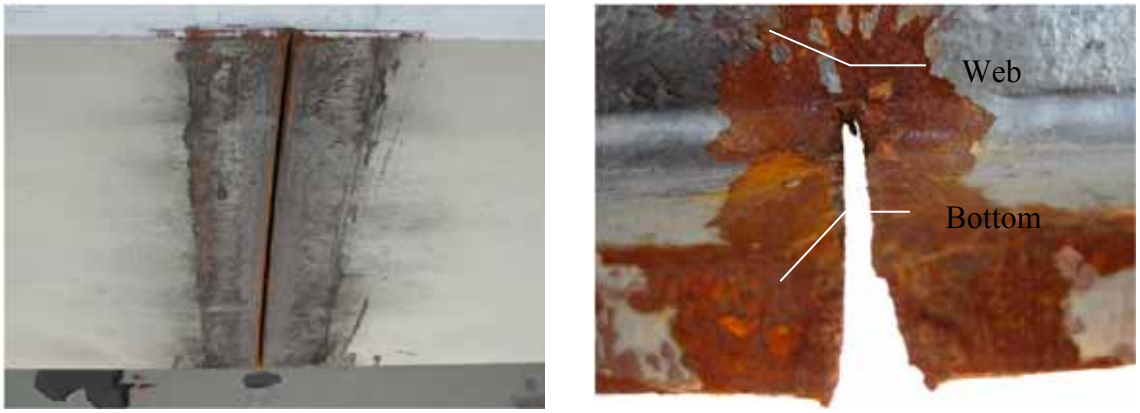


(a) Full cut of the bottom flange (b) Detained fracture at web

*Figure 1.6: Bottom flange cut of fractured girder*

For the second test, when the exterior girder had a full-depth fracture induced and the applied loads were suddenly released through the use of an explosive acting on a temporary scissor jack support system (Figure 1.7), the bridge still performed extremely well, with the fractured girder deflecting only 7.0 inches. Even in its damaged state, the bridge could support traffic and did not collapse. The third and final test, which was conducted under statically applied loads, demonstrated that the bridge tested in this study was able to carry 363,000 lbs.—more than five times greater than the legal truck load (Figure 1.8). Considering the level of damage that existed prior to this test, the capacity of the bridge was remarkable.

For all three tests, massive amounts of data were collected to capture the response of various bridge components that were critical to the redundancy of the structure. A detailed report of each test, the data collected, and the general findings of the experimental research program can be found in "Evaluating the Redundancy of Steel Bridges: Full-Scale Destructive Testing of a Fracture Critical Twin Box-Girder Steel Bridge" by Neuman (2009). In the interest of space, details of that report are not included in this document. The focus of the current report is on describing methods of modeling that can be used to compute the response of these types of bridge systems following the fracture of one of the critical tension flanges.

*Figure 1.7: Second bridge fracture test*

Incremental loading Collapsed bridge

*Figure 1.8: Loading process and bridge collapse in third bridge-fracture test*

In this report, modeling guidelines and analysis procedures are given that will allow an engineer to assess the performance of a twin steel box-girder bridge in the event that a fracture takes place in one of the girders. Two levels of modeling are provided: the first is a simplified approach that can be conducted using hand-based procedures and simple spreadsheet software, and the second is a detailed computational approach that is based on the finite element method. Both of these modeling approaches have been extensively validated against the test data collected during the experimental research program.

Following this chapter, the simplified approach to modeling the response of fracture critical twin steel box-girder bridges is provided. It is expected that engineers will utilize this approach first in all cases. Furthermore, it is expected that the results computed using this procedure will be sufficient for estimating overall load-carrying capacity for the vast majority of cases. In some situations, however, the results obtained from the simplified approach may not provide the level of detail necessary to evaluate the redundancy of these types of bridges. Hence, on occasion, it may be necessary to carry out a detailed finite element analysis to compute overall load-carrying capacity, and the second part of this report provides details and modeling guidelines for doing so. Finally, a summary of the work performed as well as some concluding remarks and recommendations are included in Chapter 7. Following the last chapter, appendices that include complete examples using the simplified analysis approach are provided.

# Chapter 2. Simplified Analytical Modeling Methods to Evaluate the Redundancy of Twin-Box Girder Bridges

## 2.1 Introduction

To assess the performance of a twin steel box-girder bridge in the event that one of the fracture critical tension flanges suffers a failure, engineers require structural analysis models capable of representing the complex behavior that occurs under such conditions. The most rigorous way to analyze such a complex system and obtain detailed results is through finite element modeling. While finite element analyses may provide the most accurate results, they require a substantial amount of effort to develop the model, significant computational resources to carry out the analyses, and expertise on the part of the analyst to develop models with significant nonlinear response. In contrast, simplified procedures for initial checks of the redundancy level of a bridge are more beneficial to engineers in practice. Thus, engineers can potentially save a significant amount of time if the simplified methods are adequate to characterize behavior of the bridge being analyzed. The development of such simple analytical methods to improve the understanding of the behavior and to evaluate the redundancy level of twin steel box-girder bridges is presented in this chapter. The simplified analysis methods were validated against the test data collected during the three-part test series described in Chapter 0.

Prior to the first test in which an explosive was used to sever the bottom flange, Sutton (2007) developed a simple analytical model that showed that the deck and the intact girder were able to provide an alternative load path when a full-depth fracture would occur at the mid-span of the fractured girder. Uncertainty in the calculation of the tensile capacity of the shear studs, however, motivated the research team to conduct a series of laboratory tests to determine the tensile capacity of a group of shear studs. These tests were initiated by Sutton (2007) and were extended by Mouras (2008). Mouras developed modifications to the existing ACI code equations to predict the findings obtained from the laboratory test program. The proposed strength equations, which are used in the examples presented in this chapter, are able to predict the strength of these alternate shear stud configurations and the effect of the haunch.

An overview of the simplified analytical modeling techniques used to evaluate the redundancy of a fracture critical twin steel box-girder bridge is presented in this chapter. In the next chapter, a detailed example is provided that demonstrates how to implement the proposed simplified modeling technique. Additional examples are provided in the appendix included at the end of this report. In total, the examples given in this report demonstrate the effect of different bridge configurations on the ultimate load that a bridge can sustain in the event that a fracture occurs.

## 2.2 Initial Strength Checks

Consistent with the experimental testing program, it is proposed that evaluations of bridge redundancy be performed for the case in which a single HS-20 truck is positioned on the bridge deck above the presumed fracture location so as to cause the most severe internal stresses to develop. Thus, on an in-service bridge, this worst-case scenario would occur when the design truck load was passing across the bridge at the location that induced the maximum internal bending moment at the same instant that a fracture event occurred at that point of maximum moment. Under these conditions, initial strength checks are performed to determine if there is

sufficient strength in the intact girder to support the weight of the bridge and the factored truck load and to evaluate if the deck has sufficient strength to transmit the load carried by the fractured girder to the intact girder. If the bridge under consideration does not satisfy these initial strength checks, a three-dimensional finite element model may developed to provide a more accurate estimate of the bridge's performance. Finite element modeling techniques for such cases are described later in this report.

### 2.2.1 Load Calculation and Moment Capacity Determination

First, the estimated load that is transmitted to the intact girder after the fracture of the other girder should be calculated. For this calculation, it is assumed that half of the total dead load and the entire truck load are carried by the intact girder. It is recommended that a load factor equal to or larger than two should be applied to the truck live load. The intact girder's positive and negative moment capacity need to be checked to determine if they are sufficient to sustain the transmitted load and the self-weight of the intact composite girder. Two moment capacity checks should be made on the intact girder resulting from this loading:

a. Positive moment region $M_{applied} < M_p$ plastic moment capacity

b. Negative moment region: $M_y$ at pier if non-compact or $M_p$ if compact.

### 2.2.2 Deck Shear and Shear Stud Tensile Capacity

The bridge deck is a vital link in the transfer of load from the fractured girder to the intact girder. The deck capacity can be calculated using a strip model of the deck (Figure 2.1) with a width equal to the shear stud spacing.

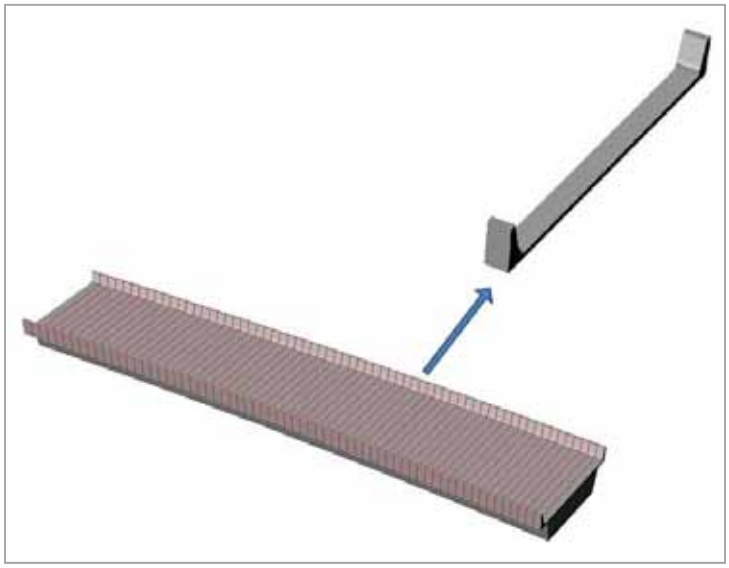

*Figure 2.1: Deck Strip*

The deck strip should be analyzed as a continuous beam with roller connections at the location of top flanges (Figure 2.2). Two strength checks need to be performed on the deck. First, the bridge deck shear capacity should be greater than the transferred shear. The shear capacity is the sum of the capacity of the individual deck strips. The transferred shear is assumed to be equal to the

entire dead load carried by the fractured girder plus the factored truck load. The unsupported load must be transferred to the intact girder, and therefore the deck shear capacity should be adequate. The maximum shear capacity is taken as the smaller of the shear corresponding to a plastic moment mechanism in the deck and the shear capacity of the deck, $V_{Deck}$. The shear developed from the plastic moment deck mechanism shown in Figure 2.3 is given by Equation 2-1,

$$V = \frac{M_1 + M_2}{S} \leq V_{Deck} \qquad \text{Equation 2-1}$$

where $M_1$ and $M_2$ are the positive and negative moment capacity of the deck, and $S$ is the distance between the mid-width of the fractured girder's interior top flange and the edge of the interior top flange of the intact girder (Figure 2.3).

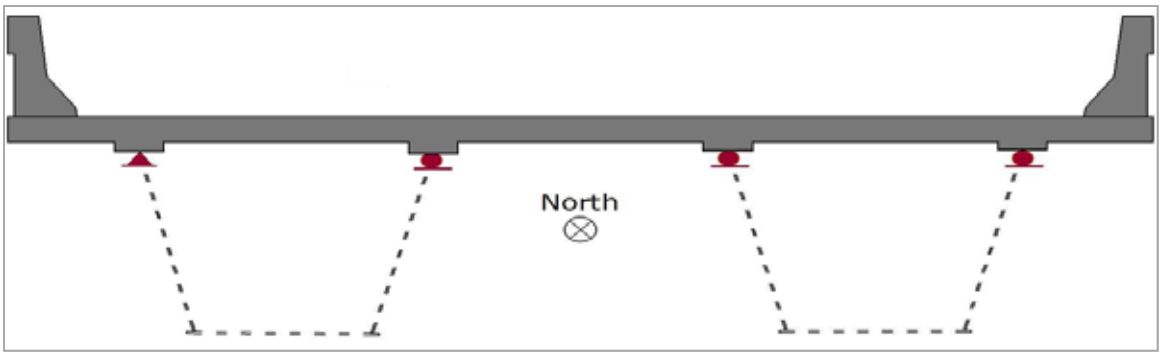


*Figure 2.2: Deck strip boundary conditions*

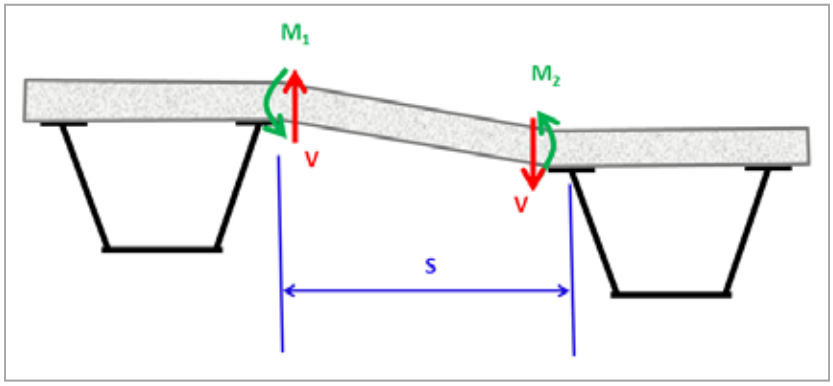


*Figure 2.3: Plastic deck mechanism*

The shear studs connecting the deck to the fractured girder must have sufficient tension capacity to develop the plastic beam mechanism in the bridge deck. The required shear stud tensile capacity can be estimated using the model of the bridge deck shown in Figure 2.4. The required tension capacity of the group of shear studs included in the strip can be calculated using Equation 2-2.

$$T \geq \frac{M_2}{b} + V \qquad \text{Equation 2-2}$$

where $T$ is the tensile capacity of the shear stud group in the strip, $M_2$ is the positive moment capacity of the deck strip, $b$ is the distance between the mid-width of the top flanges of the

fractured girder, and $V$ is the shear from the plastic deck mechanism. The tensile capacity of the shear studs group can be estimated by using the modified ACI equations developed in this research and detailed in the report "The Tensile Capacity of Welded Shear Studs" (FHWA/TX-08/9-5498-R2).

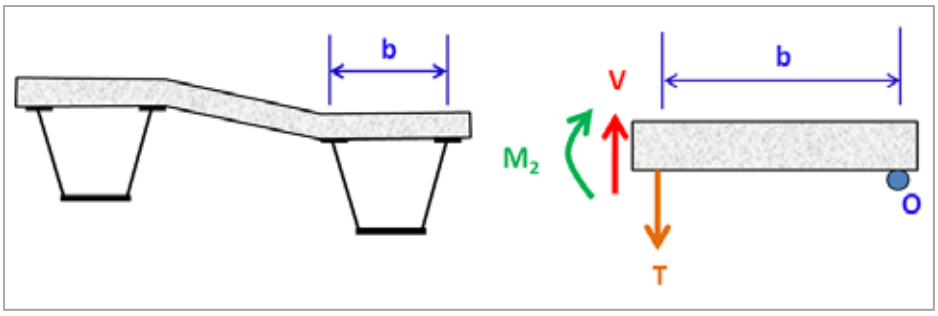


*Figure 2.4: Shear stud pull out capacity*

### 2.2.3 Shear Capacity of Intact Girder

The shear of the end panels of the intact girder should be checked to ensure that the webs have adequate capacity. The end panel's shear is limited to its buckling capacity, and the capacity of an interior support is equal to its tension field strength. The shear in the girder due to the torsion and vertical loads transferred from fractured girder need to be included in the strength check. Results from the test program on the full-scale test bridge indicated that the torsion introduced into the intact girder was nearly symmetrical; therefore, it is assumed that the intact girder has symmetrical torsional boundary conditions. It is further assumed that the live load and dead load is uniformly distributed. The torques of the dead load and live load are given in Equations 2-3 and 2-4, respectively:

$$T_{DL} = w_{0.5DL} \cdot e_{DL} \qquad \text{Equation 2-3}$$

where:

$w_{0.5DL}$ = weight of fractured girder plus the weight of one railing and 1/2 the concrete deck

$e_{DL}$ = centerline distance between the two girders for straight girders or calculated eccentricity using Equation 2-19 for curved girders

and

$$T_{TL} = w_{TL} \cdot e_{TL} \qquad \text{Equation 2-4}$$

where:

$w_{TL}$ = truck load

$e_{TL}$ = distance between intact girder's center and truck center, or calculated eccentricity (Equation 2-19).

The FSEL test bridge had a large radius of curvature, allowing the eccentricity for the torque calculation to be approximated as the distance between the two girders or the distance between the intact girder's center and the truck center. In-service twin box-girder bridges, however, may be designed with a significantly smaller radius of curvature than that of the test bridge. A decrease in the radius of curvature increases the torsion on the bridge, which must be resisted by the intact girder in the event of a fracture of a critical tension flange. Under such conditions, the eccentricity should not be taken as the distance between the centerlines of the

girders; it should be computed as the distance from the center of gravity of the loads to the line of the intact girder interior supports. The center of gravity for non-prismatic girders can be determined by using equations developed by Stith (2010), modified for the case of box-girders. In the equations presented below, polar coordinates are used, and the origin of the coordinate system is located at the center of radius of the girder. Figure 2.5 provides a schematic of a curved girder with a definition for all the variables needed for the derivation.

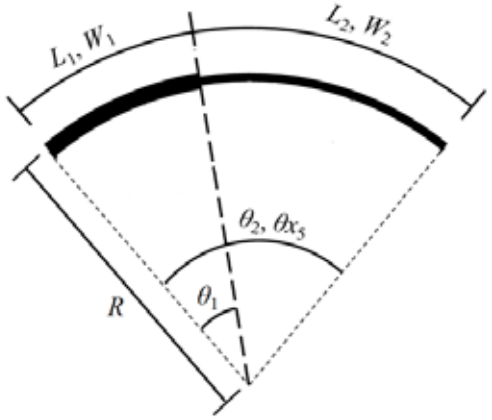


$L_1$: Length of Section 1
$L_2$: Length of Section 2
$W_1$: Weight per Unit Length of Section 1
$W_2$: Weight per Unit Length of Section 2
$\theta_0 = 0$
$\theta_1$: Internal Angle from the Beginning of the Girder to the End of Section 1
$\theta_2$: Internal Angle from the Beginning of the Girder to the End of Section 2
$R$: Radius of Curvature of the Girder

*Figure 2.5: Variable definition for center of gravity (C.G.)*

where $\theta_1$ and $\theta_2$ are given in Equation 2-5 and 2-6:

$$\theta_1 = \frac{L_1}{R} \qquad \text{Equation 2-5}$$

$$\theta_2 = \frac{L_2}{R} + \theta_1 \qquad \text{Equation 2-6}$$

The weight of the girder in Figure 2.5 can be defined as follows:

$$Total\ Girder\ Weight = \int_{\theta_0}^{\theta_1} W_1\ Rd\theta\ + \int_{\theta_1}^{\theta_2} W_2\ Rd\theta \qquad \text{Equation 2-7}$$

$$= W_1R(\theta_1 - \theta_0) + W_2R(\theta_2 - \theta_1) \qquad \text{Equation 2-8}$$

The generalized form of the total girder weight equation is provided in Equations 2-9 and 2-10, where $n$ is the number of the different cross sections along the length of the bridge under consideration:

$$Total\ Girder\ Weight = \sum_{i}^{n} \int_{\theta_{i-1}}^{\theta_i} W_i\ Rd\theta \qquad \text{Equation 2-9}$$

$$= R\sum_{i}^{n} W_i\,(\theta_i - \theta_{i-1}) \qquad \text{Equation 2-10}$$

The angular distance from the beginning of the girder to the center of gravity is determined by taking a weighted average of each segment's centroid, which is located at the angular center of each cross-section. For the girder shown in Figure 2.6, the angular distance is given by Equation 2-13:

$$\bar{\theta} = \frac{\frac{\theta_1 + \theta_0}{2}\int_{\theta_0}^{\theta_1} W_1\, R d\theta \; + \frac{\theta_2 + \theta_1}{2}\int_{\theta_1}^{\theta_2} W_2\, R d\theta}{\int_{\theta_0}^{\theta_1} W_1\, R d\theta \; + \int_{\theta_1}^{\theta_2} W_2\, R d\theta} \qquad \text{Equation 2-11}$$

$$\bar{\theta} = \frac{W_1 R\,\frac{(\theta_1 + \theta_0)(\theta_1 - \theta_0)}{2} + W_2 R\,\frac{(\theta_2 + \theta_1)(\theta_2 - \theta_1)}{2}}{W_1 R(\theta_1 - \theta_0) + W_2 R(\theta_2 - \theta_1)} \qquad \text{Equation 2-12}$$

$$\bar{\theta} = \frac{\frac{W_1 R\left({\theta_1}^2 - {\theta_0}^2\right) + W_2 R\left({\theta_2}^2 - {\theta_1}^2\right)}{2}}{W_1 R(\theta_1 - \theta_0) + W_2 R(\theta_2 - \theta_1)} \qquad \text{Equation 2-13}$$

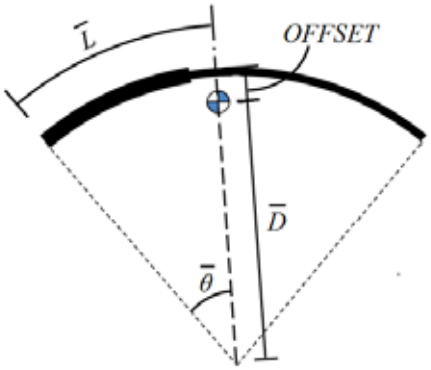


Center of Gravity
$\bar{\theta}$: Angular Distance to C.G.
$\bar{L}$: Length along Girder to C.G.
$\bar{D}$: Radial Distance to C.G.
$t_T$: Top Flange Thickness
*OFFSET*: Radial Distance of C.G. from the Girder Centerline

*Figure 2.6: C.G. Location*

The generalized form of the equation for determining the angular distance to the center of gravity is

$$\bar{\theta} = \frac{\frac{R\sum_i^n W_i\left({\theta_i}^2 - {\theta_{i-1}}^2\right)}{2}}{R\sum_i^n W_i(\theta_i - \theta_{i-1})} \qquad \text{Equation 2-14}$$

The following equation determines the location along the length of the girders to center of gravity:

$$\bar{L} = \bar{\theta} R \qquad \text{Equation 2-15}$$

The radial distance to the center of gravity is determined by taking the weighted average of the girder projected onto the $\bar{\theta}$ radial line. This distance is show schematically in Figure 2.6, and it can be computed using Equations 2-16 and 2-17:

$$\bar{D} = \frac{\int_{\theta_0}^{\theta_1} W_1 R \cos(\theta - \bar{\theta})\ Rd\theta + \int_{\theta_1}^{\theta_2} W_2 R \cos(\theta - \bar{\theta})\ Rd\theta}{\int_{\theta_0}^{\theta_1} W_1\ Rd\theta + \int_{\theta_1}^{\theta_2} W_2\ Rd\theta} \qquad \text{Equation 2-16}$$

$$\bar{D} = \frac{W_1 R^2[\sin(\theta_1 - \bar{\theta}) - \sin(\theta_0 - \bar{\theta})] + W_2 R^2[\sin(\theta_2 - \bar{\theta}) - \sin(\theta_1 - \bar{\theta})]}{W_1 R(\theta_1 - \theta_0) + W_2 R(\theta_2 - \theta_1)} \qquad \text{Equation 2-17}$$

The generalized equation to compute the radial distance to the center of gravity for a girder with multiple cross-sections is given by can be determined by the generalized form of Equation 2-18:

$$\boxed{\bar{D} = \frac{R^2 \sum_i^n W_i\ [\sin(\theta_i - \bar{\theta}) - \sin(\theta_{i-1} - \bar{\theta})]}{R \sum_i^n W_i(\theta_i - \theta_{i-1})}} \qquad \text{Equation 2-18}$$

Equation 2-18 should be used two times to compute $\bar{D}$—once for the fractured girder and once for the intact girder. Because the line of rotation of the bridge passes through the supports of the intact girder, each girder's offset from the center of gravity to the line of rotation is given by Equation 2-19:

$$e_i = \bar{D}_i - R_{INT} \cdot \cos(\phi/2) \qquad \text{Equation 2-19}$$

where:

$R_{INT}$ = Radius of curvature at the location of the interior intact girder's supports
$\varphi = L_{INT} / R_{INT}$
$L_{INT}$ = Arc length at the location of the interior intact girder's supports
Equations 2-5 through 2-19 can be used to calculate the eccentricities of each girder.

When multiplied by the dead load of each girder and the truck load, the torque applied on the end sections of the intact girder can be computed.

Assuming that half of the calculated torque is applied to each end of the intact girder, the shear flow of the closed section can be determined by Equation 2-20.

$$q = \frac{1}{2 \cdot A} \cdot \frac{(T_{DL} + T_{TL})}{2} \qquad \text{Equation 2-20}$$

where:

$T_{DL}$ = torque due to dead load, which is equal to the dead load multiplied by the eccentricity to the chord of the intact girder supports
$T_{TL}$ = torque due to truck load, which is equal to the dead load multiplied by the eccentricity to the chord of the intact girder supports

$A$ = area enclosed by the mid-thickness of the composite box-girder section

Note: The calculated torques are divided by two, because it is assumed that the end torques are equal.

The concrete deck forms the top flange of the closed box section and should be checked to ensure that it has adequate capacity to resist the shear force due to torsion. According to ACI 318-08, the shear capacity of reinforced concrete is given Equation 2-21. Equation 2-21 should always be greater that the shear due to torsion ($V_{TORSION} = q \cdot b$)

$$V_S = A_t \cdot f_{yt} \cdot b \cdot \cot(\theta) / s \qquad \text{Equation 2-21}$$

where:

$b$ = width of the concrete deck between the top flanges
$A_t$ = area of a reinforcement bar in the transverse direction
$s$ = spacing between the reinforcement bars
$\theta$ = angle of the crack with the horizontal (ACI 318-08 recommends 45°)

The shear stress developed in the webs due to torsion must be added to the shear stress due to bending of the girders using the following procedure:

**i.** Calculate the shear stress in the webs due to torsion using Equation 2-22.

$$\tau_{TORSION\ WEB} = q / t_{WEB} \qquad \text{Equation 2-22}$$

where $t_{WEB}$ = thickness of the web

**ii.** Calculate the shear stress due to bending at webs through Equation 2-23.

$$\tau_{FLEXURAL\ WEB} = V / (2 \cdot d_{WEB} \cdot t_{WEB} \cdot \cos(\beta)) \qquad \text{Equation 2-23}$$

where:

$d_{WEB}$ = height of the web
$\beta$ = angle of web inclination
$V$ = one-half of the total factored load on the span

**iii.** Ensure that the summation of the shear due to torsion and bending is less than or equal to the shear buckling stress as given below:

$$\tau_n = C \cdot 0.58 \cdot f_{yw} \geq \tau_{TORSION\ WEB} + \tau_{FLEXURAL\ WEB} \qquad \text{Equation 2-24}$$

where:

$C$ = ratio of shear-buckling resistance to the shear yield strength (AASHTO Sec. 6.10.9.3.2)

The larger tension field shear capacity can be used to check the shear at interior supports.

**iv.** The bottom flange at the pier should be checked for combined shear and compression (AASHTO Sec. 6.11.8.2.2**)**

**v.** The end diaphragm and its connection to both girders needs to be checked to ensure that it has adequate resistance to the torque applied to the intact girder. This applied torque is resisted by a couple generated by the bearings of the two girders (i.e., bearing reactions). The reaction at the bearing of the fractured girder is equal to the torque applied to the intact

girder divided by the distance between the bearings of the two girders. In the case of a continuous girder, the interior support is not as critical as the end support because some of the applied torque is resisted by the continuous girder. Thus, it is always critical to check the end diaphragm of the end support.

### 2.2.4 Evaluation

Following the steps outlined in this section (Section 2.2), the redundancy level of a twin steel box-girder bridge can be evaluated. If the bridge under investigation satisfies the following conditions, the bridge has sufficient strength to sustain load without collapsing:

**i.** Intact Girder has adequate shear and moment capacity

**ii.** Deck has adequate shear capacity

**iii.** Shear studs have adequate tension capacity

If the bridge satisfies only the first two conditions, it is still possible that it can sustain load without collapsing. Under these conditions, a yield line analysis—described in the next section—can be used to evaluate the ability of the deck to transmit load to the intact girder without the shear studs connecting the deck to the fractured girder. In the event that the capacity predicted from the yield line analysis is not adequate, a more refined analysis can be performed. Methods for developing finite element models capable of assessing the redundancy of twin steel box-girder bridges are described later in this report.

## 2.3 Yield Line Analysis

A simple yield line model was developed to capture the response of a twin steel box-girder bridge when the shear studs do not have adequate tension capacity. The plastic mechanism in the deck between the girders will not form if the shear studs pull out of the deck. The development of the yield line model was initiated after completion of the tests on the FSEL test bridge. A detailed survey of the deck's top surface indicated that the failure in the deck followed the shape of a half-ellipse (Figure 2.7). A yield line pattern was developed using a combination of straight lines that provided a similar failure shape to the one observed on the test bridge. After investigating different yield line patterns to calculate the ultimate load, it was found that the shape that gave the most conservative estimate of capacity (Figures 2.8 and 2.9) was one that consisted of straight lines lying on the perimeter of an ellipse along with two diagonals along diagonal interior fold lines. The results of the yield line analysis were in good agreement with the observed hinge locations in the deck. Thus, it was concluded that the assumed yield line shape could be used to estimate the ultimate load of the bridge.

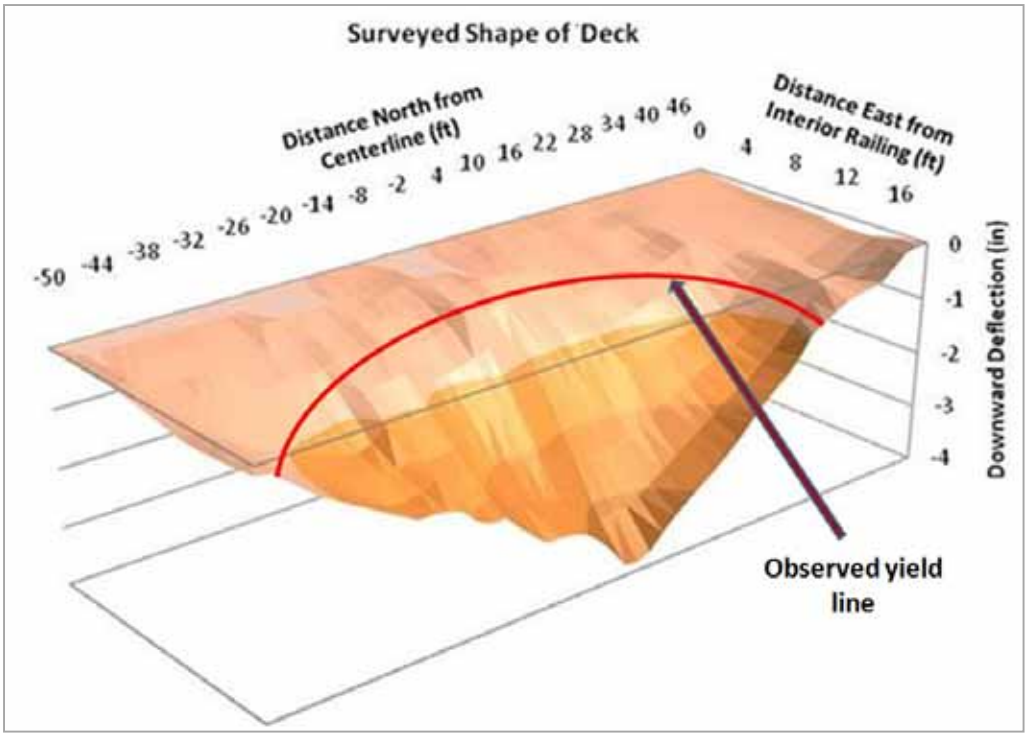


*Figure 2.7: Observed hinge line pattern*

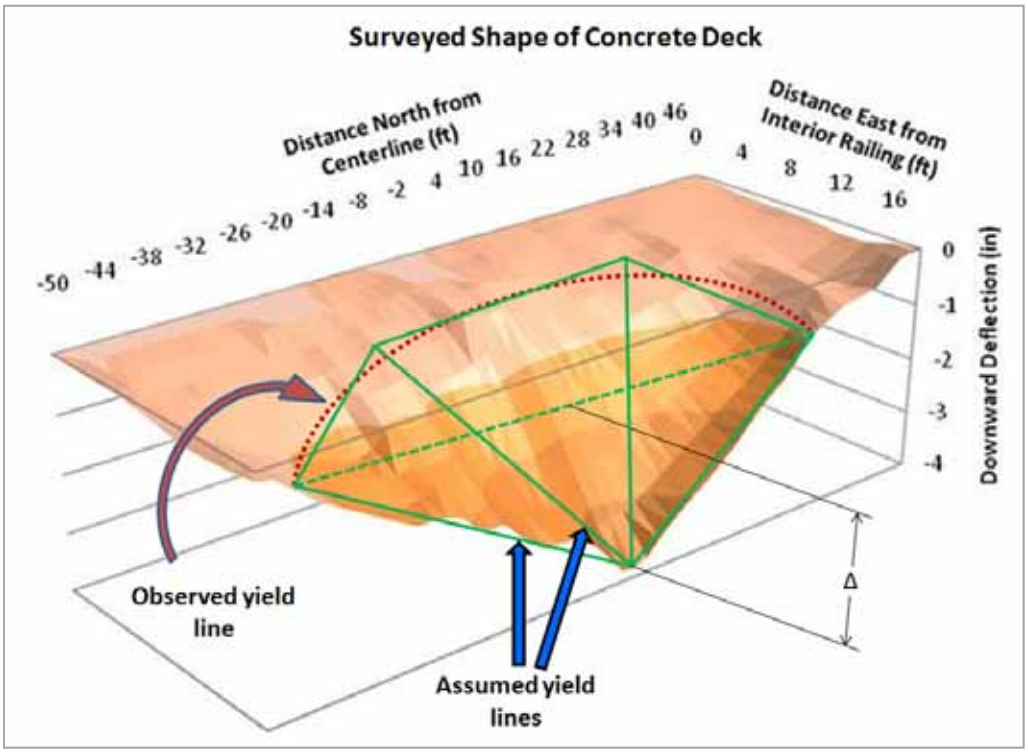


*Figure 2.8: Assumed elastic plate displaced by a virtual displacement Δ*

### 2.3.2 Description of the Yield Line Model Analysis Procedure

When a slab fails in flexure under overload conditions, the reinforcement at a region of high moment will yield first, and a plastic hinge will then form at this location in the slab. When that occurs, the slab is only able to sustain the hinging moment. The hinging region will rotate plastically with an increase of the load, and the moments associated with the additional load will be distributed to adjacent sections, eventually causing them to yield—ultimately forming a yield line in the deck.

A yield line analysis was performed using a virtual work principle which yields an upper-bound solution to the problem. To implement the procedure, a yield line pattern is chosen, and a virtual displacement is introduced at the edge of the deck above the fracture in the girder (Figure 2.8). The principle of virtual work requires that the external virtual work done by the external forces be equal to the internal virtual work done by the internal forces of each element of a structure. The external virtual work is computed from the summation of the product of the externally applied forces multiplied by the virtual displacement at the load position, which is a function of the assumed virtual displacement. The total internal virtual work due to the virtual displacement is equal to the summation of the product of the bending moment developed at the segment of the yield line multiplied by the hinging rotation of each segment. The elastic moment and rotations are ignored with this approach, which is a reasonable assumption based on the relative magnitude of the terms.

All the geometric parameters of the yield line pattern have to be defined before calculating the internal virtual work. It was assumed that a straight yield line would always initiate at the interior top flange of the intact girder, and it would extend to intersect with the inner diagonal yield lines (Figure 2.9). The yield line pattern was completed with two outer yield lines that started at the intersection of the straight line with the inner diagonal and extended diagonally to the edge of the concrete deck above the fractured girder (Figure 2.9). A series of parametric studies suggested that a minimum load solution resulted when the angle $\varphi$ between the inner diagonal and the vertical axis was held constant and equal to 55°. The length *a,* which is the horizontal distance from point A or D to the origin, was determined by finding the value that produced the minimum truck load. It should be noted that the length *a* and the magnitude of the truck load are mutually dependant. Accordingly, one of these variables should be fixed to obtain the other one. It is recommended that the live load magnitude corresponding to the number of trucks be selected first; with this value set, the length *a* for the given load magnitude can be obtained. If a valid solution for the length *a* is computed, the given truck load is a possible failure loading. In subsequent iterations, the truck load should be decreased until a valid solution for *a* no longer exists. The minimum truck load is the last one that gave a physically admissible solution for the length *a*. In contrast, if the initially chosen truck load does not provide a physically admissible solution for the length *a*, then the truck load needs to be increased in subsequent iterations. Once the length *a* has been determined, all the coordinates of the yield line end points can be defined to calculate the variables used to compute the virtual work. These coordinates were calculated by applying fundamental trigonometric relationships. In the case of a bridge with significant horizontal curvature, the coordinates of points A and B would be affected. Adjustments should be made to account for the angle $\theta$ (Figure 2.9).

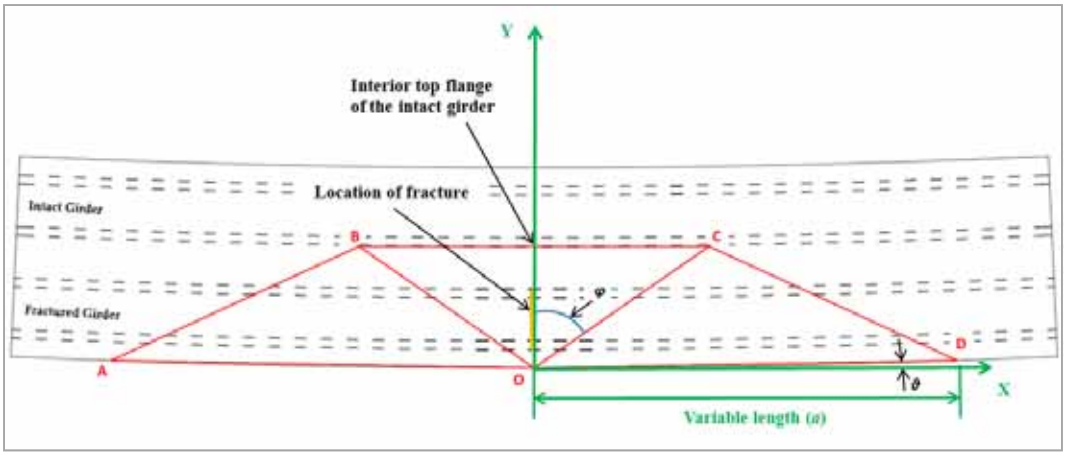


*Figure 2.9: Parameters of the yield line pattern*

The angle $\theta$ is given by Equation 2-25:

$$\theta = 0.5 \cdot \sin^{-1}(a / R) \qquad \text{Equation 2-25}$$

where $a$ (ft) is the horizontal distance of the point A or D from the origin, and $R$ (ft) is the bridge's radius of curvature. Radians should be used as units when $\sin^{-1}(a / 2 \cdot R)$ is calculated.

The bending capacity is not the same along each yield line due to the fact that the reinforcement in the deck was not normal to the yield line. If the yielding occurred along a line at an angle $\alpha$ to the reinforcement (Figure 2.10), the resultant bending capacity ($m_b$) could be calculated by inserting the bending capacities of the two directions ($m_x$, $m_y$) into Equation 2-26 (Wight and MacGregor, 2008).

$$m_b = m_x \sin^2 \alpha + m_y \cos^2 \alpha \qquad \text{Equation 2-26}$$

In the case of the straight line and the inner diagonals, the bending moment capacities can be readily calculated because the angle $\alpha$ is equal to 0° and 35°, respectively. The bending moment capacity of the outer diagonals, however, is a function of the length $a$; consequently, an expression to define $\alpha$ is needed. Equation 2-27 can be used to determine the angle $\alpha$ of the outer diagonals.

$$\alpha = \tan^{-1}\left(\frac{X_j - X_i}{Y_j - Y_i}\right) + \frac{\pi}{2} \qquad \text{Equation 2-27}$$

where ($X_i$, $Y_i$) and ($X_j$, $Y_j$) are the coordinates of the end points of the outer diagonals. For any other case that the reinforcement is not oriented as shown in Figure 2.10, the angle $\alpha$ should be determined based upon the orientation of the reinforcement.

In order to calculate the internal virtual work done by the concrete deck, the parameters needed are 1) the length of each line and 2) the angle of rotation of each plate. First, the length of each line can be calculated using the distance formula (Equation 2-28). Knowing the coordinates of each yield line's endpoints, the length of the line is equal to

$$l = \sqrt{\left(X_j - X_i\right)^2 + \left(Y_j - Y_i\right)^2} \qquad \text{Equation 2-28}$$

where, as before, ($X_i$, $Y_i$) and ($X_j$, $Y_j$) are the coordinates of the end points of the yield line.

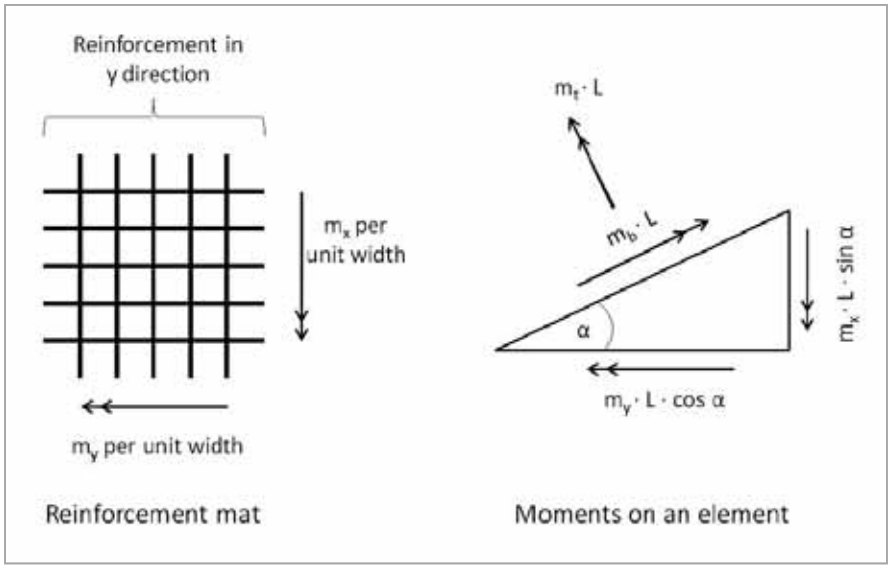


*Figure 2.10: Bending moment along a yield line at an angle α (Wight and MacGregor, 2008)*

Second, the angle of rotation of each plate can be calculated by evaluating the geometry of the displaced shape corresponding to the assumed yield line pattern. The angle between two planes is given by the angle between the normal vectors. For example, if $3x - 2y + 5z = 1$ and $4x + 2y - z = 4$ are the equations that define two planes, the angle between these planes can be determined as follows:

**i.** The two normal vectors are $n = \langle 3,-2,5 \rangle$ and $m = \langle 4,2,-1 \rangle$

**ii.** $n \cdot m = 3 \cdot 4 - 2 \cdot 2 - 5 \cdot 1 = 3$

**iii.** $\|n\| = \sqrt{3^2 + (-2)^2 + 5^2} = \sqrt{38}$, $\|m\| = \sqrt{4^2 + 2^2 + (-1)^2} = \sqrt{21}$

**iv.** Hence, the angle is equal to $\theta_{Rotation} = \arccos = \left( \frac{3}{\sqrt{38 \cdot \sqrt{21}}} \right) = 1.46 rads$

Having all the parameters defined, the internal virtual work of each line with length $l$ can be calculated as the product of $dIW = m_b \cdot l \cdot \theta_{Rotation}$.

Railings may contribute significantly to the overall load carrying capacity of a twin steel box-girder bridge that has suffered a fracture in one of its girders. Accordingly, the virtual work done by the railing should be included in the total internal virtual work calculation. As the bridge deflects downwards, the railing acts as an edge beam and resists the bending of the bridge in the longitudinal direction. The moment acting on the railing will depend on the type of railing—continuous or with expansion joints—and the location that the hinge line intersects the railing.

Figure 2.11 shows the moments acting on the railing that should be included in the calculation of internal virtual work. The work done by the railing is equal to the moment capacity of the railing times the angle of rotation. In the case of positive moment capacity, the angle of rotation of the railing is two times the angle between the ABO and CDO planes (Figure 2.9); the angle of rotation for the negative moment capacity is equal to the angle of the ABO (or the CDO) plane with the horizontal.

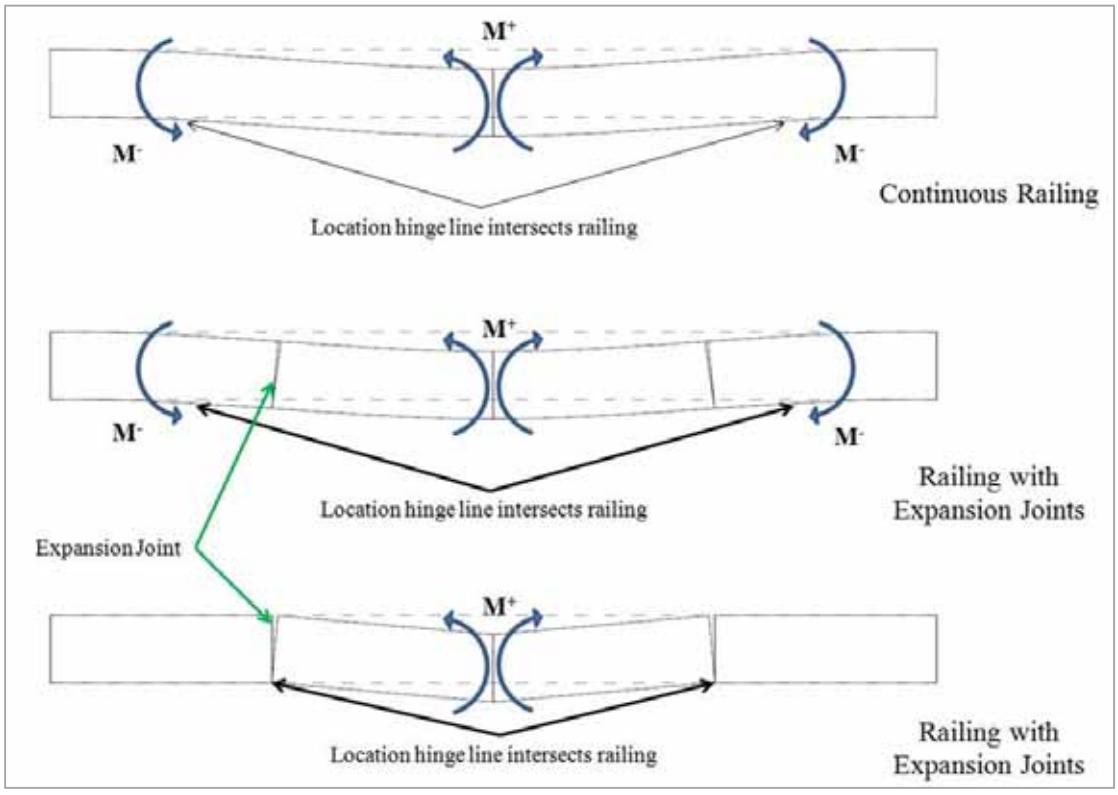


*Figure 2.11: Acting moments on the railing for different cases*

To ensure that the railing section can reach its moment capacity, the connection between the railing and the deck must have sufficient reinforcement to transmit the shear associated with flexure. The maximum shear force at the connection is equal to the compressive force applied to the railing section when the positive moment capacity is calculated. The positive moment capacity is calculated using the railing section and assuming that, at the level of the concrete deck below the railing, there is reinforcement equal to the reinforcement area existing in the effective deck width. The effective deck width can be computed according to Section 4.6.2.6 of the AASHTO LRFD Specification (2007). According to the specification, the effective width can be determined using Figure 4.6.2.6.2-2 (AASHTO, 2007), where $b$ is equal to the distance from the edge of the concrete deck above the fractured girder to the interior top flange of the intact girder, and $l_i$ is the length of railing between expansion joints. In the case that the railing is continuous, $l_i$ should be taken as the total length of the span. Under no circumstances can the effective width be taken as greater than $b$.

The assumption to include the reinforcement within the effective deck width is supported by the railing behavior observed in the full-scale bridge test conducted at FSEL. The railing

failed by crushing of the concrete in a manner that is similar to the failure of an over-reinforced concrete section. It is suspected that as the deck deflected downward under increasing increments of load, catenary behavior of the concrete deck engaged more and more reinforcement over the width of the deck. Thus, the catenary behavior increased the tension in the reinforcing bars that were embedded over an effective width, and the amount of reinforcing steel engaged in this response led to behavior representative of that corresponding to an over-reinforced section. The results of the additional tension in the deck reinforcement led to the crushing observed in the railing. The effective width of the concrete deck included in the rail strength calculation is intended to capture this behavior. In Example 1 (Chapter 5), however, it is shown that the effective width obtained from Section 4.6.2.6 of the AASHTO LRFD Specification (2007) is smaller than the observed one. Accordingly, the effective width is computed in such a way as to ensure a conservative solution. Additional details related to the computation of the effective width are given below and in the examples that appear in the next chapter and in the appendices.

The external virtual work consists of the work done by the truck load and the dead load of the bridge. The truck load should be positioned at the location where it produces the largest positive bending moment. In the case of a simply supported bridge, the maximum positive bending moment can be achieved when the middle axle of an HS-20 truck is located at the mid-span of the bridge. In the case of a continuous bridge, however, the location of the middle axle should coincide with the location of the highest positive moment. The location of highest positive moment can be obtained from the moment envelope diagram for a combination of dead load and moving truck load. Moreover, the distance between the exterior and the middle axles should be kept constant and equal to 14 ft. Regarding the position of the truck across the width of the bridge, it is suggested that the wheels on one side of the truck be positioned 2 ft away from the railing. Once the position of the truck is set, the work done by the truck load can be computed. This work is equal to the summation of each point load multiplied by the deflection of each location. The deflection of each location, however, is a function of the length $a$. The deflection of the wheel loads of an HS-20 truck load can be determined by using the ratio of congruent triangles (Equation 2-29).

$$\delta_{load} = r_{load} \cdot \Delta / r \qquad \text{Equation 2-29}$$

In this equation, $\delta_{load}$ is the deflection at the load location, $r_{load}$ is the distance of the load location from the edge of the slab above the fracture, $\Delta$ is the virtual displacement, and $r$ is the distance of a point on the yield line with the same angle $\beta$ from the positive $x$-axis as the load position (Figure 2.12). Having determined the coordinates of the truck wheels, $r_{load}$ can be computed using the Pythagorean Theorem. All the terms of Equation 2-29 are known except for $r$. The length of $r$ can be determined as follows:

**i.** For a given angle $\beta$, the equation of the line passing through the origin and the point load can be defined.

**ii.** Knowing the coordinates of the outer diagonal yield line endpoints (A and B, C and D), an equation of the line can be derived.

**iii.** The $x$-coordinate of the intersection can be found by setting equal the $y$-coordinate of the two equations and then inserting the known $x$-coordinate into the one of the equations to obtain the $y$-coordinate.

**iv.** Finally, the length *r* can be computed using the distance formula between the origin and the intersecting point.

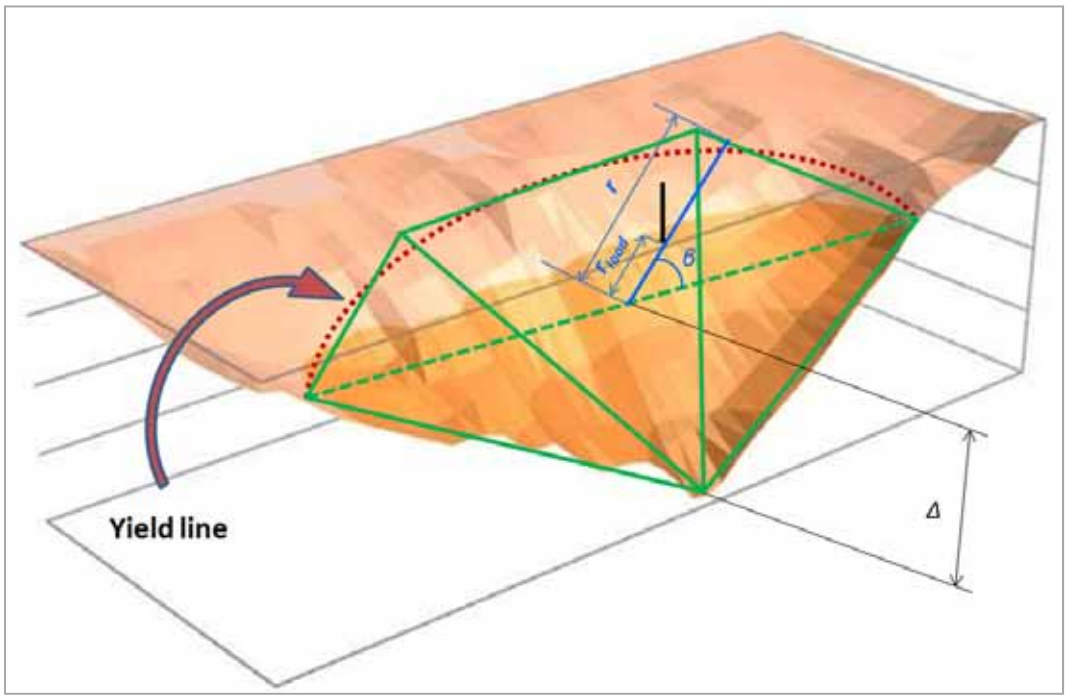


*Figure 2.12: Defining the deflection at the load location*

The work done by the dead load of the bridge should be included in the external virtual work calculation. Only the self-weight of the concrete deck and the railing inside the failure area should be included. As indicated previously, it is appropriate to use the Yield Line Model when the fractured girder is separated from the concrete deck. Consequently, the self-weight of the fractured girder is not included in the external virtual work calculation. The external work done by the railing is computed using Equation 2-30:

$$EW_{RAILING} = A_{Railing} \cdot 2 \cdot a \cdot 0.15 \cdot \Delta/2 \qquad \text{Equation 2-30}$$

where $A_{Railing}$ ($ft^2$) is the cross-sectional area of the railing, $a$ (ft) is the horizontal distance from the point A or D to the origin, and $\Delta$ is the virtual displacement. The factor 0.15 is used to account for the assumed self-weight of reinforced concrete (150 $lb/ft^3$ = 0.15$kips/ft^3$).

In a similar way, the external work done by the concrete deck can be computed by Equation 2-31and 2-32. Equation 2-31 is used to compute the work done by the middle triangle (i.e., BOC in Figure 2.9)

$$EW_{DECK\ MID\text{-}TRINGLE} = 1/2 \cdot l \cdot h \cdot t \cdot 0.15 \cdot \Delta/3 \qquad \text{Equation 2-31}$$

where $l$ (ft) is the length of the yield line lying above the interior top flange of the intact girder (BC), $h$ (ft) is the height of the triangle BOC and is equal to the distance from centerline of the interior flange of the intact girder to the edge of the flange, $t$ (ft) is the thickness of the concrete deck, and $\Delta$ is the virtual displacement. Once again, the factor 0.15 accounts for the self-weight

of reinforced concrete, which was assumed to be 150 lb/ft$^3$ = 0.15kips/ft$^3$. Additionally, the work done by the outer triangles (i.e., AOB and COD) can be approximated using Equation 2-32.

$$EW_{DECK\ OUT\text{-}TRINGLE} = 1/2 \cdot a \cdot h \cdot t \cdot 0.15 \cdot \Delta/3 \qquad \text{Equation 2-32}$$

where $a$ (ft), as before, is the horizontal distance from point A or D to the origin and $\Delta$ is the virtual displacement. Equation 2-32 is accurate for a straight bridge; as the curvature and the length $a$ increase, however, this expression overestimates the work done by the outer triangles because the areas of these triangles become smaller. An accurate expression for the work done by the outer triangles can be obtained if the term $a$ in Equation 2-32 is replaced with $l_{CD}$ *or* $l_{AB}$ from Equation 2-28, and $h_i$ is calculated according to Equation 2-33.

$$h_i = \left| \sqrt{X_i^{\,2} + Y_i^{\,2}} \cdot \sin(\theta_i + \alpha_i) \right| \qquad \text{Equation 2-33}$$

where $X_i$ , $Y_i$ are the coordinates of point D, $\theta_i$ is the angle measured from the positive $x$-axis to line OD, and $\alpha_i$ is the angle of the yield line DC obtained from Equation 2-27 (Figure 2.13). The heights of the outer triangles are equal due to symmetry (i.e., $h_{COD}$= $h_{AOB}$). Additional details of this implementation are provided in the examples that appear in the Appendix.

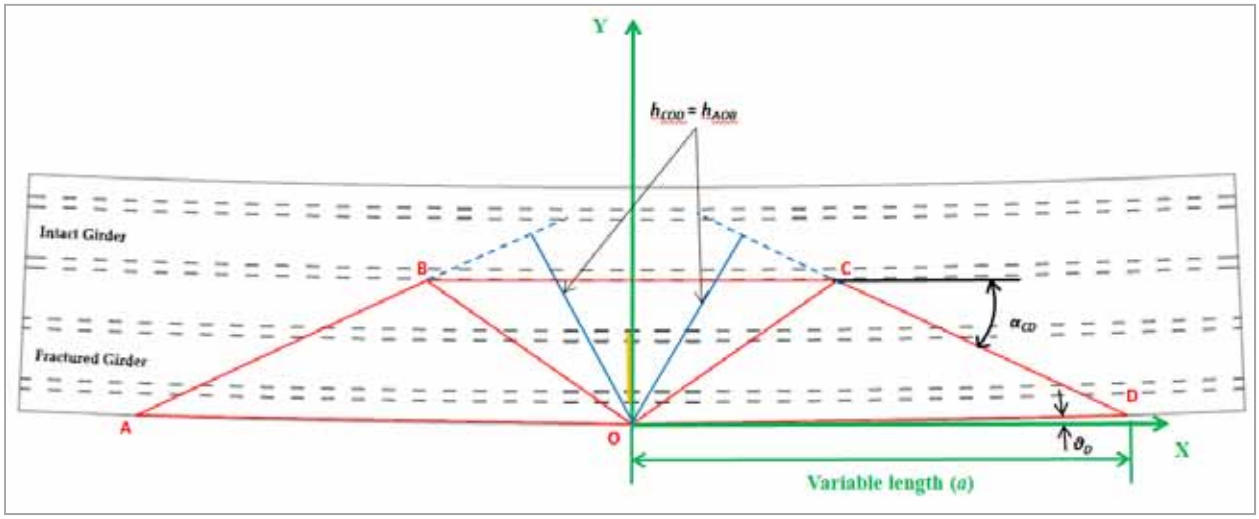


*Figure 2.13: Geometric parameters of Equation 32*

## 2.4 Yield Line Model Analysis Results of the FSEL Bridge

The Yield Line Model was successfully applied to the FSEL test bridge. Applying an HS-20 truck load to the bridge at the most severe location, the ultimate load was computed to be 3.91 × HS-20 Trucks or 281.9 kips for $f'_c$=6.26 ksi, which was the measured strength of the deck. The ultimate load was computed to be 3.66 × HS-20 Trucks or 263.84 kips for $f'_c$=4.00 ksi, which was the specified design strength of the deck. The total estimated capacity of the test bridge using an HS-20 truck loading is less than the actual load carried by the bridge—363.0 kips—for two reasons. First, the wheel loads of the truck used in the analysis produce a larger moment than that produced by the road base that was distributed over a portion of the deck during the test. Second, the positive moment capacity of the railing used in the analysis was smaller than the actual capacity due to the conservative assumption used to estimate the width of the deck participating with the railing. This approach was taken to obtain a conservative solution. The

area of the tension reinforcement bars in the effective width appears to be greater than what was assumed for the analyses in order to produce the crushing failure observed in the test. The details of the analysis of the test bridge with a truck load are given as the first example, which is presented in the following chapter.

# Chapter 3. Example 1: Analysis of the FSEL Bridge Test 2

## 3.1 Introduction

The examples provided in this chapter and in the appendix are presented to illustrate the simplified method of analysis used to model the response of a twin steel box-girder bridge following the fracture of one of its girders. Most of the calculations were performed using a spreadsheet. The goal seek option was used to find the value of the length *a* that gave the lowest estimate of overall capacity. In the first example, the procedure is applied to the FSEL test bridge using the same load configuration that was utilized during Test 2. A brief description of this test is given in Chapter 1 of this report. Additional details can be found in Neuman (2009).

Prior to its use in this research project, the FSEL test bridge was used as part of an exit-ramp on the IH 10/Loop 610 interchange in Houston, TX. The total length of this simply supported bridge is 120 ft. Figure 3.1 shows a typical cross-section of the FSEL test bridge. The top and bottom flange thickness does not change along the span of the bridge, and a T501 section is used for the railings. The radius of curvature for this bridge is 1365.39 ft.

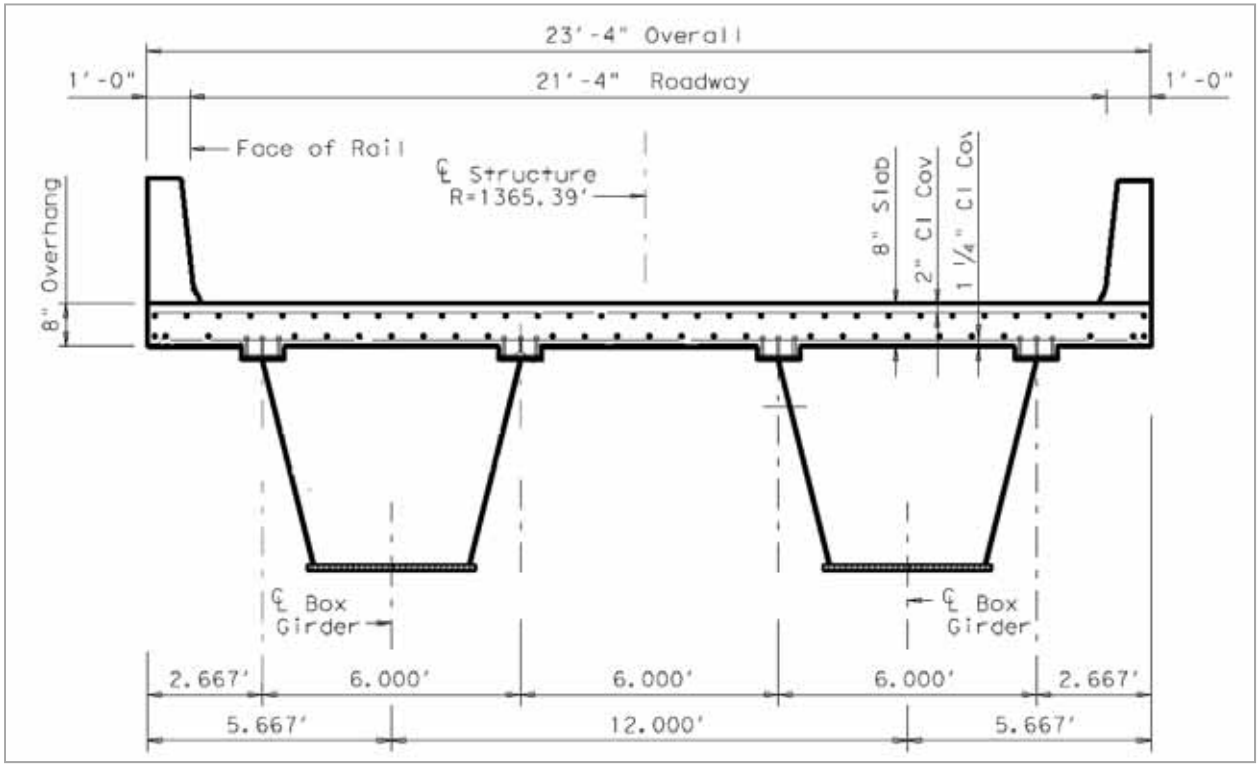


*Figure 3.1: Typical cross-section of FSEL bridge*

## 3.2 Calculation of the Transmitted Load to the Intact Girder

The analysis assumes that half of the entire weight of the bridge and the entire live load on the bridge need to be resisted by the intact girder in the event of a fracture. During the test, a simulated 76-kip truck load was applied to the bridge. The fracture of the outer girder webs and flanges was simulated by removing a temporary support through the use of an explosive charge.

The bridge carried the load without collapsing. The shear studs connecting the interior flange of the fractured girder pulled out of the bridge deck during the test. The loads are calculated below:

**Weight of one steel box girder**

$$W_{girder} = 1.15 \cdot (109 \text{ in}^2/144 \text{ ft}^2/\text{in}^2) \cdot (0.490 \text{ kips/ft}^3) = 0.427 \text{ kip/ft}$$

Notes: This is the weight of one girder. The cross-sectional area of one girder is 109 $\text{in}^2$. The density of steel is taken as 490 $\text{lb/ft}^3$. To account for internal diaphragms, stiffeners, etc., the weight of the steel girder is multiplied by a factor of 1.15.

**Concrete deck**

$$W_{deck} = (280 \cdot 8 / 144 \text{ ft}^2) \cdot (0.150 \text{ kip/ft}^3) = 2.33 \text{ kip/ft}$$

Notes: The width of the concrete deck is 23 ft-4 in. = 280 in. The density of concrete is taken as 150 $\text{lb/ft}^3$. The deck thickness is 8 in.

**T501 railing**

$$W_{railings} = 2 \cdot (311.75/144 \text{ ft}^2) \cdot (0.150 \text{ kip/ft}^3) = 0.65 \text{ kip/ft}$$

Notes: This value is multiplied by two to account for two rails. The cross-sectional area of one rail is calculated as 311.75 $\text{in}^2$

**Simulated truck**

$$W_{truck} = 76 \text{ kips}$$

Note: The total load of the simulated HS-20 truck used during the test is 76 kips. In subsequent calculations, the value of 72 kips is used to represent an actual HS-20 truck load.

**Load to be transmitted**

$$F = (W_{girder} + W_{deck}/2 + W_{railings}/2) \cdot L + W_{truck}$$

$$F = (0.427 + 2.33/2 + 0.65/2) \cdot 120 + 76 = 306.04 \text{ kips}$$

$$F = 306.04 \text{ kips}$$

## 3.3 Calculation of Maximum Moment on the Bridge

**Mid-span moment due to dead load**

$$M_{DL} = (2 \cdot W_{girder} + W_{deck} + W_{railings}) \cdot L^2/8 = (2 \cdot 0.427 + 2.33 + 0.65) \cdot 120^2/8$$

$$M_{DL} = 7{,}063.2 \text{ kip-ft}$$

**Moment due to truck load**

The position of the 76-kip truck load, the shear diagram, and the moment diagram are shown in Figure 3.2. The maximum moment is located at the mid-span of the bridge, and it is equal to $M_{max}$ = 9,048.6 kip-ft.

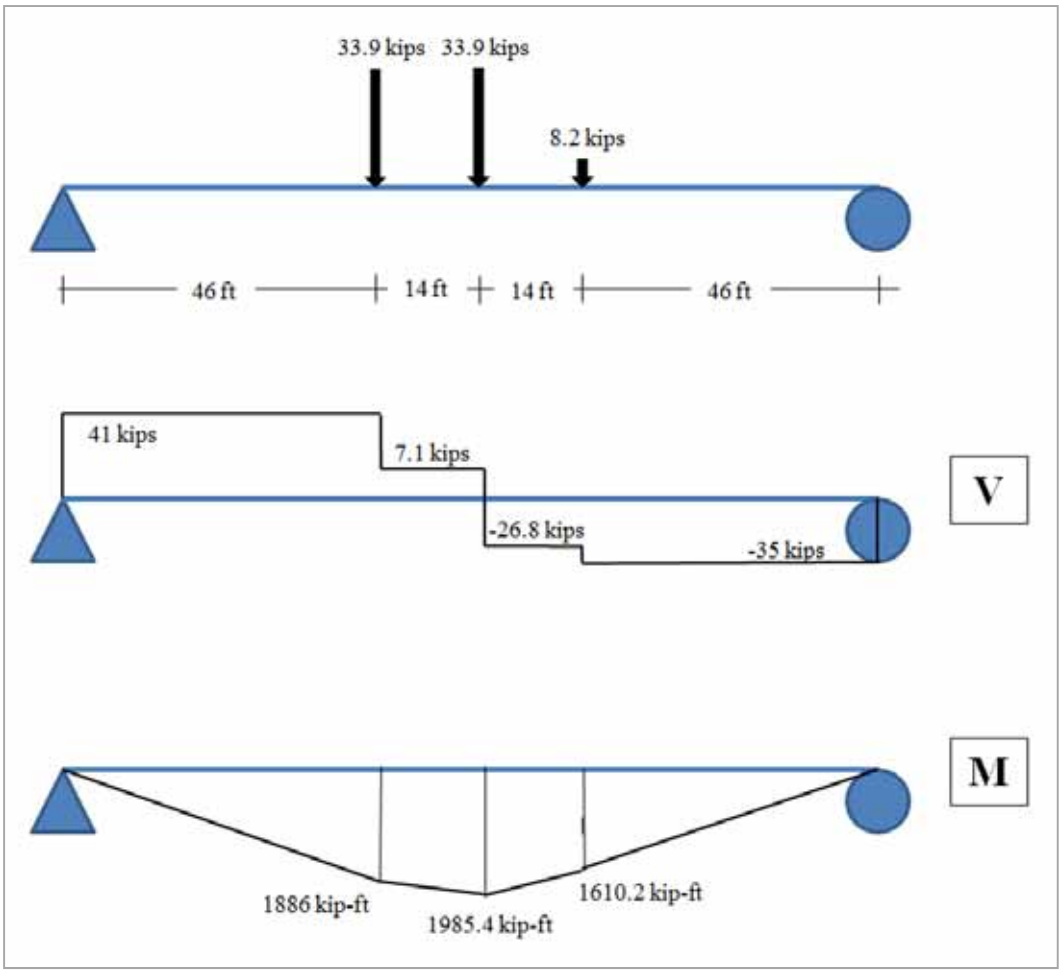


*Figure 3.2: Truck load location—shear and moment diagram due to truck load*

## 3.4 Analysis of Composite Section

The plastic moment capacity of the intact girder is calculated to determine if it has sufficient capacity to sustain the total live load and dead load on the bridge. The composite section used for all calculations is shown in Figure 3.3. Based on lab tests, it was found that $f_{yw}$ = 60 ksi for the webs and $f_{ybf}$ = 53 ksi for the bottom flange.

Find the plastic neutral axis by setting $T = C$:
$T = A_s \cdot f_y = 47 \cdot 0.75 \cdot 53 + (2 \cdot 58.754 \cdot 0.5 + 2 \cdot 12 \cdot 0.625) \cdot 60 = 6293.25$ kips
$C_c = 0.85 \cdot f_c' \cdot t_s \cdot b_{eff} = 0.85 \cdot 6.26 \cdot 8 \cdot 140 = 5959.52$ kips
Because $T > C$, the plastic neutral axis is in the girder.
$C_s = (A_s \cdot f_y - C_c) / 2 = (6293.25 - 5959.52) / 2 = 166.87$ kips

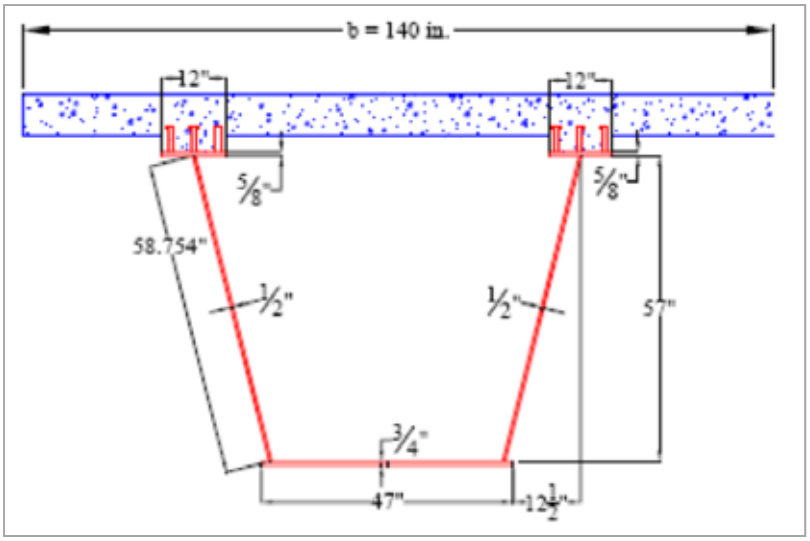


*Figure 3.3: Composite section*

Using this equation, the compressive force required in the steel section to achieve equilibrium ($C = T$) can be determined.

$$C_{tfl} = 2 \cdot t_{tfl} \cdot b_{tfl} \cdot f_{ytf} = 2 \cdot 0.625 \cdot 12 \cdot 60 = 900 \text{ kips}$$

The top flanges can resist 900 kips in compression, which is more than required to obtain equilibrium. As a result the, plastic neutral axis (PNA) lies at $x = 166.87 / (2 \cdot 12 \cdot 60) = 0.116$ in. inside the top flange as shown in Figure 3.4.


*Figure 3.4: Plastic neutral axis location*

Thus:

$C_c = 5959.52$ kips
$C_{tfl} = 166.87$ kips,
$T_{tfl} = 900 - 166.87 = 733.13$ kips
$T_{web} = A_{web} \cdot f_{yw} = 2 \cdot 0.5 \cdot 58.754 \cdot 60 = 3525.24$ kips
$T_{bottom\ flange} = A_{bottom\ flange} \cdot f_y = 47 \cdot 0.75 \cdot 53 = 1868.25$ kips

By taking moments about the PNA, the nominal plastic moment capacity can be calculated:

$M_{bottom\ flange} = T_{bottom\ flange} \cdot (3/8 + 57 - 0.116) = 106{,}974$ kip-in.
$M_{web} = T_{web} \cdot 57 / 2 = 100{,}469$ kip-in.
$M_{T\ tfl} = T_{tfl} \cdot (0.625 - 0.116) / 2 = 187$ kip-in.
$M_{C\ tfl} = C_{tfl} \cdot 0.116 / 2 = 9.68$ kip-in.
$M_{C\ concrete} = C_c \cdot (4 + 3 + 0.116) = 42{,}408$ kip-in.

Note: The 3-in. term added in the moment arm accounts for the average haunch height and offsets the concrete deck 3 in. above the top flange of the girder.
Accordingly, $M_P$ = 106,974 + 100,469 + 187 + 9.68 + 42,408

$$M_P = 250{,}048 \text{ kip-in.} = 20{,}837 \text{ kip-ft}$$

Earlier, $M_{max}$ was found to be 9,049 kip-ft. The plastic moment capacity of the intact girder is adequate to sustain the dead load of the bridge plus the truck load.

## 3.5 Analysis of Concrete Deck

The bending and shear capacity of the concrete deck are checked to ensure that they are adequate to resist the moment and the shear produced by the unsupported load of the fractured girder. These capacities are based on a 1-ft wide transverse deck section as shown in Figure 3.5.

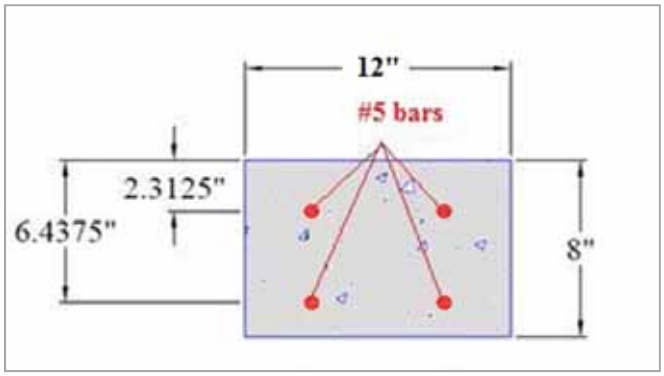


*Figure 3.5: Typical one foot wide section of the concrete deck*

**Positive Moment Capacity**

The assumed strain and stress profile at failure are shown in Figure 3.6:

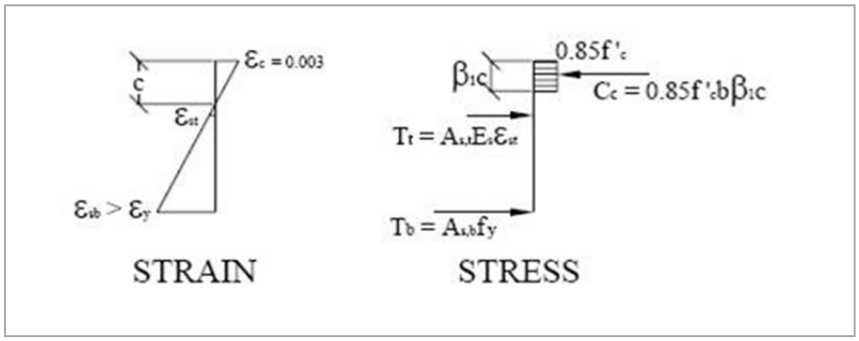


*Figure 3.6: Strain and stress gradients at positive moment regions*

According to ACI 318-08, it is assumed that the ultimate strain of concrete is 0.003 in./in. and the bottom reinforcement yields prior to failure. The top reinforcement is included in the calculations to provide for more accurate results than would be obtained if its contribution were

neglected. Based on the results of laboratory tests to characterize material properties, the concrete strength is taken as 6.26 ksi, and the reinforcement strength is taken as 60 ksi.

Let $C = T$:

$C = 0.85 \cdot fc' \cdot \beta_1 \cdot c \cdot b = 0.85 \cdot 6.26 \cdot 0.7 \cdot 12 \cdot c = 44.70 \cdot c$

Note: $\beta_1 = 0.70$ for 6.26 ksi concrete.

$\varepsilon_{s,\,bottom} = 0.003 \cdot (6.4375 - c) / c$

$\varepsilon_{s,\,top} = 0.003 \cdot (2.3125 - c) / c$

$T_{bottom} = A_{s,bottom} \cdot f_y = 0.62 \cdot 60 = 37.2$ kips

$T_{top} = A_{s,top} \cdot \varepsilon_{s,\,top} \cdot E_s = 0.62 \cdot 29{,}0000 \cdot \varepsilon_{s,top} = 17{,}980 \cdot \varepsilon_{s,top}$

$44.70 \cdot c = 37.2 + 17{,}980 \cdot \varepsilon_{s,top}$

$44.70 \cdot c = 37.2 + 17{,}980 \cdot 0.003 \cdot (2.3125 - c) / c$

Iterations need to be performed until the neutral axis depth is found. For this case, the solution is found to be $c = 1.494$ in.

$\varepsilon_{s,\,bottom} = 0.00993 >$ Yield strain (= 0.00207 for 60 ksi)

$\varepsilon_{s,\,top} = 0.001644 <$ Yield strain (= 0.00207 for 60 ksi)

$C = 66.78$ kips

$T_{bottom} = 37.2$ kips

$T_{top} = 29.55$ kips

Taking moments about the NA to solve for nominal moment capacity

$M_n^+ = C \cdot (c - \beta_1 \cdot c / 2) + T_{top} \cdot (2.3125 - c) + T_{bottom} \cdot (6.4375 - c)$

$M_n^+ = 66.78 \cdot (1.494 - 0.7 \cdot 1.494/2) + 29.55 \cdot (2.3125 - 1.494) + 37.2 \cdot (6.4375 - 1.494)$

$M_n^+ = 272.93$ kips-in. $= 22.74$ kips-ft

**Negative Moment Capacity**

The assumed strain and stress failure profile are shown in Figure 3.7.

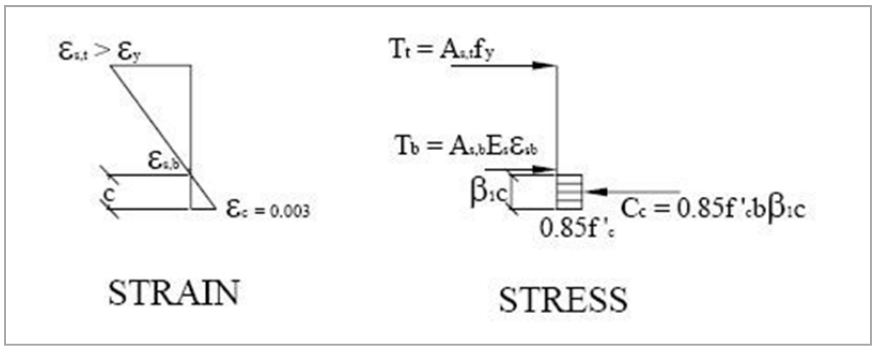


*Figure 3.7: Strain and stress gradients at negative moment regions*

According to ACI 318-08, it is assumed that the ultimate strain of concrete is 0.003 in./in. and the top reinforcement yields prior to failure. Similarly to the calculations carried out to determine the positive moment capacity, the bottom reinforcement is included in the calculations to determine the negative moment capacity.

Let $C = T$:

$$C = 0.85 \cdot fc' \cdot \beta_1 \cdot c \cdot b = 0.85 \cdot 6.26 \cdot 0.7 \cdot 12 \cdot c = 44.70 \cdot c$$

Note: $\beta_1 = 0.70$ for 6.26 ksi concrete.

$$\varepsilon_{s,\ bottom} = 0.003 \cdot (1.5625 - c) / c$$

$$\varepsilon_{s,\ top} = 0.003 \cdot (5.6875 - c) / c$$

$$T_{bottom} = A_{s,bottom} \cdot \varepsilon_{s,\ bottom} \cdot E_s = 0.62 \cdot 29{,}0000 \cdot \varepsilon_{s,bottom} = 17{,}980 \cdot \varepsilon_{s,bottom}$$

$$T_{top} = A_{s,top} \cdot f_y = 0.62 \cdot 60 = 37.2 \text{ kips}$$

$$44.70 \cdot c = 37.2 + 17{,}980 \cdot \varepsilon_{s,bottom}$$

$$44.70 \cdot c = 37.2 + 17{,}980 \cdot 0.003 \cdot (1.5625 - c) / c$$

Iterations need to be performed until the neutral axis depth is found. The solution for this case is $c = 1.199$ in.

$\varepsilon_{s,\ bottom} = 0.00091 <$ Yield strain (= 0.00207 for 60 ksi)

$\varepsilon_{s,\ top} = 0.01123 >$ Yield strain (= 0.00207 for 60 ksi)

$C = 53.60$ kips

$T_{bottom} = 16.35$ kips

$T_{top} = 37.2$ kips

Taking moments about the NA to solve for nominal moment capacity

$$M_n^- = C \cdot (c - \beta_1 \cdot c / 2) + T_{top} \cdot (5.6875 - c) + T_{bottom} \cdot (1.5625 - c)$$

$$M_n^- = 53.60 \cdot (1.199 - 0.7 \cdot 1.199/2) + 37.2 \cdot (5.6875 - 1.199) + 16.35 \cdot (1.5625 - 1.199)$$

**$M_n^- = 214.69$ kips-in. = 17.89 kips-ft**

**Bending and Shear Capacity Check**

Based on the assumption that the shear studs have sufficient tensile capacity to prevent a pull-out failure, the deflected shape of the concrete deck and the bending moment diagram are given in Figure 3.8.

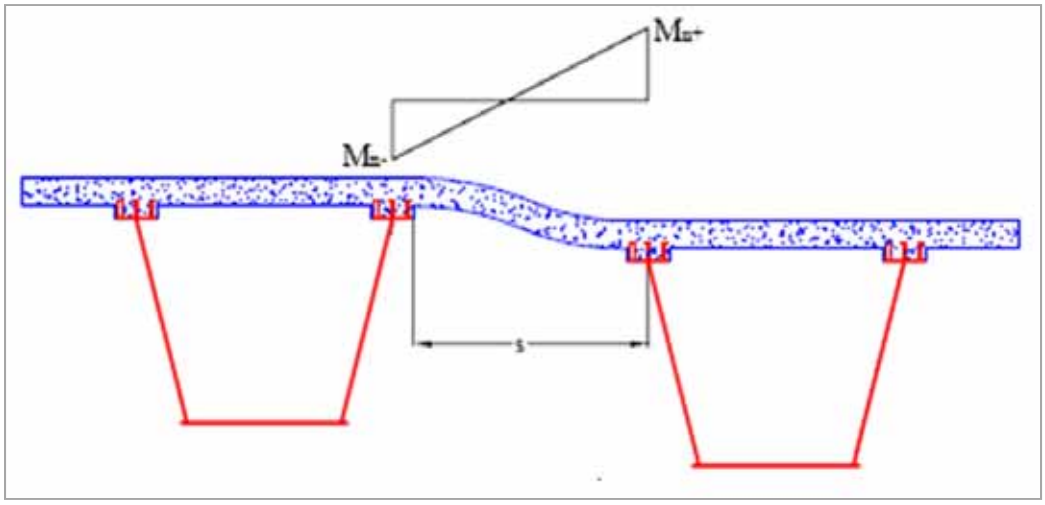


*Figure 3.8: Deflected shape and moment diagram before any failure of shear studs*

$V = (M_n^+ + M_n^-)/s$ = (22.74 kip-ft + 17.89 kip-ft)/5.5 ft = **7.39 kips per foot of deck**

Note: The spacing, *s*, is equal to the distance between the mid-width of the fractured girder's interior top flange and the edge of the interior top flange of the intact girder (5.5 ft).

The shear capacity is calculated using the ACI equation for shear shown below, which neglects the contribution of the reinforcement. The capacity is based on a 1-ft wide transverse deck section. The depth used in this equation is the depth to the centroid of the tension reinforcement (6.4375 in.).

$$V_c = 2 \cdot \sqrt{f'_c} \cdot b \cdot d = 2 \cdot \sqrt{6260} \cdot 12 \cdot 6.4375 = \textbf{12.22 kips}$$

Thus, the shear capacity of the deck is controlled by the shear of the plastic deck mechanism (7.39 kips/ft). Therefore, the total length required to transfer the 306.04-kip force is:

$$l_M = 306.04 / 7.39 = 41.41 \text{ ft}$$

41.41 / 120 = **34.51 % of the span length**

**Shear Stud Check**

In order to determine the tensile strength of the shear stud group, the guidelines given by Mouras (2008) are followed. The shear stud connection in the FSEL bridge consists of a group of three 5-in. tall shear studs spaced transversely. The haunch along the length of the bridge is 3 in. By using Equation 3-1 and 3-2 given below, the tensile capacity of the shear studs group is calculated to be 15.02 kips throughout the bridge.

$$N_b = k_c \cdot \sqrt{f'_c} \cdot h_h^{1.5} \qquad \text{Equation 3-1 (ACI 318-08)}$$

$$N_{cbg} = \frac{A_{NC}}{A_{NCO}} \cdot \psi_{g,N} \cdot \psi_{ec,N} \cdot \psi_{ed,N} \cdot \psi_{c,N} \cdot N_b \qquad \text{Equation 3-2 (modified ACI 318-08)}$$

where:

$N_b$ = concrete cone breakout strength of a single isolated stud in a continuous piece of cracked concrete (15.19 kips)

$k_c$ = 24 for cast-in-place shear studs
$f_c'$ = concrete compressive strength (6260 psi)
$h_h$ = modified height of shear stud in concrete ($h_h = h_{ef} - d_h$ = 4.625-3=1.625 in. < 12/3=4 → $h_h$ =4 in.)
$h_{ef}$ = effective height of shear stud in concrete, which is equal to the length of stud less the height of the stud head ($h_{eff}$ =5-0.375 = 4.625in.)
$d_h$= haunch height (3 in.)
$c_{a,min}$ = distance between outer stud and the edge of flange ($c_{a,min}$ = 1.5 in.)
$N_{cbg}$ = design concrete breakout strength of a stud or group of studs (33.47 kips)
$A_{Nc}$ = projected concrete cone failure area of a stud group ($A_{Nc}$ = 3 $h_{ef} w_h$ = 166.5 in$^2$)
Note: $A_{Nc}$ = 3 $h_{ef} w_h$ because haunch is confined over the full height of the projected cone failure area.
$A_{Nco}$ = projected concrete cone failure area of a single stud in continuous concrete ($A_{Nco}$ = 9$h_h^2$ = 144 in$^2$)
$\Psi_{g,N}$ = group effect modification factor for studs on a bridge girder ($\Psi_{g,N}$ = 0.90 for 3 studs spaced transversely)
$\psi_{ec,N}$ = eccentric load modification factor ($\psi_{ec,N}$ = 1)
$\psi_{ed,N}$ = edge distance modification factor ($\psi_{ed,N}$ = 0.7+0.3 $c_{a,min}$ / (1.5 $h_{ef}$) = 0.76)
$\psi_{c,N}$ = cracked concrete modification factor ($\psi_{c,N}$ = 1.25 for cast-in studs)

Using Equation 3-2, a determination as to whether the shear studs pull out or a hinge is formed in the concrete deck can be made. A strip width equal to the shear stud spacing of 22 inches is used to calculate the tension in the stud group.

$N_{cbg}$ =$T$ = 15.02 kips, $M_2/b + V$ = 22.74 · (22/12) / 6 + 7.39 · (22/12) = 20.50 kips

Because $T < M_2/b + V$, the shear studs pull out, which is consistent with test observations.

**Shear Check of the Composite Section at the Supports due to Torsion and Bending**

The entire weight of the bridge and the live load are applied to the intact girder. The shear due to this loading, which is developed at the end of the span, is calculated as follows:

$$V = V_{DL} + V_{TRUCK} = (2 \cdot 0.427 + 2.33 + 0.65) \cdot 120 / 2 + 41$$

$$V = 271.04 \text{ kips}$$

The unsupported load, which is first carried by the fractured girder, has to be transferred to the intact girder. The eccentricity between the chord of the intact girder bearings and the center of gravity (CG) of each load leads to a torque that is applied to the intact girder in addition to all the transferred loads. Due to the large horizontal curvature of the bridge ($R$ = 1365.39 ft), the eccentricities of each load are assumed to be equal to the distance between the CG of each load and the centerline of the intact girder bearings. Table 3.1 summarizes all the eccentricities.

**Table 3.1: Unit moment capacities of the concrete deck**

| | Live or Dead Load | Eccentricity |
|---|---|---|
| | | (ft) |
| **1** | Fractured Girder (FG) | 12 |
| **2** | Railing above FG | 17.17 |
| **3** | Deck above FG | 11.83 |
| **4** | Intact Girder (IG) | 0.00 |
| **5** | Railing above IG | 5.17 |
| **6** | Deck above IG | 0.17 |
| **7** | Truck | 11.25 |

Thus, the torques due to each load are equal to:
$t_{FG}$ = 51.24 · 12 = 614.88 kip·ft
$t_{RFG}$ = 39 · 17.17 = 669.63 kip·ft
$t_{DFG}$ = 139.8 · 11.83 = 1,653.83 kip·ft
$t_{IG}$ = 51.24 · 0 = 0 kip·ft
$t_{RIG}$ = 39 · 5.17 = 201.63 kip·ft
$t_{DIG}$ = 139.8 · 0.17 = 23.77 kip·ft
$t_{TRUCK}$ = 76 · 11.25 = 855 kip-ft

Assuming that half of the calculated torque is applied to each end of the intact girder, the torque developed at each end section is equal to:

$$T = (614.88 + 669.63 + 1{,}653.83 - 201.63 - 23.77 + 855) / 2 = 1{,}784 \text{ kip-ft}$$

In all the above calculations for the applied torque, the curvature of the bridge is neglected due to the large radius of curvature of the test bridge. In order to include the effect of the horizontal curvature, Equations 2-5 through 2-19 need to be used. In the case of the FSEL bridge:

1. $R_{INT}$ = 1359.34 ft , $L_{INT}$ = 119.48 ft, $\varphi$ = 0.0879
2. $R_{FG}$ = 1371.2 ft, $\theta_{0FG}$ = 0 rad, $\theta_{1FG}$ = 0.0879 rads, $\bar{\theta}_{FG}$ = 0.04395 rads
3. $R_{IG}$ = 1359.34 ft, $\theta_{0IG}$ = 0 rad, $\theta_{1IG}$ = 0.0879 rads, $\bar{\theta}_{IG}$ = 0.04395 rads
4. $R_{TRUCK}$ = 1370.48 ft, $\theta_{0TRUCK}$ = 0.0204 rad, $\theta_{1TRUCK}$ = 0.03385 rads, $\bar{\theta}_{TRUCK}$ = 0.027 rads

The center of gravity of each component is found by inserting all the above values into Equation 2-18.

$$\bar{D}_{FG} = \frac{1371.2^{2} \cdot 1.96 \cdot [\sin(0.0879 - 0.04395) - \sin(-0.04395)]}{1371.2 \cdot 1.96 \cdot 0.0879} = 1370.76\,ft$$

$$\bar{D}_{IG} = \frac{1359.34^{2} \cdot 1.96 \cdot [\sin(0.0879 - 0.04395) - \sin(-0.04395)]}{1359.34 \cdot 1.96 \cdot 0.0879} = 1358.90\,ft$$

$$\overline{D}_{TRUCK} = \frac{1370.48^{2} \cdot 2.72 \cdot [\sin(0.03385 - 0.027) - \sin(0.0204 - 0.027)]}{1370.48 \cdot 2.72 \cdot (0.03385 - 0.0204)} = 1370.47\ ft$$

By using Equation 2-19, the eccentricity of each component can be found as follows:

$e_{FG}$ = 1370.76 – 1359.34 · cos(119.48/(2 · 1359.34)) = 12.73 ft

$e_{IG}$ = 1358.90 – 1359.34 · cos(119.48/(2 · 1359.34)) = 0.87 ft

$e_{TRUCK}$ = 1370.47 – 1359.34 · cos(119.48/(2 · 1359.34)) = 11.12 ft

The calculated eccentricities are in a very good agreement with the assumed ones ($e_{FG}$ = 12.73 ft ≃12 ft, $e_{IG}$ = 0.87 ft ≃ 0 ft, $e_{TRUCK}$ = 11.12 ft ≃ 11.25 ft). As a result, if the bridge under consideration has a large radius of curvature, the eccentricities can be measured from the centerline of the intact girder.

To compute the shear flow of the closed cross-section, Equation 2-20 is used.

$q = T / (2 \cdot A)$ = 1,784 / (2 · 3850.36/144) = 33.36 kips/ft = 2.78 kips/in

The shear stress due to torsion at every component of the composite section is calculated as:

$\tau_{CONC.\ DECK} = q / t_{CONC.\ DECK}$ = 2.78 / 8 = 0.34 ksi

$\tau_{WEB} = q / t_{WEB}$ = 2.78 / 0.5 = 5.56 ksi

$\tau_{BOTT.\ FLANGE} = q / t_{BOTT.\ FLANGE}$ = 2.78 / 0.75 = 3.71 ksi

The flexural shear is assumed to be carried by the webs of the composite section because the contribution of the bottom flange and the concrete deck is small. The flexural shear stress in the webs of the composite section is calculated as:

$\tau_{Flexural\ WEB} = V / (2 \cdot h_{WEB} \cdot t_{WEB} \cdot \cos(14°))$ = 271.04 / (2 · 58.754 · 0.5 · 0.97) = 4.76 ksi

Note: The factor 2 accounts for the fact that the composite sections consist of two webs, which share the total flexural shear. The cos(14°) accounts for the fact that the webs are not vertical; due to their inclination, the shear force in the plane of the webs is higher than the applied shear.

The shear stress that develops in the concrete deck due to torsion is equal to 0.36 ksi. According to ACI 318-08, the shear capacity of a reinforced concrete section is,

$$V_S = A_t \cdot f_{yt} \cdot b \cdot \cot\theta / s$$

Thus,

$V_{TORSION} = q \cdot b$ = 2.78·72 = 200.16 kips ≤ $V_S = A_t \cdot f_{yt} \cdot b \cdot \cot\theta / s$ = 0.62·60·72/6 = 446.4 kips

The shear stresses in the steel girder are checked according to the AASHTO Specifications (2007). The shear stress in the webs of the end panel should be limited to either the shear-yielding or shear-buckling resistance. The nominal shear stress capacity of the web panel ($\tau_n$) is computed as the shear-buckling capacity to the shear yield strength ratio ($C$) multiplied by the plastic shear stress ($\tau_p$) ($\tau_n = C \cdot \tau_p$). The plastic shear stress is equal to $0.58 f_{yw}$. The ratio $C$ is determined as follows:

$$\text{If } \frac{D}{t_w} \le 1.12\sqrt{\frac{Ek}{f_{yw}}} \text{ then } C = 1.0$$

$$\text{If } 1.12\sqrt{\frac{Ek}{f_{yw}}} < \frac{D}{t_w} \le 1.40\sqrt{\frac{Ek}{f_{yw}}} \text{ then } C = \frac{1.12}{D/t_w}\sqrt{\frac{Ek}{f_{yw}}}$$

$$\text{If } \frac{D}{t_w} > 1.40\sqrt{\frac{Ek}{f_{yw}}} \text{ then } C = \frac{1.57}{(D/t_w)^2}\left(\frac{Ek}{f_{yw}}\right)$$

For the FSEL test bridge, $D$ = 58.75 in., $t_w$ =0.5 in., $E$ = 29,000 ksi, $f_{yw}$ =60 ksi. The factor $k$ is calculated as

$$k = 5 + \frac{5}{\left(d_0/D\right)^2}$$

where $d_0$ is the spacing from the support to the first stiffener adjacent to the support (144 in.). AASHTO limits the factor $d_0/D$ to 1.5 for end panels. In the case of the FSEL test bridge, this limit is violated because $d_0/D$=2.45>1.5. Due to this violation, the ratio is set to its actual value (i.e., $d_0/D$=2.45). Moreover, it is important to mention that the ratio of $d_0/D$=2.45 provides a lower nominal shear stress than $d_0/D$=1.5. By inserting the value of $d_0/D$ into the equation above, $k$ is calculated to be 5.83. Because

$$\frac{D}{t_w} = \frac{57}{0.5} = 114 > 1.40\sqrt{\frac{Ek}{f_{yw}}} = 74.32$$

$$C = \frac{1.57}{(D/t_w)^2}\left(\frac{Ek}{f_{yw}}\right) = 0.32 .$$

Having all the variables defined, the nominal shear stress ($\tau_n$) is equal to $\tau_n = 0.32 \cdot 0.58 \cdot f_{yw}$ = 11.14 ksi.

The total shear stress in the webs includes contributions from the flexural shear stress and the torsional shear stress. As shown in Figure 3.9, the shear stresses are added and subtracted in the east and west web, respectively. The east web controls because the shear from flexure and torsion add to each other. The total shear stress that develops in the east web is calculated to be $\tau_{TOTAL} = \tau_{WEB} + \tau_{Flexural\ WEB}$ = 5.56 + 4.76 = 10.32 ksi, which is less than the nominal shear stress capacity ($\tau_n$ = 11.14 ksi).

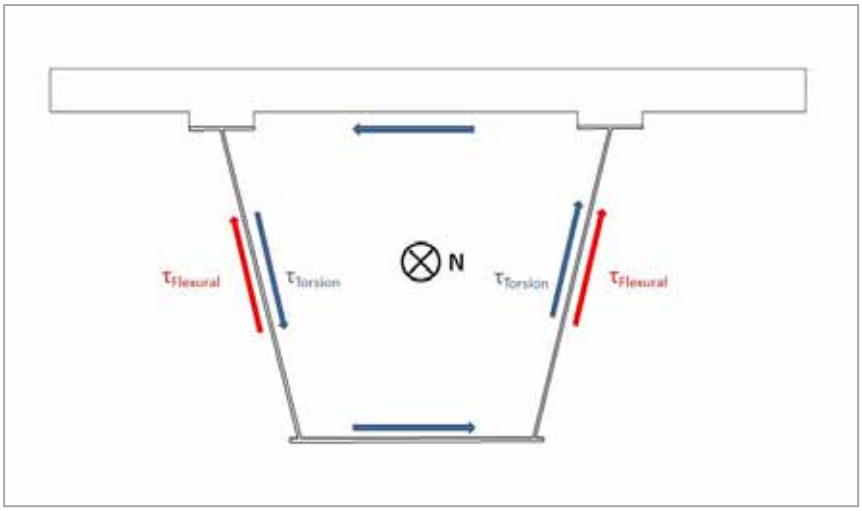


*Figure 3.9: Flexural and torsional shear stresses on the composite section*

The end diaphragm, which connects both girders, needs to be checked to ensure that it has adequate capacity to resist the torque applied to the intact girder. The force couples at the bearings of the two girders, which are produced by the torque applied on the intact girder, causes shearing of the end diaphragm. Thus, the forces acting on each side of the end diaphragm can be calculated as follows:

$V_{ED}$ = $T$ / $l_b$ = 1,784 k-ft / 12 ft = 148.67 kips, where $T$ is the torque applied to the intact girder, and $l_b$ is the distance between the two bearings.

The nominal shear strength of the end diaphragm can be computed according to AASHTO Sec. 6.10.9.2.

$V_n = C \cdot V_P$, where $V_P = 0.58 \cdot F_{yw} \cdot D \cdot t_w = 0.58 \cdot 60 \cdot 57 \cdot 0.5 = 991.8$ kips

and $C$ is calculated as

$$C = \frac{1.57}{(D/t_w)^2}\left(\frac{Ek}{f_{yw}}\right) = 0.29 \text{ because } \frac{D}{t_w} = \frac{57}{0.5} = 114 > 1.40\sqrt{\frac{Ek}{f_{yw}}} = 68.82 \text{ , where } k = 5.$$

Thus, the shear strength of the end diaphragm ($V_n$ = 0.29·991.8 = 287.62 kips) is adequate to resist the applied shearing force ($V_{ED}$ = 148.67 kips).

Summarizing the calculations, it is found that all the components of the section have adequate capacities to resist the applied load, except for the shear studs. The plastic mechanism in the deck between the girders cannot be formed due to the low tensile strength of the shear studs. As a result, a yield line analysis needs to be performed to determine the ultimate load that this bridge can sustain.

## 3.6 Analysis of FSEL Bridge Using the Yield Line Model

Following the procedure of the Yield Line Model described in the previous chapter, the ultimate load carrying capacity of the FSEL bridge can be estimated. The unit moment capacity of a 1-ft strip of the concrete deck is calculated in the same manner as presented above. Table 3.2 summarizes the basic parameters of the FSEL bridge.

**Table 3.2: Unit moment capacities of the concrete deck**

| *Span Length* | | |
|---|---|---|
| $L$ | 120.00 | ft |
| *Outer Horizontal Curvature* | | |
| $R$ | 1377.00 | ft |
| *Distance of the deck's outer edge from the intact girder's interior top flange* | | |
| $b$ | 14.17 | ft |
| *Moment Capacity of the Deck* | | |
| $m_{nT}$ | 17.62 | kip-ft |
| $m_{nL}$ | 10.27 | kip-ft |
| $m_{pT}$ | 22.74 | kip-ft |
| $m_{pL}$ | 14.76 | kip-ft |
| *Moment Capacity of the Railing* | | |
| $M_n$ | 416.27 | kip-ft |

Following the procedure described above, Table 3.3 can be constructed. All the variables presented in this table are defined as follows:

1. $a$ is equal to the horizontal distance from point A or D to the origin.
2. $\theta_i$ (radians) is the angle measured from the positive $x$-axis to the radial line that connects the origin with points D, C, or B (line OD, OC, OB in Figure 2.13).
3. $X_i$, $Y_i$ are the coordinates of points A, B, C, and D.
4. $l$ is the length of each yield line, and it is calculated by inserting the end point coordinates into the distance formula (Equation 2-28).
5. $\alpha$ is the angle of each yield line with the horizontal axis (Equation 2-27)
6. The moment capacity ($m_b$) of each hinge line is calculated according to Equation 2-26.
7. $h_i$ is the height of DOC, COB, or BOA triangle.
8. $\theta_{rotation}$ is the angle of rotation of each plane (DOC, COB, and BOA) with respect to the horizontal for yield lines along the perimeter; for diagonal yield lines, $\theta_{rotation}$ is the angle of rotation between two adjacent planes (e.g., DOC with COB, and COB with BOA)
9. The last factors ($dIW$, $IW_{Hinge}$, $IW_{Railing}$, $IW_{TOTAL}$) are, respectively, the internal work (IW) of each hinge line, the summation of the yield lines IW, the IW of the railing, and the total IW.

**Table 3.3: Internal work calculation for FSEL bridge**

| $a$ (ft) | | $\theta_i$ (rad) | $X$ | $Y$ | $l$ | $\alpha$ | $m_b$ | $h$ | $\vartheta_{rotation}$ | $dIW$ | $IW_{Hinge}$ |
|---|---|---|---|---|---|---|---|---|---|---|---|
| 41 | Perimeter | 0.015 | 41.00 | 0.61 | | | | | | | 116.71 |
| | | 0.611 | 20.24 | 14.17 | 24.79 | 0.58 | 14.54 | 22.93 | 0.044 | 15.72 | $IW_{Railing}$ |
| | | 2.531 | -20.24 | 14.17 | 40.47 | 0.00 | 16.63 | 14.17 | 0.071 | 47.50 | 52.54 |
| | | 3.127 | -41.00 | 0.61 | 24.79 | 2.56 | 14.54 | 22.93 | 0.044 | 15.72 | $IW_{TOTAL}$ |
| | Diagonals | | | | 24.70 | 0.61 | 18.43 | | 0.0415 | 18.88 | 169.25 |
| | | | | | 24.70 | 0.61 | 18.43 | | 0.0415 | 18.88 | |

As mentioned previously, the length $a$ and the magnitude of the truck load are mutually dependant. Accordingly, one of these variables should be fixed in order to obtain the other one. It is recommended that the live load magnitude corresponding to the number of trucks be selected first; with this value set, the length $a$ for the given load magnitude can be obtained. A good starting value is 2×HS-20 trucks. If a valid solution for the length $a$ is computed, the given truck load is a possible failure loading. In subsequent iterations, the truck load should be decreased until a valid solution for $a$ no longer exists. The minimum truck load is the last one that gave a physically admissible solution for the length $a$. In contrast, if the initially chosen truck load does not provide a physically admissible solution for the length $a$, then the truck load needs to be increased in subsequent iterations.

Once the length $a$ has been computed, all the variables associated with the Yield Line Model can be calculated. After several iterations, the minimum wheel multiplier was computed to be equal to 3.66. As a result, the front wheel and middle/rear wheel loads are equal to 14.64 kips and 58.56 kips, respectively. Table 3.4 summarizes the external work calculation for the minimum truck load multiplier of 3.66.

**Table 3.4: External work calculation of the truck load**

| | Truck Load | | | | | | | |
|---|---|---|---|---|---|---|---|---|
| | | $P$ | $X_{point\ Load}$ | $Y_{point\ Load}$ | $r_{LOAD}$ | $r$ | $\delta_i$ | $EW$ |
| Truck Load | Front Wheel | 14.66 | 14 | 3.42 | 14.41 | 31.41 | 0.54 | 7.93 |
| | Front Wheel | 14.66 | 14 | 9.42 | 16.87 | 24.89 | 0.32 | 4.72 |
| | Middle Wheel | 58.63 | 0 | 3.42 | 3.42 | 14.17 | 0.76 | 44.48 |
| | Middle Wheel | 58.63 | 0 | 9.42 | 9.42 | 14.17 | 0.34 | 19.65 |
| | Rear Wheel | 58.63 | -14 | 3.42 | 14.41 | 31.41 | 0.54 | 31.73 |
| | Rear Wheel | 58.63 | -14 | 9.42 | 16.87 | 24.89 | 0.32 | 18.89 |
| | | | | $EW_{TRUCK}$ | | | | 127.41 |
| | | | | $EW_{DL}$ | | | | 41.84 |
| | | | | $EW_{TOTAL} - IW_{TOTAL}$ | | | | 0.00 |

The Yield Line Model indicated that the ultimate load capacity of the FSEL bridge was 3.66×HS-20 Trucks or 263.52 kips, which is smaller than the actual load of 363.75 kips that the

bridge carried during the test. As previously mentioned, the difference between the estimated and actual load capacity is due to two reasons. First, the point loads used in the analysis produce a larger moment than the distributed load used in the test because of the way in which the road base was distributed and positioned on the bridge. Second, the positive moment capacity of the railing used for estimating the bridge capacity is smaller than the observed one because of the assumptions made in defining the effective width of the concrete deck that contributes to the railing response. These assumptions were made to ensure a conservative estimate of the overall capacity of a bridge following the fracture of one of its girders.

The initial strength checks for the bridge, which were performed earlier, should be recalculated for the truck load of 3.66 × HS-20 (263.52 kips). As before, the moment at the mid-span of the intact girder produced by this increased truck load is found to be 13,944 kip-ft, which is less than the plastic moment capacity of the intact girder section.

$$M_P = 250{,}047.67 \text{ kip-in.} = 20{,}837.31 \text{ kip-ft} > 13{,}944 \text{ kip-ft}$$

The force needed to be transferred is found to be:

$$F = (0.427 + 2.33/2 + 0.65/2) \cdot 120 + 263.52 = 493.56 \text{ kips}$$

$$F = 493.56 \text{ kips}$$

The length of the bridge needed to transfer the load $F$ based on the flexural capacity of the bridge is:

$$l_M = 493.56 / 7.39 = 66.79 \text{ ft}$$
$$66.79 / 120 = \mathbf{55.66\ \%\ of\ the\ span\ length}$$

The flexural shear at the end support is found to be:

$$V = V_{DL} + V_{TRUCK} = (2 \cdot 0.427 + 2.33 + 0.65) \cdot 120 / 2 + 142$$

$$V = 372 \text{ kips}$$

The torques due to each load are equal to:

$t_{FG} = 51.24 \cdot 12 = 614.88$ kips·ft
$t_{RFG} = 39 \cdot 17.17 = 669.63$ kips·ft
$t_{DFG} = 139.8 \cdot 11.83 = 1{,}653.83$ kips·ft
$t_{IG} = 51.24 \cdot 0 = 0$ kips·ft
$t_{RIG} = 39 \cdot 5.17 = 201.63$ kips·ft
$t_{DIG} = 139.8 \cdot 0.17 = 23.77$ kips·ft
$t_{TRUCK} = 263.52 \cdot 11.25 = 2{,}964.6$ kip-ft

Assuming that half of the calculated torque is applied to each end of the intact girder, the torque developed at the end section is equal to:

$$T = (614.88 + 669.63 + 1{,}653.83 - 201.63 - 23.77 + 2{,}964.6) / 2 = 2{,}838.77 \text{ kip-ft}$$

Knowing the applied torque at the end support, the shear flow of the end section is calculated to be:

$$q = T / (2 \cdot A) = 2{,}838.77 / (2 \cdot 3850.36/144) = 53.08 \text{ kips/ft} = 4.42 \text{ kips/in}$$

The shear stresses in the concrete deck, webs, and bottom flange are computed by following the same procedure as before:

$\tau_{CONC.\ DECK} = q / t_{CONC.\ DECK} = 4.42 / 8 = 0.55$ ksi

$\tau_{WEB} = q / t_{WEB} = 4.42 / 0.5 = 8.84$ ksi

$\tau_{BOTT.\ FLANGE} = q / t_{BOTT.\ FLANGE} = 4.42 / 0.75 = 5.89$ ksi

$\tau_{Flexural\ WEB} = V / (2 \cdot h_{WEB} \cdot t_{WEB} \cdot \cos(14°)) = 372 / (2 \cdot 58.754 \cdot 0.5 \cdot 0.97) = 6.53$ ksi

The shear stress, which develops in the concrete deck due to torsion, is equal to 0.56 ksi.

According to ACI 318-08, the shear capacity of a reinforced concrete section is $V_S = A_t \cdot f_{yt} \cdot b \cdot \cot\theta / s$. As a result,

$$V_{TORSION} = q \cdot b = 4.42 \cdot 72 = 318.24 \text{ kips} \leq V_S = A_t \cdot f_{yt} \cdot b \cdot \cot\theta / s = 0.62 \cdot 60 \cdot 72/6 = 446.4 \text{ kips}$$

The shear stress in the webs is a combination of the flexural and the torsional shear stresses. As shown in Figure 3.9, the shear stresses add together in the east web, and they must be subtracted in the west web. The east web controls in this case. The total shear stress that develops in the east web is calculated to be:

$\tau_{TOTAL} = \tau_{WEB} + \tau_{Flexural\ WEB} = 8.84 + 6.53 = 15.37$ ksi which is bigger than $\tau_n = 11.14$ ksi.

Regarding the end diaphragm, the shearing forces at each edge of the end diaphragm are equal to:

$$V_{ED} = T / l_b = 2{,}838.77 / 12 = 236.56 \text{ kips}$$

where $T$ is the torque applied on the intact girder, and $l_b$ is the distance between the two bearings.

Thus, the shear strength of the end diaphragm ($V_n = 0.29 \cdot 991.8 = 287.62$ kips) is adequate to resist the applied shearing force ($V_{ED} = 236.56$ kips).

Summarizing the calculations, it is found that the web stresses of the end section exceed the nominal stress before the collapse of the bridge. This result indicates that the webs would buckle under the applied load. Buckling of the webs, however, was not observed in the test. The difference between the predicted response and the observed behavior stems from some of the assumptions made in the development of the simplified analysis procedure to compute the response of a twin steel box-girder bridge following the fracture of one of its girders. The buckling capacity of the webs in shear is based on simply supported boundary conditions. The actual boundary conditions in a box girder may approach a fixed condition. Moreover, in experimental studies of composite girders, the webs of end panels were able to reach their tension field capacity. In the calculations performed for this example, the buckling capacity of the girder webs is low due to the large stiffener spacing in the last panels, which exceed the AASHTO maximum spacing requirements. Based upon the web buckling capacity computed using the AAHTO specifications, however, the estimated bridge capacity would be 1.48 HS-20 trucks (106.56 kips). The variation in the results computed with the simplified modeling approach suggests that, in certain cases, it may be desirable to perform detailed finite element analyses to compute the stresses in critical components. The next chapter introduces finite

element modeling techniques that can be used to compute the response of fracture critical steel box-girder bridges.

# Chapter 4. Numerical Modeling of Twin Steel Box-Girder Bridges

## 4.1 Introduction

Finite element models used to simulate the response of twin steel box-girder bridges considered for this research were developed using ABAQUS/Standard (v6.7), which is a commercially available general purpose finite element analysis software package. To incorporate nonlinear material behavior, traditional metal plasticity was used to represent steel components, and cast iron plasticity was used to represent concrete components. The choice of a metal-based plasticity formulation to represent concrete material is described in detail below. In addition to material nonlinearities, railing contact and stud connection failures were also considered in the simulation models using nonlinear spring elements and connector elements, respectively. For the railing contact, nonlinear spring elements were installed in gaps between bridge rails instead of conducting a direct contact analysis. The deck haunch placed between a steel girder top flange and the concrete deck was not modeled explicitly, but it was accounted for in the prescribed load-deformation response of the connector elements. Connector element performance was validated against small-scale laboratory tests on specimens that included a haunch and a wide array of shear stud arrangements (Mouras, 2008). Details of the computational model are described in the sections below.

## 4.2 Finite Element Model of the Bridge

A trapezoidal steel box-girder bridge consists of various components, including steel plate girders, bracing members, shear studs, a concrete deck, bridge rails, and so on. As shown in Figure 4.1, finite element models for bridges were constructed with various types of elements to represent, as realistically as possible, the box-girder bridge under investigation. The steel plates were modeled using 8-node shell elements (S8R), and the internal and external brace members were modeled using 2-node truss (T3D2) and beam elements (B31). For the concrete deck, 8-node solid elements (C3D8R) were used. The reinforcement in the concrete deck was represented using 2-node truss elements (T3D2) that were embedded into the concrete elements.

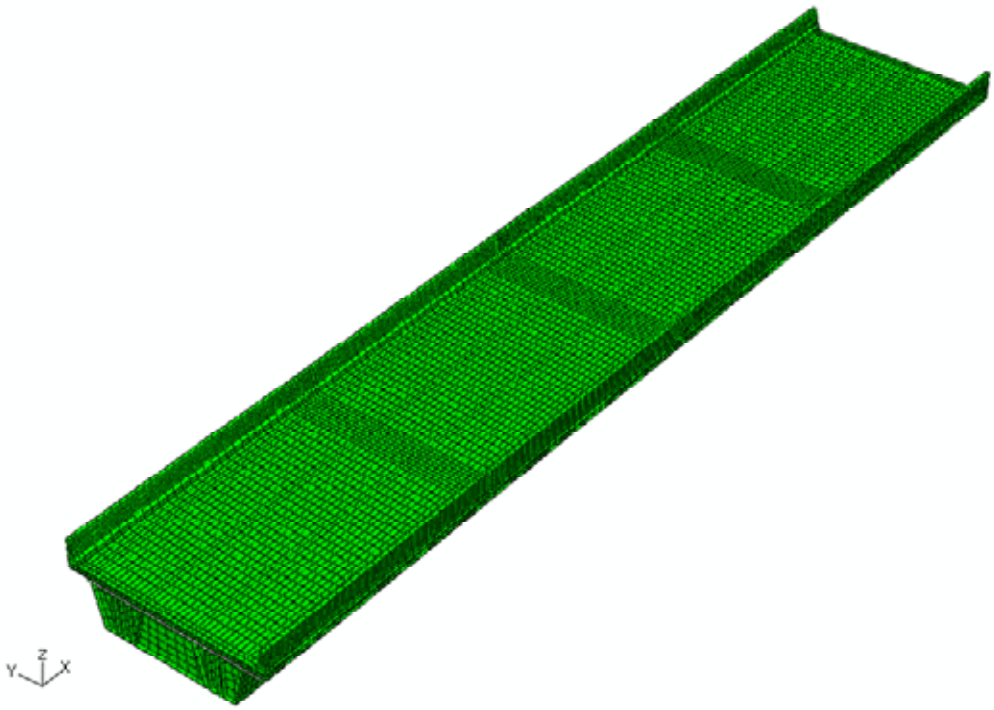


*Figure 4.1: Finite element bridge model*

In the construction of a steel box-girder bridge, shear studs are used to develop composite action between the concrete deck and the box girders. These shear studs, as shown in Figure 4.2(a), are installed on the top flanges of the box girders prior to casting of the concrete deck. Haunches above the girder top flanges, as indicated in Figure 4.2(b), allow for a uniform deck thickness along the bridge span. In the simulation model, such haunches were not modeled explicitly; instead, their effects on the pull-out strength of shear stud connections were incorporated into the vertical action of connector elements (CONN3D2). The shear resistance of the shear studs between the deck and the steel box girders was simulated with the horizontal actions of the connector elements. These actions were obtained from tests that are described later in this chapter. Bridge rails and railing interactions were modeled by 8-node solid elements and nonlinear spring elements (SPRING2), respectively, to account for railing contact. These nonlinear springs were assumed to be effective only in compression after a deflection of 3/4 in. was reached. This distance corresponded to the initial gap between rails in the finite element model and was consistent with measurements of the bridge tested at FSEL and the prescribed geometry called for in the TxDOT T501 traffic railing (TxDOT, 2003).


(a) Shear studs installed on top flange (b) Deck haunch

*Figure 4.2: Shear studs and haunches of twin box-girder bridge*

## 4.3 Material Nonlinearities and Degradation

### 4.3.1 Steel

The inelastic behavior of steel plates, brace members, and reinforcing steel were modeled as "multi-linear inelastic material model with isotropic hardening rule" (Dassault Systemes, 2007a) in both tension and compression. Based on classical metal plasticity, it was assumed that the material yielded when the equivalent stress exceeded the von Mises yield criterion; perfectly plastic behavior was assumed when the stress exceeded the yield strength. In this study, 50 ksi for the plates and 60 ksi for the reinforcing steel, respectively, were used as the yield strengths in the finite element model of the full-scale test bridge. Figure 4.3 shows the stress-strain behavior of the steel plate and rebar under uniaxial tension forces.

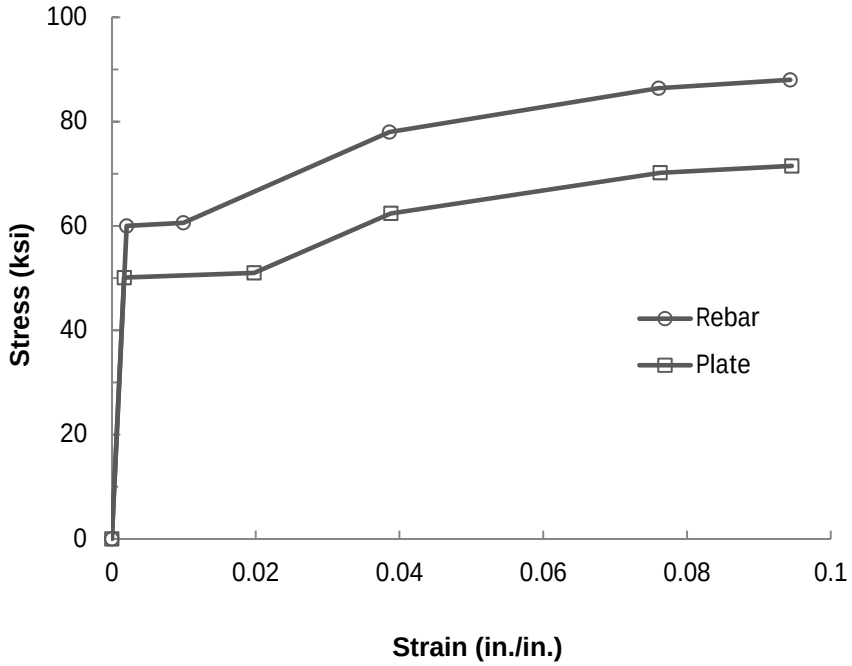


*Figure 4.3: Stress-strain behavior of steel*

### 4.3.2 Concrete

*Compressive Strength*

The concrete deck of the full-scale test bridge was constructed using TxDOT class-S-type concrete, which has a specified 28-day strength of 4,000 psi or greater. To determine concrete strength as a function of time for the full-scale bridge tested at FSEL, concrete cylinder specimens that were made when casting the deck and rails were tested at various intervals. The average compressive strength obtained from the concrete cylinder tests is plotted in Figure 4.4. The deck concrete was cast on August 17, 2006, and the railing was cast on August 24, 2006. Sixty-six days after the deck was cast, the first full-scale bridge fracture test was done, and the second bridge fracture test was conducted 293 days after the deck pour. As shown in Figure 4.4, the railing concrete strength was slightly higher than the deck concrete strength. For simplicity, however, a single concrete strength value was used to model both the deck and the railing in the bridge fracture test simulations: 5,370 psi in the first test simulation and 6,230 psi in the second test simulation. The third bridge fracture test was performed in March 2009. Although the concrete strength at that time would most probably be higher than the strength at the time of the second test due to concrete aging effects, the same concrete strength of 6,230 psi was utilized for this test simulation because specific test data on concrete strength were not available and the additional strength gain achieved following the second test was not expected to be significant.

In general, the concrete strength specified in the construction of bridge elements is typically based on the 28-day value—though some states specify the concrete strength corresponding to an age of 58 days (Russell, 2003). In practice, the specified concrete strength of bridge components typically ranges between 4,000 psi and 8,000 psi (Russell, 2003). To accurately account for the aging effect of concrete components in a bridge simulation model,

detailed strength data as a function of time would be needed. Collecting such data, however, would not be practical. Instead, the equation proposed by ACI Committee 209 (1982) can be used to estimate the strength gain of concrete as a function of time:

$$f_c'(t) = f_c'(28)\left[\frac{t}{4+0.85t}\right] \qquad \text{Equation 4-1}$$

where

$f_c'(t)$ = concrete compressive strength at age $t$ (ksi)
$t$ = curing time (day)

This equation is valid for concrete comprised of Type I cement and moist-cured at 70F°.

In the current study, when simulating the response of the bridge tested at FSEL, the most accurate material properties available were used in the simulation model. In most cases, these values were directly measured in laboratory tests; in some cases, however, they were estimated based on available data. Conversely, when evaluating the redundancy of other bridges, it was conservatively assumed that concrete components had a strength of 4,000 psi, which was the lowest specified strength of concrete reported by Russell (2003). In addition, expected strength increases with time were not included. These assumptions were made to ensure conservative estimates of the overall load carrying capacity of twin steel box-girder bridges that suffer a full-depth fracture of one of its girders.

Concrete compressive strengths were also used to specify hardening rules in tension and compression. A hardening curve in compression was constructed using Equation 4-2 as suggested by Kent and Park (1971), and the initial stiffness of the stress-strain curve in compression was used to define the tensile behavior.

$$f_c = f_c'\left[\frac{2\varepsilon}{\varepsilon_o} - \left(\frac{\varepsilon}{\varepsilon_o}\right)\right] \qquad \text{Equation 4-2}$$

where

$f_c$ = concrete compressive stress at given strain (ksi)
$f_c'$ = concrete compressive strength (ksi)
$\varepsilon$ = strain
$\varepsilon_o$ = strain at maximum stress ($\varepsilon_o = 0.002$)

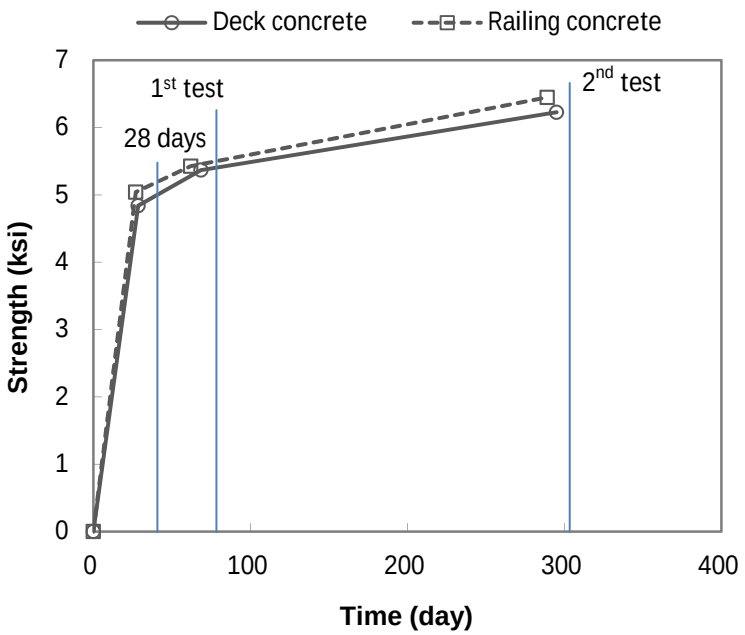


*Figure 4.4: Concrete strength gaining*

*Concrete Smeared Cracking*

The concrete deck and rails were modeled using 8-node solid elements. To account for the inelastic behavior of concrete, such as tensile cracking and compressive crushing, ABAQUS/Standard (v6.7) provides a concrete smeared cracking model and a concrete damaged plasticity model. The latter model is appropriate for cases in which high confining pressures exist, while the former model is appropriate for problems with low confining pressures (Dassault Systemes, 2007a). For the concrete deck of a twin steel box-girder bridge, high confining pressures are not expected due to the fact that the thickness of the deck is much smaller than the width and the length and because the axial restraint in the plane of the deck is limited. For this reason, the concrete smeared cracking model was initially adopted to simulate the response of the full-scale bridge tested during this research.

Various aspects of material response must be defined when utilizing the concrete smeared cracking model, including the compressive behavior, the post-tension failure behavior, the failure ratios needed to define a yield surface, as well as several other parameters. Figure 4.5 shows the uniaxial stress-strain curve and the yield surface associated with the concrete smeared cracking model.

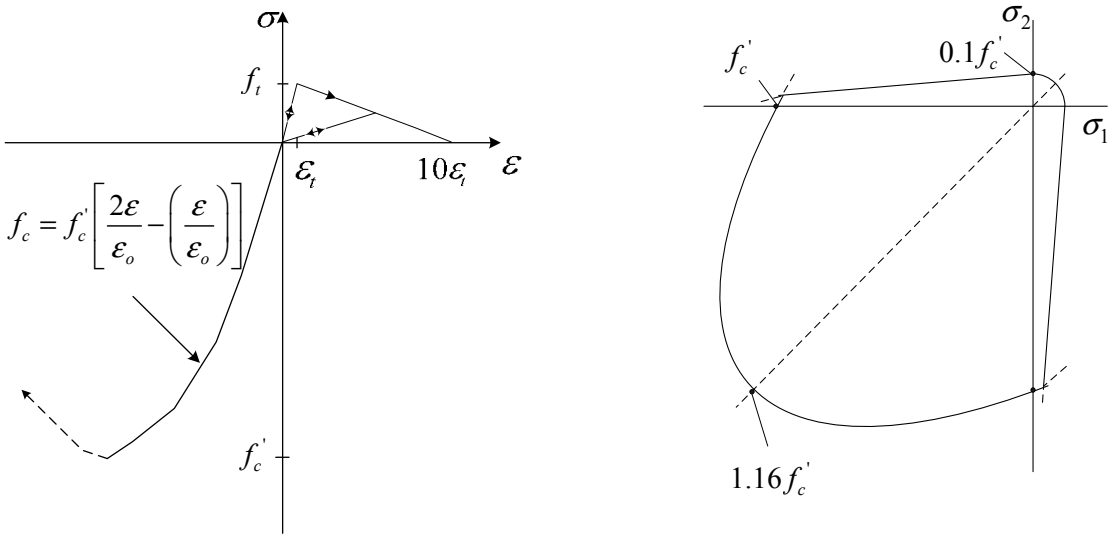


(a) Stress-strain behavior (under uniaxial force)

(b) Yield surface

*Figure 4.5: Material behavior in concrete smeared cracking model*

Finite element models that utilize the concrete smeared cracking model are known to produce results that are sensitive to mesh density (Dassault Systemes, 2007a). Therefore, concrete element size in the plane of the concrete deck was determined such that each element contained reinforcing steel because mesh sensitivity tends to be reduced by the interaction between reinforcing steel and concrete (Dassault Systemes, 2007a). Other parameters affecting the accuracy of the computed results, including material properties and element size though thickness of the deck, were calibrated using finite element simulations of lab tests on a small deck model that represented a portion of the full-scale bridge deck.

The small deck model, as shown in Figure 4.6(a), was developed based on the expected deck deflection behavior in a damaged bridge. With one girder fractured, as assumed for the redundancy evaluation, the bridge deck would initially bend transversely in double curvature to transfer loads from the fractured girder to the intact girder, as shown in Figure 4.6(b). When the deck deflects in double curvature, an inflection point results approximately at the mid-section of the deck between the two girders, and tension forces act on the shear studs of the fractured girder due to the bending of the deck. Figure 4.7 shows a small deck test specimen and a finite element simulation model used to represent the assumed bending response of the deck following the fracture of one girder. The small deck tests, also referred to as stud pull-out tests herein, were conducted by Sutton (2007) and Mouras (2008) as part of the current research program. From their tests, the load-displacement response of small deck specimens and the pull-out strengths of shear stud connections were obtained, and the measured data were used to calibrate the small deck finite element models.

(a) Small deck portion in full-scale bridge for small deck model

(b) Expected deformed shape in bridge cross-section

*Figure 4.6: Small deck model to calibrate bridge concrete slab*


Finite element model

Test setup

*Figure 4.7: Deck load-deflection test and simulation*

Figure 4.8 compares measured load-displacement data from a laboratory test on a small deck specimen with results obtained from finite element simulations. The assumed tensile

strength of the concrete for the simulations was 10% of the average concrete compressive strength, which was 5,100 psi for the small deck test specimen. To define the stress-strain behavior beyond the cracking strain, it was assumed that the stress reduces linearly to zero, where the total strain at zero stress was 10 times the cracking strain, as shown in Figure 4.5(a). This post-cracking stress-strain relationship is also referred to as strain-softening behavior (Dassault Systèmes, 2007a). The number of elements in the finite element model was 10 along the width and two along the length, as indicated in Figure 4.6(a). The prominent behavior demonstrated by the small deck simulation models, as shown in the Figure 4.8, was a reduction in bending stiffness near 15 kips of loading; this reduction was initiated by concrete element cracking at the bottom of the deck near the midspan. The reduced bending stiffness of the deck models eventually became negative because of the assumed post-cracking stress-strain relationship (i.e., strain softening).

In addition to strain softening, the number of elements through the thickness of the deck affected the stiffness of the simulation models. In Figure 4.8, the deck model with three elements through the thickness shows a higher rate of stiffness reduction after the bottom of the deck cracked than did the other cases with five or seven elements. This tendency could be a result of the different rates of bending stiffness loss depending on the element size of the small deck models. Once the stress in one translational direction of an element exceeds the cracking strength, the element loses its resistance entirely in that stress direction. Therefore, a more gradual reduction in bending stiffness can be achieved as the number of elements through the thickness of a deck model is increased. According to the small deck simulation results, 10 elements along the deck width and five elements through the deck thickness resulted in good agreement between the measured and the predicted load-displacement response of the specimens.

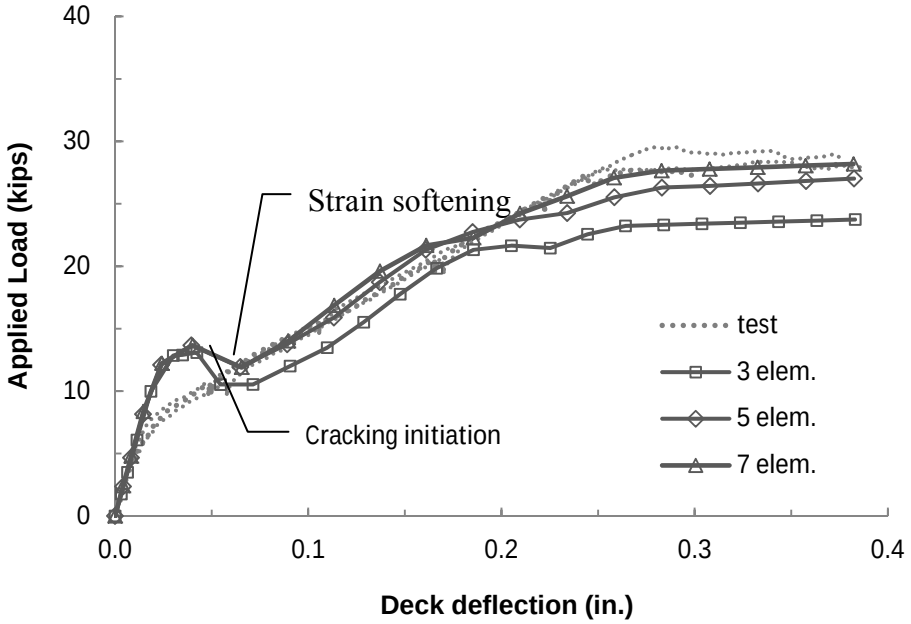


*Figure 4.8: Deflection behavior of small deck (concrete smeared cracking)*

The same mesh density and material parameters obtained from the small deck simulations were utilized to construct the concrete deck of the full-scale bridge finite element model. The

finite element simulation of the full-scale bridge with the assumed damage and loading conditions for the redundancy evaluation, however, was unable to run to completion due to a numerical instability in the concrete deck response. Such instability was initiated by local cracking failures in the deck, which eventually caused convergence problems in the very early stages of the analysis as the cracks on the top of the deck extended longitudinally from the midspan of the bridge. In the smeared concrete cracking model, a cracking failure of concrete initiates strain-softening behavior. Usually, conducting a finite element analysis allowing for softening behavior with a force-controlled loading procedure is numerically challenging, which sometimes requires excessive computation time and frequently terminates prior to completion due to numerical convergence problems (Dassault Systemes, 2007a).

### 4.3.3 Cast Iron Plasticity

As a result of the convergence problems encountered with the initial finite element simulations of the full-scale bridge, the cast iron plasticity model was investigated to determine if it could provide suitably accurate predictions of response without encountering the numerical difficulties that resulted when using the concrete smeared cracking model. While it would seem that a constitutive model based on a metal plasticity formulation would be an inappropriate choice for modeling concrete material, the cast iron plasticity formulation includes several features that make it well suited for the current application. Most importantly, the cast iron plasticity model is able to represent different strengths for tension and compression. To do so, the cast iron plasticity model utilizes a composite yield surface, and it is assumed that tension yielding is governed by a maximum principal stress and that compression yielding is governed by deviatoric stresses (Dassault Systemes, 2007b).

Figure 4.9 shows the uniaxial behavior and the yield surface of the cast iron plasticity model, which was used to model concrete material behavior in this study. Basically, the model has a von Mises-type yield surface, but it is truncated by a Rankine fracture criterion to incorporate a reduced yield strength in tension. Under a plane stress state, the von Mises yield surface has an elliptical shape, and the Rankine yield surface is a square (Ugural, 1995). Figure 4.9(b) depicts the resultant yield surface under a biaxial stress state. This yield surface has a shape similar to that of the concrete smeared cracking model under a biaxial stress state, as shown in Figure 4.5(b).

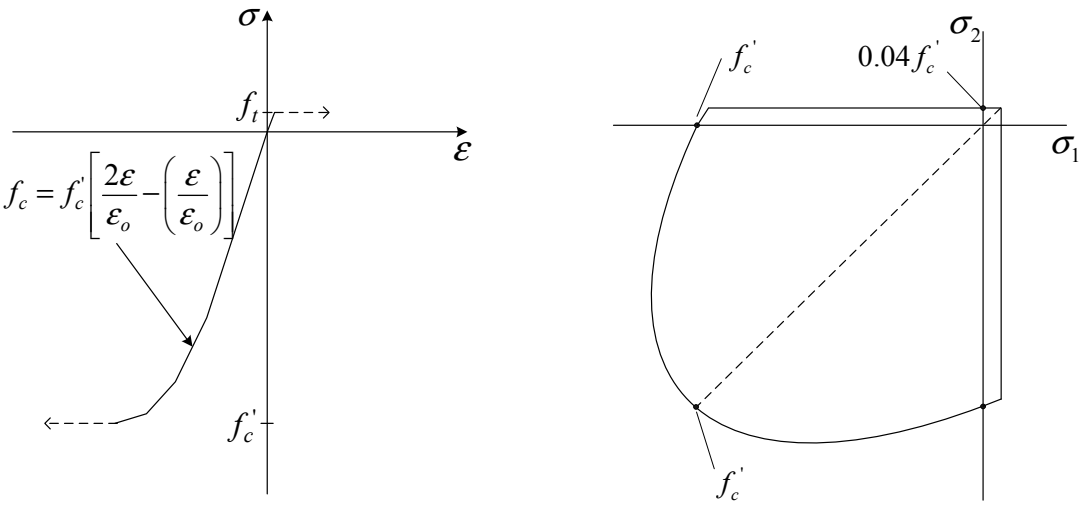


(a) Stress-strain behavior

(b) Yield surface
(under uniaxial force)

*Figure 4.9: Material behavior in cast iron plasticity model*

As mentioned previously in Section 4.3.3, the material parameters and the mesh density are important factors that can affect the computed finite element analysis results. With the cast iron plasticity model, the primary material parameters that define the yield surface are the compressive strength and the tensile strength. The assumed post-yielding behavior in both tension and compression is perfectly plastic, which is a less severe condition numerically than the strain softening of the concrete smeared cracking model. To determine an appropriate value for the tensile strength of this inelastic material model, finite element simulations of the small deck tests were conducted, and the deflection response of the simulations was compared with the test results. Figure 4.10 shows the simulated load-deflection behavior of the small deck models along with measured test data. The number of elements used in the simulation was 10 along the deck width and five across the deck thickness, and cracking was assumed to occur at 10% of the compressive strength for both concrete material models shown in the figure. As expected, because of the post-yielding stress-strain behavior, the deck model utilizing the cast iron plasticity model was stiffer than that of the concrete smeared cracking model.

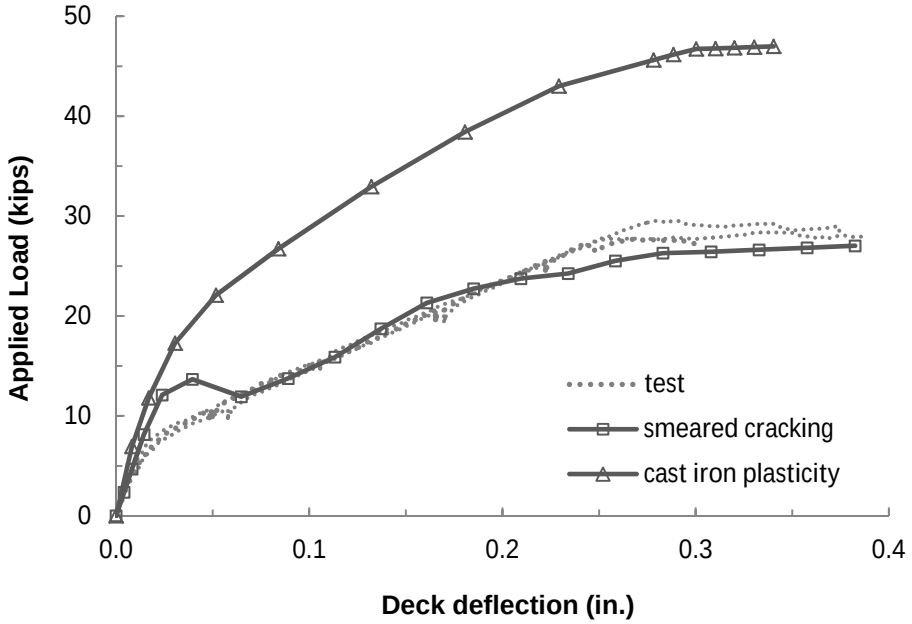


*Figure 4.10: Deflection behavior of small deck (cast iron plasticity)*

In order to match the measured deflection behavior of the small deck model using the cast iron plasticity material model, the tensile strength and the number of elements through the thickness were varied. Figure 4.11 shows the analysis results of a parametric evaluation that considers various concrete tensile strengths for models utilizing five elements through the thickness of the concrete deck. The investigated range of tensile strengths was 4% to 10% of the compressive strength: $0.04\,f_c'$, $0.06\,f_c'$, $0.08\,f_c'$, and $0.1\,f_c'$. Even with the tensile strength reduced to 4% of the compressive strength, the small deck finite element model showed a stiffer deflection response than the measured test results. Reducing the tensile strength further might have led to a better correlation between the measured and computed response, but too low a tensile strength increases the chances of numerical instability during the analysis. Furthermore, using too small a value outside a realistic range of potential material parameters is also not desirable. Therefore, it was decided to decrease the number of elements through the thickness of the small deck model from five to three because the bending stiffness of the deck model tended to decrease as the number of elements through the thickness diminished, as discussed in the small deck simulations with the concrete smeared cracking model.

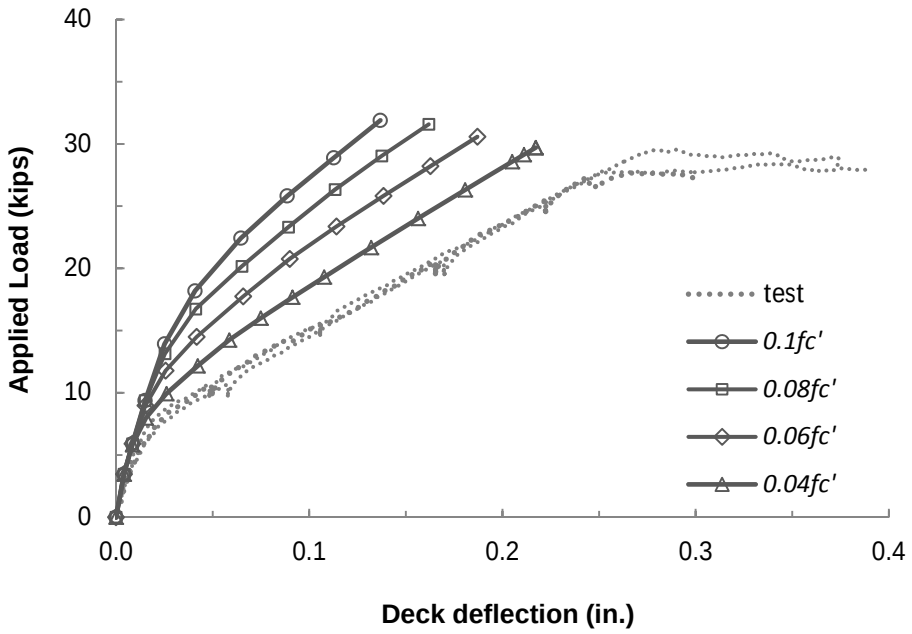


*Figure 4.11: Tensile strength effect on deck deflection response*

Using three elements through the thickness of the small deck finite element model, four different tensile strengths were considered for investigating the sensitivity of the computed results to this parameter. Rather than focusing entirely on the load-deflection response at individual points, absorbed energy (defined as the area under the load-deflection curve) was used to compare the computed results with the measured results (Figure 4.12). With this approach, while there may be slight variations in the localized behavior computed in the small deck model response, overall behavior would be considered to be in good agreement if the absorbed energy compared well between the tests and the simulations. For this particular study, a limiting deflection of 0.14 in. was used when computing the absorbed energy. This value was selected based on an analysis of the simulation results and the collected test data. Thus, it was felt that 0.14 in. of displacement was large enough to capture significant nonlinear behavior in the deflection response over a wide range of possible tensile strengths (Figure 4.11). In Figure 4.11, the initial large change in slope of the load-deflection curve occurs when the stresses in the elements at the bottom of the deck reach their tensile capacity as a result of bending in the specimen. Another slope change occurs when the loading is approximately equal to 30 kips (Figure 4.11), which is due to the breakout failure of concrete surrounding a shear stud. This phenomenon, however, was taken into account by the mechanical behavior of the connector elements that were incorporated into the model to represent a shear stud embedded into the deck through a haunch. Thus, for the purposes of evaluating the concrete model, a limiting deflection of 0.14 in. was selected so that the computed response, at least for the cases of tensile strength considered, would remain less than the breakout capacity of the shear studs in the model. A detailed discussion of the connector element behavior is presented below.

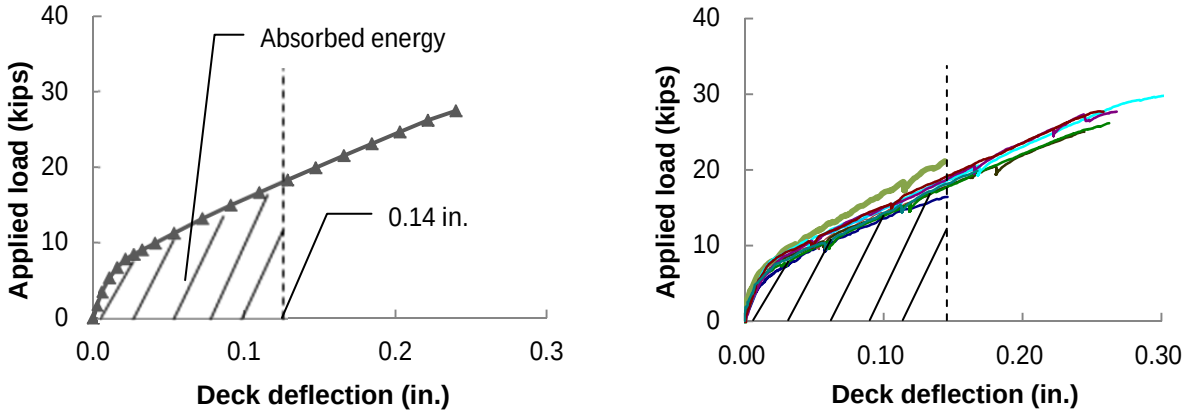


(a) Deck model with cast iron plasticity (b) Small deck test results

*Figure 4.12: Deck top deflection vs. tension force*

Figure 4.13 shows the differences in the absorbed energy between the finite element simulations and the experimental results. The differences in absorbed energy were normalized by the average absorbed energy obtained from the test data. When the tensile strength of the cast iron plasticity model was lowered to 4% of the compressive strength, the normalized energy difference between the simulation results and the test data became only 0.29%.

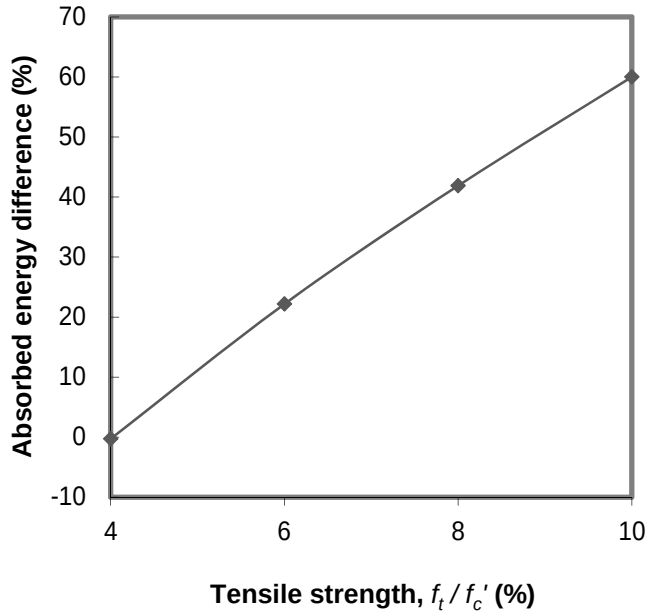


*Figure 4.13: Normalized energy difference between tests and FE analysis*

Figure 4.14 shows the deck deflection response of the small deck model using this tensile strength and the mesh density described above (i.e., only three elements through the thickness). Its general deflection response shows excellent agreement with the test results. Therefore, the tensile strength was assumed to be 4% of the compressive strength for the concrete material used in the finite element simulations, and this tensile strength was also used to construct full-scale bridge models. As stated previously, the small deck simulation results were affected not only by

material parameters such as the tensile strength but also by the mesh density of the model. Furthermore, the tensile strength and mesh density for the full-scale bridge model were selected based on the particular bending behavior observed in the damaged twin box-girder bridge tested during this research project. Therefore, the tensile strength and the mesh density selected for this research may not be suitable for other types of bridge slabs or concrete structures.

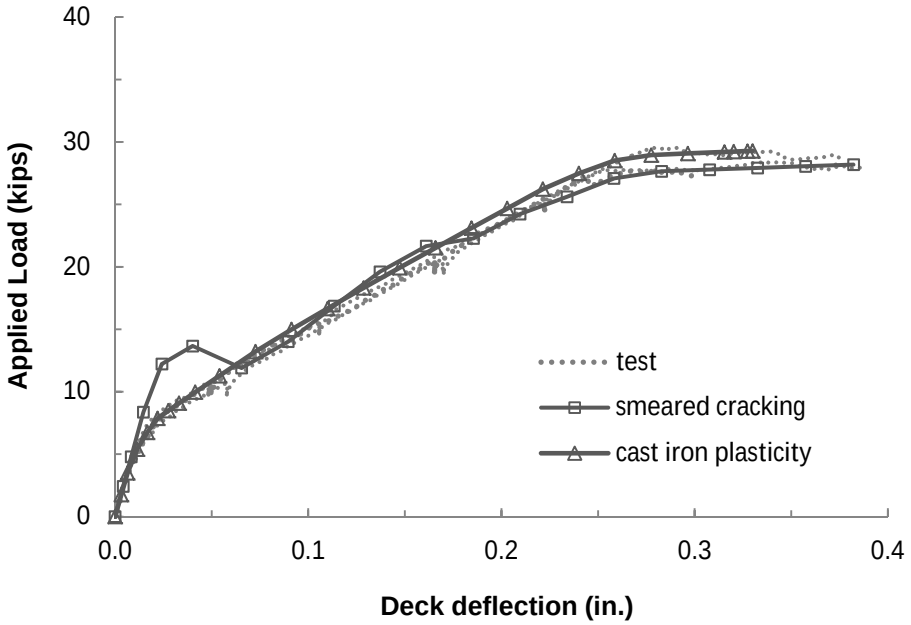


*Figure 4.14: Deflection behavior of calibrated cast iron plasticity deck model*

### 4.3.4 Shear Stud and Haunch

A haunch, as shown in Figure 4.2(b), is typically used in bridge construction to help maintain a uniform thickness of the concrete deck. One potential drawback with the use of a haunch, particularly as it relates to the current study, is that it can reduce the penetration length of a shear stud into the deck. Such reduced penetration of the stud could limit the available shear and tensile capacity of the connection between the concrete deck and the steel girders. For this reason, the AASHTO LRFD Specification (2007) requires that shear connectors penetrate at least 2 in. into the deck, and the TxDOT Bridge Detailing Manual (2001) limits the maximum haunch height to 3 in. when there is no reinforcement in the haunch region.

Shear studs installed on the top flange of a steel box girder provide a mechanical connection between the girders and the concrete deck for the primary benefit of transferring horizontal shear forces. The transfer of these shear forces leads to the development of composite action between the steel girders and the concrete deck. Chemical bonding and friction between the top flange of a girder and the deck might also provide limited load-transferring capability, but they were not considered in this study due to their limited strength and the uncertainty in computing their contributions. Therefore, only mechanical interaction between the shear studs and the concrete deck were considered in the finite element bridge models developed for this research project.

In the redundancy evaluation of a twin steel box-girder bridge, the assumed damage level was the full-depth fracture of one of the girders (i.e., fracture of the bottom flange and webs of one girder). Once the assumed damage was induced to the bridge finite element model, the shear studs could be required to carry significant tension forces due to the self-weight of the steel girder and the transverse bending of the concrete deck that results from the fracture. If the tension force in the studs becomes too large, it could cause a tensile failure to occur between the concrete deck and the steel box girders. Such a failure might be attributed to yielding of the stud or breakout of the concrete. Therefore, bridge models were constructed in such a way that connector elements imitating the stud connections could capture the tension failure behavior. Mechanical properties and failure mechanisms of the connector elements are detailed in the following paragraphs.

Shear Strength and Load-Slip Behavior

Topkaya (2002) investigated the ultimate shear strength and load-slip behavior of shear studs experimentally. Based on push-out tests, he proposed the ultimate shear strength $Q_u$ and the load-slip relationship $Q$ as follows:

$$Q_u = 2.5 A_{sc} \left( f_c' E_c \right)^{0.3} \qquad \text{Equation 4-3}$$

where

$A_{sc}$ = cross-sectional area of shear stud (in.$^2$)
$f_c'$ = concrete compressive strength (ksi)
$E_c$ = elastic modulus of concrete (ksi)

$$Q = Q_d \frac{3\left(\frac{\Delta}{0.03}\right)}{1+2\left(\frac{\Delta}{0.03}\right)} \qquad \text{Equation 4-4}$$

where

$\Delta$ = slip of shear stud (in.)
$Q_d$ = shear load at 0.03 in. displacement (kip)

$Q_d$ is defined as the shear load where the shear displacement becomes 0.03 in., and the suggested empirical equation is as follows:

$$Q_d = 1.75 A_{sc} \left( f_c' E_c \right)^{0.3} \qquad \text{Equation 4-5}$$

In the full-scale test bridge, three 5-in. long and 7/8-in. diameter shear studs were installed in a row transversely on the girder top flanges. For simplicity, the three studs were modeled with a single connector element to represent the group. For example, the compressive strength of concrete used in the second and third bridge test simulations was 6.23 ksi. The modulus of elasticity of concrete for this case is 4,499 ksi (Equation 4-6), which is based on the guidelines in ACI Section 8.5.1 (ACI318-08 Appendix D).

$$E_c = 57000\sqrt{f_c'} \qquad \text{Equation 4-6}$$

Equation 4-6 is empirically based, and the values of $E_c$ and $f_c'$ must be specified in psi.

Because the shear stud diameter was 7/8 in. and three studs were grouped as one connector element, the total area of shear studs is 1.325 in.$^2$, and the ultimate strength is 97.38 kips according to Equation 4-3. According to Equation 4-5, $Q_d$ is 68.16 kips. Inserting this value into Equation 4-4, the shear load-slip relationship can be obtained, and it is plotted in Figure 4.15. Beyond 0.3 in. displacement, where the maximum shear strength is reached, perfectly plastic behavior was assumed in this study. This shear load-slip relationship was utilized to define the horizontal response of connector elements used to represent shear studs at the interface between the steel flanges and the concrete deck.

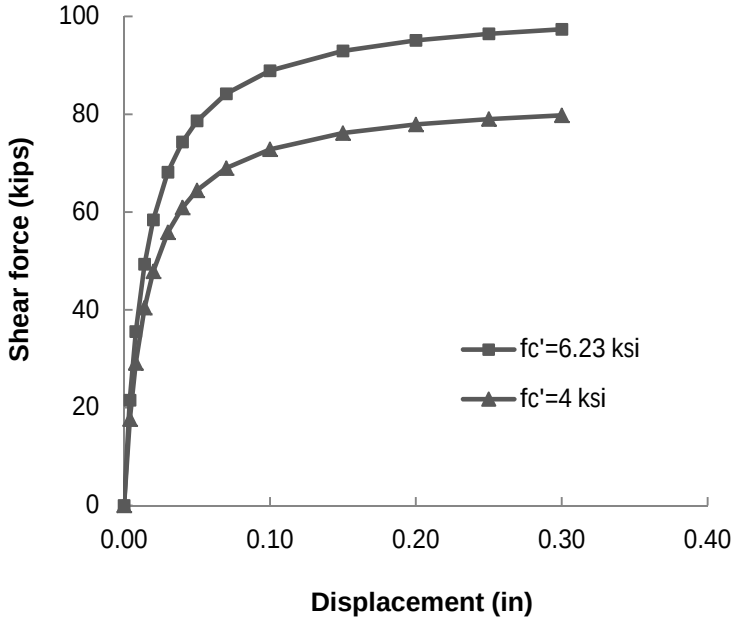


*Figure 4.15: Shear force vs. stud slip*

Pull-Out Strength and Load-Deflection Behavior

Sutton (2007) and Mouras (2008) studied the pull-out strength of shear studs embedded in concrete decks. As described in the previous section, they used small deck specimens that were capable of representing transverse bending of a concrete bridge deck between points of inflection. According to their test results, all specimens failed through concrete breakout (i.e., yielding of shear studs was not observed). The pull-out strength varied depending on the presence of a haunch, the length of shear studs, the number of shear studs, and the arrangement of shear studs (i.e., longitudinally or transversely oriented). To quantify the pull-out strength of shear studs embedded in a reinforced concrete deck, they used an ACI equation (ACI318-08 Appendix D) developed for anchor strength. In the case of specimens with a haunch, the ACI equation predicted pull-out strengths that did not agree well with the measured test data. The variation in measured and predicted values was attributed to the presence of a haunch in some specimens, which is not accounted for in the ACI equation. To account for the haunch effect on the pull-out strength of shear stud connections, Mouras (2008) proposed the following modifications to the ACI equation:

$$N_{cbg} = \frac{A_{Nc}}{A_{Nco}} \psi_{g,N} \psi_{ec,N} \psi_{ed,N} \psi_{c,N} N_b \qquad \text{Equation 4-7}$$

$$N_b = k_c \sqrt{f_c'} h_{ef}'^{1.5} \qquad \text{Equation 4-8}$$

$$h_{ef}' = h_{ef} - h_h \geq \frac{w_h}{3} \qquad \text{Equation 4-9}$$

$$\psi_{ed,N} = 0.7 + 0.3 \frac{c_{a,\min}}{1.5 h_{ef}'} \leq 1.0 \qquad \text{Equation 4-10}$$

$$\psi_{ec,N} = \frac{1}{\left(1 + \frac{2e_N'}{3h_{ef}'}\right)} \qquad \text{Equation 4-11}$$

where

$N_{cbg}$ = design concrete breakout strength of a stud or group of studs (lb)
$A_{Nc}$ = projected concrete cone failure area of a stud group (in.$^2$)
$A_{Nco}$ = projected concrete cone failure area of a single stud (= 9 $h_{ef}^2$) (in.$^2$)
$\psi_{g,N}$ = group effect modification factor
1 stud : 1.00
2 studs spaced transversely : 0.95
3 studs spaced transversely : 0.90
Stud spaced longitudinally : 0.80
$\psi_{ec,N}$ = eccentric load modification factor
$\psi_{ed,N}$ = edge distance modification factor (when $c_{a,min} \leq 1.5 h_{ef}'$)
$\psi_{c,N}$ = cracked concrete modification factor
Cracked concrete with a stud installed : 1.00
Uncracked concrete : 1.25
$N_b$ = concrete breakout strength of a single isolated stud (lb)
$k_c$ = 24 (cast-in-place shear studs)
$h_{ef}'$ = effective height, excluding the haunch height (in.)
$h_{ef}$ = effective stud height under the stud head (in.)
$h_h$ = haunch height (in.)
$w_h$ = width of haunch in the cross-section of a bridge span (in.)
$c_{a,min}$ = smallest edge distance measured from center of stud to the edge of concrete (in.)
$e_N'$ = eccentricity of resultant stud tensile load

In addition to the maximum pull-out strength of shear stud connections, load-deformation data are needed to define the vertical behavior of connector elements under tension forces. Figure 4.16 shows a typical load-displacement response of shear studs in tension. The applied load in the load-displacement response is linearly proportional to the displacement until it reaches the pull-out strength. Beyond the pull-out strength, the load quickly drops because of a

brittle concrete cone failure. For simplicity, two lines were used to simulate the load-displacement response for the vertical behavior of the connector elements. The two lines were constructed using the displacement $U_m$ corresponding to the pull-out strength and the displacement corresponding to failure. The maximum or failure displacement was selected to be 12 times $U_m$ to match the measured test data and to ensure a smooth change of the deflection curve so as to avoid a numerical divergence problem in the finite element analyses.

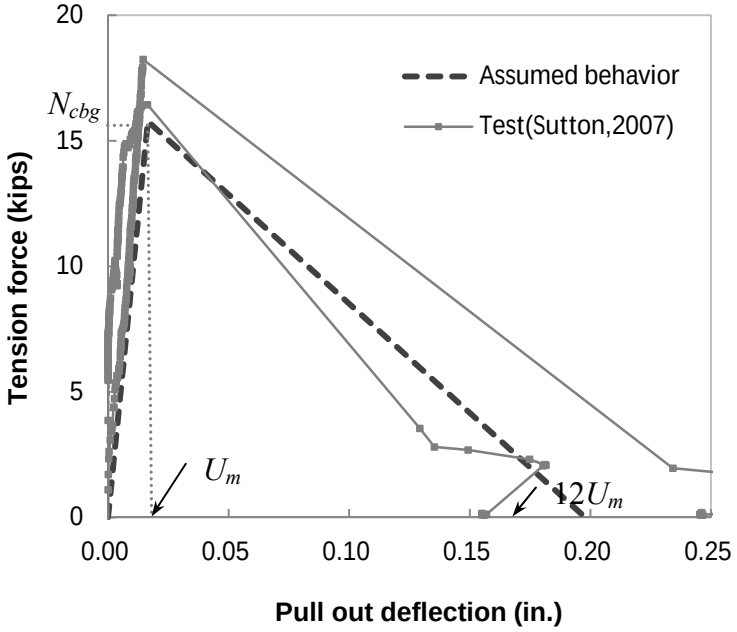


*Figure 4.16: Tension force vs. stud pull-out deflection*

To determine the value of $U_m$, a regression analysis of the data was conducted using the test results of Sutton (2007) and Mouras (2008). As shown in Figure 4.17, the displacement $U_m$ tends to increase as the effective stud height, normalized by the bridge deck thickness ($h_d$), increases.

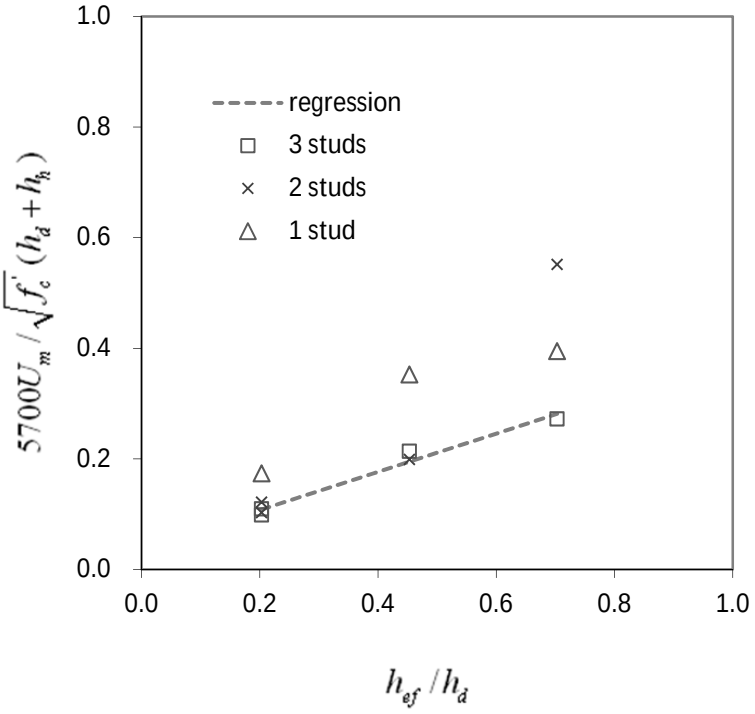


*Figure 4.17: Displacement at pull-out strength*

The figure also shows some scatter depending on the number of studs installed in a row. Although the dependency of $U_m$ on the number studs in a row is not clear because of the limited amount of data available, specimens containing two studs in a row or one stud show higher deformation at the pull-out strength than specimens with three studs. In this study, all bridges investigated—including the full-scale test bridge—had three studs in a row. Therefore, to reduce the uncertainty in the selection of $U_m$, the cases with two studs in a row or one stud were excluded from the regression analysis, and only cases with three studs were used to construct Equation 4-12.

$$U_m = \frac{\sqrt{f_c'}\,h_{dh}}{5700}\psi_{h,U} \qquad \text{Equation 4-12}$$

$$\psi_{h,U} = 0.038 + 0.346\frac{h_{ef}'}{h_d} \qquad \text{Equation 4-13}$$

where

$U_m$ = relative displacement at pull-out strength (in.)
$\psi_{h,U}$ = haunch height effect modification factor
$h_d$ = deck height (in.)
$h_{dh}$ = deck height including haunch (in.)

Shear Strength Degradation by Stud Pull-Out Failure

Based on results from stud pull-out tests, embedded shear studs in a reinforced concrete deck fail in tension due to the formation of a concrete breakout cone in a zone surrounding the studs. In cases where a haunch is present and the studs are not deeply embedded, which is consistent with the full-scale bridge tested at FSEL as part of this research project, failure is associated with the haunch breaking off from the deck. This mode of failure governs the pull-out strength of the stud connection. After stud pull-out failure occurs, there is clearly no longer any shear resistance mechanism because the studs are completely embedded in the haunch that is no longer connected to the deck. This observation suggests that the shear resistance should be interrelated with the tensile failure of the studs. To achieve this relationship, a linear damage model was applied to the shear resistance of the connector elements. According to the applied linear damage model, a reduction in the shear resistance of the connector elements is initiated when the vertical tension force exceeds the pull-out strength. After damage initiation, damage is assumed to evolve linearly, which reduces the shear resistance of the studs as deformation increases. Eventually, there is a complete loss of resistance as shown schematically in Figure 4.18.

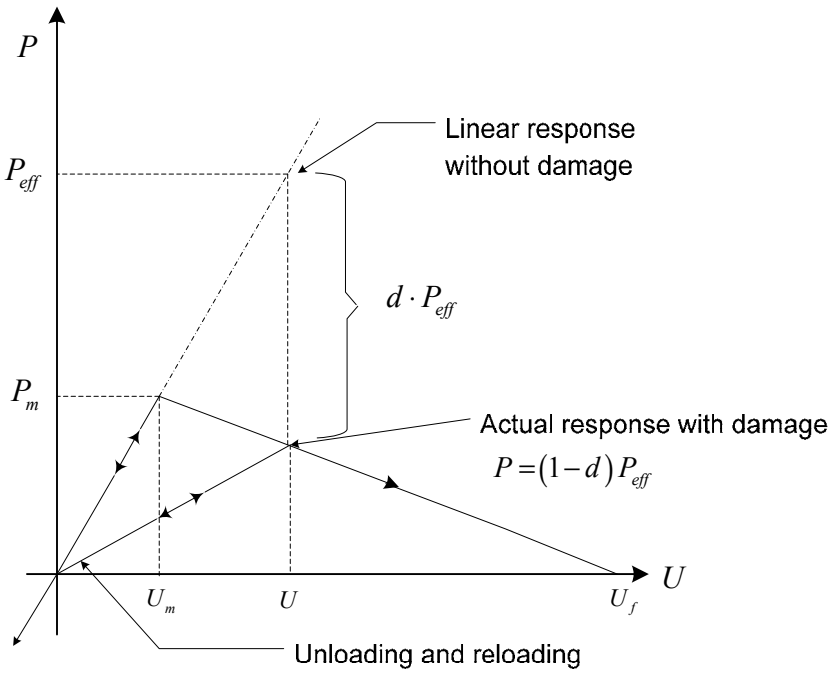


*Figure 4.18: Damage initiation and evolution mechanism (Dassault Systemes, 2007a)*

To investigate the behavior of a single connector element with the assumed linear damage model under combined shear and tensile loading, the same displacement magnitudes were applied transversely (for shear) and vertically (for tension), both acting on one end node of a connector element. Although a linear damage evolution was assumed for the shear resistance, Figure 4.19 shows a nonlinear load-deflection response in the shear load-slip behavior. This response is due to the nonlinear plasticity hardening rule of the shear studs, which was presented in the previous section.

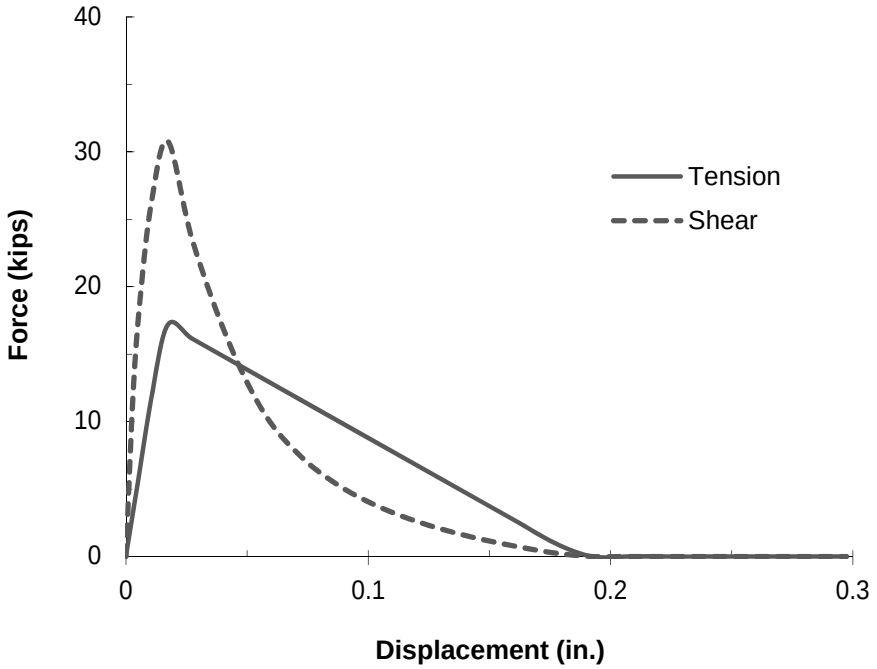


*Figure 4.19: Single connector element behavior under tension and shear forces*

*Railing Interaction*

Under normal loading conditions, a reinforced concrete bridge rail is not considered to be a structural component when analyzing the response of a bridge because it has gaps for expansion joints. The primary function of a railing is to provide safety for vehicles on a bridge. When a bridge is subjected to large deflections due to severe damage, however, railing gaps may close. Once such gaps close, the railing may be able to carry significant forces in the longitudinal direction of a bridge. This situation is similar to having a deep beam at the edges of the bridge.

In this study, a simplified modeling approach was used to account for the possibility of the engagement of rail sections. Rather than performing a direct contact analysis, nonlinear springs in expansion joint gaps were used. For a direct contact analysis, a refined mesh density is needed at contact surfaces in order to obtain suitably accurate results, and convergence problems frequently arise when the analysis includes nonlinear material properties (Dassault Systemes, 2007a). In modeling a full-scale bridge, significant effort and computational resources are needed to create a finite element model with appropriate mesh refinement in regions where contact can occur. Furthermore, convergence problems associated with small contact regions can lead to excessively long run times and potentially prevent an analysis from running to completion due to convergence issues. For these reasons, spring elements inserted between rails were used to simulate the potential railing engagement though expansion joints. Once rails engage, it is possible that limited shear forces may be transferred due to friction, but this effect was ignored in the finite element models developed for this research. It was assumed that spring elements in expansion joint gaps transferred only normal forces.

Before the gaps in the railings become completely closed, no normal forces should develop in the spring elements. This behavior is captured in the spring load-deflection behavior shown in Figure 4.20. This figure shows that the spring elements resist only compression forces

once the deflection exceeds 3/4 in., which was the initial gap distance of the rails in the test bridge and the value specified by TxDOT. Beyond the 3/4-in. deflection, a stiffness that was 100 times greater than the concrete stiffness was assumed for the spring element to simulate railing contact. The specific stiffness value is not very important, but it must be large enough to cause a large increase in force; however, it must not be so large as to lead to numerical inaccuracies in the conditioning of the structural stiffness matrix. The value selected provided reasonable results, and the computed response was not very sensitive to variations in the selected stiffness value.

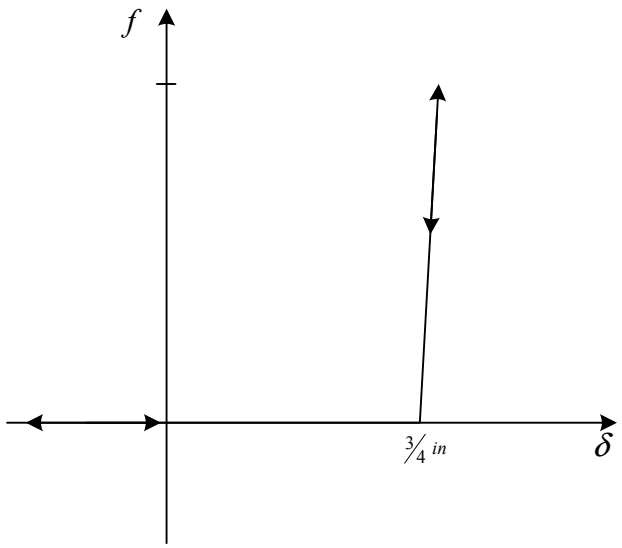


*Figure 4.20: Spring element behavior between rails*

In the following chapter, modeling procedures to represent the full-scale bridge tested at FSEL as part of this research project are introduced. The computed results are compared with measured test data to verify the validity of the modeling approach developed for this study.

# Chapter 5. Finite Element Modeling Techniques for Evaluating Bridge Redundancy Applied to the FSEL Test Bridge

## 5.1 Introduction

As described previously in this report, the full-scale bridge that was used in the experimental testing program (Figure 5.1) had been in service as an HOV lane near the intersection of Interstate IH 10 and Loop 610 in Houston prior to being reconstructed at the University of Texas, and thus it is representative of steel box-girder bridges used throughout the state of Texas. In total, three separate tests were performed on the full-scale bridge. Below, a brief overview of the testing program is given. Detailed information describing each of the tests and the measured data that were collected are available in Neuman (2009). The purpose of the first bridge fracture test was to investigate how the sudden loss of the bottom flange of one girder in the bridge affected bridge performance. A rapid failure of the bottom flange of the exterior girder, which simulates what is expected to occur during a fracture event, was achieved using a linear-shape-charge explosive to cut through the complete width of the bottom flange at the midspan. The second test was conducted to determine whether the bridge could sustain the sudden potential energy release of a specified live load and the bridge self-weight in a damaged condition (bottom flange and 83% web removal of exterior girder). For the rapid release of the loads, a temporary truss support was placed in a prearranged location beneath the bridge's bottom flange, and then the web was cut with a torch from the bottom flange to a point about 10 in. below the top flange. The temporary truss support was designed to rapidly release the load it was carrying by severing a tension tie using an explosive in a similar fashion as the first test. The third test was performed to investigate the reserve load-carrying capacity of the damaged bridge and the contributions made by individual bridge components to the overall capacity of the system. To apply loads incrementally in the experiment, road base was placed on the deck along with concrete blocks. Loading continued until the bridge collapsed.

*Figure 5.1: Full-scale test bridge*

## 5.2 First Bridge Test (Bottom Flange Removal)

### 5.2.1 Test Procedure

The first bridge test was performed to investigate how the bridge would respond when the bottom flange of one girder suddenly fails as might be expected if a fracture were to occur. The bottom flange is currently classified as a fracture-critical member in the two-girder bridge system. An explosive was used to cut the bottom flange extremely rapidly to simulate the sudden loss of the whole bottom flange of one girder (east side girder) at the midspan as shown in Figure 5.2. For safety purposes, the explosive was encased in a blast shield, which was attached underneath the bottom flange of the east girder and tethered to a concrete block placed under the bridge. Concrete blocks intended to simulate the AASHTO standard HS-20 design truck load were placed on the deck such that those blocks caused a maximum positive bending moment on the damaged location. Detailed descriptions of the bridge test setup and the results that were collected have been reported by Neuman (2009).


*Figure 5.2: 1st bridge fracture test (bottom flange removal by explosion)*

### 5.2.2 Simulation Procedure

The finite element simulation procedure for modeling the response of this bridge fracture test can be divided into three main analysis categories: bridge construction, load application, and simulation of bottom flange fracture, as shown in Table 5.1. The analysis steps in the bridge construction category are intended to incorporate loading histories through the erection and construction process in which the deck acts non-compositely with the girders. For the first analysis step, all of the deck, railing, and rebar elements—except girder elements—were deactivated to simulate the non-composite section behavior of the bridge. During bridge construction, only the steel box girders resisted the deck and railing weight before the concrete deck hardened. Therefore, deck and railing elements were removed using the element deactivation technique in ABAQUS/Standard v6.7 to simulate non-composite section response because the deactivated elements have no effect on the mass and the stiffness of the system. After deactivating these elements, equivalent pressure loads for the self-weight of the deck and railing were evenly applied on the girder top flanges. As a result, the applied loads on the girder top flanges were resisted only by the steel girders.

The deactivated elements maintain their initial node locations when they are deactivated. The node locations of deck and railing elements need to be shifted, however, so that they deform consistently with the girders because uncured concrete flows freely before it is hardened. For this reason, dummy elements for the deck and railing were used to follow such node location shifts. The dummy elements shared the same nodes with the original deck and railing elements, but they had very low stiffness ($10^{-4}$ × concrete stiffness) and were almost without mass ($10^{-9}$ × concrete density) so as not to affect the bridge stiffness and weight. As a result, because the original deck and railing elements were deactivated and an equivalent pressure load was applied to the top flanges of the girders, the deck and railing nodes deformed freely, following the girder deflection due to the dummy elements. After this procedure, the deck and railing elements were reactivated, without strain changes, in the deformed position to simulate the hardened concrete, and the equivalent pressure load was removed.

**Table 5.1: Simulation procedures for first bridge fracture test**

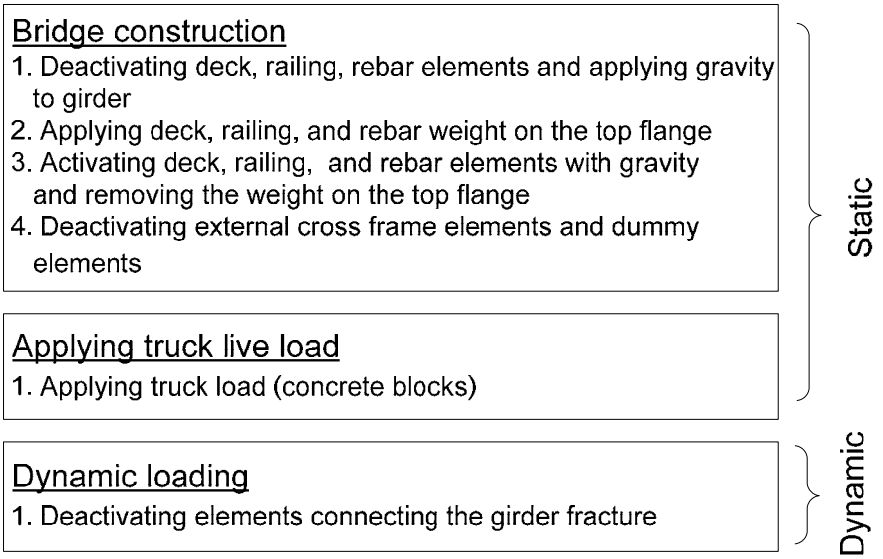


The truck live load, simulated using concrete blocks in the bridge test, was applied to the top nodes of the deck using concentrated loads in the finite element model. These concentrated loads had the same axle spacing as the concrete blocks used during the test. For the bottom flange cutting, the fracture path was predefined on the bottom flange of the east girder, as shown in Figure 5.3. The selected damage location was at the midspan because this location is where the maximum positive bending moment is caused by a moving vehicle in a simply supported bridge. Shell elements adjoining the predefined fracture path shared duplicate nodes. These independent nodes were initially joined by connector elements (CONN3D2) with welding properties to mimic the intact condition of the bottom flange. The cutting of the bottom flange was simulated, therefore, by just removing the connector elements using the element deactivation technique. The removal of the connector elements was sudden, as was the explosive damage inflicted during the first bridge fracture test. Computationally, this step was carried out using a transient dynamic analysis with a "step-amplitude" loading in ABAQUS/Standard v6.7.

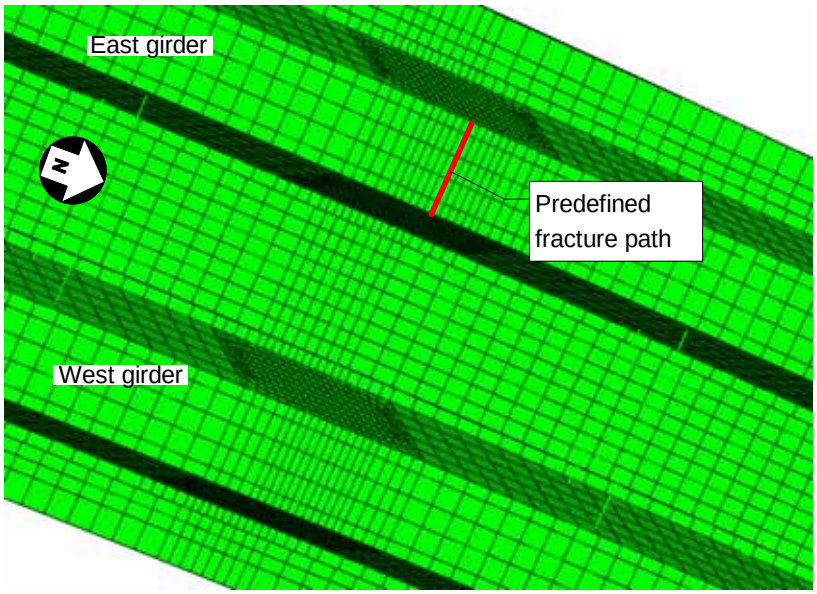


*Figure 5.3: Predefined bottom flange fracture path (looking upward from underneath bridge)*

### 5.2.3 Bridge Test and Simulation Results

After the first bridge fracture test, it was observed that the bottom flange was severed completely along its width and through its depth. The fracture, however, did not propagate into the webs as shown in Figure 5.4. Despite the bottom flange fracture of one girder, the test bridge did not show any significant damage, and the resultant girder deflections were very small.

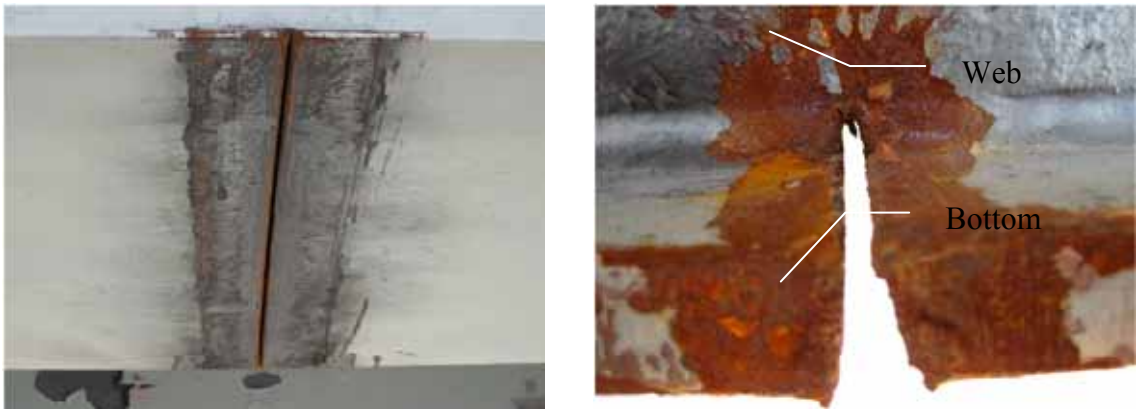


Full cut of the bottom flange  Detained fracture at web

*Figure 5.4: Bottom flange cut of fractured girder*

Figure 5.5 shows the relative girder deflection changes of the west girder (WG) and the east girder (EG) before and after the bottom flange was severed with the explosive. Data shown in this figure are based on the static deflection that resulted after the girder came to rest. Thus, the values do not show the peak dynamic deflection that occurred shortly after the fracture was induced. The girder deflections were measured using a laser level having ±1/16 in. accuracy. The baseline of the deflection measurements was the deformed position of the steel box girders

before the concrete deck cured. Therefore, the deflection due to the self-weight of the steel box girders was excluded in the relative deflection measurement. In Figure 5.5, the deflection of the east girder is larger than that of the west girder because the applied concrete block loads (used to simulate an HS-20 truck) were biased transversely toward the east girder to create the worst-case loading scenario on the fractured girder (Neuman, 2009).

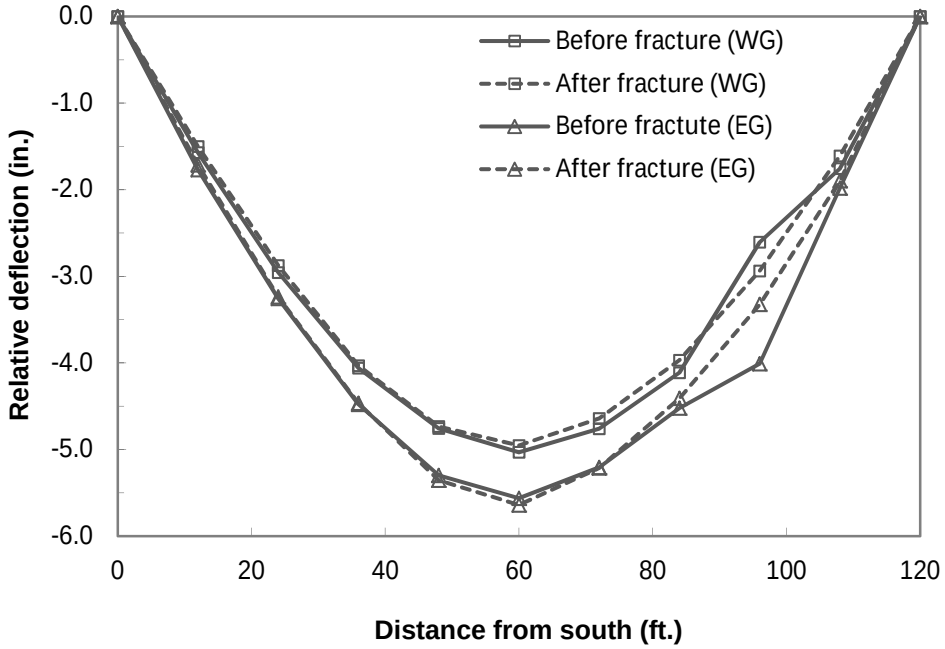


*Figure 5.5: Relative deflection of intact and fractured girder*

According to the surveyed data, the east girder deflected downward 5.56 in. at its midspan (relative to the baseline) when the concrete blocks were loaded and before the bottom flange fracture occurred. The resulting additional deflection of the east girder was only 0.08 in. after its bottom flange was fractured. This result is inconclusive, however, as it is within the specified accuracy of the laser level. Moreover, the deflection surveys were conducted on different days and at different times, which could mean that different environmental conditions affected the bridge deflection (i.e., temperature gradient change could affect the bridge deflection measurements). Therefore, the measured additional deflection might not be caused solely by the bottom flange fracture of the east girder. Nonetheless, the measured deflections and post-test observations of the bridge indicate that the fracture of the bottom flange of the exterior girder caused limited damage to the overall load-carrying capacity of the bridge.

The finite element simulations gave girder deflections that were similar to those obtained from the surveyed data. Figure 5.6 compares the measured deflections of the fractured girder with those predicted by the finite element model following the fracture of the bottom flange. The predicted deflection at the midspan by the finite element model was 5.23 in., which was slightly less than the measured deflection of 5.64 in. Considering the accuracy of the laser level and the possibility for environmental conditions to affect the measured deflections, however, the prediction by the finite element model was considered to be acceptable.

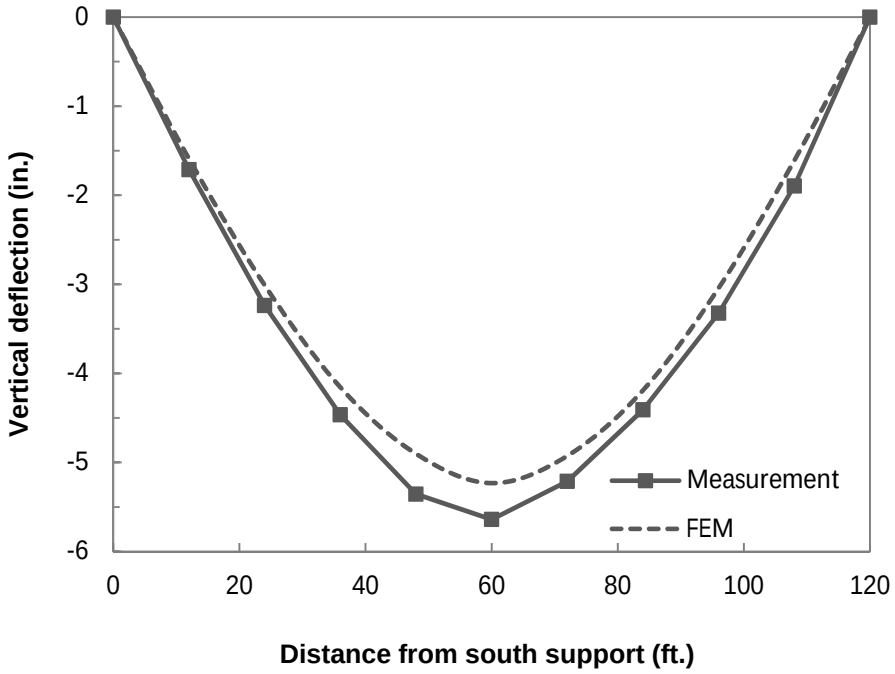


*Figure 5.6: Relative deflection of fractured girder after bottom flange removal*

## 5.3 Second Bridge Test (Bottom Flange and Web Removal)

### 5.3.1 Test Procedure

The purpose of the second bridge test was to investigate whether or not the FSEL bridge could sustain a simulated dynamic loading following a nearly full-depth fracture of the exterior girder. For the test setup, the fracture in the bottom flange from the first bridge test was manually extended up the height of the web using an acetylene torch. In order to apply the additional web damage without the loss of the gravitational potential energy of the bridge, temporary truss supports were installed under the fractured girder prior to the cutting of the webs. Figure 5.7 shows the condition of the bridge after the webs had been cut.

After inducing the additional web damage, concrete blocks were placed on the top of wooden blocks on the deck to represent truck axles. The concrete blocks were intended to simulate the AASHTO HS-20 truck load, but it had a slightly different total weight—4 kips higher than the HS-20 truck. Figure 5.8 shows a schematic of the concrete block loading configuration used in the second bridge fracture test. The assumed spacing of axles was 14 ft, and the middle axle was positioned at the midspan to cause the maximum vertical bending moment at the fracture location. The transverse location of the concrete blocks was biased toward the east girder side so that the axle (wooden block) corners were placed 2 ft away from the east railing. This configuration was intended to simulate the worst-case loading condition that could be achieved by a single truck on the test bridge.


(a) Second bridge test setup


(b) Manually extended cut to webs

*Figure 5.7: Temporary support and web cutting*

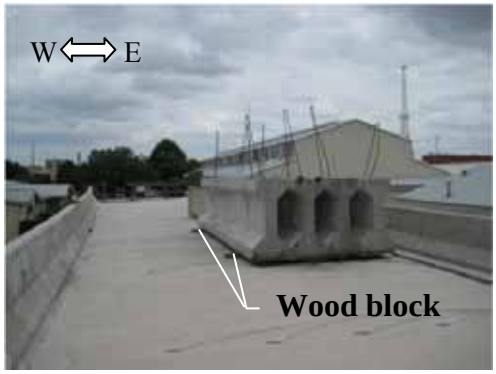


*Figure 5.8: Simulated live truck load configuration (AASHTO HS-20)*

For the second bridge fracture test, the temporary truss supports were designed so that they could collapse nearly instantaneously without interfering with the response of the bridge as it deflected downward. The temporary truss supports designed by Neuman (2009) satisfied these requirements successfully. They became structurally unstable once horizontal ties, as shown in Figure 5.9, were severed by explosive contact charges, and they quickly dropped down before the bridge girder deflected. This behavior was clearly observed in the high-speed video recording of the test; captured still images from the high-speed video are shown in Figure 5.10.

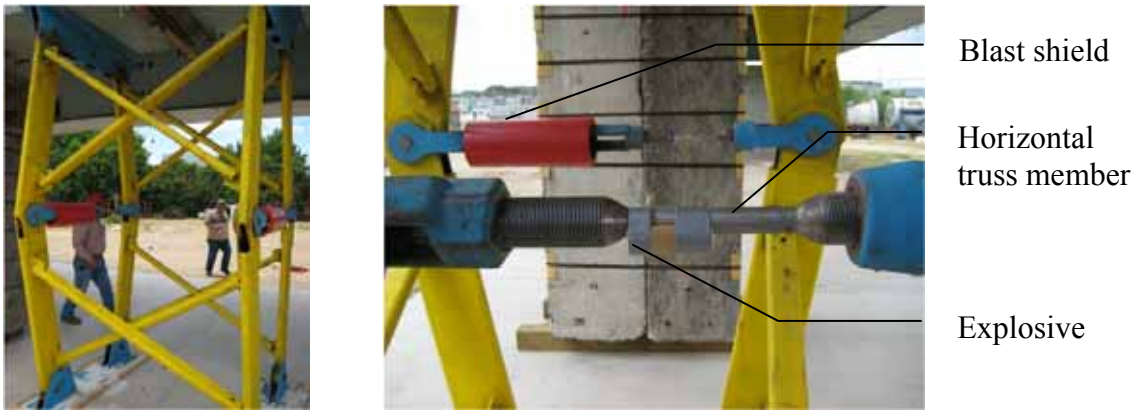


*Figure 5.9: Temporary truss support and explosive setup*

*Figure 5.10: Second bridge fracture test (bottom flange and web removal)*

### 5.3.2 Simulation Procedure

To simulate the damage and loading scenario used in the second full-scale bridge fracture test, the finite element analysis followed procedures similar to those in the first bridge test. The finite element simulation of the second bridge test was composed of three major analysis steps, as described in Table 5.2: bridge construction, applying temporary boundary conditions and girder damage, and removing the temporary boundary conditions.

**Table 5.2: Simulation procedures for second bridge fracture test**

| | |
|---|---|
| Bridge construction<br>1. Deactivating deck, railing, rebar elements and applying gravity to girder<br>2. Applying deck, railing, and rebar weight on the top flange<br>3. Activating deck, railing, and rebar elements with gravity and removing the weight on the top flange<br>4. Deactivating external cross frame elements and dummy elements | Static |
| Applying B.C. and girder fracture<br>1. Applying temporary boundary condition<br>2. Deactivating elements connecting the girder fracture<br>3. Applying truck load (concrete blocks) | |
| Dynamic loading<br>1. Removing temporary boundary condition suddenly | Dynamic |

The bridge construction step was used to incorporate loading histories associated with non-composite behavior before casting the concrete deck, as discussed in the first bridge fracture test simulation procedure. For the next step, temporary boundary conditions were applied to the bottom flange, spanning 5 ft and centered on the midspan of the east girder where the temporary truss supports were placed. The temporary boundaries constrained the vertical translation of the east girder while the bottom flange damage, the web damage, and the simulated truck live load were applied to the simulation model. To incorporate damage on the east girder, connector elements initially binding separated nodes along a predefined fracture path were deactivated. The predefined fracture path and temporary boundaries under the bottom flange are shown in Figure 5.11. The truck live load represented by the concrete blocks in the bridge test was simulated with concentrated forces acting on the bridge deck.

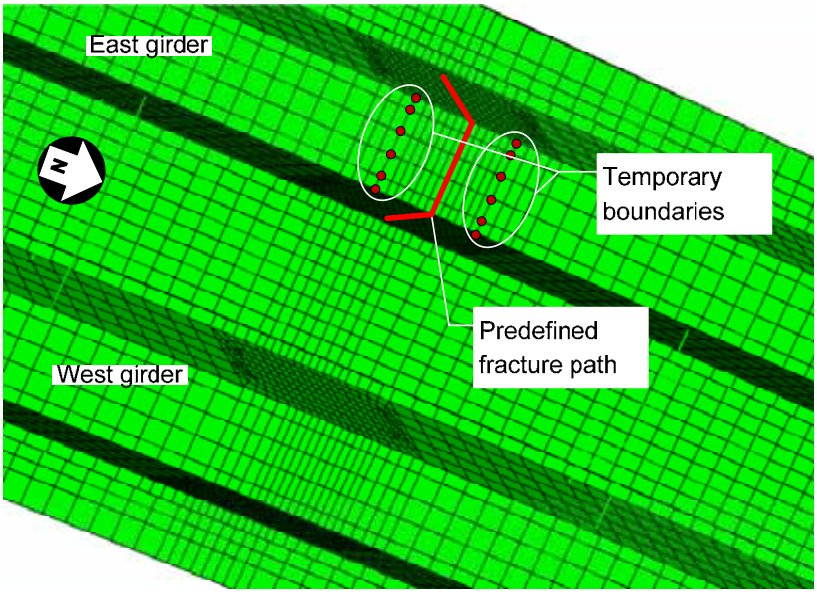


*Figure 5.11: Predefined fracture path in east girder (looking upward from underneath bridge)*

After the loading step of the truck live load, the temporary boundaries were eliminated to simulate the sudden removal of the temporary truss supports in the bridge fracture test. To computationally achieve dynamic loading effects caused by the abrupt removal of the temporary supports, a transient dynamic analysis was conducted with a step amplitude loading condition.

### 5.3.3 Bridge Test and Simulation Results

After the second bridge fracture test, visual inspections were conducted to investigate the overall condition of the bridge. During the initial inspections, the only damage observed included tensile cracks on the deck and crushed cover concrete on the top of the east railing at the midspan. Analytical models of the deck response (Samaras, 2009) and finite element simulations, however, predicted that extensive stud pull-out failures would occur along the inside of the fractured girder. For this reason, the corrugated metal deck spanning between the girders and used as formwork during the construction of the deck was removed to inspect the stud connections closely, and it revealed that a large amount of haunch separation along the inside of the fractured girder had in fact occurred (Figure 5.12(a)). Along the outside of the fractured girder, both longitudinal and diagonal cracks were observed where the studs connected with the concrete deck, as shown in Figure 5.12(b). These cracks developed near the midspan. As indicated by the figure, haunch separation on the inside of the girder was more severe than on the outside.

In the test bridge, haunch separation was initiated by stud pull-out failure near the midspan of the bridge. As the pull-out failures propagated along the bridge span, the haunch started to separate from the concrete deck above the fractured girder. Figure 5.13 shows the predicted length of haunch separation along the inside of the fractured girder (FG-In) and along the outside (FG-Out); the figure also shows the measured haunch separation along the inside of the fractured girder. A comparison of the results indicates that the finite element model over-predicted the separation length along the inside of the fractured girder—96 ft predicted compared to 67 ft measured. Along the outside of the fractured girder near the midspan, cracking in the

haunch spanned 14 ft, but the cracking pattern was irregular, as shown in Figure 5.12(b) (i.e., diagonal and longitudinal cracks were both observed). This cracking pattern suggests that the outside haunch failed due to a combination of tension and shear. Because the degree to which haunch separation occurred along the outside of the fractured girder could not be accurately measured, only the simulation model prediction is included in Figure 5.13; the predicted separation length was 32 ft.

(a) (b)

*Figure 5.12: Haunch separation of fractured girder*

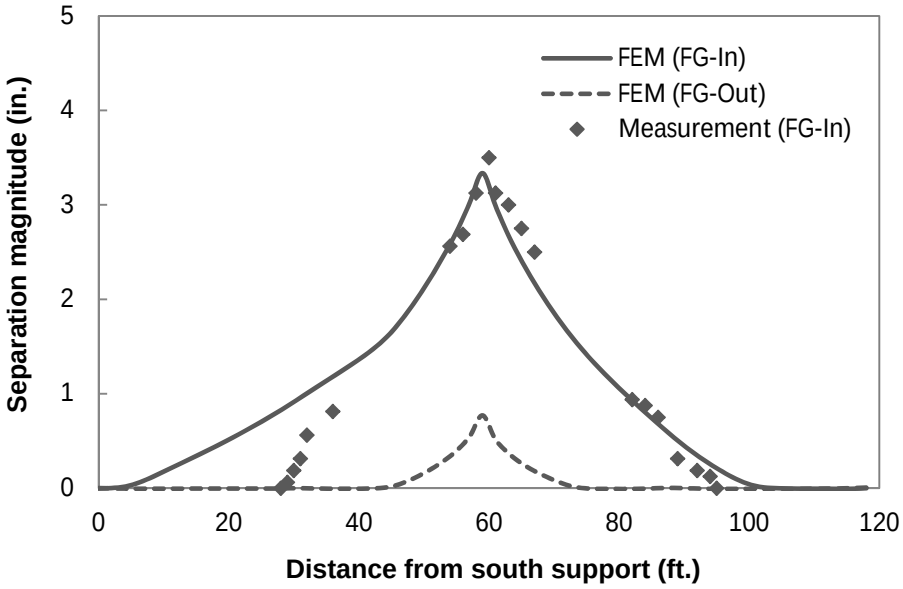


*Figure 5.13: Haunch separation along bridge span*

Concerning the over-prediction of the haunch separation length, there are various possible reasons: haunch slope, participation of the metal deck, dynamic effects on material strength, and potentially others. In the test bridge, the edge of the haunch was sloped transversely due to the corrugated metal stay-in-place forms used to construct the deck (Figure 5.14). The

presence of such a haunch slope could change the stud pull-out strength because it reduces the concrete breakout cone size less than does a haunch with right angles. The test data used to define the stud pull-out strength was based on tests with haunches constructed with vertical sides (Mouras, 2008). The strain rate of the dynamic loading could also affect the stud pull-out strength because material strength is affected by the loading rate. Figure 5.15 shows the variation in stud pull-out strength as a function of the loading rate based on tests conducted by Mouras (2008). According to the test results, when the strain rate reached 30.67 in./in./msec.—the maximum obtained during the testing program—the pull-out strength increased by about 40% over the static test results. The finite element simulation model, however, did not consider such an increase in pull-out strength caused by the high strain rate; for simplicity and due to a lack of data, constitutive models used in the finite element simulations were not strain-rate dependent.

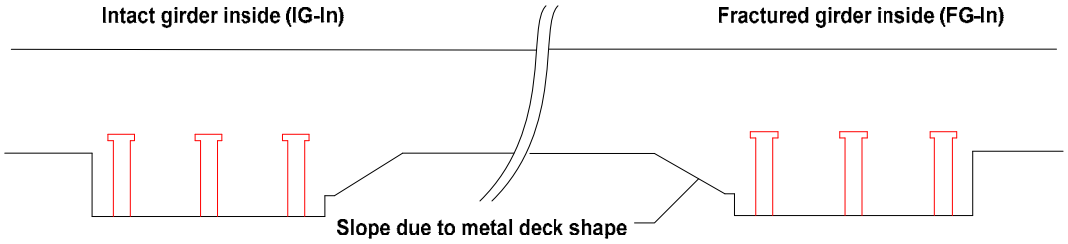


*Figure 5.14: Haunch slope in cross-sectional plane*

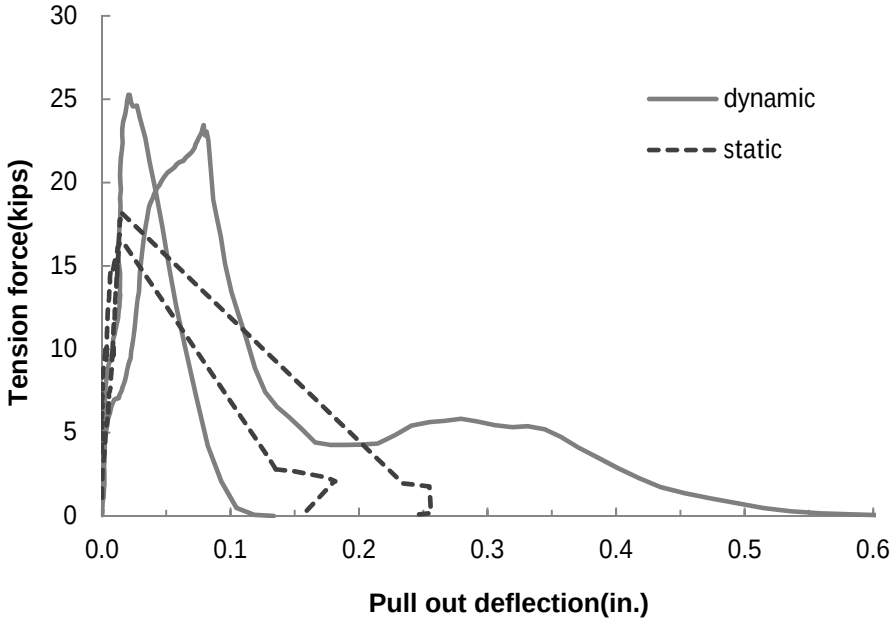


*Figure 5.15: Dynamic and static stud pull-out test (Mouras, 2008)*

Figure 5.16 shows the girder midspan deflections as a function of time obtained from the finite element simulation. The dashed line indicates the vertical deflection of the intact girder (IG-CL), and the solid line represents the vertical deflection of the fractured girder (FG-CL);

both quantities were obtained from the centerline position of the bottom flange. To obtain the centerline deflections at the midspan of the bridge, edge deflections of the bottom flange of each girder were averaged. Because of the simulated girder fracture and the transversely biased loading position of the live load, the vertical displacement of the fractured girder was significantly larger than that of the intact girder (Figure 5.16). It is important to note that haunch separations are included in the vertical displacements that are plotted because the girder displacements were computed from the response of the bottom flanges.

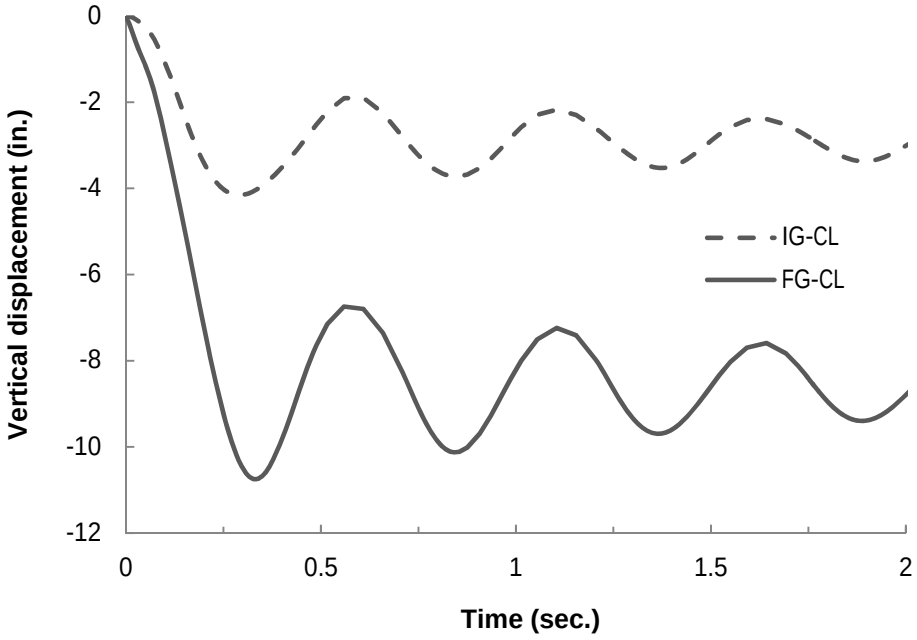


*Figure 5.16: Dynamic girder displacement*

During the bridge test, an attempt was made to measure the dynamic displacement of the fractured girder at its midspan using a string potentiometer attached to the center of the bottom flange, but the string potentiometer was damaged from the explosion used to collapse the temporary truss supports. Consequently, displacements of the bottom flanges were measured after the test bridge came to rest; these static displacements were compared with those obtained from the finite element simulation. Displacement values from the finite element model were obtained by averaging the peak dynamic displacements after three periods of oscillation (Figure 5.16). This approach was taken because it was too computationally demanding to carry the dynamic analyses further in time, and the results showed significant damping. As a result, taking the average value after three periods of oscillation was reasonable. Figure 5.17 shows the static displacement results of the intact and the fractured girders, comparing the measured test data with the computed values. In the bridge fracture test, the vertical displacement at the midspan of the intact girder was 4.16 in., and the finite element model predicted a value that was only 2% higher than the test result. Conversely, for the vertical displacement of the fractured girder, the measured data and predicted value did not compare closely. The measured deflection of the fractured girder following the test was 7.02 in., but the girder deflection in the simulation model was 8.63 in. (23% higher).

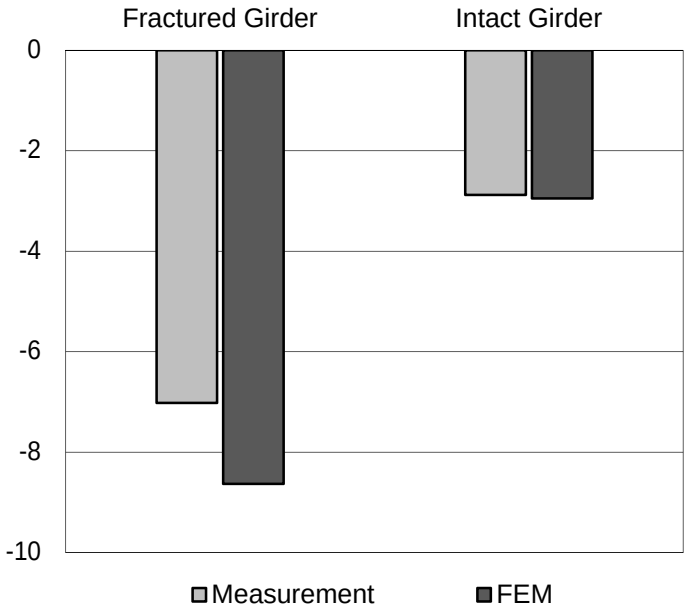


*Figure 5.17: Static displacements of test and simulation*

One reason for such a large difference between the measured and predicted displacement of the fractured girder can be attributed to the over-predicted separation length of the haunch in the simulation model compared with that in the bridge fracture test as discussed previously. During the bridge fracture test and the simulation, the deflected shape of the reinforced concrete deck transitions from double curvature to single curvature. Figure 5.18 shows the displacement at the top of the deck across the width of the bridge following the removal of the temporary supports in the bridge fracture test simulation. Early in time ($t$=0.06 sec.), the graph shows that the deck bends in double curvature; as time progresses, however, the shape transitions to single curvature. This transition in the deformed shape was initiated by stud pull-out failure on the inside of the fractured girder. As the pull-out failure propagated along the length of the bridge, the bridge haunch separated from the concrete deck, leading to single curvature bending of the deck. Haunch separation in the bridge cross-section is schematically depicted in Figure 5.19. Recall that this phenomenon was described previously in Chapter 2 during the development of the simplified modeling procedure. Once the haunch of the fractured girder separated from the deck, the transverse bending stiffness of the deck diminished. Subsequently, the tensile loading attributed to the fractured girder self-weight had to be carried by the studs on the outside of the fractured girder, which increased the bending moment arm for transverse bending of the deck. Therefore, with a wider separation of the haunch on the inside of the fractured girder, a larger deflection could be expected in the fractured girder than what was observed in the test.

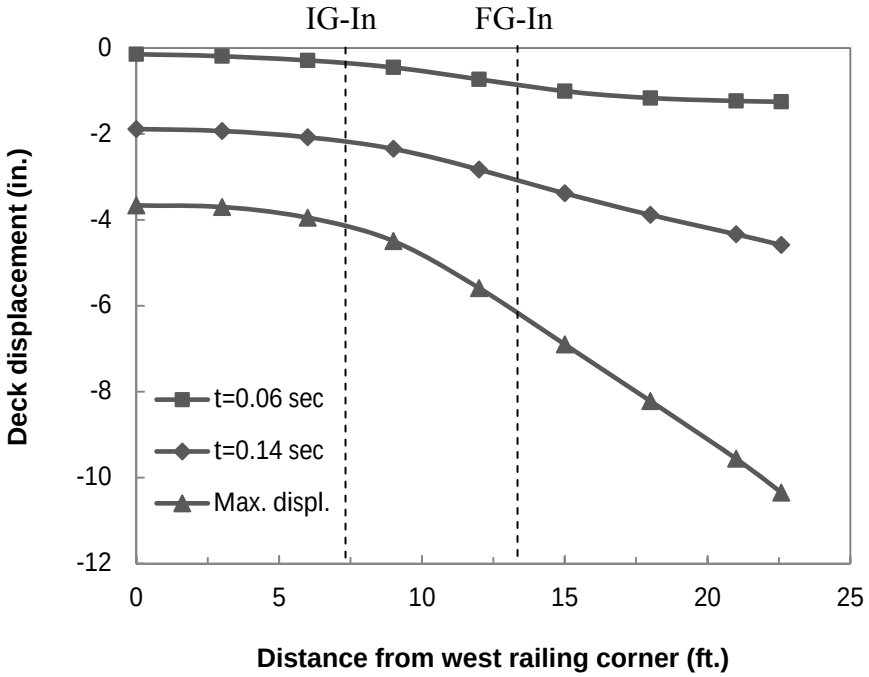


*Figure 5.18: Deck displacement at midspan*

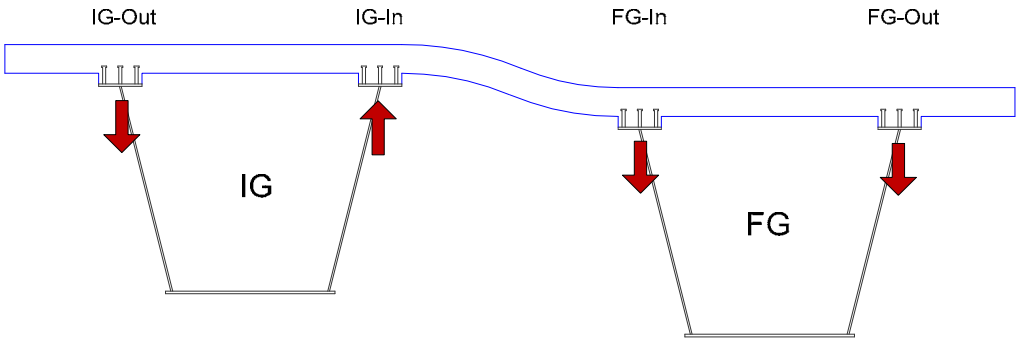


(a) Deck deflection before haunch separation

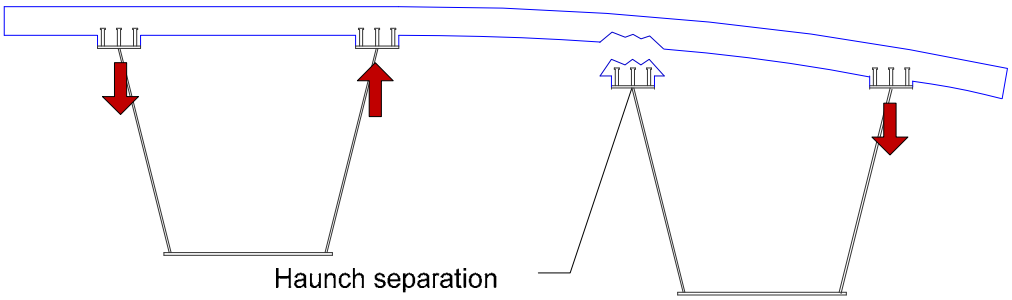


(b) Deck deflection after haunch separation

*Figure 5.19: Deck deflection shape change caused by haunch separation*

Figure 5.20 shows the longitudinal strain as a function of time at the centerline of the bottom flange of the intact girder at a location 6 ft away from the midspan. The strains from the simulation and the bridge show good correspondence, though the peak measured strain from the test was 13% higher than the simulation result. During the second bridge fracture test, it is important to note that the crack induced from the acetylene torch propagated 1 in. upward on the outside of the fractured girder, but this crack extension was not accounted for in the finite element simulation. Therefore, in the test bridge, more energy could be released than in the simulation, which may be one of the reasons why there is a slight discrepancy between the measured and computed results. Regarding the period of oscillation, there is a slight difference between the measured and computed values. This difference is most likely attributed to the differences between the actual damped response of the bridge and the assumptions made about damping in the finite element model. In the simulation, 5% damping was assumed—which is a common assumption for cracked reinforced concrete (Newmark, 1982 )—and the natural frequency of the first mode of the bridge model was utilized to determine a damping factor. Because no forced vibration testing of the bridge was carried out, the actual damped response was not precisely known. Nonetheless, the computed and measured results show good agreement.

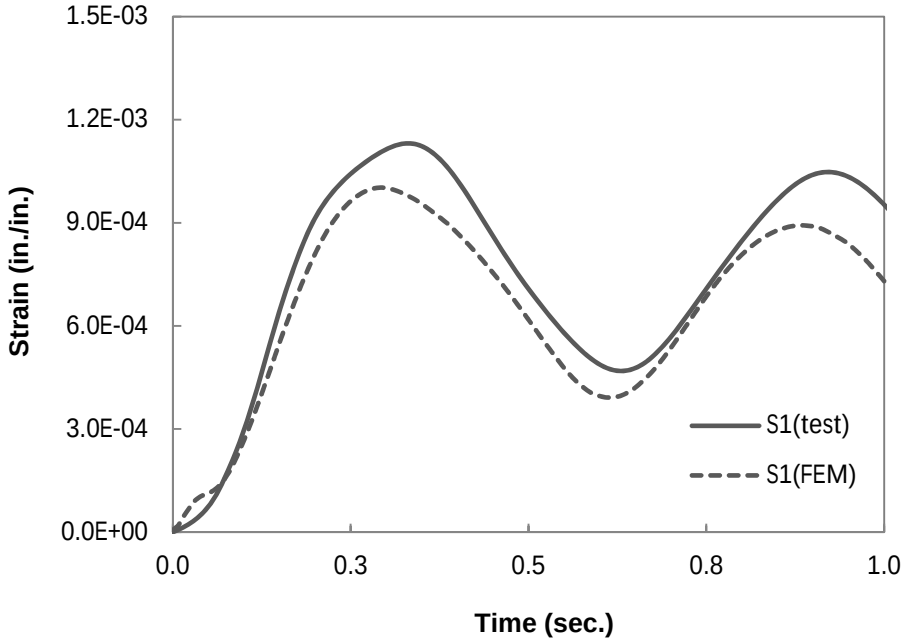


*Figure 5.20: Longitudinal strain response by dynamic loading*

## 5.4 Third Bridge Test (Remaining Capacity Evaluation)

### 5.4.1 Test Procedure

The third bridge test was performed to determine the ultimate load-carrying capacity of the FSEL bridge in its damaged state. It should be noted that no attempts were made to repair the bridge following either of the first two tests. The concrete blocks used to simulate the truck live load in the second bridge fracture test were rearranged for the third test, and one additional concrete block was utilized to create a bin that could accommodate the road base that was used

to incrementally load the bridge (Figure 5.21). Accordingly, the total weight of the concrete blocks in the third bridge fracture test was 82.1 kips. Figure 5.21 shows a schematic of the concrete block configuration on the bridge deck. The concrete blocks were symmetrically arranged about the bridge midspan, and they were transversely biased toward the fractured girder. Wooden planks used to support the concrete blocks were located 2 ft away from the east railing.

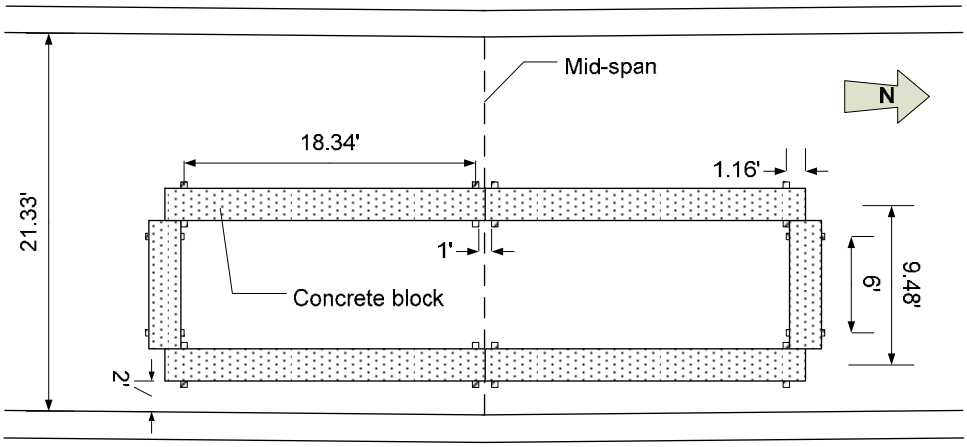


*Figure 5.21: Concrete block configuration on bridge deck*

While positioning the concrete blocks on the deck, the crack in the outside web of the fractured girder propagated toward the top flange, as shown in Figure 5.22. Prior to this crack propagation, the crack was sharpened by the 1-in. crack extension upward from the point where the torch cut terminated during the second bridge fracture test. The total loaded weight of the concrete blocks was 40.9 kips when the crack propagation occurred. This sudden crack propagation caused the bridge to vibrate, but the small oscillations quickly subsided. The crack on the inside web did not propagate when the concrete blocks were placed on the bridge. Though the weight and positioning of the blocks represented a less severe load case than the bridge withstood during the second test, it is believed that the cold weather present during the placement of the blocks during the third bridge test contributed to the crack extension (Neuman, 2009).

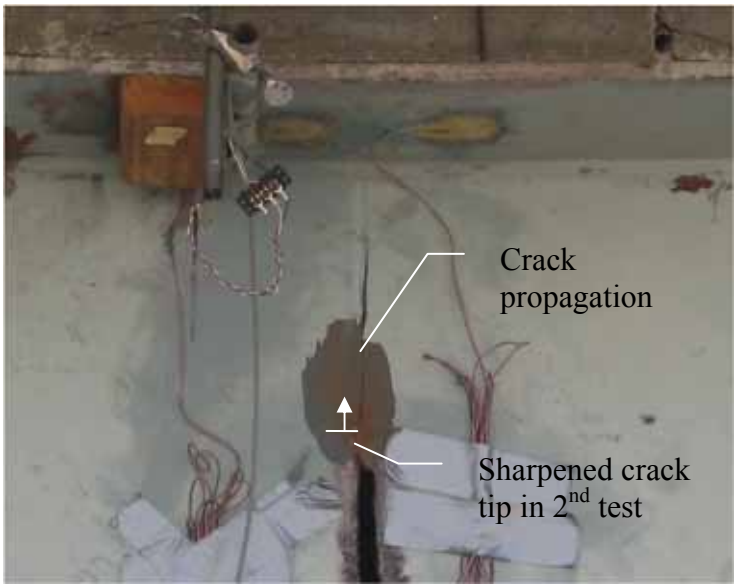


*Figure 5.22: Crack propagation in fractured girder outside web*

Figure 5.23(a) shows the loading process used during the third test on the FSEL bridge. Road base, consisting primarily of gravel and dirt, was placed in an air-operated lift bucket using a small backhoe. The lift bucket was attached to the lifting hook of a crane. Once the bucket was filled, the weight of the road base was measured using a load cell attached to the end of the crane hook. After the crane lifted the bucket and the weight was recorded, the lift bucket was positioned above the bridge, and the road base was placed inside the concrete bin located on the bridge deck (Figure 5.21). When 258.3 kips of road base was loaded onto the bridge, there was no more space available inside the bin. Therefore, it was decided to apply additional road base between the concrete blocks and the east railing. The bridge finally collapsed when the total applied load of the concrete blocks and road base reached 363 kips—more than five times the legal truck load—as shown in Figure 5.23(b).

(a) Incremental loading

(b) Collapsed bridge

*Figure 5.23: Loading process and bridge collapse in third bridge fracture test*

### 5.4.2 Simulation Procedure

The third bridge test simulation consisted of three main steps similar to those in the previous bridge test simulations, as presented in Table 5.3. Recall that for the second bridge fracture test, approximately 83% of the full height of the web was cut using an acetylene torch. During the second test, a fracture initiated from the top of the cut on the outside web of the fractured girder and extended approximately 1 in. upward toward the top flange. While applying the concrete blocks for the third bridge test, this web crack extended to the top flange. The inside web crack also propagated up from the crack manually induced prior to the second test, and this cut extended through the entire depth of the web during the third bridge test. For these reasons, it was assumed that the entire web depth of the fractured girder was fractured. Accordingly, the web connector elements along the predefined fracture path were removed through the entire web height for the third bridge test simulation. Because the loading was incremental, the connector elements binding separated nodes along the predefined crack path were statically deactivated from the bottom flange to the top flange.

**Table 5.3: Simulation procedures for third bridge fracture test**

| | |
|---|---|
| Bridge construction<br>1. Deactivating deck, railing, rebar elements and applying gravity to girder<br>2. Applying deck, railing, and rebar weight on the top flange<br>3. Activating deck, railing, and rebar elements with gravity and removing the weight on the top flange<br>4. Deactivating external cross frame elements and dummy elements | Static |
| Applying girder fracture and truck live load<br>1. Deactivating elements connecting cracks in girder<br>2. Applying truck load (concrete blocks) | Static |
| Applying additional Load<br>1. Applying additional load (road base) | Dynamic |

After removing the web connections, the weight of the concrete blocks and the road base were applied to the bridge using pressure forces placed consistently with the bridge test as shown in Figure 5.24. When 258.3 kips of road base was placed inside the concrete bin during the third bridge test, there was no more space available to accommodate any additional material inside the bin. Consequently, additional road base was placed outside the bin between the east railing and the concrete block forming the eastern edge of the bin. To match the loading location of this additional road base, the pressure load for the additional road base was applied between the east railing and the concrete block as shown in the Figure 5.24(d). For simulating the last step of applying the road base, a dynamic analysis was conducted using a ramped-loading condition; this approach was not intended to account for any dynamic loading effects associated with placing the road base. During the last analysis step, various local component failures were expected to

occur, such as concrete cracking or crushing, haunch separation, and so on. Although those component failures might not necessarily mean collapse of the test bridge, they could cause computational problems with the static analysis procedure, potentially resulting in an analysis failure due to numerical convergence problems. Therefore, a dynamic analysis with a ramped-loading condition was used to avoid such numerical problems.

(a) Concrete block and road base

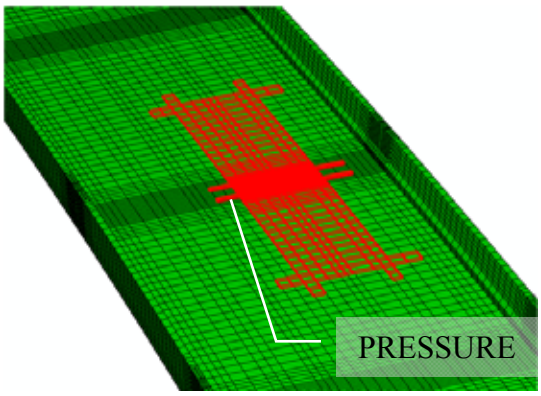

(b) Simulated pressure load

(c) Additional road base

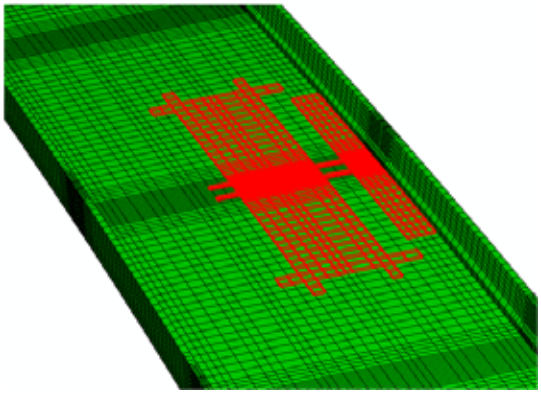
(d) Simulated additional load

*Figure 5.24: Applying concrete block and load base load*

### 5.4.3 Bridge Test and Simulation Results

Data collected from the third bridge test were used to determine the ultimate strength of the bridge and the contribution made by each bridge component in resisting the applied loads. It was observed that the shear studs and the concrete deck had important roles in redistributing the applied loads to undamaged regions of the bridge. The rails also redistributed loads and initially reduced the deflection of the fractured girder before stud pull-out failures occurred. The finite element model developed for this research successfully captured the progressive bridge component failures that were found in the bridge fracture test and closely predicted the measured collapse load.

*Failure Sequence of the Bridge*

With the exception of the haunch separation along the outside of the intact girder near midspan, the simulation model predicted failure modes consistent with those observed in the bridge test. In Figure 5.25, the failure sequences predicted by the simulation and those observed during the bridge test are compared at each prominent component failure event. The failure sequence leading to the collapse of the bridge initiated with the concrete deck cracking due to transverse bending. As the loading continued, extensive tensile cracking started to form on the top of the concrete deck above the inside top flange of the intact girder and propagated along the bridge span. As the bridge continued to deform under the applied loads and transverse bending increased across the width of the deck, the demand on the shear studs along the inside of the fractured girder exceeded the pull-out strength, leading to extensive pull-out failures on both top flanges of the fractured girder. As the pull-out failures propagated along the bridge span, the inside haunch of the fractured girder began to separate from the bottom of the deck near the midspan of the bridge. As the separated haunch length along the inside of the fractured girder kept extending over the bridge span, the bridge deck experienced large deformations near the midspan, and the expansion joint at the top of the east railing closed over most of its height. Because of the contact forces acting over the depth of the expansion joint of the east rail at the midspan location, crushing of cover concrete became pronounced. As the east railing began to pick up loading and started to crush, the haunch separation along the inside of the fractured girder continued to extend as did the haunch separation along the outside of the fractured girder near the midspan. Separation of the haunch along the outside of the fractured girder was arrested when the separation had propagated to the next expansion joint along the length of the bridge. As the damage in the haunches of the fractured girder and the east railing progressed, the bottom of the reinforced concrete deck next to the interior top flange of the intact girder began to crush as a result of the transverse bending of the deck. Crushing at this location started at the midspan and propagated in both the north and south directions along the bridge span. This crushing of the deck was not readily detectable during the test because the permanent metal deck forms between the girders did not allow the concrete to be observed directly, but the extensive cracking on the top of the deck along a line corresponding to the position of the interior top flange of the intact girder and deck rotation about this line provided evidence that the bottom of the deck was crushed. As the applied load approached the maximum load, shear stresses along the haunch on the outside of the fractured girder increased, and bridge collapse eventually occurred when a shear failure took place over the entire length of the outside haunch of the fractured girder.

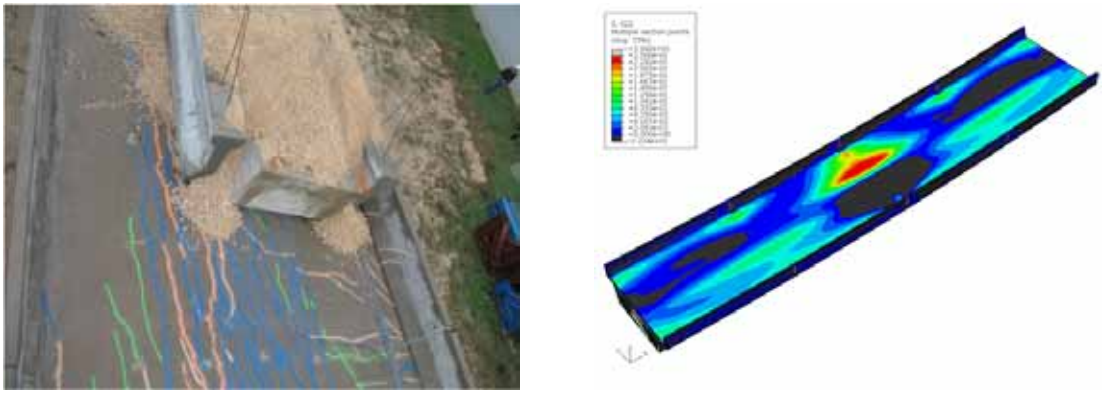

(a) Tensile cracking on top of the deck above IG-In top flange

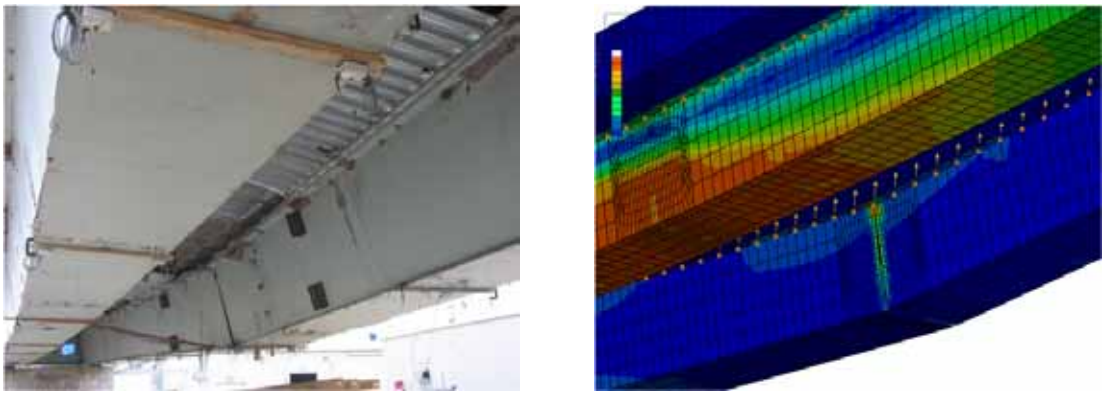

(b) Haunch separation along FG-In haunch

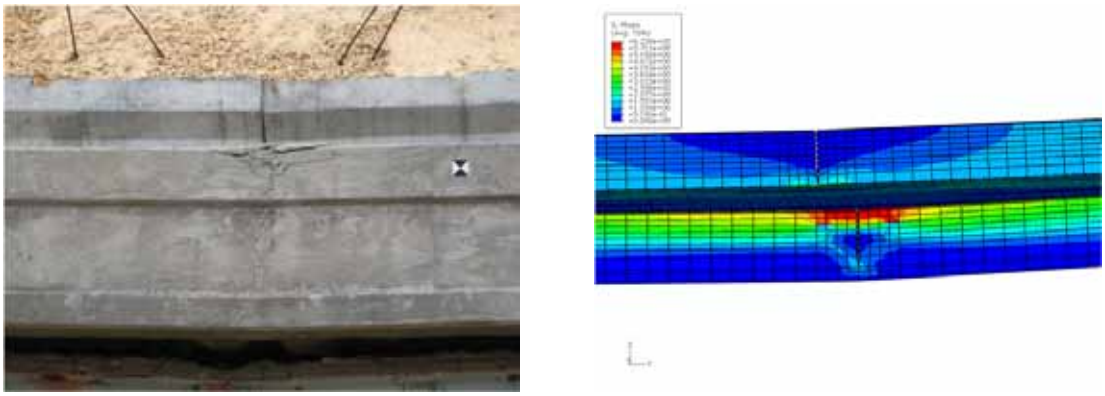

(c) Railing crushing from top

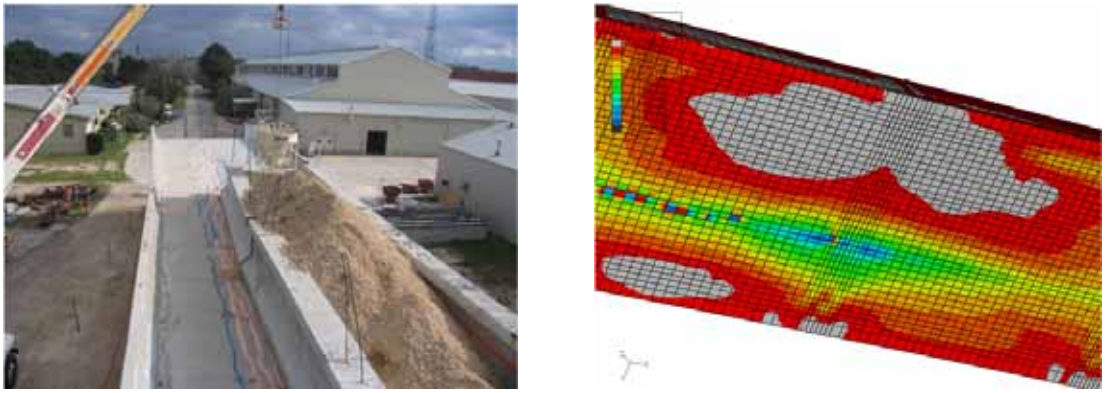

(d) Deck hinge formation along IG-In top flange

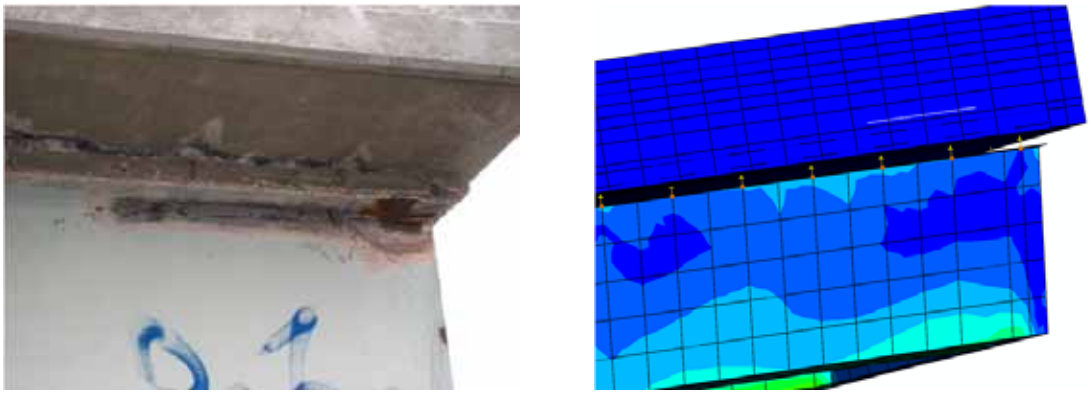

(e) Shear and tension failure of shear studs along FG-Out haunch

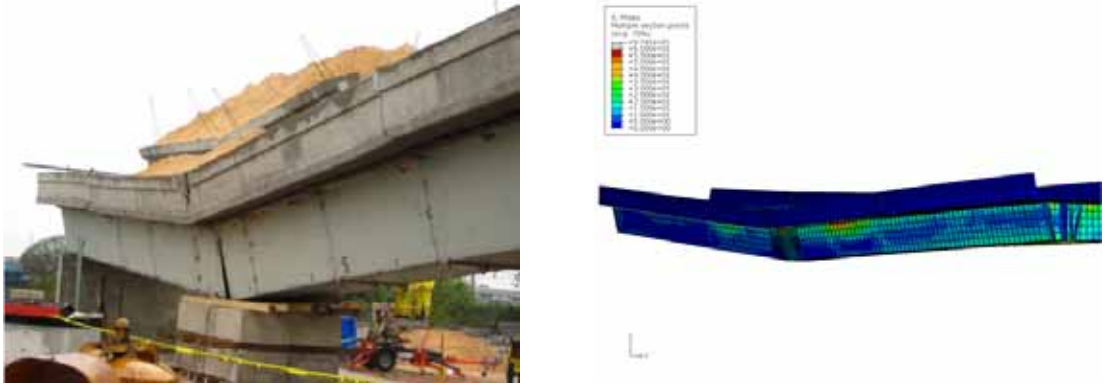

(f) Bridge collapse

*Figure 5.25: Bridge component failure sequence*

*Girder Deflection Response*

The girder vertical deflections measured in the third test are compared with the simulation results in Figure 5.26. The solid lines show the measured test data, and the dashed lines show the simulation results. During the bridge test, there was a sudden vertical deflection in the fractured girder when the applied load reached 160 kips, which is indicated with the first plateau in Figure 5.26. This sudden increase of the deflection was caused by the haunch separating from the outside of the fractured girder. The haunch separation initiated near the

midspan and suddenly extended approximately 20 ft to both the north and the south (i.e., a total separation of approximately 40 ft), which is shown in Figure 5.27. Further separation of the haunch on the outside of the fractured girder did not occur until the applied load reached approximately 363 kips, which was the maximum load applied to the test bridge. Unlike the actual test, in the finite element simulation, the haunch separated gradually along the outside of the fractured girder until the applied loading reached 308 kips; no further haunch separation occurred until the applied load reached 413 kips, which was the maximum load the bridge could carry in the simulation. Although the gradual haunch separation in the simulation was not consistent with the sudden jump observed during the test, the simulation predicted 36 ft of haunch separation along the outside of the fractured girder, which is similar to the actual haunch separation length of approximately 40 ft observed during the test.

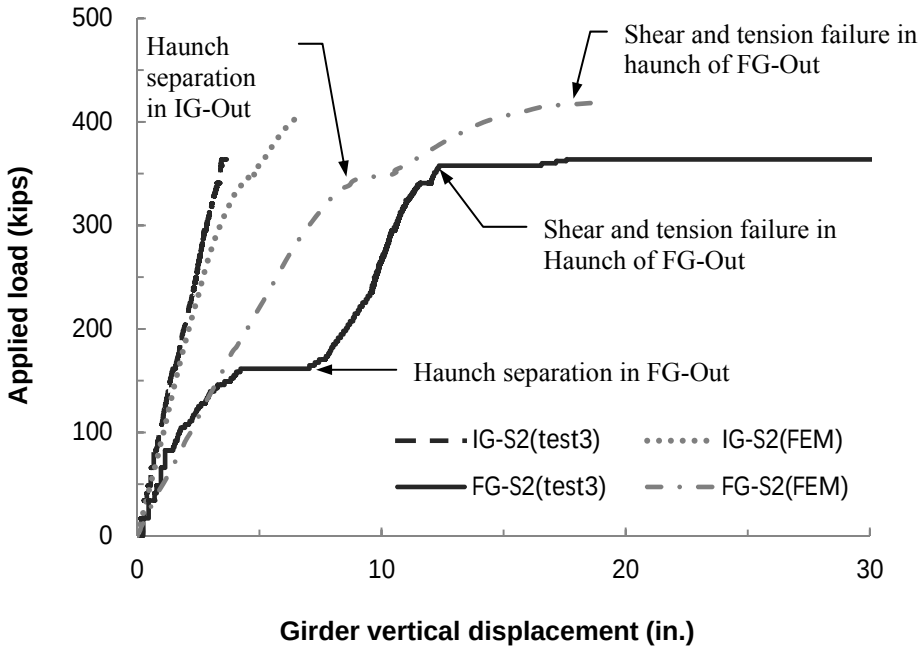


*Figure 5.26: Girder deflection response (18 ft away from midspan)*

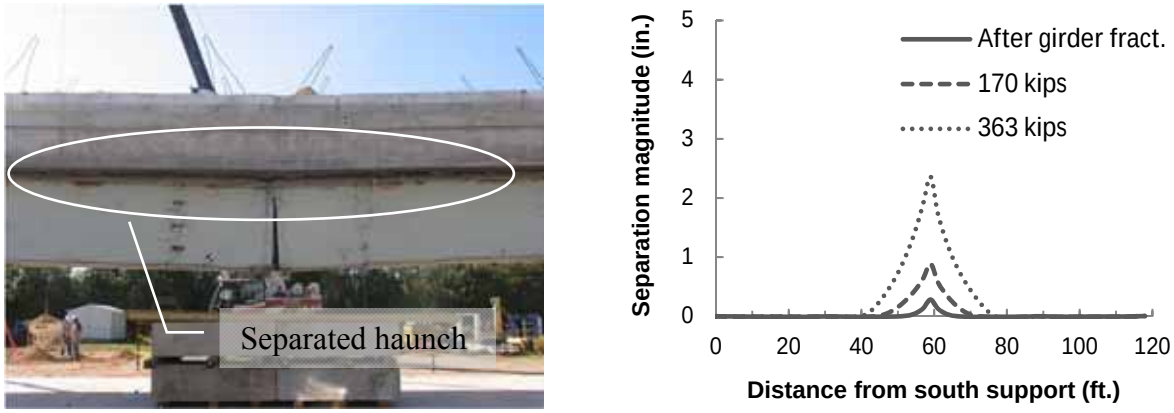


(a) Third bridge test (b) Simulation model

*Figure 5.27: Haunch separation in FG-Out*

Another prominent feature in the girder deflection response of the test bridge occurred at the maximum load. When the applied load reached 363 kips, the fractured girder deflected significantly, and the bridge collapsed. This large deflection was initiated by the slip between the outside top flange of the fractured girder and the concrete deck, as shown in Figure 5.28. Along the outside haunch of the fractured girder, horizontal cracks and diagonal cracks were observed, which suggests that failure of the stud connection was due to the interaction of tension and shear forces. In the simulation model, shear forces in the connector elements became large along the outside of the fractured girder when the applied load approached its maximum value of 413 kips. Although the simulation showed a failure mode that was similar to that of the test bridge, the maximum load of the simulation model was 14% higher than that of the test bridge.


*Figure 5.28: Slip between the deck and girder top flange along FG-Out*

A notable point for this discrepancy is the shear strength equation (Equation 4-3) for the connector elements used to simulate the response of the shear studs in the bridge. As discussed in Chapter 4, Topkaya's (2002) experimental equations (Equations 4-3 and 4-4) for shear strength and shear load-slip behavior were based on stud push-out tests, and these equations were utilized in the simulation model for the shear response of the connector elements. In his tests, Topkaya (2002) used direct shear forces to investigate the shear load-slip behavior of shear studs embedded in a concrete block. Therefore, his equation might overestimate the shear strength of stud connections when a tension force is present. In the simulation model, the shear and tension responses of the connector elements were dealt with independently, and it was assumed that they did not affect each other's strength (i.e., they were uncoupled). The only exception was the shear strength degradation due to stud pull-out failure, as discussed in Chapter 4. This degradation model, where stud pull-out failure can lead to shear failure, does not account for the possibility of the shear strength or the pull-out strength being affected by the interaction of the combined shear-tension force acting on the shear studs. Thus, the shear strength of a stud connection might be affected if a high tension force—one that is less than the pull-out strength—exists on that connection. Likewise, the pull-out strength may be influenced by the presence of shear forces acting on a stud connection.

Besides the possibility of the combined force effect (shear-tension force interaction) influencing the shear or the pull-out strength of a stud connection, the geometry of the haunch might also affect the shear strength. In the bridge test, deck-slip failure started at a location about 20 ft away from the midspan and extended both northward and southward. It was observed that

cracks causing the deck slip were formed horizontally along the junction where the haunch was connected to the bottom of the deck and diagonally through the haunch height, as shown in the Figure 5.28. This observation suggests that the shear failure strength of stud connections could be affected by the haunch. In the test setup utilized by Topkaya (2002), studs were embedded in a flat concrete block without a haunch; thus, equations used to predict shear response do not account for the potential influence of a haunch. In his tests, shear failure of the stud connection was initiated by concrete crushing around the stud. In the case where a haunch is present, extensive cracking in the haunch could influence the failure mechanism—an ultimately the shear capacity—of stud connections.

To investigate the effects of stud shear strength on the ultimate load-carrying capacity of the bridge, a test simulation with a lower shear strength than the strength computed from the shear strength equation (Equation 4-3) was conducted. Figure 5.29 shows the simulation results using a reduced shear strength for the connector elements. A reduction in shear strength of approximately 23% was utilized in the simulation, which corresponds to the shear strength of a 3/4-in. diameter shear stud (the real shear stud diameter was 7/8 in.). The simulation with the reduced shear strength predicted a maximum load capacity that was only 9% higher than the value measured during the bridge test, which demonstrates the significant impact that a small change in the specified capacity of the shear studs can have on the prediction of overall bridge capacity. Although the simulation with the reduced shear strength showed better agreement with the measured results, additional research is needed to develop expressions that can accurately account for the interaction of shear and tension forces acting on a stud embedded in a haunch.

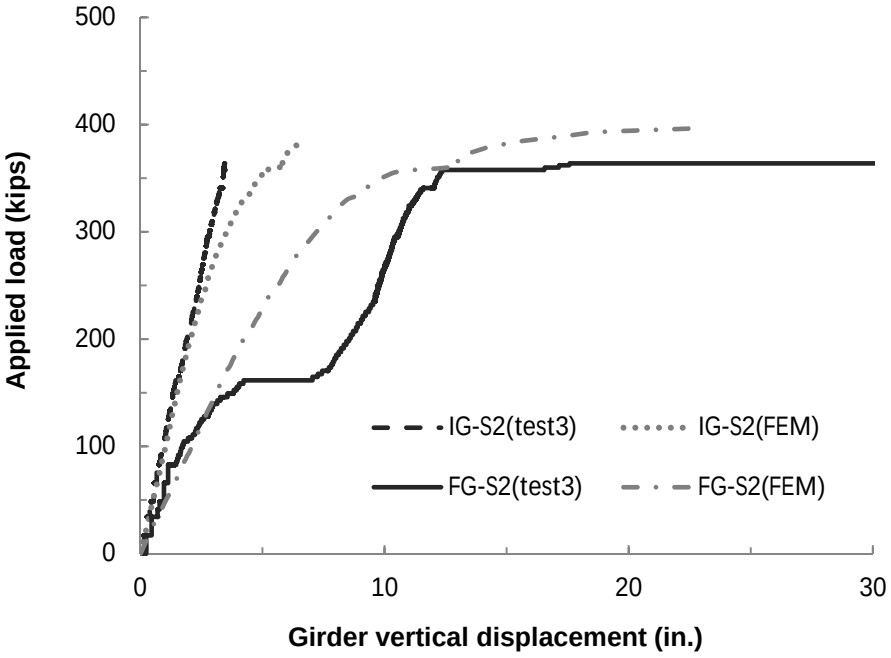


*Figure 5.29: Girder deflection response with reduced shear strength*

The simulation model indicated a failure mode that was not observed during the test. Unlike the experiment, the simulation showed separation of the haunch and deck along the outside of the intact girder, leading to an abrupt increase of the fractured girder deflection as the

applied load approached 350 kips. This haunch separation initiated near the midspan. Once the haunch separated along the outside of the intact girder, the bridge lost transverse bending resistance, and the concrete deck rotated about the bridge's longitudinal axis because the outside and the inside haunches of the fractured girder had already separated near the midspan prior to the outside haunch separation of the intact girder. This difference in response between the simulation and test is believed to be attributed to the underestimated pull-out strength of the stud connection computed from the modified pull-out strength equation (Equation 4-7) as discussed in the previous section.

Railing Engagement

In the test bridge, the concrete cover on top of the east railing at the midspan location spalled off during the second bridge test, and the railing remained closed (i.e., in contact) at the top following the test. As the applied load was increased during the third bridge test, the concrete at the top of the railing began to crush, and the crushing propagated downward along the height of the rail. When the applied load reached approximately 360 kips, a large amount of concrete spalled off, as shown in Figure 5.30. The depth of spall was approximately 2/3 the height of the railing.

(a) Railing crush during test (b) Railing crush after collapse

*Figure 5.30: East railing crush at midspan*

To account for the engagement of the rails at the midspan expansion joint, nonlinear spring elements were used rather than conducting a direct contact analysis. As discussed in the previous chapter, this choice was made based on computational efficiency. Figure 5.31(a) shows strain gauges installed on the inside of the east rail, and Figure 5.31(b) compares the longitudinal strains obtained from the bridge test with those computed from the finite element simulation. Railing contact occurred progressively from the top to the bottom of the east rail, which was confirmed by the strain gauge readings. Figure 5.31(b) indicates that the simulation successfully captures the progressive contact of the rails along the railing height; however, the computed strains start to deviate from the test results after railing contact initiated. It is uncertain why such discrepancies exist, but they could be attributed to such factors as spalling of concrete cover, crushing and cracking of the rail concrete, and the presence of non-uniform contact forces through the width of the railing. The simplified modeling approach used in this study is not capable of representing these localized effects. After the bridge test, a large amount of spalled

concrete cover was observed on the inside of the east rail at midspan. This observation suggests that the concrete strain gage readings may not accurately represent the strain variation in the rails during the test. In addition, it is likely that the contact forces that existed through the width of the railing were not uniform because the large deck deflection above the fractured girder caused the rails to rotate about a longitudinal axis parallel to the bridge span. The simulation model could not account for these effects because of limitations in the material model that was used to represent concrete and due to a limited mesh density through the width of the rails.

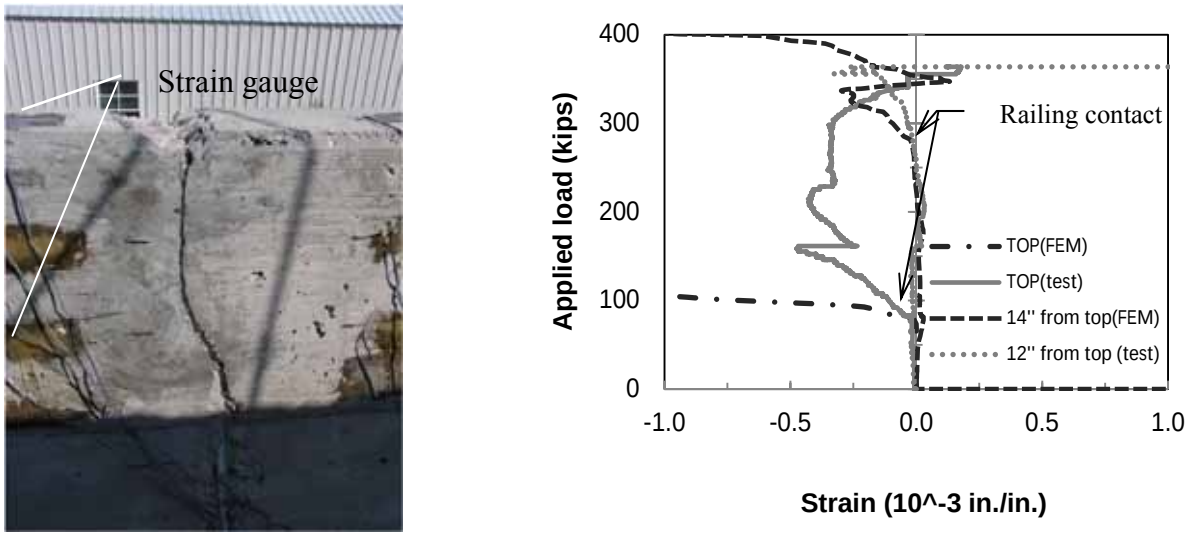


(a) Strain gauge setup (b) Strain response through railing height

*Figure 5.31: Longitudinal strain response along railing height*

## 5.5 Summary of Modeling Guidelines

The finite element simulations described above and in the previous chapter demonstrated the importance of capturing component failures in the deck, haunch, and shear studs if an accurate assessment of overall load-carrying capacity is to be made. A primary goal of this research project was the development of modeling guidelines that can used to simulate the response of a twin steel box-girder bridge following the fracture of one of its girders. Because of the wide variety of finite element software programs available—each having their own capabilities and limitations—it is important that the recommended modeling guidelines be provided in a general manner so that they can be implemented across a wide range of software. Accordingly, it is recommended that finite element models used to assess bridge redundancy include the following features:

- Detailed finite element mesh that accurately captures the geometry of the bridge under investigation.
- Discrete modeling of concrete and reinforcing steel.
- Inelastic material response for both steel and concrete. Concrete constitutive models that account for softening can be used, though they are not essential.
- Discrete modeling of shear stud connections with detailed load-deformation response that is validated against test data.

- Inclusion of bridge rails in finite element model.
- Contact modeling to account for closing of expansion joints. This modeling can be simplified by using nonlinear springs, or a direct contact analysis can be conducted if desired.
- Accounting for large (i.e., nonlinear) deformations.

## 5.6 Summary

Three sets of tests on a full-scale box-girder bridge were performed at the Ferguson Structural Engineering Laboratory at The University of Texas at Austin. The first bridge test involved rapidly severing the bottom flange of the exterior girder using explosives. The bridge demonstrated excellent performance despite the loss of the bottom flange. At the midspan position of the fractured girder, the bridge experienced a residual deflection of less than 1 in., and there was no damage evident to any components of the bridge. In the second bridge test, the webs of the east (exterior) girder were cut using an acetylene torch while the bridge was supported by a temporary truss system. The cut extended from the bottom flange fracture that existed following the first test up towards the top flanges, with 83% of the web height in a "pre-fractured" condition. With a simulated HS-20 truck positioned so as to generate the most severe loading, explosives were used to cause the sudden failure of the temporary truss system supporting the bridge. The failure of the temporary truss supports allowed the sudden release of the gravitational potential energy of the truck live load and the bridge self-weight. The test bridge successfully sustained the induced damage and sudden release of the loads, though some of the components were damaged. The last bridge test was conducted to investigate the remaining load-carrying capacity of the damaged bridge. It sustained approximately 363 kips—more than five times the HS-20 truck load.

The finite element models developed to simulate the bridge tests compared well with the collected data and post-test observations. Furthermore, the finite element models successfully captured prominent bridge component failures that were observed during the second and the third bridge tests. A comparison of the test data with the simulation models suggested the possibility that equations used to define the behavior of connector elements used to represent shear studs in the bridge could overestimate the shear strength of stud connections and could underestimate the pull-out strength. According to the bridge tests and the simulations, prominent failures of the bridge components were the haunch separation, initiated by stud pull-out failures, and crushing of the concrete rail. Therefore, including such component contributions is crucial for modeling a bridge to evaluate redundancy. In the next chapter, various factors that can affect the ultimate load capacity of a fracture critical twin steel box-girder bridge are presented.

# Chapter 6. Parameters Affecting Bridge Load-Carrying Capacity

## 6.1 Introduction

Twin steel box-girder bridges have various load-transferring mechanisms that allow them to sustain traffic loads even they suffer a full-depth fracture of one of their main girders, as demonstrated by the full-scale bridge tests and the corresponding simulations presented previously in this report. To better identify the sensitivity of the research findings to variations in some of the key performance parameters, finite element simulations were performed. Parameters studied included changes in shear stud length, variations in horizontal curvature, variations in bridge span length, and degree of structural indeterminacy (i.e., bridges with simple spans compared to bridges with continuous spans).

To investigate how variations in these parameters affect the load-carrying capacity of these types of fracture critical bridges, incremental load-displacement analyses were conducted for bridge models that were subjected to initial fractures of the bottom flange and webs of one girder, which is the same approach previously utilized to model the response of the FSEL test bridge during the third test. The applied external loading consisted of an HS-20 truck positioned at the most critical location, but each axle load was increased proportionally until collapse was detected or the load reached five times one HS-20 truck load, whichever came first.

## 6.2 Concrete Strength and Truck Live Load

The HS-20 standard design truck utilized in this parameter study has a slightly different configuration than the simulated loading that was used in the third bridge test simulation. An HS-20 truck has three axles spaced 14 ft apart longitudinally and two axles spaced 6 ft apart transversely; the total truck weight is 72 kips. To apply a live load beyond one truck load, each axle load was increased proportionally to its original axle load. Although the simulated truck live load for the third bridge test (Chapter 5) was intended to represent an HS-20 truck loading configuration, it did not have distinct loading axles because of the manner in which the road base was applied to the test bridge.

To quantify the effects of changes in loading configuration and concrete material strength on the overall capacity of the test bridge, fractured girder deflections were computed for three different cases as shown in Figure 6.1. The solid line in this figure shows the results of the simulated loading from test 3, while the intermediate dashed line shows the results for the case when the loading is changed to an HS-20 truck loading. As mentioned above, the axle loads for the HS-20 truck loading were increased proportionally relative to the original axle loads of one truck. Therefore, in this figure, a 144 kip load means placing one HS-20 truck on top of another. Comparing the results shown in the figure, it is clear that the HS-20 loading has a more severe effect on the overall performance of the bridge than the simulated loading used during the third bridge test. One reason for these results is that the HS-20 loading configuration has a longer lever arm for transverse bending than the simulated loading because the road base of the simulated load used during the third test was distributed over a wider region of the deck than the more concentrated loading of the HS-20 truck.

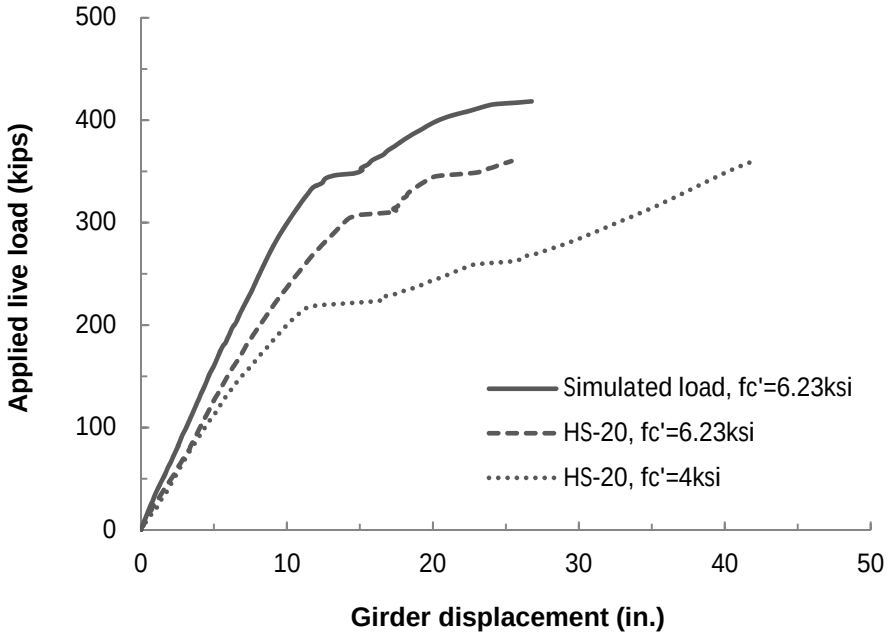


*Figure 6.1: Fractured girder deflection at midspan (loading type and concrete strength effect)*

In addition to the issue of loading configuration differences, it is important to consider variations in concrete compressive strengths because of the wide range that has been used in the bridge industry. According to Russell's report (2003), specified concrete strengths used for bridge deck construction have varied predominantly from 4,000 psi to 8,000 psi. In order to have consistent evaluations on bridge load-carrying capacities for the current parameter studies, a concrete compressive strength of 4,000 psi was used; when representing the actual bridge tests described in Chapter 5, measured material strengths from concrete cylinder tests were specified in the finite element models. The concrete compressive strength not only affects the bending stiffness of a bridge deck, but according to Equation 4-3 and 4-8, it also influences the shear strength and the tensile strength of a stud connection (i.e., decreased concrete strength reduces the shear and the tensile strength of a stud connection). The dotted line in Figure 6.1 is the computed girder deflection for a bridge model that has a concrete deck with a specified compressive strength of 4,000 psi. As expected, the results show a lower stiffness and a lower load-carrying capacity than the other cases. Consequently, in order to develop conservative estimates of the remaining capacity of fracture critical twin steel box-girder bridges subjected to the full-depth fracture of one girder, loads are assumed to be positioned and proportioned according to the axle loads of an HS-20 truck, and concrete material strengths are conservatively estimated to be 4,000 psi.

## 6.3 Background Information on Bridges Investigated during Parameter Studies

Four bridge models that differed in span length were utilized to investigate various parameters affecting bridge load-carrying capacity. Box-girder dimensions and geometries of these models are presented in Figure 6.2 and Table 6.1. The values provided in Table 6.1 are representative dimensions at girder fracture locations. These dimensions were collected from

shop drawings provided by TxDOT. Among the four prototype bridges shown in Table 6.1, three bridges (S200, S170, and C130) are currently in service as part of the WOODWAY exit ramp near the intersection of Interstate IH 10 and Loop 610 in Houston, and the other one (S120) is the test bridge reconstructed at the Ferguson Structural Engineering Laboratory at The University of Texas at Austin. The three models in Table 6.1 are simply supported bridges and are labeled with an "S" in the front of the model name; the model with the label "C" is a continuous bridge having two equal spans.

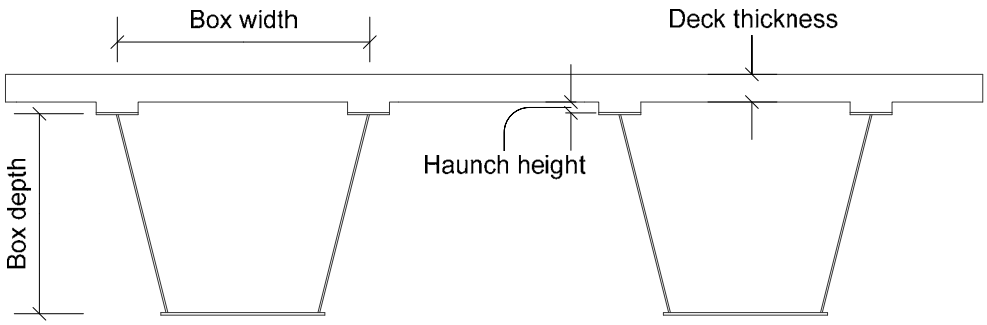


*Figure 6.2: Cross-section view of twin steel box-girder bridge*

**Table 6.1: Box girder dimensions at fracture location**

| Model | Span length (ft) | Box girder dimension | | | | | |
|---|---|---|---|---|---|---|---|
| | | Thickness (in) | | | Width(in) | Height (in) | Span/Depth |
| | | Bot. flange | Web | Top flange | | | |
| S200 | 200 | 2.00 | .75 | 1.75 | 84.0 | 86.0 | 27.9 |
| S170 | 170 | 1.50 | .75 | 1.50 | 84.0 | 86.0 | 23.7 |
| C130 | 130 | 0.88 | .50 | 0.75 | 84.0 | 53.2 | 29.1 |
| S120 | 120 | 0.75 | .50 | 0.64 | 72.0 | 57.7 | 25.0 |

## 6.4 Bridge Component Contributions on Bridge Capacity

### 6.4.1 Stud Length and Deck Haunch

The robustness of stud connections plays an important role in the overall load-carrying capacity of a bridge because they enable the bridge to maintain composite action between the steel girders and the concrete deck. Under normal conditions when both girders are fully intact, the stud connections primarily resist shear forces. In the event that a girder fracture occurs, however, high tension forces will act on the stud connections of the fractured girder. During the bridge tests carried out under this research project, such tension forces initiated pull-out failures of the stud connections along the fractured girder, leading to a significant reduction in the transverse bending stiffness of the bridge.

Based on stud pull-out test results (Mouras, 2008), the pull-out strength of a stud connection is proportional to the embedded length of a stud into the deck because a longer length increases the concrete failure cone size surrounding a stud. The presence of a haunch between the bottom of the deck and the top flanges of the steel girders, however, reduces the effective

embedded length of a stud. In addition to the embedded length reduction, the haunch also influences the failure cone shape and thereby reduces the concrete surface area available to resist applied tension forces. Because of these two factors, the pull-out strength of a stud embedded in a haunch is less than it would be in the case no haunch is present. In spite of these drawbacks, a haunch is commonly used in bridge construction because it is needed to maintain a uniform concrete deck thickness. For this reason, the effect of a haunch on the pull-out strength of a stud connection was considered in the bridge parameter studies, and the height of the haunch was consistently assumed to be 3 in., which is the maximum haunch height allowed by the TxDOT Bridge Detailing Manual (2001) provided no other reinforcing scheme for the haunch is provided.

Figure 6.3 shows the pull-out strength for different stud configurations obtained from laboratory tests (Mouras, 2008) along with the predicted results from Equation 4-7. The pull-out strength is plotted against the effective stud length, $h'_{ef}$ , normalized by the haunch width, $w_h$. The variable $h'_{ef}$ is defined as the length a stud is embedded into the concrete deck, excluding the haunch height and the stud head. As shown in Figure 6.3, stud pull-out strength goes up as the effective stud length becomes longer and the concrete strength increases.

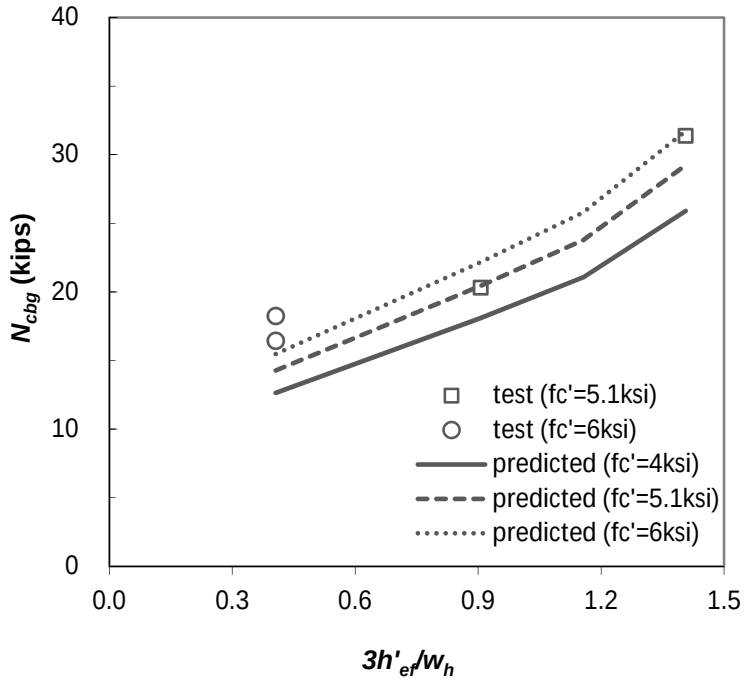


*Figure 6.3: Tensile strength variation along stud length*

To investigate the effects of shear stud pull-out strength on bridge load-carrying capacity, finite element bridge models excluding rails were studied. Rails were excluded from these models in an attempt to isolate the effects of the shear stud strength on overall performance. For these analyses, the assumed concrete strength was 4,000 psi, and the HS-20 loading configuration was used. Figure 6.4 shows the girder displacements for bridge models with a span of 120 ft. In this figure, girder displacements of a bridge model with 5-in. stud connections are plotted with solid lines, and displacements of a bridge model with 9-in. studs are plotted with

dashed lines. This figure shows that the displacements of both girders are reduced when the stud length is increased, and such displacement reductions are significant in the fractured girder. This tendency was consistently observed through simulations of bridge models with other span lengths (C130, S170, and S200).

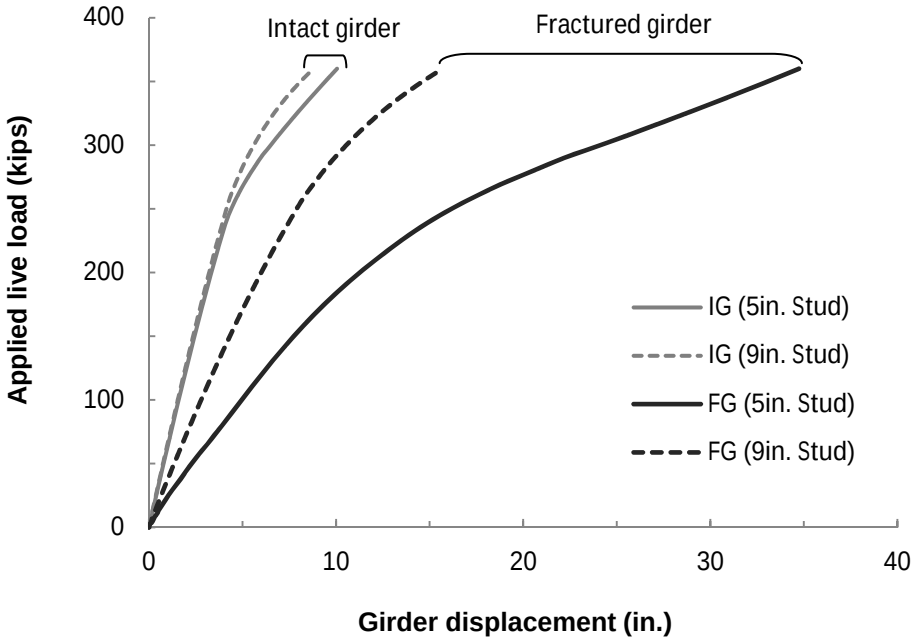


*Figure 6.4: Girder deflection at midspan (stud length effect)*

A detailed study of the simulation results indicated that such displacement reductions were related to differences in haunch separation behavior. In all models studied, prominent haunch separations occurred along the insides of fractured girders, which resulted in transverse bending stiffness reductions across bridge decks and led to large increases in the displacements of the fractured girders. The outside haunches of fractured girders also separated near the fracture locations in the bridge simulation models. In addition to the transverse bending stiffness reductions, these haunch separations also reduced the vertical bending stiffness of bridges by removing composite behavior between the concrete decks and the steel girders. Computed results suggest that as the haunch separation length increases, bridges will demonstrate reduced stiffnesses and larger deflections. Figure 6.5 shows the separated haunch length along the inside of the fractured girder for a model with 5-in. studs. When a separation magnitude representing the vertical displacement of a stud connector element exceeded its pull-out displacement, $U_m$, computed from Equation 4-12, it was assumed that the stud connection was separated from the deck. To investigate the separated length of a haunch as a function of the embedded stud length, haunch separation lengths were plotted against applied live loads following a girder fracture event. These results are shown in Figure 6.6, where the separation lengths are normalized by the bridge span length and the applied loads are normalized by one HS-20 truck load. The separated haunch lengths of the 9-in. stud model are less than those of the 5-in. stud model—both on the inside and the outside of the fractured girder—which led to a stiffer response and smaller deflections for the fractured girder in the 9-in. stud model compared to the model with 5-in. studs.

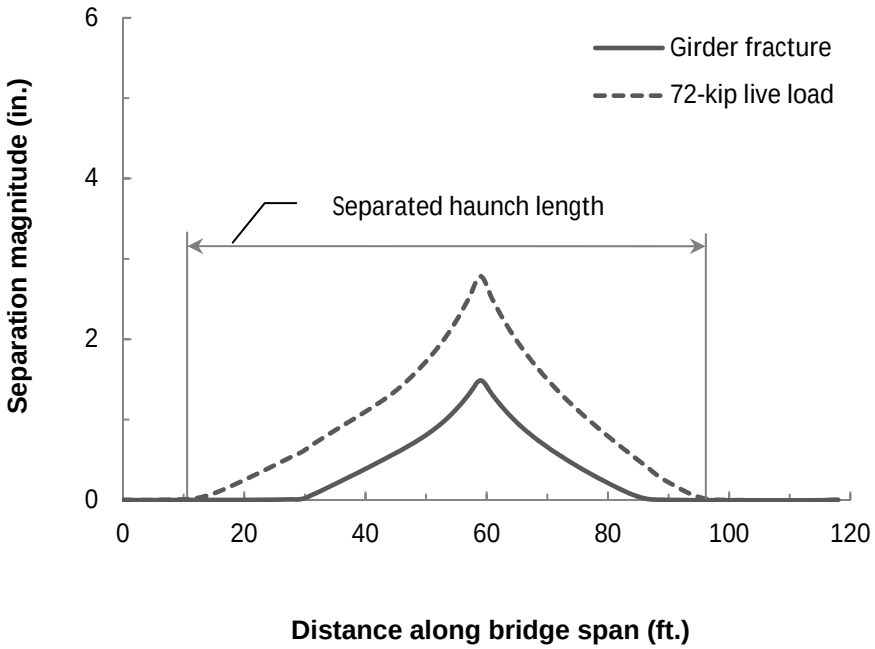


*Figure 6.5: Haunch separation in FG-In (5in. stud model)*

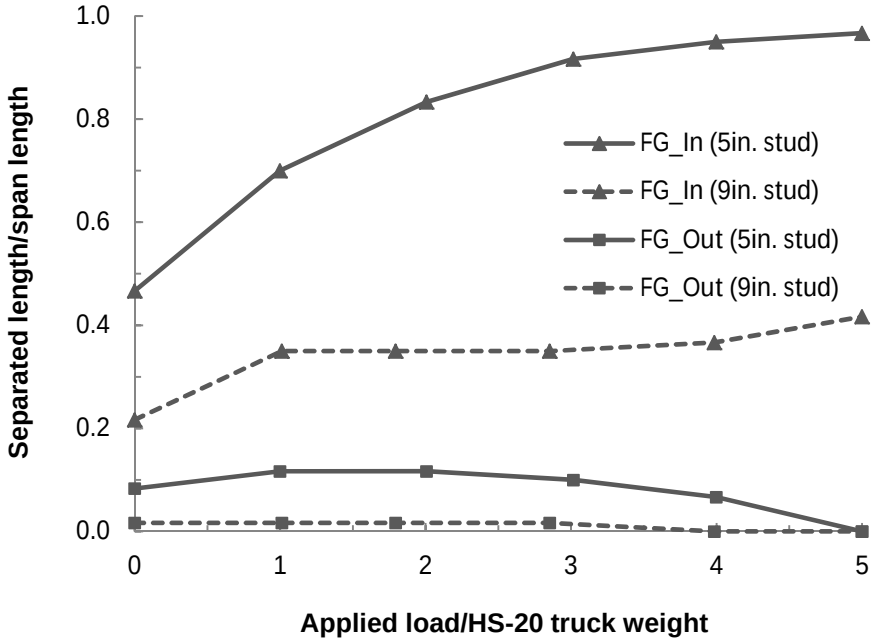


*Figure 6.6: Separated haunch length variation along applied load*

### 6.4.2 Railing

Bridge deflections with and without the presence of a railing were investigated using a TxDOT standard T501 rail as shown in Figure 6.7; this rail was selected because it is widely used in practice. For models that included rails, expansion joints were placed above the fracture location to minimize the potential increase in bending stiffness rails may offer at that location. For consistency with the full-scale test bridge, all finite element models assumed that expansion

joints were spaced every 30 ft along the span, and gap openings between rail sections were assumed to be 3/4-in. As with the models used to represent the FSEL test bridge, spring elements were placed in the expansion joints to account for potential contact of railing sections in the event that large deflections could cause the expansion joints to close.

*Figure 6.7: T501 rail of FSEL bridge*

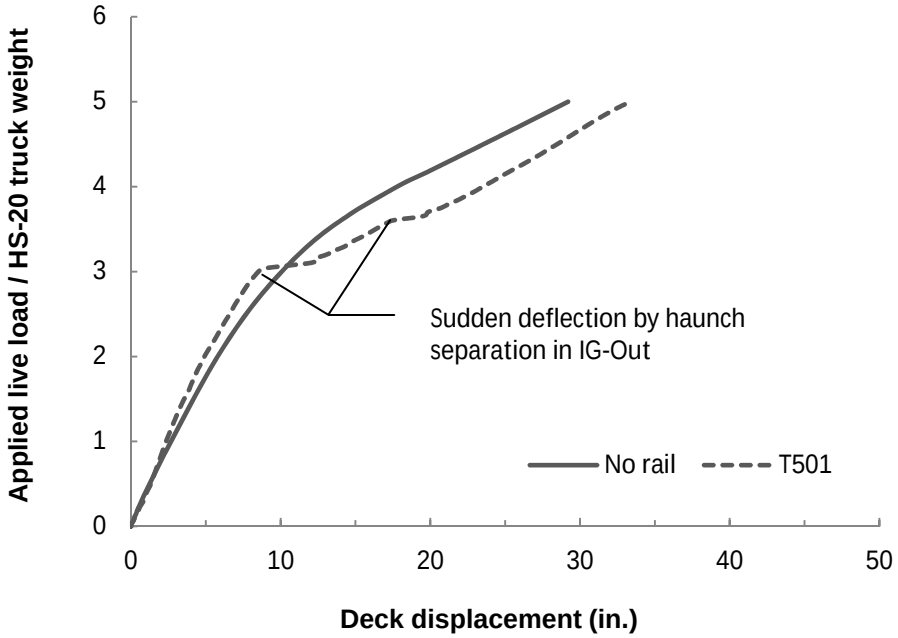


*Figure 6.8: Deck deflection of fractured girder centerline at midspan*

Figure 6.8 shows deck displacements of bridge models with 120-ft spans after the fracture of one girder. The displacements shown are those that occurred following the girder fracture (i.e., no pre-fracture displacements due to construction loads are included). All displacements shown in subsequent figures consider only the post-fracture displacements. The deck displacements were measured on the top of the deck at the centerline of the fractured girder.

Initially, as expected, the bridge model with rails deflects less than the model without rails; however, the total deflection at the peak load is greater for the model with rails than the one that does not include rails. A prominent feature shown in the figure is the sudden increase in the deck displacement for the model that included rails as the applied live load approached 216 kips. This load is equivalent to three HS-20 trucks. Conversely, a sudden increase in the deck displacement was not observed in the model without rails.

According to the finite element analyses of these two models, the main notable difference in bridge component failures was the haunch separation along the outside flange of the intact girder. Such haunch separation was observed only in the bridge model with rails. Figure 6.9 shows variations in the separated haunch length as a function of the applied live load. The dashed line with circle markers indicates the haunch separation length along the outside flange of the intact girder for the bridge model that included rails. As shown in this figure, the haunch separation increased abruptly when the normalized load level reached approximately three, which is equivalent to three HS-20 trucks. This haunch separation led to a reduction in the transverse bending resistance of the bridge deck, allowing a rigid rotation of the deck to take place. Therefore, the deck above the fractured girder could deflect downward abruptly, as shown in Figure 6.8. In addition, the difference in the haunch separation length shown in Figure 6.9 indicates that the separation distance is greater in the finite element model with rails than the one without rails. As discussed in the previous section, bridges are expected to exhibit less stiff behavior as haunch separation distances increase due to a reduction in the transverse bending stiffness and in the vertical bending stiffness of the bridge. Results presented in Figure 6.9 support this observation.

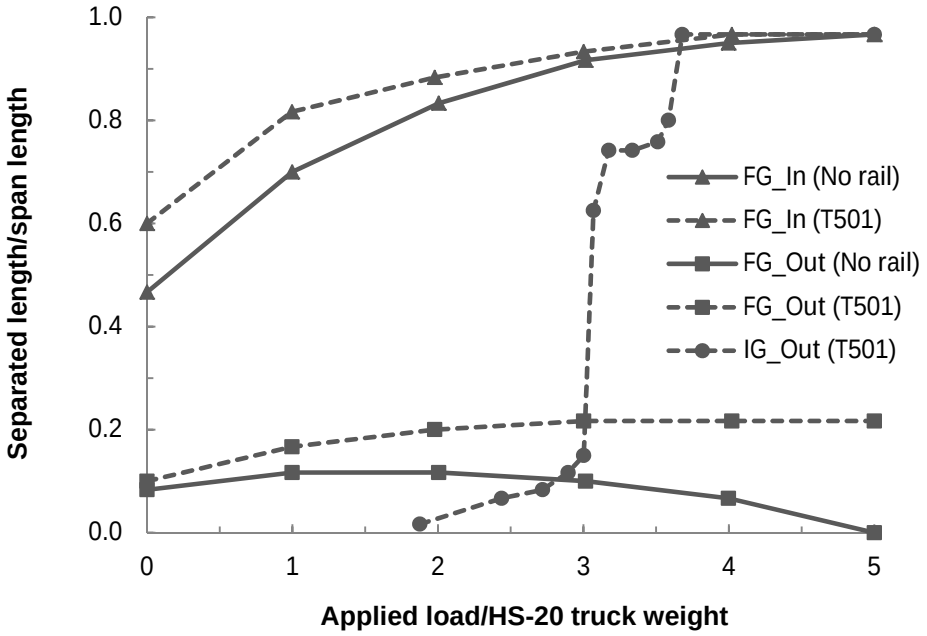


*Figure 6.9: Separated haunch length difference depending on railing presence*

A detailed investigation of the response helps explain the results shown above in which, near the onset of failure, bridge models with rails deflect more than models that do not include

rails. Under low levels of applied load, the bridge model with rails showed a slightly stiffer behavior in the deck displacement response than the model without rails. When the sudden haunch separation occurred along the outside flange of the intact girder, the deflection of the bridge model with rails became larger than the one without rails, and this trend continued up until the peak load was achieved. To explain this behavior, there is a need to focus on the variations in the haunch separation length along the outside of the fractured girder; Figure 6.9 shows a noticeable difference between the T501-rail model and the no-rail model. In Figure 6.9, the length over which the haunch separates in the no-rail bridge model—plotted with solid lines and squares—initially increases as the applied load increases, but it starts to decrease once the loading exceeds a single HS-20 truck (i.e., 72 kips). This behavior was caused by the localized large deflection of the deck above the fractured girder. Because of the position of the applied live load, the deck deflection at this location increased at a faster rate than that of the girder. As a result, the deck and girder moved closer to each other, with the deck eventually supported by the girder. When the girder and concrete deck came together, the haunch separation distance became zero. Conversely, for the case of the finite element model that included the T501 bridge rail, this reduction and eventual closure of the haunch separation distance was not observed (Figure 6.9). It is believed that this result is caused by the engagement of the railing above the fractured girder. Once bridge rail sections are engaged, they increase the bending stiffness of the deck because they act like deep beams at the edge of the deck. The increased bending stiffness reduces the deck deflection and prevents the deck from coming to rest on top of the fractured girder as was observed in the bridge model that neglected the presence of the rails. Eventually, however, haunch separation along the outside flange of the intact girder causes the displacements in the model with rails to exceed those of the model without rails.

## 6.5 Curvature Effect on Bridge Capacity

Steel box-girder bridges are frequently used in curved regions of highway interchanges because of their high torsional resistance. As the radius of curvature of a bridge decreases, torsional stresses increase due to the eccentricity from boundary supports. In cases where a bridge is damaged, such as the fracture of one girder assumed for a redundancy evaluation, bridge curvature may negatively affect a bridge's load-carrying capacity because the bridge would lose a significant level of torsional resistance due to the girder fracture. For this reason, curvature effects were investigated for bridge models with 120-ft spans.

Figure 6.10 shows shear stresses in the bottom flanges at the midspan location of three bridge models having different radii of curvature: 1.) an infinite radius (i.e., a straight bridge), 2.) a radius of curvature equal to 1365 ft, which is equivalent to the full-scale test bridge, and 3.) a radius of curvature equal to 800 ft, which is near the lower limit seen in typical field applications. As expected, higher stresses were observed in curved bridges with smaller radii of curvature than those in bridges with larger radii of curvature; for all cases considered, the actual magnitude of these stresses was small. As indicated in Figure 6.11, the vertical displacements of the fractured girders showed behavior consistent with that of the shear stresses. Although the bridge curvature does not affect the vertical deflection notably in these cases, the effect might be significant in cases where the span length is much longer than these models. Therefore, additional research is needed to clarify the curvature effects on this type of bridges. Nonetheless, using the modeling guidelines described in this report, both simplified analysis methods and detailed finite element models can be used to study the effects of changes in horizontal curvature on overall bridge redundancy.

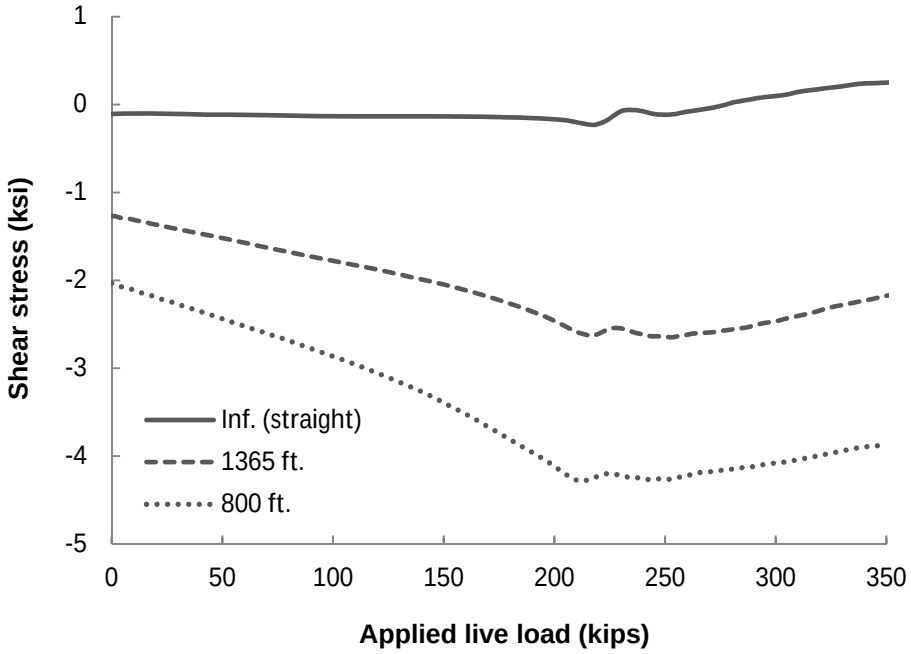


*Figure 6.10: Shear stress of bottom flange at midspan*

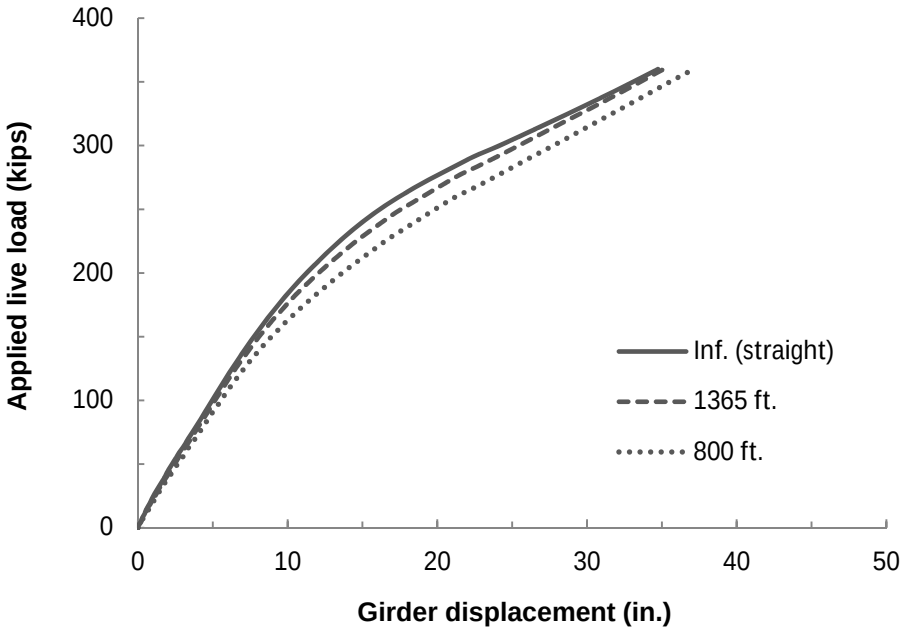


*Figure 6.11: Fractured girder deflection at midspan (curvature effect)*

## 6.6 Structural Indeterminacy

Unlike a simply supported bridge, bridges with continuous spans are statically indeterminate and therefore inherently possess some degree of system redundancy. Thus, if a twin steel box-girder bridge is constructed continuously over multiple supports, its response

following the fracture of one girder can be redistributed to a neighboring girder as well as neighboring spans—potentially improving its chances to survive a fracture event more effectively than a simply supported bridge. To investigate the possible beneficial effects of structural indeterminacy, the post-fracture behavior of the two-span continuous bridge model (C130), as described in Table 6.1, was analyzed in this study.

In the analysis of the simply supported bridge models described previously, the girder fracture location was selected to be at the midspan because the maximum positive bending moment caused by the bridge self-weight and a truck live load occur at this location. To determine the location where positive bending moment was maximized by bridge self-weight and a live load for the continuous-span bridge model, a moving load analysis was conducted. Before applying the moving load to the bridge, deck self-weight was applied on the top flanges of the bridge girders with gravity loading for girder self-weight (to account for non-composite section behavior), and then the moving load representing a truck live load was applied by changing its location by 2-ft increments along the bridge span. Figure 6.12 shows the results of the moving load analysis for the C130 model. The solid line shows the normal stress envelope induced by the bridge self-weight (dead load, DL) and the moving load (live load, LL). The normal stress was measured in the bottom flange of the girder for which the simulated fracture was to be specified. As shown in Figure 6.12, it was found that the maximum normal stress occurred at 51 ft away from the simple support, which corresponded to a relative position of 40% of one span length. Therefore, this location was specified as the fracture location of the continuous-span bridge model.

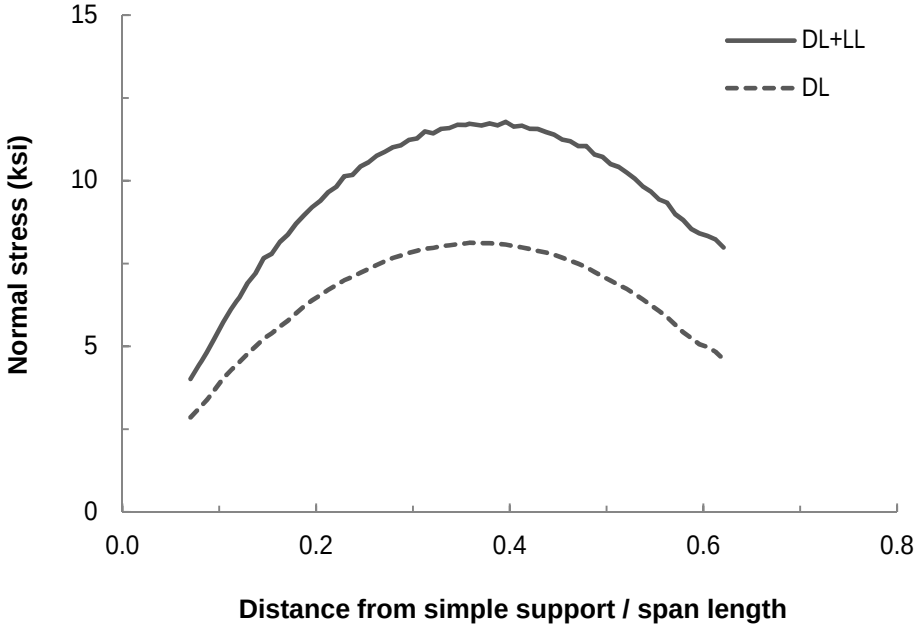


*Figure 6.12: Normal stress envelop curve along bridge span*

Figure 6.13 compares the girder deflection behavior of the simply supported bridge model (S120) and the two-span continuous bridge model (C130). It is important to note that these results are for the case when no railing is included in either model. Due to the differences

in cross-section size and other dimensions (Table 6.1), it is not appropriate to compare the computed results directly. Nonetheless, it is important to identify differences in the response behavior of these models and to recognize that the continuous-span model had a longer span and a smaller cross-section than the simple-span model.

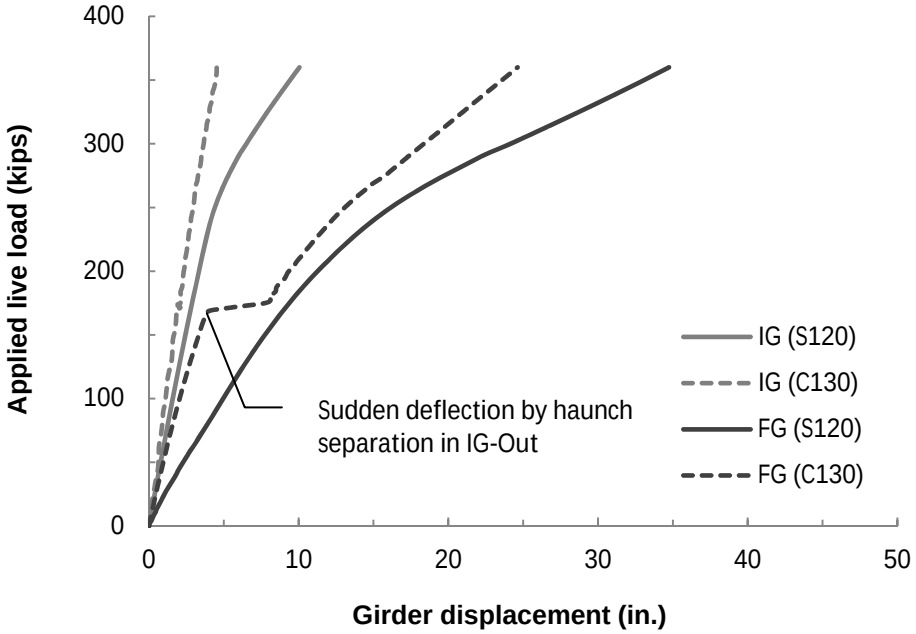


*Figure 6.13: Girder deflection at midspan (continuous span)*

Notably different responses were observed between these two models for the fractured girder deflection behavior, as shown in Figure 6.13. As the applied load reached approximately 160 kips, haunch separation along the outside of the fractured girder was observed near the fracture location of the continuous-span bridge model. It was caused by the cantilever action emanating from the interior support side of the bridge. Because of the position of the assumed fracture location relative to the layout of this two-span continuous bridge, the far end rested on a simple support that could not provide such cantilever action. Thus, the interior side that could develop cantilever action restrained the far side resting on the simple support. This restraint caused the tension force on the stud connections near the girder fracture location to increase, eventually causing haunch separation to occur locally near the fracture location along the outside of the fractured girder.

An interesting observation is that the continuous-span bridge model showed a relatively stiff deflection response even though it suffered a sudden haunch separation along the outside of the fractured girder. To further investigate this post-haunch-separation behavior, T501 rails were added to these two models. As indicated above, the presence of rails in a redundancy evaluation can greatly affect the computed pull-out forces acting on the stud connections. In the S120 simple-span model, including a T501 rail caused stud pull-out forces to increase to the point that haunch separation occurred along the outside of the intact girder. This haunch separation caused large deflections to occur in the fractured girder under the loading range considered (i.e., 5 times

an HS-20 truck load). Figure 6.14 shows the analysis results for these two bridge models with the T501 railing.

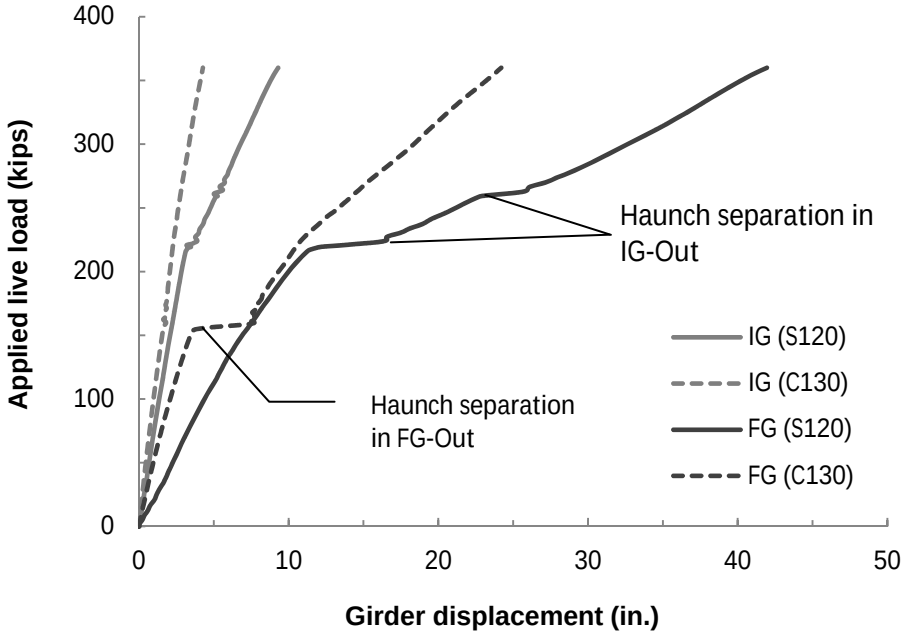


*Figure 6.14: Girder deflection at midspan (continuous span with T501 rail)*

Although haunch separation occurred along the outside of the fractured girder in the continuous-span bridge model and caused a sudden increase in the deflection of the fractured girder, the continuous-span bridge model demonstrated a stiffer deflection response than the simple-span model, particularly for the fractured girder. The differences in girder displacements between these two models became large after haunch separation along the outside of the intact girder was initiated in the simple-span model. Interestingly, such haunch separation along the outside of the intact girder did not occur for the continuous-span bridge model. This behavior is a result of the fact that, even with the full-depth fracture of one girder, vertical bending resistance can develop in the continuous-span bridge due to cantilever action. Accordingly, the applied load can be transferred longitudinally along the bridge span. Conversely, in the simple-span model, the applied load must be transferred through transverse bending of the deck, which causes an increase in the pull-out forces on the stud connections along the outside of the intact girder. This increase in the pull-out forces on the studs eventually causes haunch separation to occur. These results imply that the continuous-span bridge has a higher post-fracture load-carrying capacity than the simple-span bridge despite the fact that it has a longer span and a smaller cross-section.

## 6.7 Bridge Span Length and Dynamic Amplification Factor

Three simple-span bridges that differed in their span lengths were analyzed to investigate post-fracture load-carrying capacity as a function of span length. Figure 6.15 shows girder deflection behavior for these bridge models, and it is interesting to note that the results do not show any significant span length dependency. However, considering the ratio of span length to steel box-girder depth—values are indicated on top of each fractured girder deflection plot—the

fractured girder deflections increase as this ratio increases. Intact girder deflections also tended to behave similarly with the fractured girder until yielding in the bottom flange of the 120-ft span bridge model (S120) was initiated.

In addition to the investigation of bridge load-carrying capacity, the dynamic amplification factor attributed to suddenly released loads—associated with the assumed damage and loading scenario for the redundancy evaluations considered in this research—was studied using the three simple-span bridge models (S120, S170, S200) and the continuous-span bridge model (C130). The dynamic amplification factor was obtained by dividing the maximum dynamic deflection of the intact girder by the static deflection of the girder.

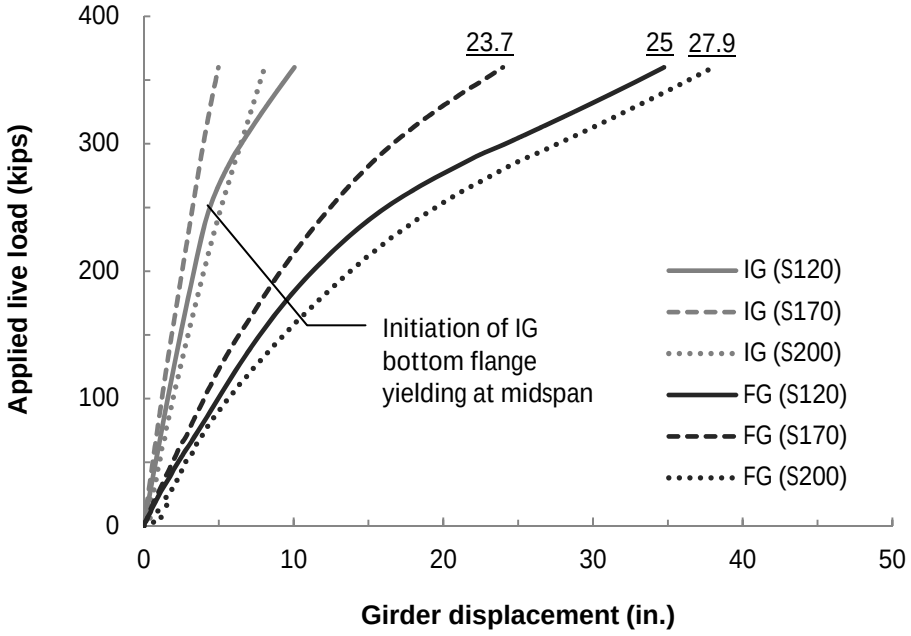


*Figure 6.15: Girder deflection at midspan (span length effect)*

In Figure 6.16, the computed dynamic amplification factors are plotted against bridge span normalized by the depth of the steel girders. The plot shows that for the simply supported bridge models, the dynamic amplification factor decreases as the ratio of the span to the box depth increases. With only one continuous-span bridge model used in the parameter study, trends in the response of the dynamic amplification factor for these types of bridges remain uncertain. Nonetheless, according to the analyses of these bridge models, the dynamic amplification factor varied in a narrow range between 1.36 and 1.58. This observation is important, as other specifications for redundancy evaluation of cable stay bridges require a load amplification factor of 2 (PTI Cable Stayed Bridge Committee, 2007), which is much greater than what was observed in these analyses or in the stud pull-out test results reported by Mouras (2008).

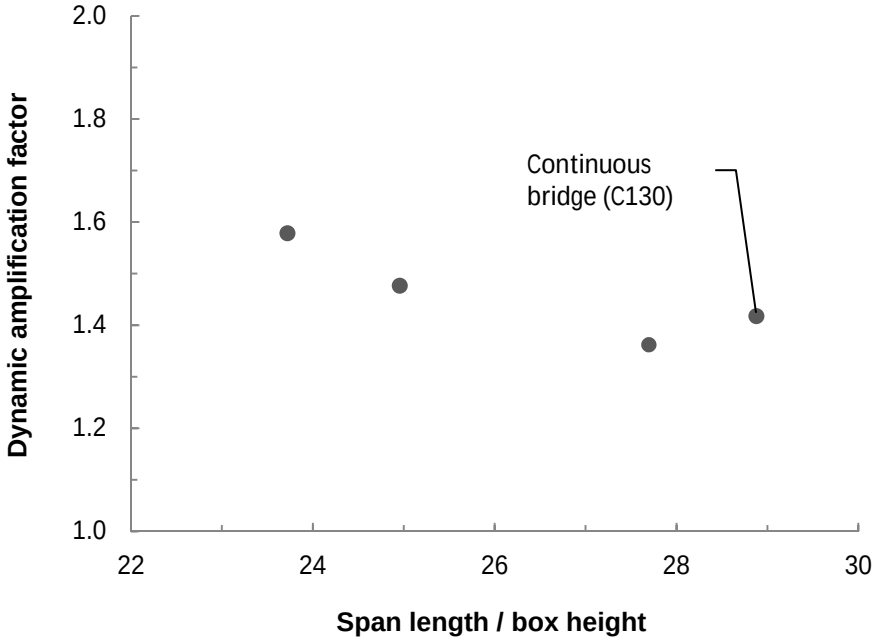


*Figure 6.16: Dynamic amplification factor*

## 6.8 Summary

In this chapter, the following parameters were investigated to determine their influence on the load-carrying capacity of a twin steel box-girder bridge: stud length, railings, bridge curvature, structural indeterminacy, and span length. It was found that the pull-out strength of stud connections played a major role in the post-fracture behavior of these types of bridges. Results from this research program indicate that the pull-out strength of a stud connection is negatively influenced by the presence of a haunch and limits the maximum load a twin steel box-girder bridge can carry following the fracture of one of its girders. T501 bridge rails act as deep beams at the edges of the concrete deck and can carry substantial loads after their expansion joints close. In the models studied, their presence initially reduced the deck deflection compared to the models that did not include rails; however, models with rails showed an increase in the pull-out forces acting on the stud connections, which resulted in the haunch separating along the outside of the intact girder near the fracture location. This haunch separation caused the deflection in the fractured girder to increase abruptly. Another parameter that was varied in the finite element models developed for this research was the radius of curvature, and the results showed sensitivity to changes in this value. As the radius of curvature decreased, deflections in the fractured girder increased. Structural redundancy achieved through a continuous-span bridge positively affected the overall load-carrying capacity of the twin steel box-girder bridges analyzed for this research. The continuity of the bridge helped it sustain the applied load without causing haunch separation along the outside of the intact girder. Finally, post-fracture girder deflections showed a stronger dependence on the span length-to-depth ratio than the span length itself. As the ratio of span to depth increased, the fractured girder deflections also increased.

In the following chapter, conclusions about the modeling of twin steel box-girder bridges for redundancy evaluations are provided, and recommendations for future research are given. The conclusions are based on the findings obtained from the detailed testing program executed

during this study, from implementation of the simplified modeling procedure described at the beginning of this report, and from detailed finite element analyses conducted for this project.

# Chapter 7. Conclusions and Recommendations

## 7.1 Summary of Research

The AASHTO LRFD Bridge Design Specifications (AASHTO, 2007) currently classify twin steel box-girder bridges as fracture critical. According to this designation, such a bridge "contains one or more fracture critical members whose failure is expected to result in the collapse of the bridge or the inability of the bridge to perform its function." The purpose of the research program described in this report was to investigate and to quantify the inherent redundancy that this type of bridge possesses—contrary to the current fracture critical bridge classification. To meet this goal, a comprehensive research program was carried out that included three tests on a full-scale fracture critical bridge (Neuman, 2009), laboratory tests to quantify the tension capacity of shear stud connections (Sutton, 2007 and Mouras, 2008), development of a simplified modeling method to evaluate the redundancy of twin steel box-girder bridges (Samaras, 2009), and development of modeling guidelines to conduct detailed finite element simulations (Kim, 2010). In this report, a brief summary of the testing program was provided; emphasis, however, was on the presentation of a simplified procedure to estimate the load-carrying capacity of a twin steel box-girder bridge following the fracture of one of its girders and on methods for creating detailed finite element models that can be used to evaluate the redundancy of these types of bridges in cases where the simplified modeling approach does not provide sufficient information or in cases where the results obtained from the simple analysis approach require refinement.

In Chapter 2 of this report, the simplified modeling approach was introduced. The initial steps of the procedure define strength checks that are needed to evaluate the redundancy of a twin steel box-girder bridge. The strength checks that require evaluation are as follows: (a) intact girder has adequate shear and moment capacity, (b) deck has adequate shear capacity, and (c) shear studs have adequate tension capacity. If the bridge under investigation satisfies only the first two conditions, it is still possible that it can sustain load without collapsing. Under these conditions, a yield line analysis can be used to evaluate the ability of the deck to transmit load to the intact girder without the shear studs connecting the deck to the fractured girder. In the event that the capacity predicted from the yield line analysis is not adequate, a more refined analysis can be performed.

For the detailed finite element models developed for this research, various simulation techniques were utilized to capture important response mechanisms that were expected to develop in a severely damaged bridge, as described in Chapter 4. These techniques were utilized to construct analysis models simulating the full-scale bridge fracture tests. These models were successful in capturing prominent bridge behavior and component failures observed during the experimental program. Various bridge models constructed in the same way as the bridge test simulation models were then used to investigate how changes in several of the design variables and bridge geometry affect the remaining load-carrying capacity of twin steel box-girder bridges following the full-depth fracture of one girder.

Based on a literature review of past bridge fractures, results collected from the full-scale bridge fracture tests, analytical studies performed using the simplified procedure developed during this project, and detailed finite element simulations, several important conclusions about the performance of twin steel box-girder bridges can be drawn. The conclusions are presented in the next section.

## 7.2 Conclusions and Recommendations

### 7.2.1 Damage Level and Loading Method

Because there are no incidents involving the fracture of twin steel box-girder bridges reported in the literature, it was necessary to assume a damage level for carrying out redundancy evaluations during this research project. In order to provide a conservative estimate of performance, and based on past experiences with damage in plate girder bridges, a full-depth fracture of one girder was assumed. Thus, the sudden fracture of one girder was selected as the damage level for evaluating redundancy in twin steel box-girder bridges.

An HS-20 standard design truck was used as the primary live load for this research project. In this study, two different types of loading schemes were utilized. First, for the purposes of carrying out a redundancy evaluation, the truck load was positioned statically on the deck at a location that would induce the maximum positive bending moment on the fracture location of the bridge under investigation. To simulate worst-case loading conditions, it was assumed that the girder fracture occurred suddenly immediately after the live load was placed above the fracture location. Second, for the purposes of computing overall load-carrying capacity, the truck live load was positioned in the same location as used for the redundancy evaluations, but the live load was incrementally increased in proportion to the axle loads until failure occurred or a predetermined load level was met.

### 7.2.2 Concrete Deck and Shear Stud Design

Based on the results of laboratory tests conducted as part of this research project, it is recommended that shear studs be sufficiently tall so that they pass beyond the bottom layer of reinforcement used in the deck. When the shear studs pass the bottom mat of reinforcement, the ductility of the connection is improved. Moreover, test results indicate that by increasing the length of the shear studs, their tensile capacity increases. If the shear studs have sufficient capacity to resist the pull-out forces that develop after a fracture, the concrete deck will reach its moment capacity, and a plastic hinge line will form above the interior top flanges of the steel girders. From an overall performance perspective, it is more desirable to form a hinge in the concrete deck than to have a shear stud failure. The hinge formation, compared to the shear stud failure, is more ductile. Furthermore, after the formation of a hinge, loads can still be transferred away from the fracture location. Design of the concrete deck and the shear studs must be considered at the same time. A high tensile capacity in the shear stud connections will have limited benefit because the moment capacity of the concrete deck will govern. Conversely, the design of a thick deck may result in shear stud pull-out failures. Thus, it is highly recommended that the design be based on a balanced section in which the shear studs fail just after the formation of hinges in the concrete deck.

### 7.2.3 Finite Element Modeling

*Concrete Deck*

In this study, the concrete deck was modeled using solid elements with embedded truss elements to simulate the reinforcing steel. Considering the importance of the concrete deck as a load transferring component in twin steel box-girder bridges, it is critical to simulate its behavior accurately. As shown in the second and third full-scale bridge tests, extensive material failures,

including extensive cracking and crushing, are inevitably expected for redundancy evaluations due to the expected damage level near the onset of collapse. To account for these material failures, a cast iron plasticity model was utilized for the concrete deck modeling rather than a concrete smeared cracking model. Though the cast iron plasticity model does not allow for the softening behavior that a smeared cracking model permits, it does have the essential feature of being able to specify different strengths for tension and compression. The cast iron plasticity model was found to be an excellent compromise between accuracy and efficiency. It produced simulation results that agreed well with benchmark tests, yet it did not cause the same types of numerical convergence problems that were experienced when the smeared cracking model was used.

Using the cast iron plasticity model, the deflection of the concrete deck was found to be sensitive to both the specified tensile strength and the mesh density. Based on parametric studies of finite element models developed to represent laboratory tests on the pull-out behavior of studs embedded in a concrete deck with a haunch, it was found that the model properly simulated deck bending behavior when the tensile strength of the model was specified to be 4% of the compressive strength with the specific mesh density of three elements through the deck thickness and ten elements along the deck width. It is important to recognize, however, that this specific tensile strength and mesh density do not apply to all cases because they were validated against a limited set of test data.

*Stud Connections*

Under normal conditions, shear studs installed on girder top flanges are subjected to shear forces induced by the composite action between the girders and the concrete deck. Results from this research have shown, however, that significant tension forces develop in shear studs of twin steel box-girder bridges as deformations increase following the fracture of a girder. Such tension forces induce stud pull-out failures, which lead to extensive haunch separation. This behavior was observed during the full-scale tests that took place under this research program and was detected in the finite element simulations. Stud pull-out failures reduce both the transverse and the vertical bending stiffness of a bridge, thereby inducing large deflections following the fracture of a girder. Because predictions of bridge redundancy are sensitive to the specified load-deformation response of shear stud connections, and because observations from full-scale tests indicate possible damage mechanisms initiated through both shear and tension, it is important that models used for redundancy evaluations account for these components of response. The experimental equations proposed by Topkaya (2002) and Mouras (2002) were used in this research and allowed for a determination of stud connection response for shear and tension independently, but no information is currently available on the coupled interaction of shear and tension in stud connections.

Even when the shear and tension response of the stud connections are defined independently, it is essential that accurate values for capacity be specified. Because of the sensitivity that the stud pull-out strength has on the predicted load-carrying capacity of twin steel box-girder bridges following the fracture of one of its girders, care must be taken to properly account for such factors as the presence of a haunch, stud embedment length, stud spacing, and stud positioning when computing the tension capacity of different shear stud arrangements. The equation used to determine shear strength, however, does not consider these factors. Thus, aside from research needed on how shear and tension interact in stud connections near the onset of

bridge collapse, additional research is needed to accurately evaluate the shear strength of stud connections when a haunch is present.

*Railing*

The presence of a railing (TxDOT standard T501 rail) in the finite element simulation models significantly affected girder deflections by causing an increase in the haunch separation length in both the fractured and the intact girders relative to models that did not explicitly model the rails. Although it reduced the deck deflection during the initial stages of response before haunch separation was initiated along the outside of the intact girder, it eventually increased the haunch separation length in both girders by locally raising tensile forces on the stud connections. Therefore, a bridge analysis that ignores the effects of railings when carrying out a redundancy evaluation may not be conservative.

*Bridge Curvature*

In this study, the response of a bridge with a span of 120 ft was evaluated considering three different bridge radii of curvature. The range considered included a bridge with an infinite radius of curvature (i.e., a straight bridge) and one with a curvature of 800 ft, which is near the limit of what is found in practice. For the redundancy evaluations, girder fracture was assumed to occur in the exterior girders of the curved bridges to achieve larger torsional forces than would be obtained by fracturing the inside girders. According to the finite element analyses of these bridge models, a decrease in the radius of curvature led to an increase in the vertical displacement of the fractured girder. Thus, it was concluded that bridge curvature can play an important role in controlling the post-fracture behavior of twin steel box-girder bridges. Because of the limited number of cases that were evaluated, however, it is recommended that additional analyses be carried out to identify the dependency of bridge redundancy on bridge radius of curvature.

*Structural Redundancy*

To investigate differences in bridge behavior between a simple-span bridge and a multiple-span bridge following the fracture of one girder, a two-span continuous bridge was analyzed using a finite element model that was developed using the guidelines presented in this report. Due to different cross-sectional dimensions and component sizes (i.e., thickness and width of bottom flange, top flange, and web), it was not reasonable to compare directly the computed response of the two-span continuous bridge model with the simply supported bridge model used for the evaluation. Nonetheless, the analyses indicated that the two-span bridge could carry load without collapsing even after a sudden haunch separation occurred along the outside of the fractured girder. Because of the cantilever action that could develop in the continuous-span bridge model, loads could be transferred longitudinally along the span of the bridge, and tension forces acting on the stud connections in the intact girder were never large enough to cause pull-out failures. Conversely, for the simple-span bridge model that was analyzed, significant reductions in stiffness or unstable behavior occurred after haunch separation took place along the outside of the intact girder. The good performance achieved by the continuous two-span bridge was a result of redundancy achieved through static indeterminacy.

## 7.3 Suggestions for Future Study

### 7.3.1 Strength of Stud Connection

In the third bridge fracture test, collapse was initiated by slipping between the outside top flange of the fractured girder and the concrete deck. After the test, it was observed that extensive horizontal and diagonal cracks developed along the outside haunch of the fractured girder. This observed damage suggests that the shear strength of a stud connection may be affected by the presence of a haunch and shear-tension interaction. Past research has not considered these factors, and equations that are currently available may over-estimate the shear strength of a stud connection. Because of the sensitivity of the computed results to changes in stud connection behavior, additional testing is needed to accurately capture the response of shear studs in a haunch under combined states of tension and shear.

### 7.3.2 Bridge Curvature

Results obtained from finite element models developed for this research indicate that as the radius of curvature decreases, the exterior girder deflections increase due to the eccentricity between the loading position and the bridge supports. Because of this eccentricity, curved bridges must resist higher torsional forces than straight bridges. For the cases studied, however, the shear stresses associated with such increased torsional forces were small compared to those developed in a straight bridge. For the bridge model that was analyzed, which was a simply supported bridge with a span of 120 ft, the shear stresses associated with torsion increased by only 4 ksi as the radius of curvature changed from infinity (i.e., a straight bridge) down to 800 ft. Because the eccentricity between the loading position and the supports is a function of bridge span, and because torsional moment increases with this eccentricity, the effects of curvature require further investigation than what was carried out during this study.

### 7.3.3 Bridge Rails

Results from this research showed that railing performance strongly influences the overall load-carrying capacity of twin steel box-girder bridges following the fracture of one girder. In this study, only the influence of T501 rails, using standard construction details, was investigated. In contrast, many other fracture critical bridges utilize bridge rails that have an intermittent base or have less depth than the T501. Consequently, it is not certain how these other rail systems influence system capacity following the failure of a critical component. As such, research is needed to assess the performance of various rail systems used on fracture critical bridges to determine how they contribute to bridge redundancy. While rails can act like deep beams on the edges of the deck and can carry significant loads, they can also lead to increased tensile forces acting on shear stud connections. Accordingly, additional research is needed to investigate how these components may be used to improve overall redundancy. While attempts should not be made to drastically change design details that can detract from the primary purpose of a railing to serve as a crash barrier, such factors as the number, size, and placement of expansion joints should be studied to determine how such details affect performance. For bridge rails that do not meet desired performance measures, retrofit methods should be investigated.

## 7.4 Closing Comments

Through three full-scale tests, the FSEL test bridge performed much better than the AASHTO Bridge Design Specifications suggest, particularly given the fact that it was a simply supported span, had expansion joints in its railings, and had all external cross-frames removed. After sustaining a full-depth fracture in its exterior girder, the test bridge demonstrated sufficient redundancy through alternate load paths to maintain loads far exceeding those for which it was designed. Detailed finite element studies considering a wide range of design parameters confirmed the redundancy of these types of bridge systems. After additional research is carried out, revisions to the current AASHTO specifications should be considered so that the behavior of these bridges following the failure of a critical tension flange can be accurately predicted and so that appropriate inspection and maintenance requirements can be prescribed. Given the demonstrated redundancy in these systems beyond that for which they have been credited, the current requirement for bi-annual inspections does not appear to be an effective use of labor or financial resources.

# References


ACI Committee 209. (1982). "Prediction of Creep, Shrinkage and Temperature Effects in Concrete Structures." Designing for Creep and Shrinkage in Concrete Structures, ACI Publication SP-76, Detroit, pp.193-300.

ACI Committee 318. (2008). Building Code Requirements for Structural Concrete (ACI 318-05) and Commentary (ACI 318R-08). ACI, Farmington Hills, MI.

AE 3145 Strain Gage Notes. (2000). "Strain Transformation and Rosette Gage Theory" http://www.ae.gatech.edu/people/jcraig/classes/ae3145/Lab2/strain-gages.html

American Association of State Highway Transportation Officials. (1977). AASHTO Standard Specification for Highway Bridges. 12th edition. Washington, D.C.

American Association of State Highway Transportation Officials/American Welding Society. (2002). AASHTO/AWS D1.5M/D1.5:2002 Bridge Welding Code. AASHTO/AWS, Washington D.C./Miami, FL.

American Association of State Highway Transportation Officials. (2004). AAHSTO LRFD Bridge Design Specifications. Washington, D.C.

American Association of State Highway Transportation Officials. (2007). AASHTO LRFD Bridge Design Specifications. Washington, D.C.

Barnard, Timothy J. (2006). "Constructing a Full-Scale Horizontally-Curved Twin Steel Trapezoidal Box Girder Bridge Segment to Determine Redundancies in Fracture Critical Bridges." M.S. Departmental Report. The University of Texas at Austin, Austin, TX.

Barsom, John M. and Rolfe Stanley T. (1999), *Fracture and Fatigue Control in Structures: Applications of Fracture Mechanics* (*Third Edition*). Butterworth-Heinemann, Woburn, MA, pp. 414-424.

Connor, Robert J., Dexter, Robert, and Mahmoud, Hussam. (2005). "Inspection and Management of Bridges with Fracture-Critical Details." National Cooperative Highway Research Program Synthesis 354. Transportation Research Board, national Academy Press, Washington, D.C.

Connor, Robert J., Kaufmann, Eric J., Fisher, John W., and Wright, William J. (2007). "Prevention and Mitigation Strategies to Address Recent Brittle Fractures in Steel Bridges." Journal of Bridge Engineering, ASCE, Vol. 12, No. 2, pp 164-173.

Dally, James W., Riley, William F. (1965). *Experimental Stress Analysis*. IIT Research Institute, Chicago.

Dassault Systemes. (2007a). *ABAQUS Analysis User's Manual*, Version 6.7, ABAQUS, Inc., Rising Sun Mills, R.I.

Dassault Systemes. (2007b). *ABAQUS Theory Manual*, Version 6.7, ABAQUS, Inc., Rising Sun Mills, R.I.

Dexter, Robert J., Connor, Robert J., and Mahmoud, Hussam. (2005). "Review of Steel Bridges with Fracture-Critical Elements." Transportation Research Record, Design of Structures 2005, No. 1928, pp. 75-82.

Espinoza, Omar. (2007). "Measurements of Deformations and Stresses due to Plate out-of-flatness in a Steel Twin Box Girder Bridge System." M.S., The University of Texas at Austin.

Fisher, John W., Pense, Alan W., and Roberts, Richard. (1977). "EVALUATION OF FRACTURE OF LAFAYETTE STREET BRIDGE." Journal of the Structural Division, ASCE, Vol. 103, No. ST7, pp.1339-1357.

Fisher, John W., Pense, Alan W., and Hausammann, Hans. (1985). "Analysis of Cracking of I-79 Bridge at Neville Island." *Fracture Problems in the Transportation Industry*, ASCE, New York, NY, USA, pp. 1-19.

Ghosn, Michel, and Moses, Fred. (1998). "Redundancy in Highway Bridge Superstructures." NCHRP Report 406, TRB, National Research Council, Washington, D.C.

Hartle, R. A., Amrhein, W. J., Wilson III, K. E., Baughman, D. R., and Tkacs, J. J. (1991). Bridge Inspector's Training Manual/90. FHWA-PD-91-015. FHWA, McLean, Va.

Hovell, Catherine. (2007). "Evaluation of Redundancy in Trapezoidal Box-Girder Bridges Using Finite Element Analysis." M.S., The University of Texas at Austin.

Idriss, R. L., White, K. R., Woodward, C. B., and Jauregui, D.V. (1995). "Evaluation and Testing of a Fracture Critical Bridge." NDT&E International, vol. 28, no. 6, pp. 339-347.

Kent, Dudley C. and Park, Robert. (1971). "Flexural Members with Confined Concrete." Journal of the Structural Division, Proceedings of the American Society of Civil Engineers, pp. 1969-1990.

Kim, Janghwan. (2010). "Finite Element Modeling of Twin Steel Box-Girder Bridges Following Girder Fracture." Ph.D. Dissertation, The University of Texas at Austin. (In progress).

Kupfer, Helmut B. and Gerstle, Kurt H. (1973). "Behavior of Concrete under Biaxial Stresses." Journal of the engineering Mechanics Division, ASCE, Vol. 99, No. EM4, pp. 853-866.

Mouras, Joshua M. (2008). "Evaluating the Redundancy of Steel Bridges: Improving the Strength and Behavior of Shear Stud Connections under Tensile Loading", M.S. Thesis. The University of Texas at Austin, Austin, TX.

Mouras, J. M., Sutton, J. P., Frank, K. H. and Williamson, E. B. (2009). "The Tensile Capacity of Welded Shear Studs." Report FHWA/TX-08/0-5498-1, Center for Transportation Research, University of Texas at Austin, Austin, TX.

Neuman, Bryce J. (2009). "Evaluating the Redundancy of Steel Bridges: Full-Scale Destructive Testing of a Fracture Critical Twin Box-Girder Steel Bridge", M.S. Thesis. The University of Texas at Austin, Austin, TX.

Newmark, N. M. and Hall, W. J. (1982). *Earthquake Spectra and Design*. Earthquake Engineering Research Institute, Berkeley, CA

Norris, Charles H., Wilbur, John B. (1960). *Elementary Structural Analysis*. McGraw-Hill Book Company Inc.

Post-Tensioning Institute (PTI) Cable-Stayed Bridge Committee. (2007). Recommendations for Stay Cable Design, Testing and Installation, 5th edition. Phoenix, AZ.

Olson, Dan. (2008). "I-35W Engineer Answers Concerns about the New Bridge," Minnesota Public Radio. http://minnesota.publicradio.org/display/web/2008/07/30/issues_2004/

Quiel, Spencer. (2003). "Forensic Analysis of the Steel Girder Fracture in the I-95 Brandywine River Bridge." Research Experience for Undergraduates Report, The University of Notre Dame.

Russell, H.G., R.A. Miller, H.C. Ozyildirim, and M.K. Tadros. (2003). "Compilation and Evaluation of Results from High Performance Concrete Bridge Projects-Final Report." (CD-ROM), Proceedings, 3rd International Symposium on High Performance Concrete and PCI National Bridge Conference, Orlando, Fla., Oct., pp. 19-22.

Samaras, V. (2009). "Simplified Methods of Evaluating the Redundancy of Twin Trapezoidal Box Girder Bridges", M.S. Thesis. The University of Texas at Austin, Austin, TX.

Scheffey, C.F. (1971). "Pt. Pleasant Bridge Collapse: Conclusions of the Federal Study." Civil Engineering, Vol. 41, No. 7.

Schwendeman, L.P., and Hedgren, A.W. (1978). "Bolted repair of fractured I-79 girder." Journal of the Structural Division, ASCE, Vol. 104, No. 2, pp. 134-143.

Stith, Jason (2010). *UT Lift User's Guide*. The University of Texas at Austin, Austin, TX.

Sutton, James P. (2007). "Evaluating the Redundancy of Steel Bridges: Effect of a Bridge Haunch on the Strength and Behavior of Shear Studs under Tensile Loading", M.S. Thesis. The University of Texas at Austin, Austin, TX.

Sutton, James. P., Mouras, Joshua M., Frank, Karl H., and Williamson, Eric B. "The Tensile Capacity of Welded Shear Studs." Center for Transportation Research at the University of Texas at Austin. FHWA/TX-08/9-5498-R2. October, 2008.

Texas Department of Transportation. (2001). Bridge Detailing Manual.

Texas Department of Transportation. (2006). Bridge Railing Manual.

Texas Department of Transportation (TxDOT). (2003). Traffic Rail: Type T501. <ftp://ftp.dot.state.tx.us/pub/txdot-info/cmd/cserve/standard/bridge/rlstde16.pdf> Published: February 2003. Accessed: 02 July 2007.

Ugural, A. C., Fenster, S. K. (1995). "Advanced strength and applied elasticity." Third Edition, Prentice-Hall PTR, Upper Saddle River, New Jersey, pp. 155-162.

VISHAY Micro-Measurements. (2008). "Strain Gage Rosettes: Selection, Application and Data Reduction", Tech Note TN-515.

Wight, James K. and MacGregor, James G. (2008). *Reinforced Concrete: Mechanics and Design* (*5th Edition*). Prentice-Hall, Upper Saddle river, NJ.

# Appendix A. Implementation of Simplified Modeling Approach: Example 2−Analysis of Woodway Bridge (Span 11)

## Introduction

This example focuses on span 11 of the Woodway exit ramp between IH 610 and the Katy Freeway in Houston, TX. This bridge is simply supported and straight (i.e., $R=\infty$), and its total length is 197.6 ft. Figure A1 shows the elevation view of span 11 of the Woodway Bridge and other general information. The top and bottom flange thickness changes along the span of the bridge. Table A1 summarizes all the dimensions of both flanges along the span of the bridge. Only three steel sections are used along the length of the span. The "Transition" sections occur due to different cutoff points for the top and bottom flanges. Figures A2 and A3 present the typical cross-section of the bridge and steel girder respectively. A typical SSTR section is used for the railing.

**Table A1: General information of bottom and top flange**

| Type of Section | Length of application measured from south | Bottom Flange | | Top Flange | |
|---|---|---|---|---|---|
| | (ft) | $t_{BF}$ (in.) | $b_{BF}$ (in.) | $t_{TF}$ (in.) | $b_{BF}$ (in.) |
| End Section | 0-51.25 | 1.50 | 44.5 | 1.25 | 18 |
| Transition Section | 51.25-59.25 | 2.00 | 44.5 | 1.25 | 18 |
| Middle Section | 59.25-138.75 | 2.00 | 44.5 | 1.75 | 18 |
| Transition Section | 138.75-146.75 | 2.00 | 44.5 | 1.25 | 18 |
| End Section | 146.75-197.6 | 1.50 | 44.5 | 1.25 | 18 |

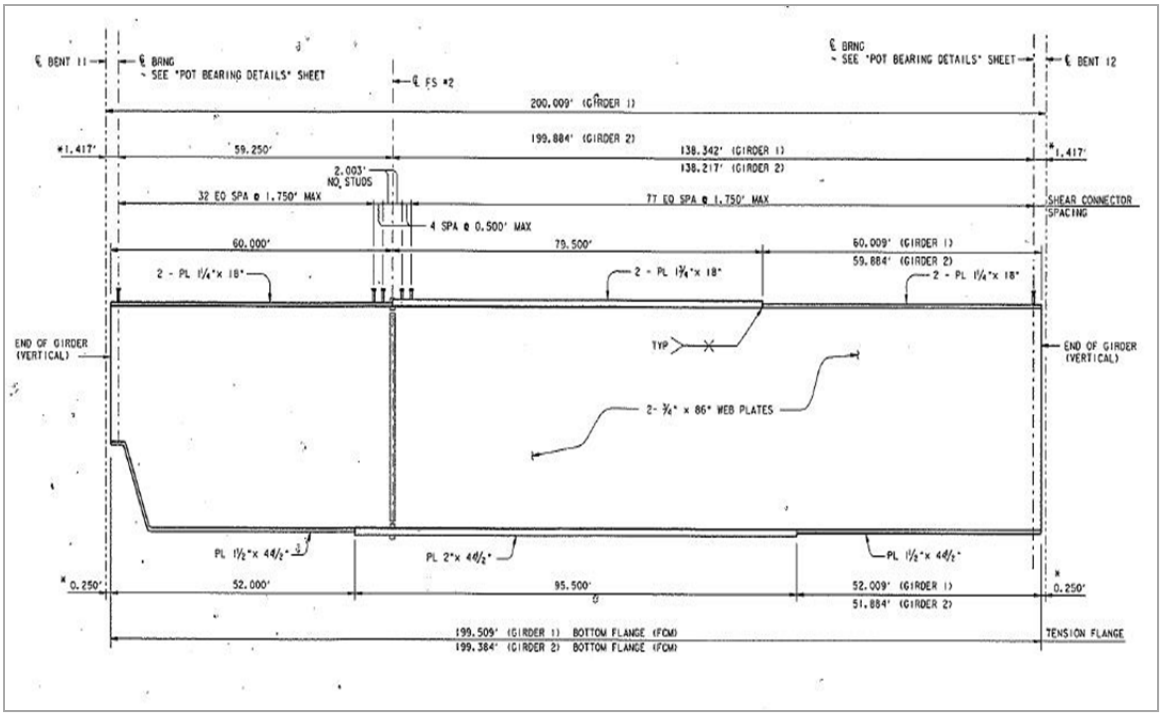


*Figure A1: Elevation view of Woodway Bridge span 11*

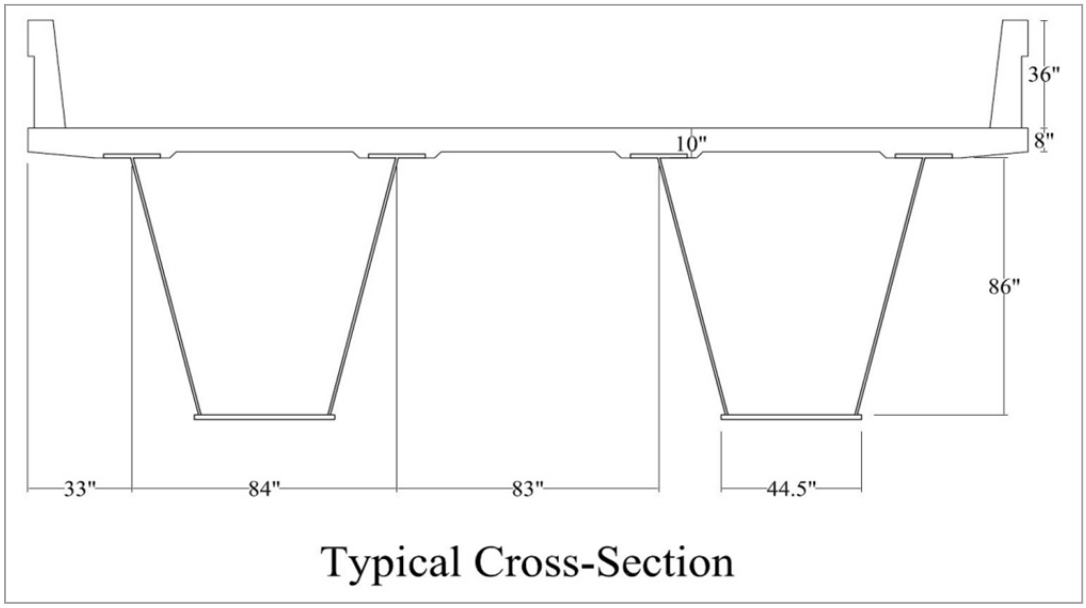


*Figure A2: Typical cross-section of the Woodway Bridge span 11*

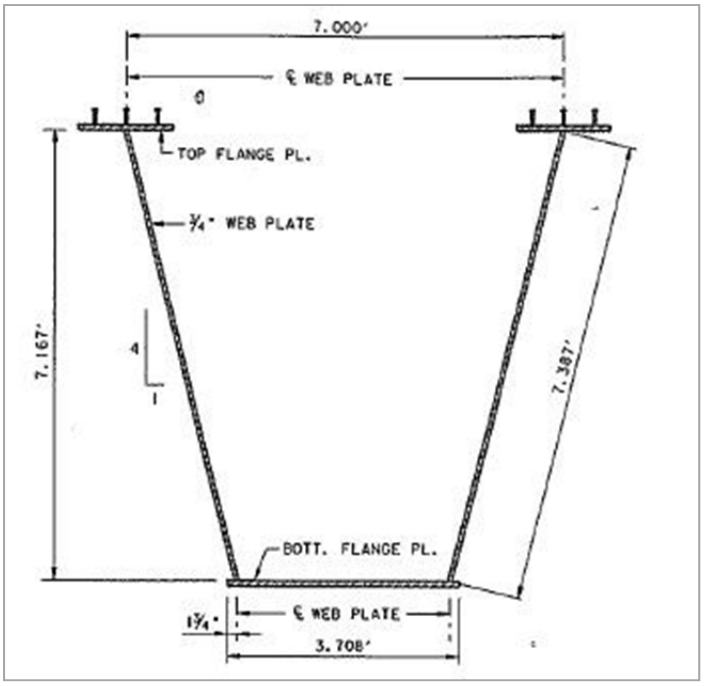


*Figure A3: Typical cross-section of the steel girder of the Woodway Bridge span 11*

## Calculation of the Transmitted Load to the Intact Girder

It is assumed that half of the entire weight of the bridge and the entire live load on the bridge is needed to be resisted from the intact girder at an event of a fracture occurs. These loads are calculated below:

**Weight of one steel box girder:**

$$W_{girder} = 1.15 \cdot (244.72/144 \text{ ft}^2) \cdot (0.490 \text{ kips/ft}^3) = 0.958 \text{ kip/ft (End Section)}$$

$$W_{girder} = 1.15 \cdot (266.95/144 \text{ ft}^2) \cdot (0.490 \text{ kips/ft}^3) = 1.044 \text{ kip/ft (Transition Section)}$$

$$W_{girder} = 1.15 \cdot (284.97/144 \text{ ft}^2) \cdot (0.490 \text{ kips/ft}^3) = 1.116 \text{ kip/ft (Middle Section)}$$

Notes: This weight if for one girder. Cross-sectional areas of End, Transition, and Middle section are 244.72 $in^2$, 266.95 $in^2$ and 284.97 $in^2$, respectively. Density of steel is taken as 490 $lb/ft^3$. To account for internal diaphragms, stiffeners, etc., the weight of the steel girder is multiplied by a factor of 1.15.

**Concrete deck:**

$$W_{deck} = (317 \cdot 8 / 144 \text{ ft}^2) \cdot (0.150 \text{ kip/ft}^3) = 2.642 \text{ kip/ft}$$

Notes: Width of concrete deck is 26 ft–5 in. = 317 in. Density of concrete is taken as 150 lb/ft3. Deck thickness is 8 in.

**SSTR Railing:**

$W_{railings} = 2 \cdot (312/144 \text{ ft}^2) \cdot (0.150 \text{ kip/ft}^3) = 0.65 \text{ kip/ft}$

Notes: Multiplied by 2 to account for two rails. Cross-sectional area of one rail is calculated to be 312 $\text{in}^2$.

**HS-20 Truck:**

$W_{truck} = 2 \cdot 72 \text{ kips} = 144 \text{ kips (load factor=2)}$

**Load to be transmitted:**

$F = \Sigma(W_{girder\ i} \cdot L_i) + (W_{deck}/2 + W_{railings}/2) \cdot \text{L} + W_{truck}$

$F = (0.958 \cdot 102.1 + 1.044 \cdot 16 + 1.116 \cdot 79.5) + (2.642 + 0.65) \cdot 197.6/2 + 144 = 672.5 \text{ kips}$

$F = 672.5 \text{ kips}$

## Calculation of Maximum Moment on the Bridge

**Moment due to dead load and truck load**

The moment at the mid-span is calculated below:

$M_{DL} = (2 \cdot \Sigma(W_{girder\ i} \cdot L_i/L) + W_{deck} + W_{railings}) \cdot L^2/8$

$M_{DL} = 2 \cdot (0.958 \cdot 102.1 + 1.044 \cdot 16 + 1.116 \cdot 79.5) \cdot 197.6/8 + (2.\ 642 + 0.65) \cdot 197.6^2/8$

$M_{DL} = 26{,}107 \text{ kip-ft}$

The values are computed knowing that the moment of a simply supported beam loaded with a uniform load follows the formula $M(x) = W \cdot x^2/2$, where $W$ is the uniform load applied on the girder and $x$ is the distance from the support. Using the moment equation, the moment at the end of the two transition sections can found—$M_{DL}(51.25)$ and $M_{DL}(59.25)$ are 7,026 kip-ft and 9,391 kip-ft respectively.

As in Example 1, the middle axle of the 144-kip truck load is positioned at the centerline of the bridge. The maximum moment at the mid-span of the bridge due to both the dead load and the truck load is calculated to be $M_{max}$ = 29,384 kip-ft. By superimposing the moment diagrams for these loads, the moments at the flange transitions are $M$ (51.25) =10,890 kip-ft and $M$ (59.25) =13,858 kip-ft.

## Analysis of Composite Section

The plastic moment capacity of the intact girder should be calculated to determine if it has the flexural capacity to sustain the live load and the dead load applied to the bridge. The moment capacity was checked at the mid-span and at the two flange transitions. The specified minimum yield strength of $f_y$ = 50 ksi is used in the calculations.

**Middle Section**

Find the plastic neutral axis by setting $T = C$:

$T = A_s \cdot f_y = (44.5 \cdot 2 + 2 \cdot 88.644 \cdot 0.75 + 2 \cdot 18 \cdot 1.75) \cdot 50 = 14{,}248.3$ kips

$C_c = 0.85 \cdot f_c' \cdot t_s \cdot b_{eff} = 0.85 \cdot 4 \cdot 8 \cdot 158.5 = 4{,}311.2$ kips

Because $T > C$, the plastic neutral axis is in the girder.

$C_s = (A_s \cdot f_y - C_c) / 2 = (14{,}248.3 - 4{,}311.2) / 2 = 4{,}968.55$ kips

Using this equation, the compressive force needed to be developed in the steel section to achieve equilibrium ($C = T$) can be computed.

$C_{tfl} = 2 \cdot t_{tfl} \cdot b_{tfl} \cdot f_y = 2 \cdot 1.75 \cdot 18 \cdot 50 = 3150$ kips

The top flanges can resist 3150 kips in compression, which is less than is required to obtained equilibrium. As a result, the plastic neutral axis (PNA) falls in the web. Assuming that $x$ is the distance from the neutral axis to the bottom of the top flange (Figure A4), the depth of the neutral axis can be determined as a function of the depth:

$x = (4{,}968.55 - 3150) / (2 \cdot 0.75 \cdot (17/16)^{0.5} \cdot 50) = 23.52$ in.

Note: The $(17/16)^{0.5}$ factor is based on the slope of the web.


*Figure A4: Plastic neutral axis location*

Thus:

$C_c = 4{,}311.2$ kips

$C_{tfl} = 3150$ kips

$C_{web} = 1818.55$ kips

$T_{web} = A_{web} \cdot f_y = 2 \cdot 0.75 \cdot (86\text{-}23.52) \cdot (17/16)^{0.5} \cdot 50 = 4830.22$ kips

$T_{bottom\ flange} = A_{bottom\ flange} \cdot f_y = 44.5 \cdot 2 \cdot 50 = 4450$ kips

By taking moments about the PNA, the nominal plastic moment capacity is calculated:

$M_{bottom\ flange} = T_{bottom\ flange} \cdot (1 + 86 - 23.52) = 282{,}486$ kip-in.

$M_{web} = C_{web} \cdot 23.52/2 + T_{web} \cdot (86\text{-}23.52) / 2 = 172{,}282.22$ kip-in.

$M_{C\ tfl} = C_{tfl} \cdot (1.75/2 + 23.52) = 76{,}844.25$ kip-in.

$M_{C\ concrete} = C_c \cdot (4 + 2 + 23.52) = 127{,}266.62$ kip-in.

Note: The 2-in. term added in the moment arm accounts for distance from the bottom of the concrete deck to the bottom of the top flange.

Thus, $M_P = 282{,}486 + 172{,}282.22 + 76{,}844.25 + 127{,}266.62$

$M_{P\ Middle\ Section} = 658{,}879$ kip-in. $= 54{,}906$ kip-ft

Previously, $M_{max}$ was found to be 29,384 kip-ft. Therefore, the plastic moment capacity is sufficiently large to sustain the entire dead load of the bridge plus the truck live load.

Following the same procedure, the plastic moment capacity of the Transition and End sections are calculated and found to be larger than the maximum moment that will be applied to these sections if a fracture of the outer girder occurred.

$M_{P\ Transition\ Section} = 633{,}734$ kip-in. $= 52{,}811$ kip-ft $> M\ (59.25) = 13{,}858$ kip-ft

$M_{P\ End\ Section} = 564{,}757$ kip-in. $= 47{,}063$ kip-ft $> M\ (51.25) = 10{,}890$ kip-ft

## Analysis of Concrete Deck

As before, the bending and shear capacity of the concrete deck are checked to ensure that they are adequate to resist the moment and the shear produced by the unsupported load of the fractured girder. These capacities are based on a 1-ft wide transverse deck section as shown in Figure A5.

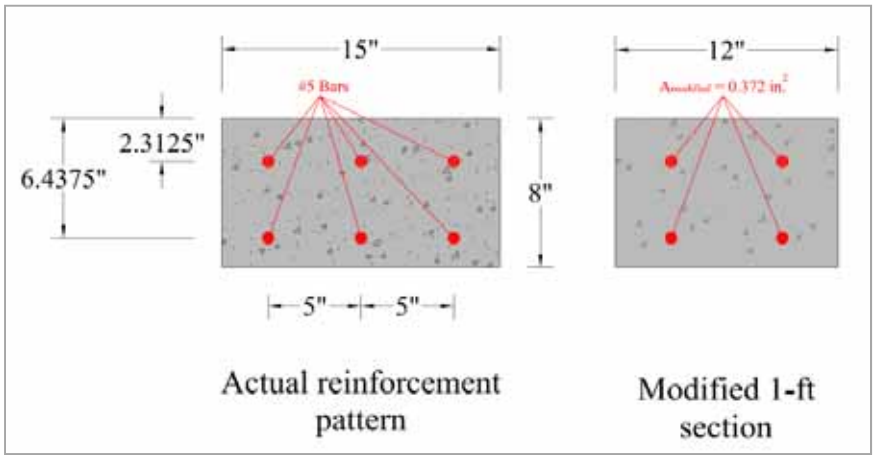


*Figure A5: Actual and modified 1-ft wide section of the concrete deck in the transverse direction*

**Positive Moment Capacity:**

The assumed strain and stress failure profile are shown in Figure A6:

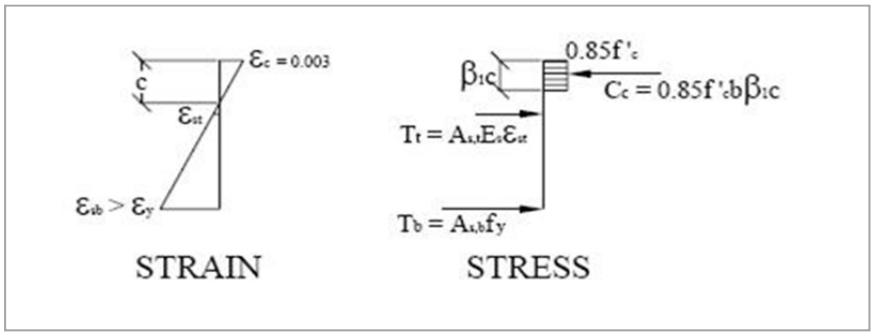


*Figure A6: Strain and stress gradients at positive moment regions*

According to ACI 318-08, it is assumed that the ultimate strain of concrete is 0.003 in./in. and the bottom reinforcement yields prior to failure. The top reinforcement is included in the calculations for accuracy. The concrete strength is taken as 4 ksi, and the reinforcement strength is taken as 60 ksi—the nominal strength specified in the bridge plans.

Let $C = T$:

$C = 0.85 \cdot fc' \cdot \beta_1 \cdot c \cdot b = 0.85 \cdot 4 \cdot 0.85 \cdot 12 \cdot c = 34.68 \cdot c$

Note: $\beta_1 = 0.85$ for 4 ksi concrete.

$\varepsilon_{s,\,bottom} = 0.003 \cdot (6.4375 - c) / c$

$\varepsilon_{s,\,top} = 0.003 \cdot (2.3125 - c) / c$

$T_{bottom} = A_{s,bottom} \cdot f_y = 2 \cdot 0.372 \cdot 60 = 44.64$ kips

$T_{top} = A_{s,top} \cdot \varepsilon_{s,\,top} \cdot E_s = 2 \cdot 0.372 \cdot 29{,}0000 \cdot \varepsilon_{s,top} = 21{,}576 \cdot \varepsilon_{s,top}$

$34.68 \cdot c = 44.64 + 21{,}576 \cdot \varepsilon_{s,top}$

$34.68 \cdot c = 44.64 + 21{,}576 \cdot 0.003 \cdot (2.3125 - c) / c$

Iterating until the neutral axis depth is found, it is determined that $c = 1.808$ in.

$\varepsilon_{s,\,bottom} = 0.00768 >$ Yield strain (= 0.00207 for 60 ksi)

$\varepsilon_{s,\,top} = 0.000837 <$ Yield strain (= 0.00207 for 60 ksi)

$C = 80.82$ kips

$T_{bottom} = 44.64$ kips

$T_{top}$ = 18.06 kips

Taking moments about the NA to solve for nominal moment capacity:

$M_n^+ = C \cdot (c - \beta_1 \cdot c / 2) + T_{top} \cdot (2.3125 - c) + T_{bottom} \cdot (6.4375 - c)$

$M_n^+ = 80.82 \cdot (1.808 - 0.85 \cdot 1.808/2) + 18.06 \cdot (2.3125 - 1.808) + 44.64 \cdot (6.4375 - 1.808)$

**$M_n^+$ = 299kip-in. = 24.98 kip-ft**

**Negative Moment Capacity**

The assumed strain and stress failure profile are shown in Figure A7:

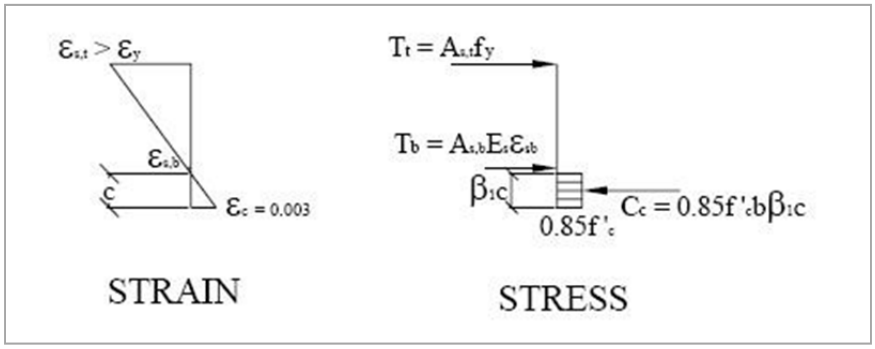


*Figure A7: Strain and stress gradients at negative moment regions*

According to ACI 318-08, it is assumed that the ultimate strain of concrete is 0.003 in./in. and the top reinforcement yields prior to failure. The bottom reinforcement is included in the calculations for accuracy. The concrete strength is taken as 4 ksi, and the reinforcement strength is taken as 60 ksi.

Let $C = T$:

$C = 0.85 \cdot fc' \cdot \beta_1 \cdot c \cdot b = 0.85 \cdot 4 \cdot 0.85 \cdot 12 \cdot c = 34.68 \cdot c$

Note: $\beta_1 = 0.85$ for 4 ksi concrete.

$\varepsilon_{s,\ bottom} = 0.003 \cdot (1.5625 - c) / c$

$\varepsilon_{s,\ top} = 0.003 \cdot (5.6875 - c) / c$

$T_{bottom} = A_{s,bottom} \cdot \varepsilon_{s,\ bottom} \cdot E_s = 2 \cdot 0.372 \cdot 29{,}0000 \cdot \varepsilon_{s,bottom} = 21{,}576 \cdot \varepsilon_{s,bottom}$

$T_{top} = A_{s,top} \cdot f_y = 2 \cdot 0.372 \cdot 60 = 44.64$ kips

$34.68 \cdot c = 44.64 + 21{,}576 \cdot \varepsilon_{s,bottom}$

$34.68 \cdot c = 44.64 + 21{,}576 \cdot 0.003 \cdot (1.5625 - c) / c$

Iterating until the neutral axis depth is found, it is determined that $c$ = 1.443 in.

$\varepsilon_{s,\ bottom}$ = 0.000248 < Yield strain (= 0.00207 for 60 ksi)

$\varepsilon_{s,\ top}$ = 0.008824 > Yield strain (= 0.00207 for 60 ksi)

$C$ = 50.04 kips

$T_{bottom}$ = 5.35 kips

$T_{top}$ = 44.64 kips

Taking moments about the NA to solve for nominal moment capacity:

$$M_n^- = C \cdot (c - \beta_1 \cdot c / 2) + T_{top} \cdot (5.6875 - c) + T_{bottom} \cdot (1.5625 - c)$$

$$M_n^- = 50.04 \cdot (1.443 - 0.85 \cdot 1.808/2) + 44.64 \cdot (5.6875 - 1.808) + 5.35 \cdot (1.5625 - 1.808)$$

$M_n^-$ = 205kip-in. = 17.13 kip-ft

**Bending and Shear Capacity Check:**

The deflected shape of the concrete deck and the bending moment diagram—assuming that the shear studs have adequate tensile capacity—is shown in Figure A8. The shear associated with the plastic deck mechanism is:

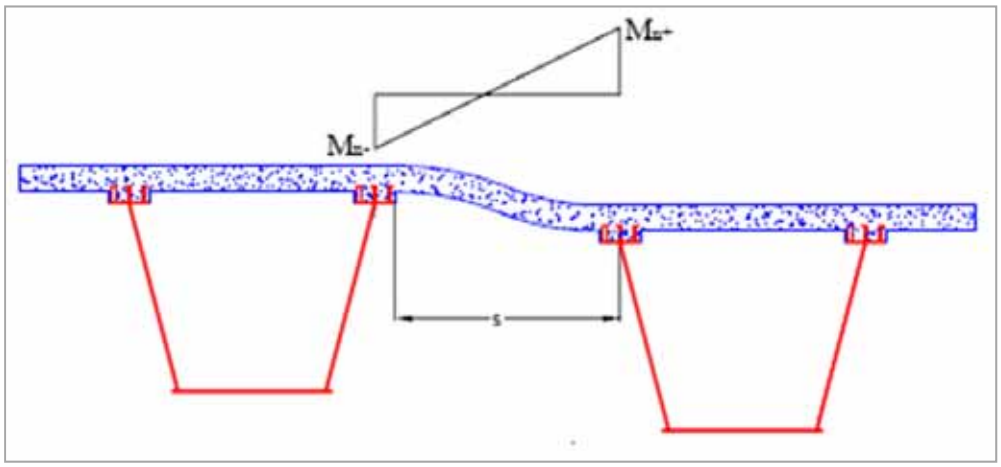


*Figure A8: Deflected shape and moment diagram before any failure of shear studs*

$$V = (M_n^+ + M_n^-)/s = (24.98 \text{ kip-ft} + 17.13 \text{ kip-ft})/6.17 \text{ ft} = \mathbf{6.83 \text{ kips}}$$

Note: The spacing, $s$, is equal to the distance between the mid-width of the fractured girder's interior top flange and the edge of the interior top flange of the intact girder (6 ft–2 in.).

The shear capacity us calculated using the ACI 3108-08 equation for shear shown below. The capacity is again based on a 1-ft wide transverse deck section. The depth used in this equation is the depth to the centroid of the tension reinforcement (6.4375 in.).

$V_c = 2 \cdot \sqrt{f'_c} \cdot b \cdot d = 2 \cdot \sqrt{4000} \cdot 12 \cdot 6.4375 =$ **9.77 kips**

Thus, the shear associated with the plastic deck mechanism controls (6.83 kips/ft), and the total length required to transfer the 672.5-kip force is:

$l_M = 672.5 / 6.83 = 98.46$ ft

98.46 / 197.6 **= 49.83 % of the span length**

**Shear Stud Check:**

In order to determine the tensile strength of a shear stud group, the guidelines recommended by Mouras (2008) are followed. The shear stud connections used in span 11 of the Woodway Bridge consist of a group of three 6-in tall shear studs spaced transversely. The haunch differs along the length of the bridge from 0.25 in. to 0.5 in. By using the modified ACI 318-08 equations presented in Chapter 3 (and shown again below for convenience), the tensile capacity of the shear stud group is calculated to be 19.06 kips throughout the bridge.

$$N_b = k_c \cdot \sqrt{f'_c} \cdot h_h^{1.5} \qquad \text{Equation 3-1 (ACI 318-08)}$$

$$N_{cbg} = \frac{A_{NC}}{A_{NCO}} \cdot \psi_{g,N} \cdot \psi_{ec,N} \cdot \psi_{ed,N} \cdot \psi_{c,N} \cdot N_b \qquad \text{Equation 3-2 (modified ACI 318-08)}$$

where:

$N_b$ = concrete cone breakout strength of a single isolated stud in a continuous piece of cracked concrete (22.31 kips)

$k_c$ = 24 for cast-in-place shear studs

$f_c'$ = specified concrete compressive strength (4000 psi)

$h_h$ = modified height of shear stud in concrete ($h_h = h_{ef} - d_h$ = 5.625-0.5=5.125 in. < 18/3=6 → $h_h$ =6 in.)

$h_{ef}$ = effective height of shear stud in concrete, which is equal to the length of stud less the height of the stud head ($h_{eff}$ =6-0.375 = 5.625in.)

$d_h$= haunch height (0.5 in.)

$c_{a,min}$ = distance between outer stud and the edge of flange ($c_{a,min}$ = 3 in.)

$N_{cbg}$ = design concrete breakout strength of a stud or group of studs (19.06 kips)

$A_{Nc}$ = projected concrete cone failure area of a stud group ($A_{Nc} = 3\ h_{ef} w_h$ = 303.75 in$^2$)

Note: $A_{Nc} = 3\ h_{ef} w_h$ because haunch confined full height projected cone area.

$A_{Nco}$ = projected concrete cone failure area of a single stud in continuous concrete ($A_{Nco}$ = $9h_h^2$ = 324 in$^2$)

$\Psi_{g,N}$ = group effect modification factor for studs on a bridge girder ($\Psi_{g,N}$ = 0.90 for 3 studs spaced transversely)

$\psi_{ec,N}$ = eccentric load modification factor ($\psi_{ec,N}$ = 1)

$\psi_{ed,N}$ = edge distance modification factor ($\psi_{ed,N}$ = 0.7+0.3 $c_{a,min}$ / (1.5 $h_{ef}$) = 0.81)

$\psi_{c,N}$ = cracked concrete modification factor ($\psi_{c,N}$ = 1.25 for cast-in studs)

The calculated tensile capacity of the group of studs is 19.06 kips. Using Equation 2-2, it can be determined whether or not the shear studs will pull out or if a hinge will be formed in the concrete deck. A strip width equal to the shear stud spacing of 21 inches is used to calculate the tension in the stud group.

$$T = M_2/b + V = 24.98 \cdot (21/12) / 7 + 6.83 \cdot (21/12) = 18.2 \text{ kips} < 19.06 \text{ kips}$$

Because the shear stud capacity exceeds the tension generated by the deck mechanism, the shear studs do not pull out, and, as a result, hinges form in the concrete deck.

**Shear Check of the Composite Section at the Supports due to Torsion and Bending:**

As described previously, it is assumed that the entire weight of the bridge and the live load are applied to the intact girder. The shear, which is developed at the end of the span due to this loading, is calculated below.

$$V = V_{DL} + V_{TRUCK} = 2 \cdot (0.958 \cdot 102.1 + 1.044 \cdot 16 + 1.116 \cdot 79.5)/2 + (2.642+0.65) \cdot 197.6/2 + 75.4$$

$V$ = 604 kips

The unsupported load, which is first carried by the fractured girder, now has to be transferred to the intact girder. The eccentricity between the chord of the intact girder bearings and the center of gravity (CG) leads to a torque that is applied to the intact girder in addition to all the transferred loads. Due to the fact that this bridge is straight (i.e., $R=\infty$), the eccentricities of each load are equal to the distance between the CG of each load and the centerline of the intact girder. Table A2 summarizes all the eccentricities.

**Table A2: Unit moment capacities of the concrete deck**

| | Live or Dead Load | Eccentricity |
|---|---|---|
| | | (ft) |
| **1** | Fractured Girder (FG) | 13.92 |
| **2** | Railing above FG | 19.83 |
| **3** | Deck above FG | 13.56 |
| **4** | Intact Girder (IG) | 0.00 |
| **5** | Railing above IG | 5.92 |
| **6** | Deck above IG | 0.35 |
| **7** | Truck | 11.17 |

Thus, the torques due to each load are equal to:

$t_{FG} = 203.24 \cdot 13.92 = 2{,}829.1$ kips·ft

$t_{RFG} = 64.22 \cdot 19.83 = 1{,}273.48$ kips·ft

$t_{DFG} = 261.03 \cdot 13.56 = 3{,}539.57$ kips·ft

$t_{IG} = 203.24 \cdot 0 = 0$ kips·ft

$t_{RIG} = 64.22 \cdot 13.92 = 893.94$ kips·ft

$t_{DIG} = 261.03 \cdot 0.35 = 91.36$ kips·ft

$t_{TRUCK} = 144 \cdot 11.17 = 1{,}608.48$ kips·ft

Therefore, the torque developed in the composite section at the support is equal to:

$T = (2{,}829.1 + 1{,}273.48 + 3{,}539.57 - 893.94 - 91.36 + 1{,}608.48) / 2 = 4{,}132.67$ kip-ft

To compute the shear flow of the closed section, Equation 2-20 is used.

$q = T / (2 \cdot A) = 4{,}132.67 / (2 \cdot 5923.68/144) = 50.23$ kips/ft $= 4.19$ kips/in

The shear stress due to torsion for every component of the composite section is calculated below:

$\tau_{CONC.\ DECK} = q / t_{CONC.\ DECK} = 4.19 / 8 = 0.52$ ksi

$\tau_{WEB} = q / t_{WEB} = 4.19 / 0.75 = 5.59$ ksi

$\tau_{BOTT.\ FLANGE} = q / t_{BOTT.\ FLANGE} = 4.19 / 1.25 = 3.35$ ksi

The flexural shear is assumed to be carried by the webs of the composite section because the contribution of the bottom flange and the concrete deck is small. The flexural shear stress in the webs of the composite section is calculated:

$\tau_{Flexural\ WEB} = V / (2 \cdot h_{WEB} \cdot t_{WEB} \cdot \cos(14°)) = 604 / (2 \cdot 88.644 \cdot 0.75 \cdot 0.97) = 4.68$ ksi

Note: The factor 2 accounts for the fact that the composite section consist of two webs, which share the total flexural shear. The cos(14°) accounts for the fact that the webs are not vertical.

The shear stress that is developed in the concrete deck due to torsion is equal to 0.52 ksi. According to ACI 318-08, the shear capacity of a reinforced concrete section is:

$V_S = A_t \cdot f_{yt} \cdot b \cdot \cot\theta / s$

As a result,

$V_{TORSION} = q \cdot b = 4.19 \cdot 84 = 351.96$ kips $\leq V_S = A_t \cdot f_{yt} \cdot b \cdot \cot\theta / s = 0.62 \cdot 60 \cdot 84 / 5 = 624.96$ kips

The shear stresses in the steel girder are checked according to the AASHTO Specifications. The shear stress in the webs of the end panel should be limited to either the shear-yielding or shear-buckling resistance. The nominal shear stress resistance of the web panel ($\tau_n$) is computed as the product of the shear-buckling resistance to the shear yield strength ratio ($C$) and the plastic shear stress ($\tau_p$) (i.e., $\tau_n = C \cdot \tau_p$). The plastic shear stress is equal to $0.58 f_{yw}$. The ratio $C$ is determined as shown below:

If $\frac{D}{t_w} \leq 1.12\sqrt{\frac{Ek}{f_{yw}}}$ then $C$=1.0

If $1.12\sqrt{\frac{Ek}{f_{yw}}} < \frac{D}{t_w} \leq 1.40\sqrt{\frac{Ek}{f_{yw}}}$ then $C = \frac{1.12}{D/t_w}\sqrt{\frac{Ek}{f_{yw}}}$

If $\frac{D}{t_w} > 1.40\sqrt{\frac{Ek}{f_{yw}}}$ then $C = \frac{1.57}{(D/t_w)^2}\left(\frac{Ek}{f_{yw}}\right)$

For span 11 of the Woodway Bridge $D$ = 88.64 in., $t_w$ =0.75 in., $E$ = 29,000 ksi, $f_{yw}$ =50 ksi. The buckling coefficient $k$ is calculated as

$$k = 5 + \frac{5}{\left(d_0 / D\right)^2}$$

where $d_0$ is the spacing from the support to the first stiffener adjacent to the support (132 in.). AASHTO limits the factor $d_0/D$ for end panels to 1.5. In the case of span 11 of the Woodway Bridge, $d_0/D$=1.49<1.5, so $d_0/D$=1.49. By inserting the value of $d_0/D$ in the equation for $k$, this value is calculated to be 7.25.

Because $\frac{D}{t_w} = \frac{88.64}{0.75} = 118.19 > 1.40\sqrt{\frac{Ek}{f_{yw}}} = 90.78$

$$C = \frac{1.57}{(D/t_w)^2}\left(\frac{Ek}{f_{yw}}\right) = 0.47 .$$

Having all the variables defined, the nominal shear stress ($\tau_n$) is equal to $\tau_n = 0.47 \cdot 0.58 \cdot f_{yw} = 13.63$ ksi.

The shear stress in the webs is a combination of the flexural and torsional shear stresses. As shown in Figure A9, the shear stresses are added and subtracted in the east and west web, respectively. Accordingly, the east web controls because the shear from flexure and torsion add. The total shear stress that is developed in the east web is calculated to be $\tau_{TOTAL} = \tau_{WEB} + \tau_{Flexural\ WEB} = 5.59 + 4.68 = 10.27$ ksi, which is less than $\tau_n = 13.63$ ksi. Summarizing the calculations, it is found that all the components of the section have adequate capacities to sustain the applied load.

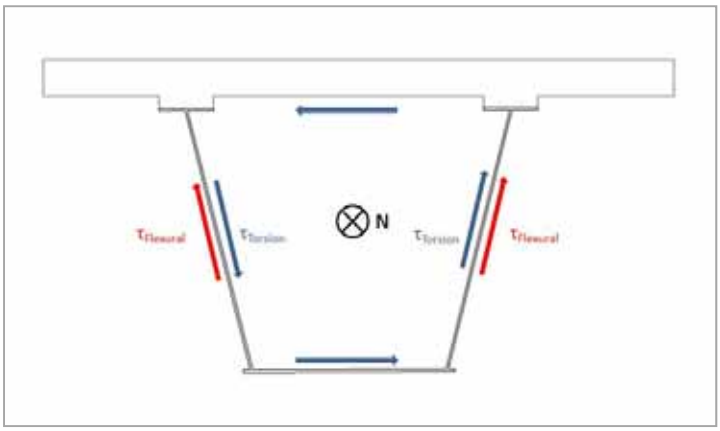


*Figure A9: Flexural and torsional shear stresses on the composite section*

The end diaphragm, which connects both girders, needs to be checked to ensure that it can adequately resist the torque applied to the intact girder. The torque applied on the intact girder is equilibrated by a force couple acting at the bearings of the two girders. This force couple causes shearing of the end diaphragm. The forces acting on each side of the end diaphragm can be calculated as follows:

$V_{ED} = T / l_b = 4{,}132.67 / 13.92 = 296.88$ kips, where $T$ is the torque applied on the intact girder and $l_b$ is the distance between the two bearings.

The nominal shear strength of the end diaphragm can be computed according to AASHTO Sec. 6.10.9.2:

$$V_n = C \cdot V_P$$

where $V_P = 0.58 \cdot F_{yw} \cdot D \cdot t_w = 0.58 \cdot 50 \cdot 86 \cdot 0.75 = 1870.5$ kips, and $C$ is calculated as

$$C = \frac{1.57}{(D/t_w)^2}\left(\frac{Ek}{f_{yw}}\right) = 0.35 \text{ because } \frac{D}{t_w} = \frac{86}{0.75} = 114.67 > 1.40\sqrt{\frac{Ek}{f_{yw}}} = 75.39 \text{ , where } k = 5.$$

Thus, the shear strength of the end diaphragm ($V_n$ = 0.35·1870.5 = 654.68 kips) is adequate to resist the applied shearing force ($V_{ED}$ = 296.88 kips).

Summarizing the calculations, it is found that all the components of the section have adequate capacities to resist the applied load, except for the shear studs. As a result, a yield line analysis needs to be performed to determine the ultimate load that this bridge can sustain. However, because the analysis indicates that overall bridge capacity is controlled by the formation of a plastic hinge line above both interior top flanges, the ultimate load is estimated from the initial checks and not from the Yield Line Model. Following the same procedure as described above, the initial checks determine the ultimate truck load that this bridge can sustain in the event of a fracture. After several iterations, it is found that the ultimate truck load is 6.03×HS-20 (434.16 kips). The buckling shear stress in the webs of the end section controls the maximum truck load that can be sustained. The moment at the mid-span of the intact girder produced by the dead load and this 434.16 kip truck load is:

$M_{P\ Middle\ Section}$ = 54,906kip-ft > $M_{max}$ = 45,866 kip-ft

$M_{P\ Transition\ Section}$ = 52,811kip-ft > $M$ (59.25) = 22,860 kip-ft

$M_{P\ End\ Section}$ = 47,063kip-ft > $M$ (51.25) = 18,677 kip-ft

The force needed to be transferred is found to be:

$F$ = (0.958·102.1 + 1.044·16 + 1.116·79.5) + (2.642+0.65) · 197.6 / 2+434.16 = 962.65 kips

$F$ = 962.65 kips

The length of the bridge needed to transfer the load $F$ based on the flexural capacity of the bridge is:

$l_M$ = 962.65 / 6.09 = 158.07 ft

158.07 / 197.6 = **80 % of the span length**

The flexural shear at the end support is found to be:

$V=V_{DL}$ + $V_{TRUCK}$=2·(0.958·102.1 + 1.044·16 + 1.116·79.5)/2 + (2.642+0.65)·197.6/2 + 227.33

$V$= 755.82 kips

The torque due to each load are equal to:

$t_{FG}$ = 203.24 · 13.92 = 2,829.1 kips·ft

$t_{RFG}$ = 64.22 · 19.83 = 1,273.48 kips·ft

$t_{DFG}$ = 261.03 · 13.56 = 3,539.57 kips·ft

$t_{IG} = 203.24 \cdot 0 = 0$ kips·ft

$t_{RIG} = 64.22 \cdot 13.92 = 893.94$ kips·ft

$t_{DIG} = 261.03 \cdot 0.35 = 91.36$ kips·ft

$t_{TRUCK} = 434.16 \cdot 11.17 = 4{,}849.57$ kips·ft

Therefore, the torque developed in the composite section at the support is equal to:

$T = (2{,}829.1 + 1{,}273.48 + 3{,}539.57 - 893.94 - 91.36 + 4{,}849.57) / 2 = 5{,}753.21$ kip-ft

Knowing the applied torque at the end support, the shear flow of the end section is calculated as:

$q = T / (2 \cdot A) = 5{,}753.21 / (2 \cdot 5923.68/144) = 69.93$ kips/ft = 5.83 kips/in

The shear stresses in the concrete deck, webs and bottom flange are computed by following the same procedure as before:

$\tau_{CONC.\ DECK} = q / t_{CONC.\ DECK} = 5.83 / 8 = 0.73$ ksi

$\tau_{WEB} = q / t_{WEB} = 5.83 / 0.75 = 7.77$ ksi

$\tau_{BOTT.\ FLANGE} = q / t_{BOTT.\ FLANGE} = 5.83 / 1.25 = 4.66$ ksi

$\tau_{Flexural\ WEB} = V / (2 \cdot h_{WEB} \cdot t_{WEB} \cdot \cos(14°)) = 755.82 / (2 \cdot 88.644 \cdot 0.75 \cdot 0.97) = 5.86$ ksi

The shear stress, which is developed in the concrete deck due to torsion, is equal to 0.73 ksi. According to ACI 318-08, the shear capacity of a reinforced concrete section is:

$V_S = A_t \cdot f_{yt} \cdot b \cdot \cot\theta / s$.

As a result,

$V_{TORSION} = q \cdot b = 5.83 \cdot 84 = 489.72$ kips $\leq V_S = A_t \cdot f_{yt} \cdot b \cdot \cot\theta / s = 0.62 \cdot 60 \cdot 84 / 5 = 624.96$ kips

As indicated previously, the total shear stress in the webs is a combination of the flexural and torsional shear stresses (Figure 9.9), and the east web controls because the shear from flexure and torsion add. The total shear stress that is developed in the east web is calculated to be:

$\tau_{TOTAL} = \tau_{WEB} + \tau_{Flexural\ WEB} = 7.77 + 5.86 = 13.63$ ksi which is equal to $\tau_n = 13.63$ ksi.

As before, the forces acting on each side of the end diaphragm can be calculated as follows: $V_{ED} = T / l_b = 5{,}753.21 / 13.92 = 413.31$ kips, where $T$ is the torque applied to the intact girder and $l_b$ is the distance between the two bearings. Thus, the shear strength in the end diaphragm ($V_n = 0.35 \cdot 1870.5 = 654.68$ kips) is adequate to resist the applied shearing force ($V_{ED} = 413.31$ kips). Summarizing the calculations, it was found that the shear stresses developed in the webs of the end section limit the ultimate load to 6.03×HS-20 Trucks (434.16 kips).

# Appendix B. Implementation of Simplified Modeling Procedure: Example 3—Analysis of Woodway Bridge (Span 17 & 18)

## Introduction

This example focuses on spans 17 and 18 of the Woodway exit ramp between IH 610 and the Katy Freeway, which is a two-span continuous bridge in Houston, TX. The length of each span is 128 ft; the radius of curvature is 3,813.72 ft for span 17 and 1,903.86 ft for span 18. Figure B1 shows the elevation view of spans 17 and 18 of the Woodway Bridge and other general information. The top and bottom flange thickness changes along the span of the bridge. Table B1 summarizes all the dimensions of both flanges along the span of the bridge. Only three steel sections are used along the length of the span. The "Transition" sections occur due to different cutoff points for the top and bottom flanges. Figures B2 and B3 present the typical cross-section of the bridge and steel girder, respectively.

**Table B1: General information of bottom and top flange**

| Span | Type of Section | Length of application measured from south | Bottom Flange | | Top Flange | |
|---|---|---|---|---|---|---|
| | | (ft) | $t_{BF}$ (in.) | $b_{BF}$ (in.) | $t_{TF}$ (in.) | $b_{BF}$ (in.) |
| 1 (17) | End | 0-80 | 7/8 | 62 | 0.75 | 14 |
| 1 (17) | Transition | 80-112 | 1 3/8 | 62 | 1 | 20 |
| 1 (17) | Pier | 112-128 | 1 3/8 | 62 | 2 | 20 |
| 2 (18) | Pier | 128-144 | 1 3/8 | 62 | 2 | 20 |
| 2 (18) | Transition | 144-176 | 1 3/8 | 62 | 1 | 20 |
| 2 (18) | End | 176-256 | 7/8 | 62 | 0.75 | 14 |

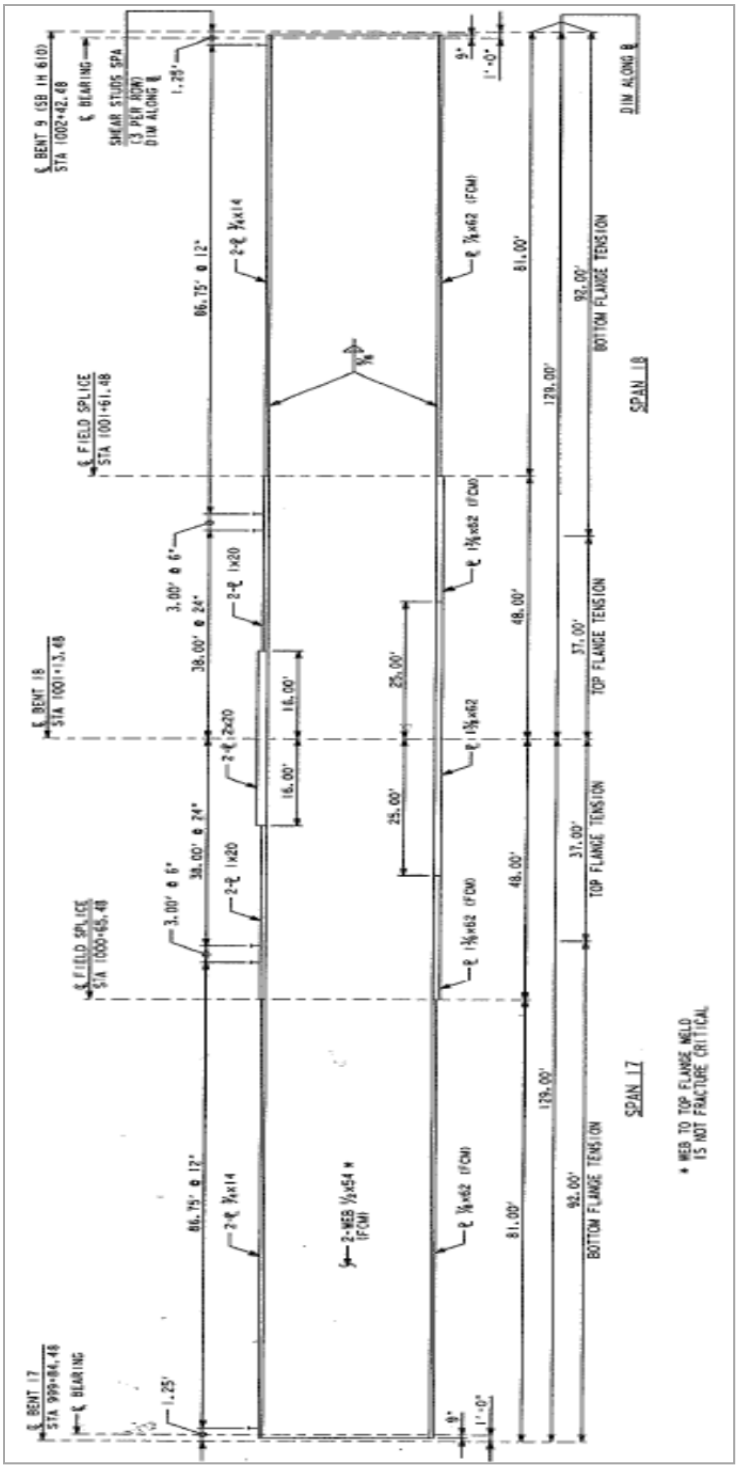


*Figure B1: Elevation view of Woodway Bridge (spans 17 and 18)*

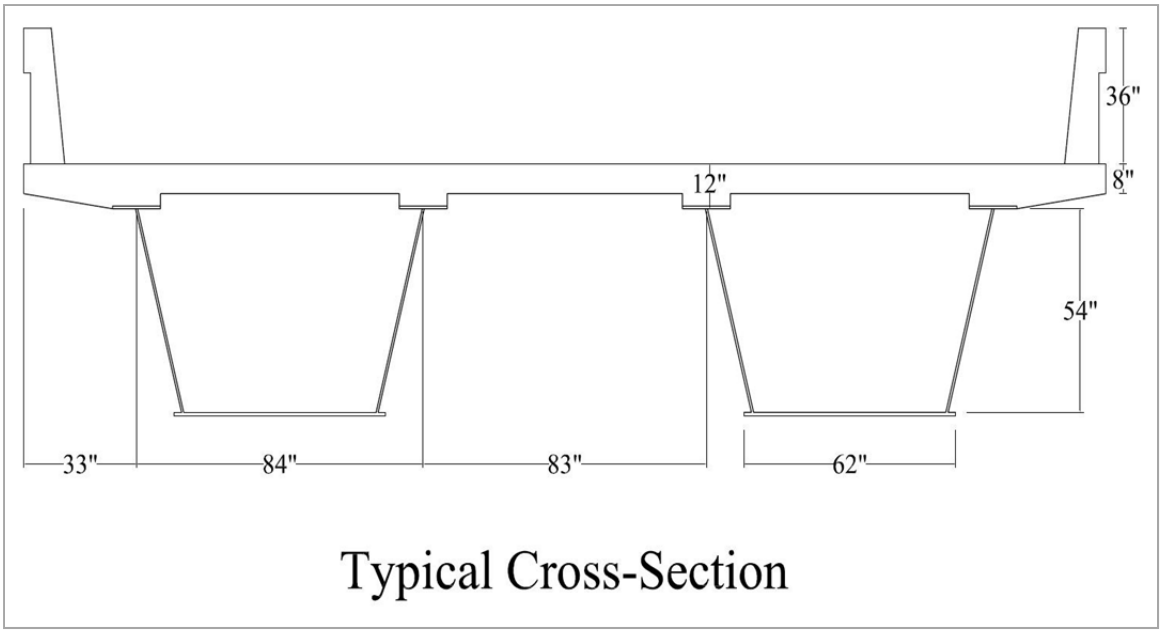


*Figure B2: Typical cross-section of spans 17 and 18 of the Woodway Bridge*

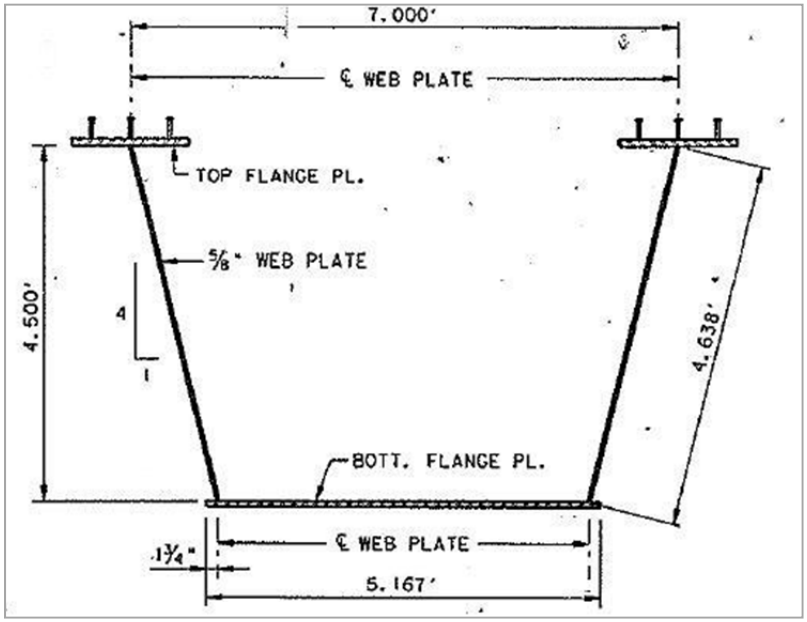


*Figure B3: Typical cross-section of the steel girder of spans 17 and 18 of the Woodway Bridge*

## Calculation of the Transmitted Load to the Intact Girder

As in the previous examples, it is assumed that half of the entire weight of the bridge and the entire live load on the bridge needs to be resisted by the intact girder in the event that a fracture occurs. These loads are calculated below:

**Weight of one steel box girder:**

$$W_{girder} = 1.15 \cdot (144.83/144 \text{ ft}^2) \cdot (0.490 \text{ kips/ft}^3) = 0.567 \text{ kip/ft (End Section)}$$

$$W_{girder} = 1.15 \cdot (194.83/144 \text{ ft}^2) \cdot (0.490 \text{ kips/ft}^3) = 0.763 \text{ kip/ft (Transitioning Section)}$$

$$W_{girder} = 1.15 \cdot (234.83/144 \text{ ft}^2) \cdot (0.490 \text{ kips/ft}^3) = 0.919 \text{ kip/ft (Pier Section)}$$

Notes: This weight is for one girder. Cross-sectional areas of End, Transition, and Pier sections are 144.83 $\text{in}^2$, 194.83 $\text{in}^2$, and 234.83 $\text{in}^2$, respectively. The density of steel is taken as 490 $\text{lb/ft}^3$. To account for internal diaphragms, stiffeners, etc., the weight of the steel girder is multiplied by a factor of 1.15.

**Concrete deck:**

$$W_{deck} = (317 \cdot 8 / 144 \text{ ft}^2) \cdot (0.150 \text{ kip/ft}^3) = 2.642 \text{ kip/ft}$$

Notes: The width of the concrete deck is 26 ft–5 in. = 317 in. The density of concrete is taken as 150 $\text{lb/ft}^3$. The deck thickness is 8 in.

**SSTR Railing:**

$$W_{railings} = 2 \cdot (312/144 \text{ ft}^2) \cdot (0.150 \text{ kip/ft}^3) = 0.65 \text{ kip/ft}$$

Notes: Multiplied by 2 to account for two rails. Cross-sectional area of one rail is calculated to be 312 $\text{in}^{2.}$

**HS-20 Truck (load factor of 2):**

$$W_{truck} = 144 \text{ kips}$$

**Load to be transmitted:**

$$F = \Sigma(W_{girder\ i} \cdot L_i) + (W_{deck}/2 + W_{railings}/2) \cdot L + W_{truck}$$

$$F = (0.567 \cdot 80 + 0.763 \cdot 32 + 0.919 \cdot 16) + (2.642 + 0.65) \cdot 128/2 + 144 = 439.17 \text{ kips}$$

$F = 439.17$ kips

## Calculation of Maximum Moment on the Bridge

Spans 17 and 18 of the Woodway Bridge were analyzed in SAP 2009 in order to indentify the location of the maximum positive bending moment. This location is where the fracture would take place. The bridge was analyzed using one moving HS-20 truck; thus, the fracture location results from the most critical location of the truck. Figure B4 illustrates the moment diagram envelope of the dead load and one moving truck. It is found that the maximum positive moment occurs at 50 ft from the south end of span 17, and its magnitude is 8448.42 kip-ft. The maximum negative moment at the inner pier is -11125.61 kip-ft.

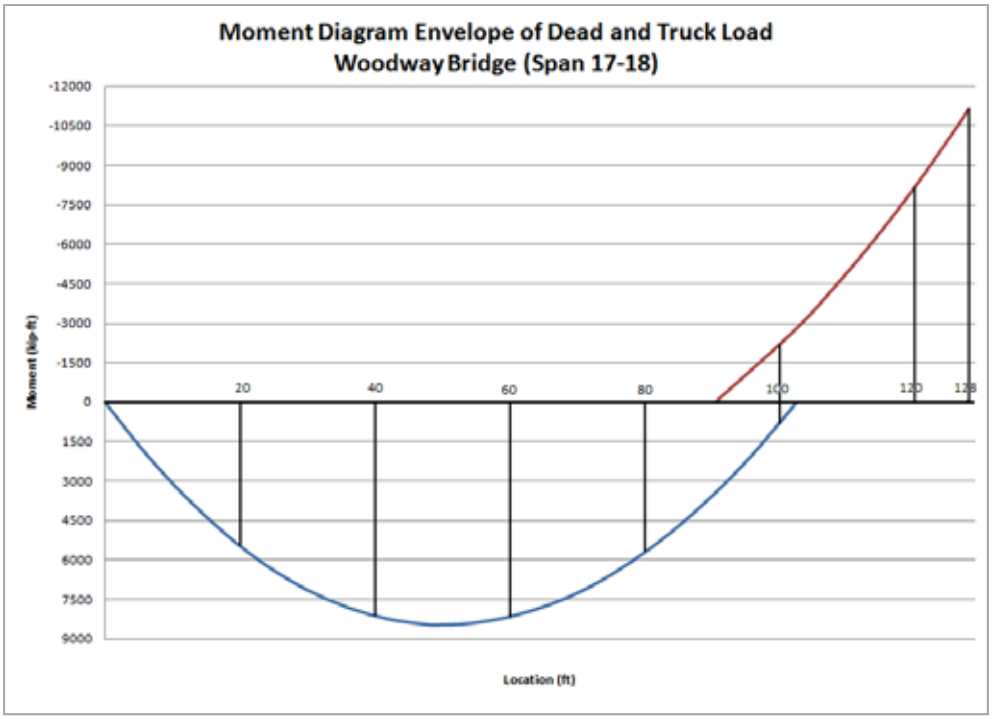


*Figure B4: Moment envelope of dead and one truck load on spans 17 and 18 of the Woodway Bridge*

## Analysis of Composite Section

The plastic moment capacity of the intact girder is calculated to determine if the intact girder has sufficient flexural capacity to sustain the entire truck and dead load applied to the bridge. The positive plastic moment capacities of the End section as well as the negative moment capacity of the Pier section are checked. Based on TxDOT minimum requirements, $f_y$ = 50 ksi is used for the components of the steel girder.

**Positive Plastic Moment Capacity of End Section:**
Find the plastic neutral axis by setting $T = C$:

$$T = A_s \cdot f_y = (62 \cdot 7/8 + 2 \cdot 55.66 \cdot 5/8 + 2 \cdot 14 \cdot 3/4) \cdot 50 = 7{,}241.25 \text{ kips}$$

$$C_c = 0.85 \cdot f_c' \cdot t_s \cdot b_{eff} = 0.85 \cdot 4 \cdot 8 \cdot 158.5 = 4{,}311.2 \text{ kips}$$

Because $T > C$, the plastic neutral axis (PNA) is in the girder.

$$C_s = (A_s \cdot f_y - C_c) / 2 = (7{,}241.25 - 4{,}311.2) / 2 = 1{,}465.03 \text{ kips}$$

Using this equation, the compressive force needed to be developed in the steel section for equilibrium ($C = T$) can be determined.

$$C_{tfl} = 2 \cdot t_{tfl} \cdot b_{tfl} \cdot f_y = 2 \cdot 3/4 \cdot 14 \cdot 50 = 1{,}050 \text{ kips}$$

The top flanges can resist 1,050 kips in compression, which is less than what is needed to obtain equilibrium. As a result, the PNA falls in the web. Assuming that $x$ is the distance from the neutral axis to the bottom of the top flange (Figure B5), the depth of the neutral axis can be found:

$$x = (1{,}465.03 - 1{,}050) / (2 \cdot 5/8 \cdot (17/16)^{0.5} \cdot 50) = 6.44 \text{ in.}$$

Note: The $(17/16)^{0.5}$ factor is based on the slope of the web.

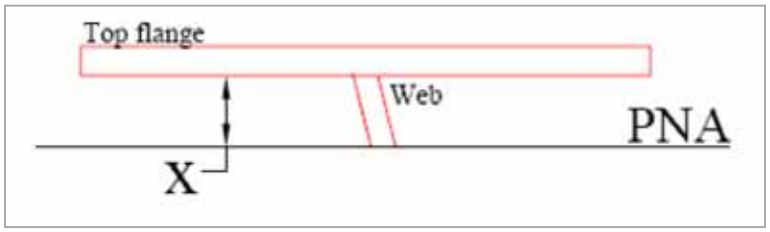


*Figure B5: Plastic neutral axis location*

Thus:

$C_c = 4{,}311.2$ kips

$C_{tfl} = 1{,}050$ kips

$C_{web} = 415.03$ kips

$T_{web} = A_{web} \cdot f_y = 2 \cdot 5/8 \cdot (54\text{-}6.44) \cdot (17/16)^{0.5} \cdot 50 = 3{,}063.98$ kips

$T_{bottom\ flange} = A_{bottom\ flange} \cdot f_y = 62 \cdot 7/8 \cdot 50 = 2{,}712.5$ kips

By taking moments about the PNA, the nominal plastic moment capacity can be calculated:

$M_{bottom\ flange} = T_{bottom\ flange} \cdot (7/16 + 54 - 6.44) = 130{,}193.22$ kip-in.

$M_{web} = C_{web} \cdot 6.44/2 + T_{web} \cdot (54 - 6.44) / 2 = 74{,}197.84$ kip-in.

$M_{C\ tfl} = C_{tfl} \cdot (3/8 + 6.44) = 7{,}155.75$ kip-in.

$M_{C\ concrete} = C_c \cdot (8/2 + 4 + 6.44) = 62{,}253.73$ kip-in.

Note: The 4-in. term added in the moment arm accounts for distance from the bottom of the concrete deck to the bottom of the top flange.
Therefore, $M_P = 130{,}193.22 + 74{,}197.84 + 7{,}155.75 + 62{,}253.73$

$M_{P\ End\ Section} = 273{,}800.54$ kip-in. $= 22{,}816.71$ kip-ft

Previously, $M^+_{max}$ was found to be 8,562.79 kip-ft. Therefore, the positive plastic moment capacity is sufficient to sustain the entire dead load of the bridge plus the truck live load.

**Negative Plastic Moment Capacity of Pier Section:**

According to AASHTO Sec. 6.11.8.2.2, the bottom flange at the pier should be checked for combined shear and compression as follows:

The slenderness ratio for the compression flange $\lambda_f = b_{fc} / t_{fc} = 57.75 / 1.375 = 42$

For $F_{yc}$= 50 ksi, $f_v$=3.23 ksi, $E$ = 29,000 ksi, $k$ = 4 and $k_s$ = 5.34

$$\Delta = \sqrt{1 - 3 \cdot \left( \frac{f_v}{F_{yc}} \right)^2} = 0.994$$

$$R_1 = \frac{0.57}{\sqrt{\frac{1}{2} \cdot \left[ \Delta + \sqrt{\Delta^2 + 4 \cdot \left( \frac{f_v}{F_{yc}} \right)^2 \cdot \left( \frac{k}{k_s} \right)^2} \right]}} = 0.571$$

$$R_2 = \frac{1.23}{\sqrt{\frac{1}{2} \cdot \left[ \frac{F_{yr}}{F_{yc}} + \sqrt{\left( \frac{F_{yr}}{F_{yc}} \right)^2 + 4 \cdot \left( \frac{f_v}{F_{yc}} \right)^2 \cdot \left( \frac{k}{k_s} \right)^2} \right]}} = 1.59$$

Because $R_1 \cdot \sqrt{\frac{k \cdot E}{F_{yc}}} = 27.5 < \lambda_f = 42 < R_2 \cdot \sqrt{\frac{k \cdot E}{F_{yc}}} = 76.58$,

$$F_{nc} = R_b \cdot R_h \cdot F_{yc} \left[ \Delta - \left( \Delta - \frac{F_{yr}}{R_h \cdot F_{yc}} \right) \left\{ 1 - \sin \left[ \frac{\pi}{2} \left( \frac{R_2 - \frac{b_{fc}}{t_{fc}} \cdot \sqrt{\frac{F_{yc}}{k \cdot E}}}{R_2 - R_1} \right) \right] \right\} \right] = 47.58 ksi$$

In order to compute the moment capacity of the pier section, the elastic section modulus of the composite cross section must be calculated. Because the contribution of concrete is negligible in the negative moment region, only the area of the reinforcing bars and the steel girder section is included in the calculation of the elastic section modulus. By using AutoCAD 2010, the moment of inertia of the pier section, neglecting the concrete portion, is calculated to be:

$I$ = 154,035.85 in$^4$ = 7.43 ft$^4$

Similarly, the distance from the extreme compressive fiber to the neutral axis is found to be:

$y_b = 28.96$ in = 2.41 ft

As a result, the elastic section modulus can be computed as the ratio of $I / y_b$

$S = I / y_b = 5{,}318.92$ in$^3$ = 3.08 ft$^3$

According to the shear–axial stress interaction equation (AASHTO Sec. 6.11.8.2.2), the allowable stress in the bottom flange is equal to 47.58 ksi. The product of the allowable stress and the elastic section modulus for the bottom flange gives the moment capacity of the pier section. Thus,

$M_{Pier\ Section}$ = 253,074.21 kip-in. = 21,089.52 kip-ft

Previously, $M_{max}$ was found to be -11125.61 kip-ft. Thus, the negative moment capacity is sufficient to sustain the entire dead load of the bridge plus the truck live load.

## Analysis of Concrete Deck

As before, the bending and shear capacity of the concrete deck need to be checked to ensure that they have sufficient capacity to resist the moment and the shear produced by the unsupported load of the fractured girder. These capacities are based on a 1-ft wide transverse deck section as shown in Figure B6.

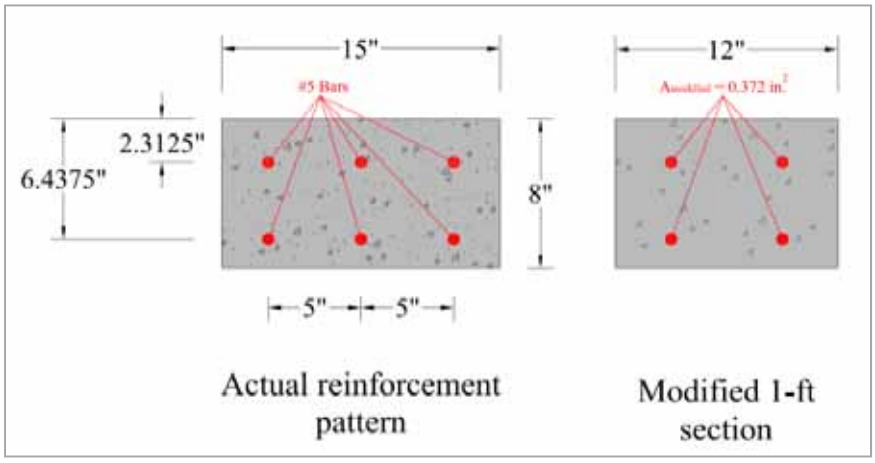


*Figure B6: Actual and modified 1-ft wide section of the concrete deck in the transverse direction*

**Positive Moment Capacity:**

The assumed strain and stress failure profile are shown in Figure B7:

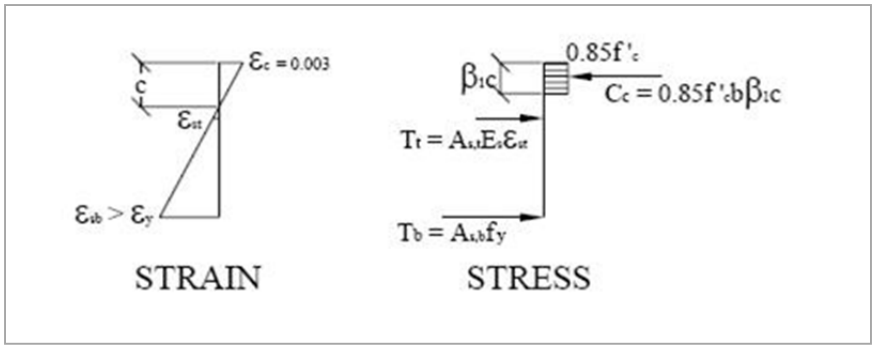


*Figure B7: Strain and stress gradients at positive moment regions*

According to ACI 318-08, it is assumed that the ultimate strain of concrete is 0.003 in./in. and the bottom reinforcement yields prior to failure. The top reinforcement is included in the calculations for accuracy. The concrete strength is taken as 4 ksi, and the reinforcement strength is taken as 60 ksi.

Let $C = T$:

$$C = 0.85 \cdot fc' \cdot \beta_1 \cdot c \cdot b = 0.85 \cdot 4 \cdot 0.85 \cdot 12 \cdot c = 34.68 \cdot c$$

Note: $\beta_1 = 0.85$ for 4 ksi concrete.

$$\varepsilon_{s,\,bottom} = 0.003 \cdot (6.4375 - c) / c$$

$$\varepsilon_{s,\,top} = 0.003 \cdot (2.3125 - c) / c$$

$$T_{bottom} = A_{s,bottom} \cdot f_y = 2 \cdot 0.372 \cdot 60 = 44.64 \text{ kips}$$

$$T_{top} = A_{s,top} \cdot \varepsilon_{s,\,top} \cdot E_s = 2 \cdot 0.372 \cdot 29{,}0000 \cdot \varepsilon_{s,top} = 21{,}576 \cdot \varepsilon_{s,top}$$

$$34.68 \cdot c = 44.64 + 21{,}576 \cdot \varepsilon_{s,top}$$

$$34.68 \cdot c = 44.64 + 21{,}576 \cdot 0.003 \cdot (2.3125 - c) / c$$

Iterating until the neutral axis depth is found, the solution is computed to be $c = 1.808$ in.

$\varepsilon_{s,\,bottom} = 0.00768 >$ Yield strain (= 0.00207 for 60 ksi)

$\varepsilon_{s,\,top} = 0.000837 <$ Yield strain (= 0.00207 for 60 ksi)

$C = 80.82$ kips

$T_{bottom} = 44.64$ kips

$T_{top} = 18.06$ kips

Taking moments about the NA to solve for nominal moment capacity

$M_n^+ = C \cdot (c - \beta_1 \cdot c / 2) + T_{top} \cdot (2.3125 - c) + T_{bottom} \cdot (6.4375 - c)$

$M_n^+ = 80.82 \cdot (1.808 - 0.85 \cdot 1.808/2) + 18.06 \cdot (2.3125 - 1.808) + 44.64 \cdot (6.4375 - 1.808)$

$M_n^+ = 299.79$ kips-in. = 24.98 kips-ft

**Negative Moment Capacity:**

The assumed strain and stress failure profile are shown in Figure B8:

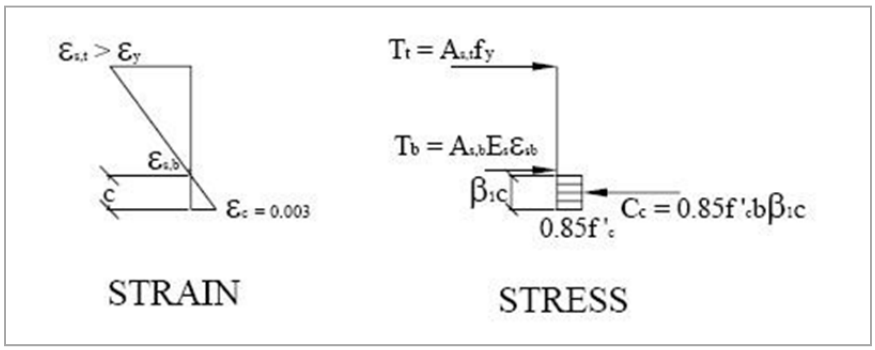


*Figure B8: Strain and stress gradients at negative moment regions*

According to ACI 318-08, it is assumed that the ultimate strain of concrete is 0.003 in./in. and the top reinforcement yields prior to failure. The bottom reinforcement is included in the calculations for accuracy. The concrete strength is taken as 4 ksi, and the reinforcement strength is taken as 60 ksi.

Let $C = T$:

$C = 0.85 \cdot fc' \cdot \beta_1 \cdot c \cdot b = 0.85 \cdot 4 \cdot 0.85 \cdot 12 \cdot c = 34.68 \cdot c$

Note: $\beta_1 = 0.85$ for 4 ksi concrete.

$\varepsilon_{s,\ bottom} = 0.003 \cdot (1.5625 - c) / c$

$\varepsilon_{s,\ top} = 0.003 \cdot (5.6875 - c) / c$

$T_{bottom} = A_{s,bottom} \cdot \varepsilon_{s,\ bottom} \cdot E_s = 2 \cdot 0.372 \cdot 29{,}0000 \cdot \varepsilon_{s,bottom} = 21{,}576 \cdot \varepsilon_{s,bottom}$

$T_{top} = A_{s,top} \cdot f_y = 2 \cdot 0.372 \cdot 60 = 44.64$ kips

$34.68 \cdot c = 44.64 + 21{,}576 \cdot \varepsilon_{s,bottom}$

$34.68 \cdot c = 44.64 + 21{,}576 \cdot 0.003 \cdot (1.5625 - c) / c$

Iterating until the neutral axis depth is found gives a solution of $c = 1.443$ in.

$\varepsilon_{s,\ bottom} = 0.000248 <$ Yield strain (= 0.00207 for 60 ksi)

$\varepsilon_{s,\,top}$ = 0.008824 > Yield strain (= 0.00207 for 60 ksi)

$C$ = 50.04 kips

$T_{bottom}$ = 5.35 kips

$T_{top}$ = 44.64 kips

Taking moments about the NA to solve for nominal moment capacity

$$M_n^- = C \cdot (c - \beta_1 \cdot c / 2) + T_{top} \cdot (5.6875 - c) + T_{bottom} \cdot (1.5625 - c)$$

$$M_n^- = 50.04 \cdot (1.443 - 0.85 \cdot 1.808/2) + 44.64 \cdot (5.6875 - 1.808) + 5.35 \cdot (1.5625 - 1.808)$$

$M_n^-$ = 205.62 kips-in. = 17.13 kips-ft

**Bending and Shear Capacity Check:**

The deflected shape of the concrete deck and the bending moment diagram—assuming that the shear studs have adequate tensile capacity—is shown in Figure B9. The shear associated with a plastic deck mechanism is

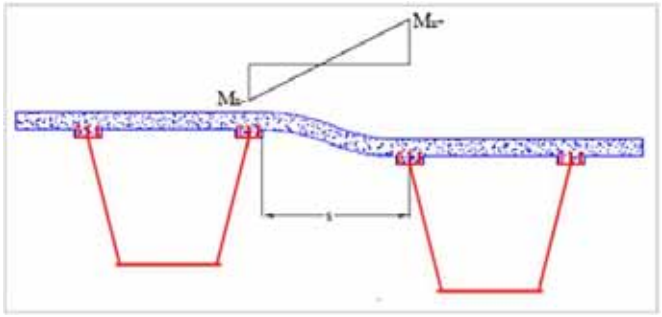


*Figure B9: Deflected shape and moment diagram before any failure of shear studs*

$$V = (M_n^+ + M_n^-)/s = (24.98 \text{ kip-ft} + 17.13 \text{ kip-ft})/6.17 \text{ ft} = \mathbf{6.82 \text{ kips}}$$

Note: The spacing, $s$, is equal to the distance between the mid-width of the fractured girder's interior top flange and the edge of the interior top flange of the intact girder (6ft 2in.).

The shear capacity is calculated using the ACI 318-08 equation for shear shown below. The capacity is based on a 1-ft wide transverse deck section. The depth used in this equation is the depth to the centroid of the tension reinforcement (6.4375 in.).

$$V_c = 2 \cdot \sqrt{f'_c} \cdot b \cdot d = 2 \cdot \sqrt{4000} \cdot 12 \cdot 6.4375 = \mathbf{9.77 \text{ kips}}$$

Thus the maximum shear capacity of the deck is equal to the shear associated with the plastic deck mechanism (6.82 kips/ft). Therefore, the total length required to transfer the 439.17-kip force is:

$l_M$ = 439.17/ 6.82 = 64.39 ft

64.72 / 128 = **50.30 % of the span length**

**Shear Stud Check:**

In order to determine the tensile strength of a shear stud group, the guidelines recommended by Mouras (2008) are followed. The shear stud connections used in spans 17 and 18 of the Woodway Bridge consist of a group of three 6-in tall shear studs spaced transversely. The haunch differs along the length of the bridge from 3.25 in. to 2 in. By using the modified ACI 318-08 equations presented in Chapter 3 (and shown again below for convenience), the tensile capacity of the shear stud group is calculated to be 16.8 kips throughout the bridge.

$$N_b = k_c \cdot \sqrt{f_c'} \cdot h_h^{1.5} \qquad \text{Equation 3-1 (ACI 318-08)}$$

$$N_{cbg} = \frac{A_{NC}}{A_{NCO}} \cdot \psi_{g,N} \cdot \psi_{ec,N} \cdot \psi_{ed,N} \cdot \psi_{c,N} \cdot N_b \qquad \text{Equation 3-2 (modified ACI 318-08)}$$

where:

$N_b$ = concrete cone breakout strength of a single isolated stud in a continuous piece of cracked concrete (15.32 kips)

$k_c$ = 24 for cast-in-place shear studs

$f_c'$ = specified concrete compressive strength (4000 psi)

$h_h$ = modified height of shear stud in concrete ($h_h = h_{ef} - d_h$ = 5.625-3.25 =2.375 in. < 14/3=4.67 in. → $h_h$ =4.67 in.)

$h_{ef}$ = effective height of shear stud in concrete, which is equal to the length of stud less the height of the stud head ($h_{eff}$ =6-0.375 = 5.625in.)

$d_h$= haunch height (3.25 in.)

$c_{a,min}$ = distance between outer stud and the edge of flange ($c_{a,min}$ = 3 in.)

$N_{cbg}$ = design concrete breakout strength of a stud or group of studs (16.8 kips)

$A_{Nc}$ = projected concrete cone failure area of a stud group ($A_{Nc}$ = 3 $h_{ef} w_h$ = 236.25 in$^2$)

Note: $A_{Nc}$ = 3 $h_{ef} w_h$ because haunch confined full height projected cone area.

$A_{Nco}$ = projected concrete cone failure area of a single stud in continuous concrete ($A_{Nco}$ = $9h_h^2$ = 196.28 in$^2$)

$\Psi_{g,N}$ = group effect modification factor for studs on a bridge girder ($\Psi_{g,N}$ = 0.90 for 3 studs spaced transversely)

$\psi_{ec,N}$ = eccentric load modification factor ($\psi_{ec,N} = 1$)

$\psi_{ed,N}$ = edge distance modification factor ($\psi_{ed,N} = 0.7+0.3\ c_{a,min} / (1.5\ h_{ef}) = 0.81$)

$\psi_{c,N}$ = cracked concrete modification factor ($\psi_{c,N} = 1.25$ for cast-in studs)

The calculated tensile capacity of the group of studs is 16.8 kips. Using Equation 2-2, the controlling failure mechanism (i.e., pull out of the shear studs or formation of a plastic hinge in the concrete deck) can be determined. A strip width equal to the shear stud spacing of 12 inches is used to calculate the tension in the stud group.

$T = 16.8$ kips, $M_2/b + V = 24.98 \cdot (12/12) / 7 + 6.82 \cdot (12/12) = 10.39$ kips

Because $T > M_2/b + V$ (i.e., shear stud capacity exceeds the tension generated by the deck mechanism), the shear studs do not pull out; as a result, hinges form in the concrete deck.

**Shear Check of the Composite Section at the Supports due to Torsion and Bending:**

As stated previously, it is assumed that the entire weight of the bridge and live load are applied to the intact girder. The shear at the abutments and at the interior pier of the bridge are 335.69 kips and 514.75 kips, respectively.

The unsupported load, which is first carried by the fractured girder, has to be transferred to the intact girder. In addition to all the transferred loads, a torque is applied to the intact girder due to the eccentricity between the chord of the intact girder bearings and the center of gravity (CG) of each load. The eccentricities of each load can be computed using Equation 2-5 through Equation 2-19. This bridge has the following geometric characteristics:

1. $R_{INT} = 1{,}896.9$ ft , $L_{INT} = 127$ ft, $\varphi = 0.06695$ rad
2. $R_{FG} = 1{,}910.82$ ft , $\theta_{0FG} = 0$ rad, $\theta_{1FG} = 0.0084$ rad, $\theta_{2FG} = 0.0251$ rad, $\theta_{3FG} = 0.067$ rad, $\overline{\theta}_{FG} = 0.0303$ rads
3. $R_{RFG} = 1{,}917.07$ ft , $\theta_{0FG} = 0$ rad, $\theta_{1FG} = 0.067$ rad, $\overline{\theta}_{FG} = 0.0335$ rad
4. $R_{DFG} = 1{,}910.72$ ft , $\theta_{0FG} = 0$ rad, $\theta_{1FG} = 0.067$ rad, $\overline{\theta}_{FG} = 0.0335$ rad
5. $R_{IG} = 1{,}896.9$ ft , $\theta_{0IG} = 0$ rad, $\theta_{1IG} = 0.0084$ rad, $\theta_{2IG} = 0.0251$ rad, $\theta_{3IG} = 0.067$ rad, $\overline{\theta}_{IG} = 0.0303$ rad
6. $R_{RIG} = 1{,}890.65$ ft , $\theta_{0FG} = 0$ rad, $\theta_{1FG} = 0.067$ rad, $\overline{\theta}_{FG} = 0.0335$ rad
7. $R_{DIG} = 1,\ 897$ ft , $\theta_{0FG} = 0$ rad, $\theta_{1FG} = 0.067$ rad, $\overline{\theta}_{FG} = 0.0335$ rad
8. $R_{TRUCK} = 1{,}911$ ft, $\theta_{0TRUCK} = 0.0335$ rad, $\theta_{1TRUCK} = 0.0482$ rad, $\overline{\theta}_{TRUCK} = 0.04085$ rad

The center of gravity of each component is found by inserting the above values in Equation 2-18.

$$\overline{D}_{FG} = 1910.45 ft$$

$$\overline{D}_{RFG} = 1916.71 ft$$

$$\overline{D}_{DFG} = 1910.36 ft$$

$$\overline{D}_{IG} = 1896.53 ft$$

$$\overline{D}_{RIG} = 1890.30 ft$$

$$\overline{D}_{DIG} = 1896.65 ft$$

$$\overline{D}_{TRUCK} = 1910.98 ft$$

By using Equation 2-19, the eccentricity of each component can be found as follows:

$e_{FG}$ = 1,910.45 - 1,896.9 · cos(0.06691/2) = 14.61 ft

$e_{RFG}$ = 1,916.71 - 1,896.9 · cos(0.06691/2) = 20.87 ft

$e_{DFG}$ = 1,910.36 - 1,896.9 · cos(0.06691/2) = 14.52 ft

$e_{IG}$ = 1,896.53 - 1,896.9 · cos(0.06691/2) = 0.69 ft

$e_{RIG}$ = 1,890.3 - 1,896.9 · cos(0.06691/2) = -5.54 ft

$e_{DIG}$ = 1,896.65 - 1,896.9 · cos(0.06691/2) = 0.81 ft

$e_{TRUCK}$ = 1,910.98 - 1,896.9 · cos(0.06691/2) = 15.14 ft

As a result, the torques due to each load are computed to be:

$t_{FG}$ = 84.48 · 14.61 = 1,234.25 kips·ft

$t_{RFG}$ = 41.6 · 20.87 = 868.19 kips·ft

$t_{DFG}$ = 169.09 · 14.52 = 2,455.19 kips·ft

$t_{IG}$ = 84.48 · 0.69 = 58.29 kips·ft

$t_{RIG}$ = 41.6 · (-5.54) = -230.46 kips·ft

$t_{DIG}$ = 169.09 · 0.81 = 136.96 kips·ft

$t_{TRUCK}$ = 144 · 15.14 = 2,180.16 kips·ft

Therefore, the torque developed in the composite section at the support is equal to:

$T$ = (1,234.25 + 868.19 + 2,455.19 + 58.29 -230.46 + 136.96 + 2,180.16) / 2 = 3,351.29 kip-ft

To compute the shear flow of the closed section, Equation 2-20 is used.

$$q = T / (2 \cdot A) = 3{,}351.29 / (2 \cdot 4{,}534.07/144) = 53.22 \text{ kips/ft} = 4.44 \text{ kips/in}$$

The shear stress due to torsion in every component of the composite section is calculated as:

$$\tau_{CONC.\ DECK} = q / t_{CONC.\ DECK} = 4.44 / 8 = 0.56 \text{ ksi}$$

$$\tau_{WEB} = q / t_{WEB} = 4.44 / 0.625 = 7.1 \text{ ksi}$$

$$\tau_{BOTT.\ FLANGE} = q / t_{BOTT.\ FLANGE} = 4.44 / 1.375 = 3.23 \text{ ksi}$$

The flexural shear is assumed to be carried by the webs of the composite section because the contribution of the bottom flange and the concrete deck is small. The flexural shear stress in the webs of the composite section is calculated below:

$$\tau_{Flexural\ WEB\ Abutm.} = V_1 / (2 \cdot h_{WEB} \cdot t_{WEB} \cdot \cos(14°)) = 335.69 / (2 \cdot 55.656 \cdot 5/8 \cdot 0.97) = 4.97 \text{ ksi}$$

$$\tau_{Flexural\ WEB\ Pier} = V_2 / (2 \cdot h_{WEB} \cdot t_{WEB} \cdot \cos(14°)) = 514.75 / (2 \cdot 55.656 \cdot 5/8 \cdot 0.97) = 7.63 \text{ ksi}$$

Note: The factor 2 accounts for the fact that the composite sections consist of two webs, which share the total flexural shear. The cos(14°) accounts for the fact that the webs are inclined.

The shear stress that develops in the concrete deck due to torsion is equal to 0.56 ksi. According to ACI 318-08, the shear capacity of a reinforced concrete section is:

$$V_S = A_t \cdot f_{yt} \cdot b \cdot \cot\theta / s.$$

Consequently,

$$V_{TORSION} = q \cdot b = 4.44 \cdot 84 = 372.96 \text{ kips} \le V_S = A_t \cdot f_{yt} \cdot b \cdot \cot\theta / s = 0.62 \cdot 60 \cdot 84/5 = 624.96 \text{ kips}$$

The shear stresses in the steel girder are checked according to the AASHTO Specifications. The shear stress in the webs of the end panel should be limited to either the shear-yielding or shear-buckling resistance. The nominal shear stress resistance of the web panel ($\tau_n$) is computed as the product of the shear-buckling resistance to the shear yield strength ratio ($C$) times the plastic shear stress ($\tau_p$) (i.e., $\tau_n = C \cdot \tau_p$). The plastic shear stress is equal to $0.58 f_{yw}$. The ratio $C$ is determined as below:

$$\text{If } \frac{D}{t_w} \le 1.12\sqrt{\frac{Ek}{f_{yw}}} \text{ then } C = 1.0$$

$$\text{If } 1.12\sqrt{\frac{Ek}{f_{yw}}} < \frac{D}{t_w} \le 1.40\sqrt{\frac{Ek}{f_{yw}}} \text{ then } C = \frac{1.12}{D/t_w}\sqrt{\frac{Ek}{f_{yw}}}$$

$$\text{If } \frac{D}{t_w} > 1.40\sqrt{\frac{Ek}{f_{yw}}} \text{ then } C = \frac{1.57}{(D/t_w)^2}\left(\frac{Ek}{f_{yw}}\right)$$

For spans 17 and 18 of the Woodway Bridge, $D$ = 55.66 in., $t_w$ =5/8 in., $E$ = 29,000 ksi, $f_{yw}$ =50 ksi. The factor $k$ is calculated as

$$k = 5 + \frac{5}{\left(d_0/D\right)^2}$$

where $d_0$ is the spacing from the support to the first stiffener adjacent to the support (128 in.). AASHTO limits the factor $d_0/D$ for end panels to 1.5. The end panel of the bridge considered in this example is located at the end of the girder, and $d_0/D$=2.30>1.5; thus, $d_0/D$=2.30. By inserting the value of $d_0/D$ in the equation for $k$, this value is calculated to be 5.95.

Because $\frac{D}{t_w} = \frac{55.66}{5/8} = 89.06 > 1.40\sqrt{\frac{Ek}{f_{yw}}} = 82.24$

$$C = \frac{1.57}{(D/t_w)^2}\left(\frac{Ek}{f_{yw}}\right) = 0.68$$

Having all the variables defined, the nominal shear stress ($\tau_n$) is computed to be $\tau_n = 0.68 \cdot 0.58 \cdot f_{yw}$ = 19.72 ksi.

The total shear stress in the webs is due to a combination of the flexural and torsional shear stresses. As shown in Figure B10, the shear stresses are added and subtracted in the east and west web, respectively. The east web controls because the shear from flexure and torsion add. The total shear stress that develops in the end panel of the east web is calculated to be $\tau_{TOTAL} = \tau_{WEB} + \tau_{Flexural\ WEB}$ = 7.1 + 7.63 = 14.73 ksi at the abutment and $\tau_{TOTAL} = \tau_{WEB} + \tau_{Flexural\ WEB}$ = 7.1 + 4.97 = 12.07 ksi at the interior pier. Both values are less than $\tau_n$ =19.72 ksi based on AASHTO Specifications. Summarizing the calculations, it is found that all the components of the section have adequate capacities to sustain the applied load.

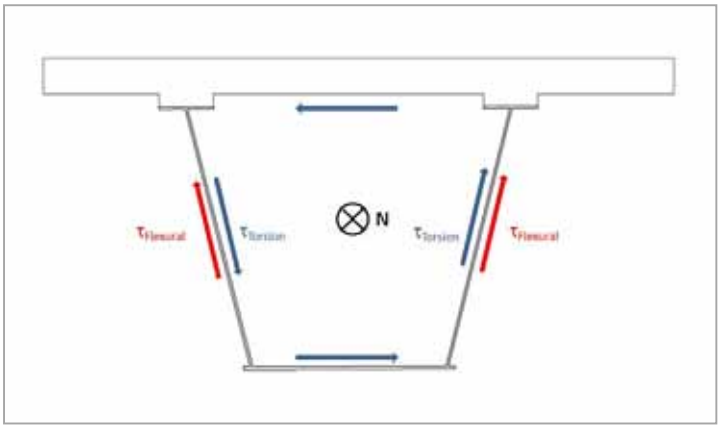


*Figure B10: Flexural and torsional shear stresses on the composite section*

The end diaphragm, which connects both girders, must be checked to ensure that it has adequate capacity to resist the torque applied to the intact girder. This torque is equilibrated through the reaction forces acting at the bearings, and these reaction forces cause shearing in the end diaphragm. The forces acting on each side of the end diaphragm can be calculated as follows:

$V_{ED} = T / l_b = 3{,}351.29 / 13.92 = 240.75$ kips, where $T$ is the torque applied on the intact girder and $l_b$ is the distance between the two bearings. The nominal shear strength of the end diaphragm can be computed according to AASHTO Sec. 6.10.9.2.

$V_n = C \cdot V_P$, where $V_P = 0.58 \cdot F_{yw} \cdot D \cdot t_w = 0.58 \cdot 50 \cdot 52.38 \cdot 0.75 = 1139.27$ kips, $k$=5, and $C$ is calculated as $C = \dfrac{1.12}{D/t_w}\sqrt{\dfrac{Ek}{f_{yw}}} = 0.86$ because

$$1.12\sqrt{\frac{Ek}{f_{yw}}} = 60.31 < \frac{D}{t_w} = \frac{52.38}{0.75} = 69.84 < 1.40\sqrt{\frac{Ek}{f_{yw}}} = 75.39$$

Thus, the shear strength of the end diaphragm ($V_n$ = 0.86·1139.27 = 979.77 kips) is adequate to resist the applied shearing force ($V_{ED}$ = 240.75 kips).

Because the analysis presented above indicates that the capacity of this bridge is controlled by the formation of a plastic hinge line above both interior top flanges, the ultimate load is estimated from the initial checks and not from the Yield Line Model. Following the same procedure as described in Example 2, the initial checks determine the ultimate truck load that this bridge will sustain in the event of a fracture. After several iterations, it is found that the ultimate truck load is 4.30×HS-20 (309.6 kips). The buckling shear stress in the webs of the end section controls the maximum truck load that this bridge can sustain. The moment at the mid-span of the intact girder produced by the dead load and this 309.6-kip truck load is:

$M_{P\ End\ Section} = 22{,}816.71$ kip-ft $> M^{+}_{max} = 12{,}211$ kip-ft

The bottom flange at the pier section needs to be checked for torsion and bending. According to AASHTO Sec. 6.11.8.2.2, the slenderness ratio for the compression flange is

$\lambda_f = b_{fc} / t_{fc} = 57.75 / 1.375 = 42$

For $F_{yc}$= 50 ksi, $f_v$=4.43 ksi, $E$ = 29,000 ksi, $k$ = 4 and $k_s$ = 5.34

$$\Delta = \sqrt{1 - 3 \cdot \left(\frac{f_v}{F_{yc}}\right)^2} = 0.988$$

$$R_1 = \frac{0.57}{\sqrt{\frac{1}{2} \cdot \left[\Delta + \sqrt{\Delta^2 + 4 \cdot \left(\frac{f_v}{F_{yc}}\right)^2 \cdot \left(\frac{k}{k_s}\right)^2}\right]}} = 0.572$$

$$R_2 = \frac{1.23}{\sqrt{\frac{1}{2}\cdot\left[\frac{F_{yr}}{F_{yc}} + \sqrt{\left(\frac{F_{yr}}{F_{yc}}\right)^2 + 4\cdot\left(\frac{f_v}{F_{yc}}\right)^2\cdot\left(\frac{k}{k_s}\right)^2}\right]}} = 1.594$$

Because $R_1 \cdot \sqrt{\frac{k\cdot E}{F_{yc}}} = 27.55 < \lambda_f = 42 < R_2 \cdot \sqrt{\frac{k\cdot E}{F_{yc}}} = 76.78$,

$$F_{nc} = R_b \cdot R_h \cdot F_{yc}\left[\Delta - \left(\Delta - \frac{F_{yr}}{R_h \cdot F_{yc}}\right)\left\{1 - \sin\left[\frac{\pi}{2}\left(\frac{R_2 - \frac{b_{fc}}{t_{fc}}\cdot\sqrt{\frac{F_{yc}}{k\cdot E}}}{R_2 - R_1}\right)\right]\right\}\right] = 47.31 ksi$$

As before, the moment capacity of the pier section is equal to the product of the elastic section modulus and the allowable stress. The elastic section modulus remains constant and is equal to:

$S = I / y_b = 5{,}318.92 \text{ in}^3 = 3.08 \text{ ft}^3$

According to AASHTO Sec. 6.11.8.2.2, the allowable stress in the bottom flange is equal to 47.31 ksi. Thus, the moment capacity of the pier section is equal to:

$M_{Pier\ Section} = 251{,}638.10$ kip-in. $= 20{,}969.84$ kip-ft $> M_{max} = 13{,}107$ kip-ft

Thus, the negative plastic moment capacity has sufficient capacity to sustain the entire dead load of the bridge plus the truck live load.
The force needed to be transferred is found to be:

$F = (0.567 \cdot 80 + 0.763 \cdot 32 + 0.919 \cdot 16) + (2.642 + 0.65) \cdot 128/2 + 309.6 = 604.77$ kips

$F = 604.77$ kips

The length of the bridge needed to transfer the load $F$ based on the flexural capacity of the bridge is:

$l_M = 604.77 / 6.82 = 88.68$ ft

$88.68 / 128 =$ **69.28 % of the span length**

The flexural shear at the abutment and the interior support is found to be:

$V_{Abutm} = V_{DL} + V_{TRUCK} = 214.63 + 260.27$, $V_{Abutm} = 474.9$ kips

$V_{Pier} = V_{DL} + V_{TRUCK} = 377.14 + 295.86$, $V_{Pier} = 673$ kips

The torques associated with each load are:

$t_{FG}$ = 84.48 · 14.61 = 1,234.25 kips·ft

$t_{RFG}$ = 41.6 · 20.87 = 868.19 kips·ft

$t_{DFG}$ = 169.09 · 14.52 = 2,455.19 kips·ft

$t_{IG}$ = 84.48 · 0.69 = 58.29 kips·ft

$t_{RIG}$ = 41.6 · -5.54 = -230.46 kips·ft

$t_{DIG}$ = 169.09 · 0.81 = 136.96 kips·ft

$t_{TRUCK}$ = 309.6 · 15.14 = 4,687.34 kips·ft

Therefore, the torque developed in the composite section at the support is equal to:

$T$ = (1,234.25 + 868.19 + 2,455.19 + 58.29 -230.46 + 136.96 + 4,687.34) / 2 = 4,604.88 kip-ft

To compute the shear flow of the closed section, Equation 2-20 is used.

$q = T / (2 \cdot A)$ = 4,604.88 / (2 · 4,534.07/144) = 73.12 kips/ft = 6.09 kips/in

The shear stresses in the concrete deck, webs, and bottom flange are computed by following the same procedure as before:

$\tau_{CONC.\ DECK} = q / t_{CONC.\ DECK}$ = 6.09 / 8 = 0.76 ksi

$\tau_{WEB} = q / t_{WEB}$ = 6.09 / 0.625 = 9.74 ksi

$\tau_{BOTT.\ FLANGE} = q / t_{BOTT.\ FLANGE}$ = 6.09 / 1.375 = 4.43 ksi

$\tau_{FlexuralWEB\ Abutm.} = V_{Abutm} / (2 \cdot h_{WEB} \cdot t_{WEB} \cdot \cos(14°))$ = 474.9 / (2·55.656·5/8·0.97) = 7.04 ksi

$\tau_{FlexuralWEB\ Pier} = V_{Pier} / (2 \cdot h_{WEB} \cdot t_{WEB} \cdot \cos(14°))$ = 673 / (2·55.656·5/8·0.97) = 9.98 ksi

The shear stress that develops in the concrete deck due to torsion is equal to 0.76 ksi. According to ACI 318-08, the shear capacity of a reinforced concrete section is:

$V_S = A_t \cdot f_{yt} \cdot b \cdot \cot\theta / s$.

Thus,

$V_{TORSION} = q \cdot b$ = 6.09·84 = 511.56 kips ≤ $V_S = A_t \cdot f_{yt} \cdot b \cdot \cot\theta / s$ = 0.62·60·84/5 = 624.96 kips

As stated previously, the shear stress in the webs is a combination of the flexural and torsional shear stress, and the response of the east web controls because the shear from flexure and torsion add. The total shear stress that develops in the east web is calculated to be:

$\tau_{TOTAL\ Abutm} = \tau_{WEB} + \tau_{FlexuralWEB\ Abutm} = 9.74 + 7.04 = 16.78$ ksi $< \tau_n = 23.49$ ksi.

$\tau_{TOTAL\ Pier} = \tau_{WEB} + \tau_{FlexuralWEB\ Pier} = 9.74 + 9.98 = 19.72$ ksi $= \tau_n = 19.72$ ksi.

The end diaphragm, which connects both girders, has adequate capacity to resist the torque applied to the intact girder.

$V_{ED} = T / l_b = 4{,}604.88 / 13.92 = 330.81$ kips, where $T$ is the torque applied on the intact girder and $l_b$ is the distance between the two bearings. Thus, the shear strength of the end diaphragm ($V_n = 0.86 \cdot 1139.27 = 979.77$ kips) is adequate to resist the applied shearing force ($V_{ED} = 330.81$ kips). Finally, it is found that the ultimate load is equal to 4.30×HS-20 Trucks (309.6 kips).